A STUDY OF THE EFFECTS OF IRON DEFICIENCY ON CARDIAC FUNCTION

A THESIS SUBMITTED FOR THE DEGREE OF DOCTOR OF PHILOSOPHY

UNIVERSITY OF OXFORD



YU JIN CHUNG

UNIVERSITY COLLEGE

MICHAELMAS TERM 2017

For Mom and Dad

Gold is for the mistress — silver for the maid —

Copper for the craftsman cunning at his trade.

'Good!' said the Baron, sitting in his hall,

But Iron — Cold Iron — is master of them all

Cold Iron by Rudyard Kipling

ACKNOWLEDGMENTS

First, I would like to take a moment to acknowledge and appreciate the mice whose lives were sacrificed in order to carry out the studies that make up this thesis. My hope is that the scientific content presented here will add to and benefit our current understanding of cardiac iron deficiency such that their sacrifice was worthwhile.

The research presented in this thesis was supported by **Vifor Pharmaceuticals**. Thank you very much for the generous funding that made this work possible.

My time at Oxford would not have been so enjoyable and successful had it not been for the many wonderful people I have met along the way. I am very fortunate to have been a part of two outstanding laboratories at Oxford, the Robbins and Swietach groups. To **Peter, and Pawel**, I am forever grateful for your unwavering support, unlimited patience and for giving me the opportunity to be a part of your team. I have learned and grown so much, and it is all thanks to your excellent mentorship over the past few years. To **Keith**, thank you for always lending an ear and guiding me onto the right path when times were rough. **Caleb, Lisa and Carolyn**, thank you very much for your scientific guidance when it came to bioinformatics, metabolism and MRI.

Kate and Magda, I cannot thank you enough for all of your scientific support and all the fun times we had in and out of the lab. **Mark and Aminah**, this last year would not have been the same without you. Our morning coffee runs, spontaneous outings and friendly banter has gotten me through what was definitely the most difficult year of my DPhil. **Antao**, you are the master of patching. I am sorry for "cells no good" a lot of the times and thank you so much for your experimental contributions – Chapter 6 would not be the same without you! Many thanks to **David (DOC and DON), Matthew and Peter S.**, for always sharing your scientific wisdom and numerous life lessons. Finally, **Vincent**, thank you for listening to all my complaining; you are the wise one of the two of us. I can say with confidence that I am truly blessed to have had you all in my life.

To **Einar**, my wonderful and most amazing fiancé, thank you for helping me through the good, the bad and the ugly that these past few years have brought upon us. Thank you for keeping me grounded and keeping me sane. You are my rock and I love you so much.

Last but not least, to **Mom and Dad** – words cannot describe how thankful I am for your unconditional love and support. Thank you for raising me well and always believing in me. You are the best parents any child could ask for. I love you and I dedicate this thesis to you.

ABSTRACT

Yu Jin Chung *DPhil Thesis*

University College *Michaelmas Term 2017*

A STUDY OF THE EFFECTS OF IRON DEFICIENCY ON CARDIAC FUNCTION

The research presented in this thesis is an interdisciplinary study of the effects of iron deficiency on cardiac physiology. The aim of the study was to gain insight into the mechanism by which cardiac function is affected by iron deficiency, induced through the administration of an iron-deficient diet, on a murine model.

Chapter 3 of this thesis introduces the mouse model, demonstrating that the administration of an iron-deficient diet does lead to iron deficiency, and in some animals, anaemia. It also provides *in vivo* evidence of impairment of heart function in iron-deficient animals. Alterations in cardiac function could be rescued by correction of the iron deficiency by intravenous iron supplementation.

Chapter 4 describes the study which investigated the effects of iron deficiency on the cardiac gene expression profile using RNA-sequencing technology. This study revealed that the administration of an iron-deficient diet leads to many genome-wide changes, some of which are likely to be related to the cell's stress response.

Chapter 5 presents the study into cardiac metabolism. Iron-deficient hearts were found to have increased glycolytic flux and lactate production. Alterations in metabolism occurred in the absence of changes in mitochondrial numbers or morphology. Instead, the proposed mechanism for changes in cardiac energetics is hypoxia of the cardiac tissue.

Chapter 6 reports the findings of the study which explored the effects of an iron-deficient diet on the cardiac calcium signaling pathway. Iron deficiency was associated with higher diastolic calcium levels and decreased calcium transient amplitude, which could be prevented by reversal of iron deficiency by intravenous supplementation of iron.

Overall, this thesis provides evidence that severe iron-deficiency anaemia is sufficient to cause modest impairment of cardiac function and that this functional impairment is the result of complex alterations that occur at the genetic, metabolic and signaling level.

ABBREVIATIONS USED IN THIS THESIS

[Hb]	Blood haemoglobin concentration
2OG	2-oxoglutarate
ACC	Acetyl-CoA carboxylase
ALAT	Alanine amino transferase
AM	Acetoxymethyl
AMPK	5'-AMP activated protein kinase
ASPA	Animals (Scientific Procedures) Act of 1986
BMP	Bone morphogenic protein
bp	Base pairs
BSA	Bovine serum albumin
cAMP	Cyclic adenosine monophosphate
CA	Carbonic anhydrase
CaT	Ca^{2+} transient
Ca_v1	L-type Ca^{2+} channel (*also LTCC*)
CBRG	Computational Biology Research Group
cDNA	Complimentary DNA
CHF	Chronic heart failure
CICR	Ca^{2+}-induced Ca^{2+}-release
CO	Cardiac output
CoA	Coenzyme A
COX4	Cytochrome oxidase subunit 4
CPT	Carnitine palmitoyltranferase
DCYBT	Duodenal cytochrome B
DCIP	Dichlorophenolindohenol
DE	Differentially expressed
DFO	Desferrioxamine
DMT-1	Divalent metal transporter 1

EC	Excitation contraction
ECG	Electrocardiogram
EDS	End-systolic volume
EDV	End-diastolic volume
EF	Ejection fraction
EPO	Erythropoiesis
ERFE	Erythroferrone
ESR	Environmental stress response
ETC	Electron transport chain
FA	Fatty acid
FAD+	Oxidized $FADH_2$
$FADH_2$	Reduced flavin adenine dinucleotide
FCM	Ferric carboxymaltose
FHL1	Four-and-a-half LIM domain 1
FLVCR1	Feline leukemia virus subgroup C receptor 1
FPN	Ferroportin
GAGE	Generally Applicable Gene Set Enrichment
gDNA	Genomic DNA
GLUT	Glucose transporter
GO	Gene Ontology
H3K	Histone 3 lysine
HAT	Histone acetyltransferase
HCP1	Haem carrier protein 1
HDAC	Histone deacetylase
HF	Heart failure
HFE	High iron (Fe)
HH	Hereditary haemachromatosis
HIF	Hypoxia inducible factor
HJV	Hemojuvelin
HK	Hexokinase
HMT	Histone methyltransferase

HRE	Hypoxia response element
HRP	Horse radish peroxide
HSP90	Heat shock protein 90
I_{LTCC}	L-type Ca^{2+} current
IA+FCM	Iron-adjusted mice supplemented with FCM
IAD	Iron-adjusted diet
ICP-MS	Inductively coupled plasma-mass spectrometry
ID+FCM	Iron-deficient mice supplemented with FCM
IDD	Iron-deficient diet
IL-6	Interleukin 6
IRE	Iron response element
IRIDA	Iron-refractory iron-deficiency anaemia
IRP	Iron response protein
IV	Intravenous
IVC	Individually ventilated cages
KDM	Lysine demethylase
KEGG	Kyoto Encyclopedia of Genes and Genomes
KME	KCl, Mops and EGTA
LDH	Lactate dehydrogenase
LIP	Labile iron pool
LTCC	L-type Ca^{2+} channel
LV	Left ventricle
LVEF	Left ventricular ejection fraction
MAPK	Mitogen activated protein kinase
MCD	Malonyl-CoA decarboxylase
MCU	Mitochondrial Ca^{2+} uniporter
mm10	Mouse reference genome 10
mNCE	Mitochondrial Na^{+}/Ca^{2+} exchanger
mNHE	Mitochondrial Na^{+}/H^{+} exchanger
MR	Magnetic resonance
MRI	Magnetic resonance imaging

mRNA	Messenger RNA
MRS	Magnetic resonance spectroscopy
mtDNA	Mitochondrial DNA
NAD+	Oxidized NADH
NADH	Reduced nicotinamide adenine dinucleotide
NCX	$Na+/Ca^{2+}$-exchanger
NFAT	Nuclear factor of activated T-cells
NGS	Next generation sequencing
NMR	Nuclear magnetic resonance
NRAMP1	Natural resistance associated macrophage protein 1
NTBI	Non-transferrin-bound iron
PBS	Phosphate buffered saline
PC	Principal component
PCA	Principal component analysis
PCFT	Proton-coupled folate transporter
PCr	Phosphocreatine
PDK	Pyruvate dehydrogenase
PFKM	Phosphofructokinase, muscle
PHD	Prolyl hydroxylase domain
PKA	Protein kinase A
PKC	Protein kinase C
PLN	Phospholamban
PMCA	Sarcolemmal Ca^{2+} ATPase
PP	Phosphoprotein phosphatase
Pro	Proline
PTM	Post-translational modification
PVDF	Polyvinylidene fluoride
PXLE	Pro-X-Leu-Glu motif
REVIGO	Reduce + visualize Gene Ontology
RIN	RNA integrity number
RNA-seq	RNA-sequencing

ROS	Reactive oxygen species
RV	Right ventricle
RVEF	Right ventricular ejection fraction
RyR2	Ryanodine receptor 2
SAM	Sequence Alignment/Map
SDS	Sodium dodecyl sulfate
SEM	Standard error of the mean
SERCA	Sarco/endoplasmic reticulum Ca^{2+} ATPase
sFe	Serum iron
sFt	Serum ferritin
SLN	Sarcolipin
SR	Sarcoplasmic reticulum
STAR	Spliced Transcripts Alignment to a Reference
sTf	Serum transferrin
SV	Stroke volume
TCA	Citric acid cycle
TEM	Transmission electron microscopy
TfR	Transferrin receptor
TMPRSS6	Matriptase-2 protein (transmembrane protease, serine 6)
TNF-α	Tumor necrosis factor α
TSat	Transferrin saturation
ub	Ubiquitin
UTR	Untranslated region
VHL	von Hippel Lindau
WTSS	Whole transcriptome shotgun sequencing
ZIP	Zirt/Irt-like protein

Gene name	**Protein name**
Actb	β-actin
Atp2a2	SERCA
Bmp6	BMP6
Cacna1c	LTCC
Cybrd1	DCYTB
Dmt1	DMT1
Epas	HIF-2α
Fpn	FPN
Gapdh	GAPDH
Hamp	Hepcidin
Heph	Hephaesin
Hfe	HFE
Hfe2	HJV
Ryr2	RyR2
Slc11a2	DMT1
Slc40a1	FPN
Slc8a1	NCX
Tfr1 or *Tfrc*	TfR1
Tmprss6	TMPRSS6
Ubc	Ubiquitin C

STATEMENT OF AUTHORSHIP

The work presented in this thesis is solely the work of the submitter of the thesis, Yu Jin Chung, with the following exceptions:

1. Chapter 3 – ICP-MS was conducted by Mr Phil Holdship at the Department of Earth Sciences, University of Oxford, as a paid service. This was due to the necessity for specialised equipment.
2. Chapter 4 – cDNA library preparation and RNA-sequencing was conducted by the Oxford Genomics Centre at the Wellcome Trust Centre for Human Genetics, University of Oxford, as a paid service. This was due to the necessity for specialised equipment.
3. Chapter 6 – Measurement of L-type Ca^{2+} current using a voltage clamp protocol was carried out as part of a collaboration by Dr Antao Luo, a member of the Swietach group at the Department of Physiology, Anatomy and Genetics, University of Oxford.

Of note, only the assay itself was conducted by the respective individuals, while all experimental planning, sample preparation and post-experimental analysis was conducted by the submitter of this thesis.

Furthermore, all diagrams and figures found in this thesis are original creations of the submitter of this thesis, and were generated using Adobe Illustrator.

TABLE OF CONTENTS

ACKNOWLEDGMENTS i

ABSTRACT ii

ABBREVIATIONS USED IN THIS THESIS iii

STATEMENT OF AUTHORSHIP ix

TABLE OF CONTENTS x

LIST OF FIGURES AND TABLES xviii

CHAPTER 1 : GENERAL INTRODUCTION 1

1.1 Iron physiology 2

1.1.1 Iron distribution in the body 3

1.1.2 Iron absorption 4

1.1.3 Iron transport and delivery to tissues 5

1.1.4 Iron storage 6

1.1.5 Iron recycling 7

1.2 Mechanisms of iron homeostasis 8

1.2.1 Systemic iron homeostasis: The hepcidin/FPN axis 8

1.2.2 Regulation of intracellular iron utilization 10

1.3 Causes and consequences of iron imbalance 12

1.3.1 Iron overload 12

1.3.2 Iron deficiency 14

i) The epidemiology and prevalence of iron deficiency 14

ii) Causes of iron deficiency 14

1.4 Clinical measurement of iron status 16

1.5 Iron in the heart 18

1.5.1 Iron homeostasis in the heart 18
1.5.2 Iron overload and cardiac disease 18
1.5.3 Iron deficiency and cardiac disease 19
1.6 Interplay between iron and oxygen homeostasis 20
1.6.1 The hypoxia inducible factor and the oxygen sensing pathway 20
1.6.2 Hypoxia and iron homeostasis 23
1.6.3 Alternative links between oxygen and iron 24
1.7 Summary and thesis aims 25

CHAPTER 2 : ANIMAL MODEL AND GENERAL METHODS 26

2.1 Chapter overview 26
2.2 Mouse model 27
2.2.1 General animal housing and breeding 27
2.2.2 Dietary model of systemic iron deficiency 27
2.3 Experimental Methods 28
2.3.1 Frozen tissue preparation 28
2.3.2 Adult primary cardiomyocyte isolation 28
2.3.3 SDS-PAGE and Western blotting 30
2.3.4 RNA extraction and cDNA synthesis 31
2.3.5 Genomic DNA extraction 31
2.3.6 Quantitative real-time PCR (qPCR) 31
2.3.7 Statistical analysis 33

CHAPTER 3 : PHYSIOLOGICAL CONSEQUENCES OF IRON DEFICIENCY 34

3.1 Chapter overview 34
3.2 Introduction 35
3.2.1 Iron, iron deficiency and cardiac function 35
3.2.2 Iron deficiency in chronic heart failure 35
3.2.3 Iron supplementation in chronic heart failure 36
3.2.4 Monitoring cardiac function in mice using magnetic resonance imaging 37

3.2.5 Study aims 38

3.3 Methods 39

3.3.1 Mouse model 39

3.3.2 Blood sampling 40

3.3.3 Quantitative PCR 40

3.3.4 Cine-MR imaging 41

3.3.5 Pentra chemical analysis 44

3.3.6 Isolation of primary cardiomyocytes 44

3.3.7 Inductively coupled plasma-mass spectrometry 44

3.3.8 Immunofluorescence 45

3.4 Results 47

3.4.1 Characterisation of a dietary model of iron deficiency 47

i) Effects on body mass and blood haemoglobin (Cohort 1) 47

ii) Effects on physiological iron status (Cohort 2) 49

iii) Long-term consequence of an iron-deficient diet (Cohorts 1-3) 51

iv) Effect of iron supplementation on iron status of iron-deficient animals (Cohort 4) 52

v) Determination of total elemental iron in tissues following an iron-deficient diet 55

vi) Effects of an iron-deficient diet on the hepcidin/FPN axis. 59

3.4.2 Effects of iron deficiency on cardiac function 61

i) Serial measures of cardiac function during the course of dietary iron restriction (Cohort 1) 61

ii) Effect of iron supplementation on cardiac function (Cohort 4) 69

3.5 Discussion 75

3.5.1 Validation of a mouse model of iron deficiency through diet 75

i) Abnormal body mass and haemoglobin due to an iron-deficient diet 75

ii) Serum and tissue iron status and cellular iron homeostasis 77

iii) Iron supplementation rescues iron status 79

iv) Implications of the current study 79

3.5.2 Iron deficiency and iron supplementation on cardiac function 81

i) Iron deficiency alters cardiac function 81

ii) Iron supplementation improves cardiac dysfunction 83

iii) Ageing reduces cardiac efficiency 84

3.5.3 Limitations of the current study 85

3.6 Conclusions 86

CHAPTER 4 : CONSEQUENCES OF IRON DEFICIENCY ON THE CARDIAC GENE EXPRESSION 87

4.1 Chapter overview 87

4.2 Introduction 88

4.2.1 Genomic basis of cardiac remodelling in heart failure 88

4.2.2 Epigenetic basis of cardiac remodelling 89

i) Histone methylation in heart failure 89

ii) Histone demethylases in heart failure 90

4.2.3 Link between histone methylation and iron homeostasis 91

4.2.4 RNA-sequencing 92

4.2.5 Study aims 93

4.3 Methods 94

4.3.1 Mouse model 94

4.3.2 RNA-sequencing 94

4.3.3 SDS-PAGE and Western blot 95

4.3.4 qPCR 96

4.4 Results 97

4.4.1 Assessment of RNA quality prior to sequencing 97

4.4.2 The analysis pipeline 98

4.4.3 Determination of variation in dataset: Principal component analysis and cluster dendrogram 99

4.4.4 Differential gene expression analysis using DESeq2 and EdgeR 101

4.4.5 Gene Ontology enrichment using REVIGO 103

4.4.6 Differentially regulated KEGG pathways using GAGE and visualized with PathView 104

4.4.7 Effect of an iron-deficient diet on genes involved in iron homeostasis 108

4.4.8 Effect of an iron-deficient diet on epigenetic regulation: histone methylation 109

4.5 Discussion 111
4.5.1 An iron-deficient diet leads to epigenetic alterations 111
4.5.2 Iron-deficiency leads to differential regulation of stress-responsive processes and pathways 113
4.5.3 Systemic iron-deficiency does not appear to evoke a response involving the cardiac iron homeostasis pathway 114
4.5.4 Limitations of the current study 114
4.5.5 Selection of pathways for functional studies 115
I) Alterations in metabolic pathways 116
II) Differential regulation in the calcium signaling pathway 119
4.6 Conclusions 122

CHAPTER 5 : EFFECTS OF IRON DEFICIENCY ON CARDIAC METABOLISM 123

5.1 Chapter overview 123
5.2 Introduction 124
5.2.1 Energy metabolism in the heart 124
5.2.2 Fatty acid metabolism in the heart 124
i) Fatty acids: The major energy source in the heart 124
ii) Regulation of fatty acid metabolism 125
5.2.3 Glucose metabolism in the heart: Regulation of glucose metabolism through glycolysis 126
5.2.4 The metabolic fate of pyruvate 128
i) Pyruvate to acetyl-CoA 128
ii) Pyruvate to lactate 129
iii) Pyruvate to alanine 130
5.2.5 Metabolic state in the diseased heart 130
5.2.6 Mitochondrial structural damage and metabolic dysfunction 132
5.2.7 Metabolism in altered iron status 132
5.2.8 Magnetic resonance spectroscopy and dynamic nuclear polarization 133
5.2.9 Study aims 135
5.3 Methods 136
5.3.1 Animal model 136
5.3.2 Blood sampling 136

5.3.3 Dynamic Nuclear Polarization (DNP)-hyperpolarised-$^{13}C_1$ MRS 136
5.3.4 Quantitative real-time PCR 139
5.3.5 Measurement of serum free fatty acid concentration 140
5.3.6 Western blot 140
5.3.7 Mitochondrial complex assays 141
5.3.8 Transmission electron microscopy (TEM) 145

5.4 Results 147
5.4.1 Acquisition of [1-C^{13}]pyruvate spectra in the *in vivo* mouse heart 147
5.4.2 *In vivo* cardiac metabolism using hyperpolarised magnetic resonance spectroscopy 149
5.4.3 Assessment of the gene expression of pyruvate-handling enzymes 152
5.4.4 Effect of systemic iron deficiency on HIF 152
5.4.5 Effect of an iron-deficient diet on HIF-α protein expression 154
5.4.6 Effect of systemic iron deficiency on circulating glucose and fatty acid concentration 155
5.4.7 Effect on an iron-deficient diet on aerobic respiration: Oxidative phosphorylation 155
5.4.8 Effect on an iron-deficient diet on mitochondrial morphology 159

5.5 Discussion 161
5.5.1 Summary of iron status of animals used in this study. 161
5.5.2 Cohort 2: Metabolic switch in iron-deficient animals is likely a consequence of anaemia caused by iron deficiency 163
5.5.3 Cohort 3: Metabolic state is likely a combination of oxidative and anaerobic respiration 165
5.5.4 Cohort 1: A metabolism driven by glucose oxidation? 169
5.5.5 Limitations of the current study 169

5.6 Conclusions 171

CHAPTER 6 : EFFECTS OF IRON DEFICIENCY ON CARDIAC CALCIUM SIGNALING 172

6.1 Chapter overview 172

6.2 Introduction 173
6.2.1 Calcium in the heart 173
6.2.2 Regulation of intracellular Ca^{2+} handling 175

i) Biophysical properties of Ca^{2+}-handling channels and transporters 175
ii) Structural and spatial considerations: The dyad 178
iii) Ca^{2+} leaks and flux balance 178
iv) Ca^{2+} buffering 179
6.2.3 Ca^{2+} handling in cardiovascular disease and heart failure 180
i) Ryanodine receptor in heart failure 180
ii) SERCA in heart failure 181
iii) L-type Ca^{2+} channel in heart failure 182
iv) NCX in heart failure 183
6.2.4 Cardiac Ca^{2+} and iron handling 183
6.2.5 Study aims 184
6.3 Methods 185
6.3.1 Mouse model 185
6.3.2 qPCR 185
6.3.3 Western blot 186
6.3.4 Adult primary cardiomyocyte isolation 187
6.3.5 Whole-cell voltage clamp 187
6.3.6 Ca^{2+} imaging 189
6.4 Results 192
6.4.1 Validation of RNA-sequencing data by qPCR 192
6.4.2 Western blot analyses of Ca^{2+}-handling proteins 192
6.4.3 Effect of an iron-deficient diet on L-type Ca^{2+} channel current 193
6.4.4 Effect of an iron-deficient diet on membrane capacitance 194
6.4.5 Effect of an iron-deficient diet on Ca^{2+} transients 195
6.4.6 Effect of an iron-deficient diet on SR Ca^{2+} stores 195
6.4.7 Effect of an iron-deficient diet on NCX and SERCA activity 197
6.4.8 Effect of an iron-deficient diet on LTCC-RyR coupling 197
6.4.9 Effect of an iron-deficient diet on isoprenaline-stimulated CaTs 198
6.5 Discussion 199
6.5.1 An iron-deficient diet affects diastolic [Ca^{2+}] and CaT amplitude 199
6.5.2 FCM supplementation restores Ca^{2+} handling in the heart 204
6.5.3 Iron deficiency and supplementation does not affect response to β-adrenergic stimulation 204

6.5.4 Impaired cardiac energetics are not limiting for SERCA activity and SR Ca^{2+} loading 205
6.5.5 Perturbations in Ca^{2+} handling can relate to cardiac dysfunction in iron-deficient animals 206
6.5.6 Role of iron in altering Ca^{2+} handling 207
6.5.7 Novelty of the current study 208
6.5.8 Limitations of the current study 210
6.6 Conclusions 211

CHAPTER 7 : CONCLUSIONS 213

7.1 Final summary of thesis 214
7.2 Future work 217
7.2.1 Systemic vs cardiac-specific model of iron deficiency 217
7.2.2 Effect of iron deficiency on cardiac buffering capacity 218
7.2.3 Determination of RyR2 density in iron deficiency 218
7.2.4 Investigating the effects of iron deficiency in a model of heart failure 218
7.3 Concluding remarks 220

CHAPTER 8 : REFERENCES 221

LIST OF FIGURES AND TABLES

Figure 1.1 Iron in the biological system. 2

Figure 1.2 Systemic iron homeostasis. 3

Figure 1.3 Regulation of intracellular iron utilization. 11

Figure 1.4 HIF target genes. 21

Figure 1.5 Post-translational regulation of HIF-α. 22

Figure 2.1 Langendorff perfusion rig for isolation of primary cardiomyocytes. 29

Figure 2.2 Selection of housekeeper gene for qPCR in mouse heart tissue. 33

Figure 3.1 Schematic of the experimental mouse model. 40

Figure 3.2 Cine-MRI setup. 41

Figure 3.3 Cine-MRI analysis. 43

Figure 3.4 Body mass and blood haemoglobin concentration. 47

Figure 3.5 Various parameters to determine iron status following 6 weeks of diet. 50

Figure 3.6 Serial measure of iron status following 6, 9 or 24 weeks of diet. 51

Figure 3.7 Body mass and blood haemoglobin concentration measurements. 53

Figure 3.8 Measure of iron status following iron supplementation. 54

Figure 3.9 Measurement of total elemental iron by ICP-MS. 56

Figure 3.10 Determination of elemental iron following 6, 9 and 24 weeks of diet. 58

Figure 3.11 Real time qPCR comparison of *Hamp* and *Fpn* mRNA expression. 59

Figure 3.12 Immunofluorescence staining for FPN. 60

Figure 3.13 Assessment of cardiac function by cine-MRI. 62

Figure 3.14 Assessment of cardiac function over long-term dietary intervention. 63

Figure 3.15 Cardiac function parameters following iron supplementation. 71

Figure 4.1 Assessment of RNA integrity. 97

Figure 4.2 The analysis pipeline. 99

Figure 4.3 Visual representation of the dataset. 100

Figure 4.4 Hierarchical heat map of differentially expressed genes. 102

Figure 4.5 Visual representation of GO terms. 106

Figure 4.6 Gene expression of iron-sensitive proteins involved in iron homeostasis. 108

Figure 4.7 Histone H3 methylation marks. 110

Figure 4.8 Differential regulation of cardiac oxidative phosphorylation. 117

Figure 4.9 Differential regulation of cardiac pyruvate metabolism. 118

Figure 4.10 Differential regulation of the calcium signaling pathway. 120

Figure 4.11 Calcium signaling in the context of cardiac muscle contraction. 121

Figure 5.1 Hyperpolarised DNP MRS setup. 138

Figure 5.2 Example mouse spectra of [^{13}C]pyruvate. 148

Figure 5.3 Fate of hyperpolarised pyruvate metabolism. 150

Figure 5.4 Gene expression of enzymes catalysing the conversion of pyruvate. 151

Figure 5.5 Gene expression of various glycolytic enzymes. 153

Figure 5.6 HIF-α protein expression. 154

Figure 5.7 Assessment of OXPHOS complex activity in total protein lysate. 157

Figure 5.8 Assessment of the expression of COX4. 158

Figure 5.9 Representative electron micrograph. 160

Figure 6.1 Ca^{2+} signaling pathway in the cardiac couplon. 174

Figure 6.2 Time line of animal model. 185

Figure 6.3 Ca^{2+} imaging protocols. 190

Figure 6.4 Validation of RNA-seq gene expression by qPCR. 192

Figure 6.5 Ca^{2+} channel protein expression comparison. 193

Figure 6.6 L-type Ca^{2+} channel electrophysiology. 194

Figure 6.7 CaT imaging of live cardiomyocytes loaded with FuraRed. 196

Figure 6.8 CaT imaging of live cardiomyocytes loaded with Fluo-3 dye. 198

Figure 6.9 Summary of results involving CaTs. 202

Figure 6.10 Summary of results involving caffeine-evoked response. 203

Figure 6.11 Consequences of perturbations in diastolic Ca^{2+} level. 212

Table 3.1 List of antibodies used in this chapter. 46

Table 3.2 Body mass and blood haemoglobin concentration. 48

Table 3.3 Parameters measured for determination of iron status. 50

Table 3.4 Effect of iron supplementation on iron status. 53

Table 3.5 Total elemental iron measured by ICP-MS. 58

Table 3.6 Serial measure of *in vivo* cardiac function assessed by cine-MRI. 64

Table 3.7 Effect of iron supplementation on *in vivo* cardiac function. 72

Table 4.1 Epigenetic modulations associated with heart disease. 91

Table 4.2 List of antibodies used in this chapter. 95

Table 4.3 List of primers used in this chapter. 96

Table 4.4 Over-represented GO terms. 105

Table 4.5 Differentially regulated pathways. 107

Table 5.1 List of primers used in this chapter. 140

Table 5.2 List of antibodies used in this chapter. 141

Table 5.3 Measure of iron status. 162

Table 6.1 List of primers used in this chapter. 186

Table 6.2 List of antibodies used in this chapter. 187

CHAPTER 1:

GENERAL INTRODUCTION

1.1 IRON PHYSIOLOGY

Iron is fundamental to life. In the cellular environment, iron can exist in either the bivalent ferrous (Fe^{2+}) or trivalent ferric (Fe^{3+}) states (Jankowska *et al.*, 2012; Papanikolaou and Pantopoulos, 2005). This confers iron the ability to readily engage in redox reactions, which are essential for a variety of biological processes, notably those involving metabolism and utilization of oxygen. (Figure 1.1).

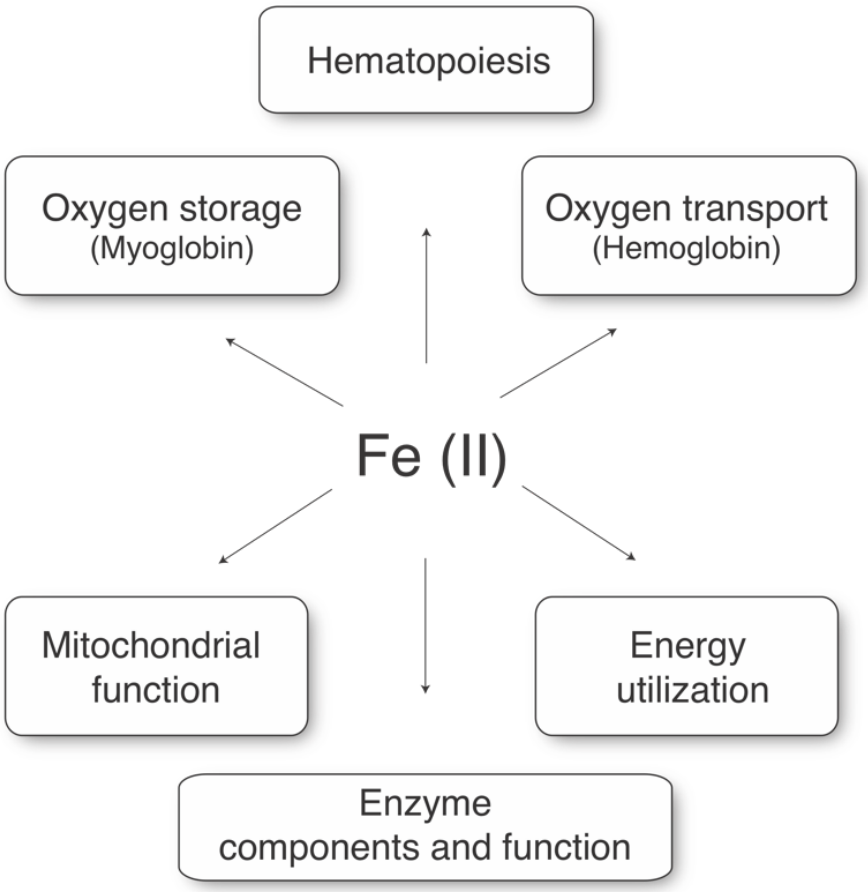


Figure 1.1 Iron in the biological system. Iron is an essential micronutrient which is required in a wide range of biological processes.

1.1.1 Iron distribution in the body

Total body iron content in an adult human ranges between 3-4 g (Templeton, 2002). Approximately 60-70% of this is used for haemoglobin synthesis (Papanikolaou and Pantopoulos, 2005). Ten to fifteen percent of the body's total iron can be found in skeletal and cardiac muscles, as part of myoglobin, cytochrome, and non-haem enzymes (Hentze *et al*., 2004; Jankowska *et al.*, 2012; Papanikolaou and Pantopoulos, 2005). The remaining iron is stored in liver hepatocytes, the spleen and bone marrow (Figure 1.2) (Hentze *et al.*, 2004; Templeton, 2002).

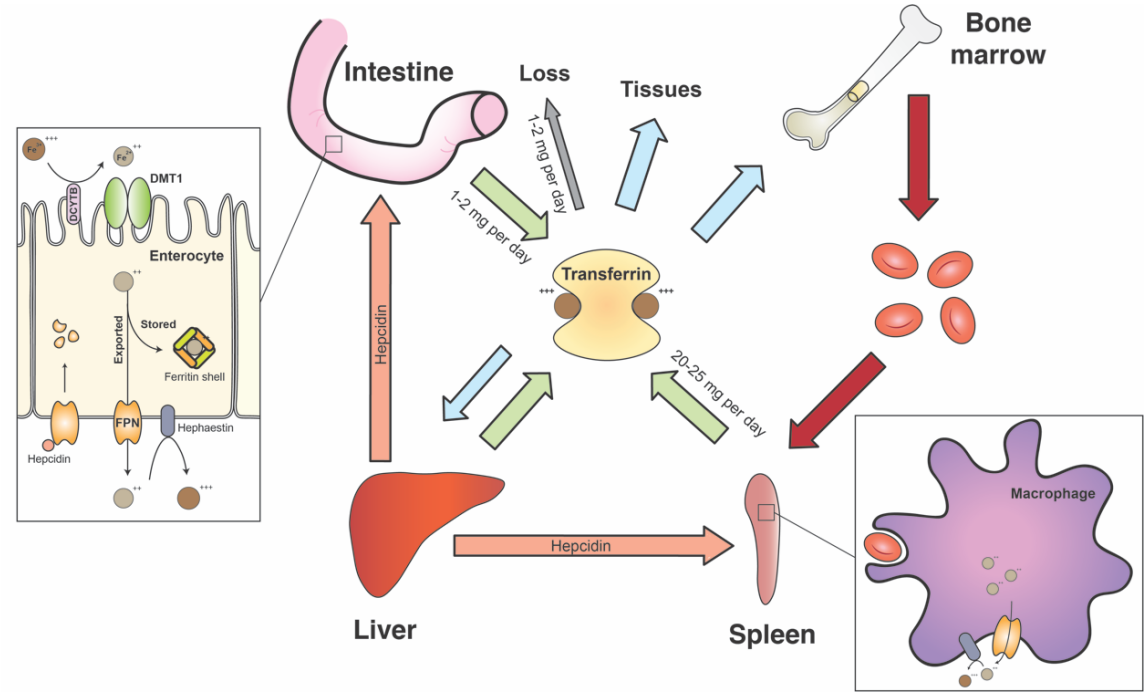


Figure 1.2 Systemic iron homeostasis. Dietary iron is taken up in the duodenal enterocytes and iron is recycled by macrophages in the spleen. Both of these contribute to the pool of transferrin-bound iron in plasma. Iron is used in the bone marrow for erythropoiesis; iron is also delivered to other tissues throughout the body. Liver derived hepcidin modulates iron export via regulation of ferroportin (FPN). Excess iron is stored in ferritin shells.

In the cell, much of the iron is shuttled into the mitochondria where haemoproteins and iron-sulphur clusters are synthesised (Hentze *et al.*, 2004). Many cytoplasmic and nuclear proteins also require iron as a cofactor in order to carry out essential functions such as metabolism, proliferation and survival (Templeton, 2002).

Iron homeostasis in the body is predominantly maintained by two major pools of iron: the liver and macrophages. Iron is stored primarily in the liver and is released into the circulation when plasma iron levels are low (Hentze *et al.*, 2004). Iron is also recycled from the catabolism of senescent or damaged erythrocytes by macrophages in the spleen (Hentze *et al*., 2010). In both cases, iron is exported into the plasma by the only known mammalian iron exporter ferroportin (FPN) (Huang *et al.*, 2011).

1.1.2 Iron absorption

No regulated pathway exists for the excretion of iron. Nevertheless, iron can be lost through shedding of skin and intestinal cells, blood loss, urine and sweat (Jankowska *et al.*, 2012). To replenish this loss, approximately 1-2 mg of dietary iron is absorbed per day in the gut (Hentze *et al.*, 2010). Absorption of iron occurs across the apical membrane of enterocytes of the mid-upper villus and the small intestine (Anderson and Frazer, 2017). Inorganic iron in the diet, which exists in the oxidised state (Fe^{3+}), is first reduced to Fe^{2+} by the membrane-associated ferrireductase duodenal cytochrome B (DCYTB) and transported into the cell by the divalent metal transporter 1 (DMT-1) (Mastrogiannaki *et al.*, 2013).

Once in the cell, iron is released into circulation through FPN across the basolateral surface of the cell, where it binds the iron transport protein transferrin and is transported to tissues

throughout the body (Jankowska *et al.*, 2012; Mastrogiannaki *et al.*, 2013). Loading onto transferrin requires the oxidation of Fe^{2+} back to Fe^{3+} and this reaction is mediated by hephaestin, a membrane-bound multi-copper oxidase (Hentze *et al*., 2010).

Haem iron, mainly found in red meat products, is also an important source of dietary iron. The absorption of haem-iron also occurs at the apical membrane of duodenal enterocytes and is more efficiently absorbed than inorganic iron. Although a definitive mechanism is still lacking, it has been suggested that uptake of haem-iron is mediated by what was first identified as the transporter haem carrier protein 1 (HCP1) (Le Blanc *et al.*, 2012). It is now known that HCP1 is actually a proton-coupled folate transporter (PCFT), which, in addition to its primary role in folate uptake, also has a low affinity for haem, thus thought to have a secondary role involving haem transport (Laftah *et al.*, 2009).

In the cell, the haem can be exported into circulation in the intact form via the haem exporter FLVCR1 (feline leukaemia virus subgroup C receptor 1) (Mercurio *et al.*, 2015). Alternatively, the haem is catabolised by microsomal haem oxygenases and the free iron is then released into circulation via the same export pathway followed by inorganic iron (Le Blanc *et al.*, 2012).

1.1.3 Iron transport and delivery to tissues

Iron in the bloodstream is bound to transferrin for transport to different tissues in the body. Each transferrin molecule can bind up to two atoms of iron. Under normal conditions, approximately 30% of the iron-binding sites on transferrin are occupied. This provides considerable buffering capacity against the accumulation of the toxic non-transferrin-bound iron (NTBI) (Anderson and Frazer, 2017).

Circulating iron is transported into the cells by transferrin receptor type-1 (TfR1)-mediated endocytosis (Huang *et al.*, 2011; Jankowska *et al.*, 2012). Clathrin-coated endosomes are internalized and iron is released into the cytosol through the acidification of the endosome. Here, iron enters the labile iron pool (LIP) and can either be used immediately or sequestered within the iron-storage protein ferritin for later use (Huang *et al.*, 2011; Ponka, 1999).

Although the transferrin-mediated transport of iron represents the major pathway for cellular iron import, it is not the only one. Recent studies have shown that iron can also be taken up in the NTBI form by a family of zinc ion transporters Zrt/Irt-like proteins (ZIPs) and L-type calcium channels (Chattipakorn *et al.*, 2011; Fujishiro *et al.*, 2012).

1.1.4 Iron storage

When exogenous supply of iron is diminished or scarce, stored iron becomes a critical source of intracellular iron. Due to the toxicity of free iron, in the cell, stored iron is sequestered by the iron-storage protein ferritin (Anderson and Frazer, 2017; Hentze *et al.*, 2010). Ferritin is a large, 450 kDa, globular protein made of 24 subunits which are arranged to form a spherical shell with a large hollow cavity in the centre. A single molecule of ferritin which can hold up to 4,500 atoms of iron in its central core. This high capacity for iron binding provides the cell with an enormous ability to sequester and to store large quantities of iron for later use (Anderson and Frazer, 2017).

1.1.5 Iron recycling

The recycling of iron is an important component of iron homeostasis and represents a major source of systemically available iron. Macrophages in the spleen and bone marrow phagocytose aged or damaged erythrocytes and catabolize haem using haemoxygenases (Hentze *et al.*, 2010). Iron is released from phagolysosomal vesicles via the natural resistance associated macrophage protein 1 (NRAMP1), a divalent metal transporter homologous to DMT-1, and is exported into circulation via FPN.

1.2 MECHANISMS OF IRON HOMEOSTASIS

1.2.1 Systemic iron homeostasis: The hepcidin/FPN axis

Central to the regulation of systemic iron is the 25 kDa peptide hormone hepcidin. Hepcidin is primarily synthesised and secreted by hepatocytes and is considered to be the master regulator of iron homeostasis (Cohen-Solal *et al.*, 2014; Jankowska *et al.*, 2012). When plasma iron levels are high, hepcidin binds FPN, causing its internalization and degradation, thereby blocking intracellular iron export and reducing levels of circulating iron (Huang *et al.*, 2011; Jankowska *et al.*, 2012). Depleted iron stores, hypoxia and ineffective erythropoiesis decrease expression of hepcidin, whereas liver iron-overload and increased circulating iron up-regulates hepcidin production (Cohen-Solal *et al.*, 2014; Huang *et al.*, 2011; Jankowska *et al.*, 2012).

The regulation of hepcidin expression occurs at the transcriptional level via the bone morphogenic protein (BMP)/SMAD signaling pathway. This pathway involves the binding of BMP ligands to type I and type II serine threonine kinase receptors, which results in the phosphorylation of cytoplasmic SMAD1, 5 and 8 proteins. Subsequently, these SMAD proteins form a complex with SMAD4 and translocate to the nucleus, where they promote the transcription of a wide range of genes, including *Hamp*.

This signaling pathway is further regulated by the BMP co-receptor hemojuvelin (HJV) protein, a glycosylphosphatidyl inositol-linked cell surface protein expressed predominately in skeletal muscle cells and hepatocytes (De Domenico *et al.*, 2007). Binding of HJV to BMP ligands and receptors enhance SMAD phosphorylation in response to BMP signals. The matriptase-2 protein (TMPRSS6), encoded by the

transmembrane protease, serine 6 gene, cleaves HJV (Rishi *et al.*, 2015). This process of cleaving interrupts and suppresses BMP/SMAD signaling and consequently reduces transcription of *Hamp*. TMPRSS6 is modulated by intracellular iron concentrations and by BMP6, both at the mRNA and protein level (Meynard *et al.*, 2011).

The final piece in the regulation of *Hamp* expression is the haemochromatosis protein HFE. Under conditions of low serum iron, HFE competes with transferrin for binding to TfR1. However, when circulating iron is elevated, HFE preferentially binds to TfR2. Together, they associate with HJV, BMP and the BMP receptor to form the putative iron signaling complex which enhances downstream SMAD signaling (Pantopoulos, 2008).

Further to the regulation of hepcidin via the BMP/SMAD pathway, recent studies have discovered that errythroferone (ERFE), an erythroid hormone produced in response to erythropoietin (EPO), is a potent suppressor of hepcidin (Rishi *et al.*, 2015). In this way, EPO can modulate the bioavailability of iron to satisfy elevated need of iron for haemoglobin synthesis and erythroid proliferation (Gammella *et al.*, 2015a).

It is worth mentioning that although liver hepcidin is known to be the major contributor to systemic iron homeostasis, hepcidin is also produced locally in other tissues, including the heart, brain, kidney, alveolar macrophages and splenic macrophages (Rishi and Subramaniam, 2017). This implicates an ability for specific tissues to regulate their own iron metabolism, independent of systemic mechanisms of iron homeostasis.

1.2.2 Regulation of intracellular iron utilization

In the cell, iron storage and uptake are regulated post-transcriptionally by the iron-regulatory proteins 1 and 2 (IRP1 and IRP2) (Huang *et al.*, 2011; Jeanteur, 2012; Ponka, 1999). IRPs are RNA-binding proteins that modulate the translation of a number of transcripts involved in iron homeostasis. All IRP-target mRNA contain a recognition stem-loop structure known as the iron-responsive elements (IREs) in either the 5' or 3' untranslated regions (UTRs) (Anderson and Frazer, 2017; Huang *et al.*, 2011). Binding of IRPs to the 3' UTR increases mRNA stability by protecting the transcript from degradation by 3'-5' exonucleases. On the other hand, binding to a 5' UTR suppresses translation by blocking access of the translation machinery to the transcript (Huang *et al.*, 2011).

The activity of IRPs is modulated by cellular LIP (Figure 1.3). IRPs adopt an mRNA binding conformation when iron availability is low (Huang *et al.*, 2011; Ponka, 1999). Iron-replete conditions diminish their binding activity and iron-loading leads to the conversion of IRP1 into cytosolic aconitase and the degradation of IRP2 by an iron-dependent ubiquitin-proteasome pathway (Hentze *et al.*, 2004; Huang *et al.*, 2011).

The dependence on iron for the regulation of IRP activity is designed to elicit the appropriate response to variations in intracellular iron concentrations. Under conditions of low iron availability, IRPs bind to the 5' UTR of the ferritin mRNA. This blocks its translation and ensures that little ferritin is produced when iron storage is not required. At the same time, the translation of *Fpn* is also suppressed in a similar manner and the *Tfr1* and *Dmt1* transcripts are stabilised by the binding of IRPs to their 3' UTR, thereby

increasing iron retention and uptake in the cell. When cellular iron levels are high, IRPs are degraded, thereby limiting cellular iron uptake, increasing iron export and promoting storage.

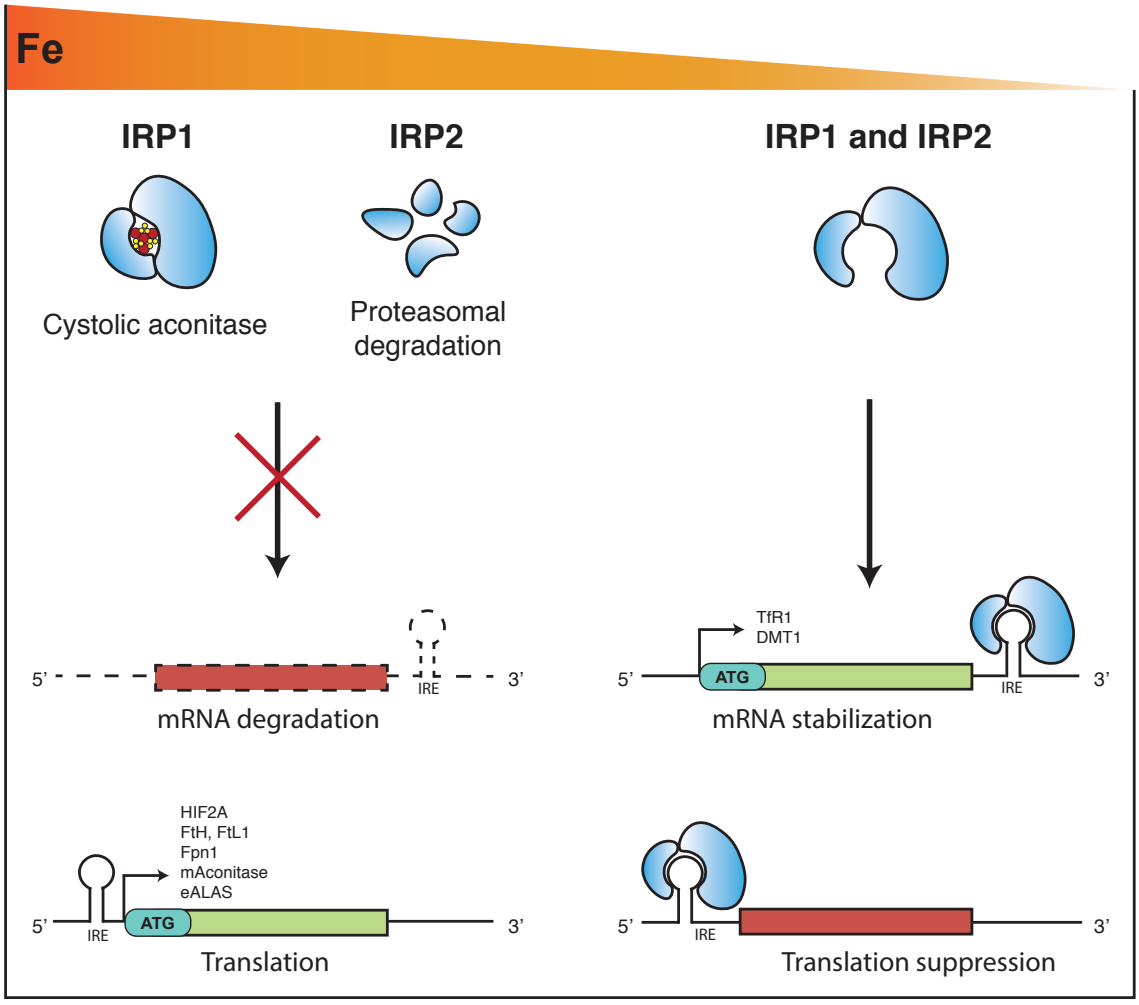


Figure 1.3 Regulation of intracellular iron utilization. IRPs are in the IRE-binding conformation when iron availability is low. When intracellular iron levels are high, IRP1 is converted to cystolic aconitase and IRP2 is degraded via the proteasomal pathway.

In the last decade, additional mechanisms of iron homeostasis been observed in yeasts. Working with *Saccharomyces cerevisiae*, both Pedro-Segura *et al.* (2008) and Sato *et al.*, (2016) demonstrated that under conditions of low iron bioavailability, yeasts activate pathways targeting the degradation of Fe-S cluster-containing mitochondrial proteins such as succinate dehydrogenase and NADH dehydrogenase. In this way, previously sequestered iron is released to the labile pool for use in more essential cellular functions in response to iron deficiency.

1.3 CAUSES AND CONSEQUENCES OF IRON IMBALANCE

1.3.1 Iron overload

The redox capability of iron makes it an essential trace element; yet, this very trait makes it toxic in excess. Iron can undergo Fenton-type reactions, producing noxious free radicals, such as reactive oxygen species (ROS), which can damage cellular components (Huang *et al.*, 2011; Papanikolaou and Pantopoulos, 2005). Therefore, accumulation of iron beyond the antioxidant capacity of the cell leads to cellular oxidative stress.

Many diseases are associated with iron overload and generally arise from a background of hereditary haemochromatosis (HH), a condition of excess iron salt deposition in tissues (Huang *et al.*, 2011; Mastrogiannaki *et al.*, 2013; Schipper, 2012). Common manifestations of HH include skin pigmentation, liver dysfunction, diabetes and cardiomyopathy due to iron accumulation in the skin, liver, pancreas and heart, respectively.

HH typically arises from mutations in the genes encoding proteins involved in the regulation of iron homeostasis. The most common type of HH (Type 1) is caused by mutations in the *Hfe* gene (Kawabata, 2017). Mutations in the *Hfe2* (Type 2A), *Tfr2* (Type 3), *Hamp* (Type 2B) and *Bmp6* gene have also been identified in patients. In all of these cases, iron overload is due to an inappropriately low hepcidin concentration in the serum despite clear tissue iron overload (Pantopoulos, 2008). Furthermore, these mutations are inherited in an autosomal recessive pattern.

HH can also be caused by germline mutations in the *Slc40a1* gene, which encodes for FPN. The disease can be cause by either a *loss-of-function* (Type 4A) mutation, which results in the accumulation of iron predominately in reticuloendothelial cells, or a *gain-of-function* (Type 4B) mutation, which causes accumulation of iron in parenchymal cells (Kawabata, 2017; Wallace, 2016). Both of these are inherited in an autosomal dominant manner and, unlike types 1, 2A, 2B and 3, type 4 HH results in iron overload despite high levels of serum hepcidin (Kawabata, 2017).

Finally, iron overload can also be acquired secondary to repeated blood transfusions. This is true the case in β-thalassemia, an autosomal recessive genetic disorder which affects beta-, but not alpha-globin production, thus resulting in excess alpha-globin chains, which aggregate within erythroid precursors and induce apoptosis of the cells (Ginzburg and Rivella, 2011; Leecharoenkiat *et al.*, 2016). Patients with severe case of β-thalassemia suffer from anaemia, defined as low haemoglobin or haematocrit levels, arising from ineffective erythropoiesis and require regular blood transfusions to minimize the effects of chronic anaemia. An unfortunate side-effect of this treatment is iron overloading, and

the most common cause of death in transfusion-dependent patients is cardiomyopathy as a consequence of iron overload (Leecharoenkiat *et al.*, 2016).

1.3.2 Iron deficiency

i) The epidemiology and prevalence of iron deficiency

Iron deficiency remains as one of the most common nutritional disorders, affecting more than 2 billion people globally (von Haehling *et al*., 2015; Stoltzfus and Dreyfuss, 1998). It is most prevalent in infants, children, young adults, women, elderly, and those with chronic inflammatory diseases (von Haehling *et al*., 2015). In women, menstruation and pregnancy pose an additional burden. Developing countries are responsible for over 60% of all documented cases of iron deficiency (Lopez *et al.*, 2016), but the condition is also prevalent in industrialised countries, where it affects a third of pre-school-age children and pregnant women (von Haehling *et al.*, 2015).

ii) Causes of iron deficiency

Iron deficiency occurs when iron stores cannot meet the demands of the body. Iron status exists in a continuum and therefore, iron deficiency can be manifested in varying degrees of severity. Anaemia typically occurs as a result of prolonged iron deficiency, and is considered a severe stage of iron deficiency (Stoltzfus, 2003; Stoltzfus and Dreyfuss, 1998).

The development of iron deficiency is a slow process since there is no regulated excretory pathway for iron. Furthermore, aside from erythropoiesis, iron is required in other organs, playing key roles in metabolism, immune responses and various essential cellular

functions (von Haehling *et al*., 2015). When physiological iron stores diminish, the human body prioritises the use of iron for erythropoiesis, therefore red cell mass tend to remain undisturbed until late in the course of iron depletion (von Haehling *et al.*, 2015). Thus, iron deficiency is typically sub-clinical until anaemia is severe, but the functional consequences at the cellular and/or tissue level may already exist by the time a diagnosis is made (Stoltzfus and Dreyfuss, 1998).

There are two forms of iron deficiency: absolute and functional. Absolute iron deficiency reflects a state of low or depleted iron stores, often with intact mechanisms of iron homeostasis (von Haehling *et al.*, 2015; Jankowska *et al.*, 2013). Common causes of absolute iron deficiency include: increased requirement during infancy and adolescence, low dietary iron intake, acute or chronic blood loss or decreased intestinal absorption due to gastrectomy, duodenal by pass or bariatric surgery (Camaschella, 2017).

Functional iron deficiency occurs when iron supply to tissues is inadequate even though total body iron stores are normal or elevated, reflecting an altered state of iron distribution (Camaschella, 2017; Lopez *et al*., 2016). This form of iron deficiency, also referred to as anaemia of chronic disease, is common in acute or chronic inflammation, during which iron is sequestered in macrophages, enterocytes, and hepatocytes due to an increase in circulating hepcidin and subsequent downregulation of FPN (von Haehling *et al.*, 2015; Lopez *et al.*, 2016). This regulation is part of a biological defence mechanism, reducing the availability of iron for pathogens when fighting infectious disease. However, because this results in retention of iron in macrophages and other tissues, ironically, chronic inflammation often causes anaemia (Kawabata, 2017).

Although iron deficiency is usually acquired, it can also occur through genetic predisposition. One example is a rare disease called iron-refractory iron-deficiency anaemia (IRIDA). This is an autosomal recessive genetic disorder caused by a mutation in the TMPRSS6 gene (Camaschella, 2017). The mutation renders the TMPRSS6 protein inactive, thereby causing an up-regulation (and hence over-activation) of hepcidin and subsequent down-regulation of FPN, blocking iron absorption from the gut and iron release from macrophages (Camaschella, 2015, 2017). Therefore, IRIDA patients have abnormally high levels of serum hepcidin and very low levels of circulating iron and suffer from iron-deficiency anaemia (Anderson and Frazer, 2017).

1.4 CLINICAL MEASUREMENT OF IRON STATUS

Currently, the most commonly used biomarker for determining systemic iron status is ferritin concentration in the serum or plasma. Ferritin is normally synthesised in the endoplasmic reticulum and used within the cell to store surplus iron. However, small amounts of ferritin are also secreted into circulation from the cell. The amount secreted correlates strongly with intracellular iron concentration, thus plasma ferritin concentrations reflect the cells' iron stores (Anderson and Frazer, 2017; Finch *et al.*, 1986).

Normal ferritin levels range between 30-300 μg/L in men and 10-200 μg/L in women (Finch *et al.*, 1986). This wide variation is attributed to differences in iron balance and hormonal states (i.e. in women, pregnancy or menstruation) of the individual. In addition, because ferritin expression is enhanced during inflammation, its measured values are usually interpreted in parallel with levels of C-reactive protein, also an acute phase reactant (Bermejo and García-López, 2009; Finch *et al.*, 1986). This is especially relevant

when diagnosing iron deficiency, since normal or elevated ferritin levels may not reflect true iron status in the presence of an inflammatory response. Hyperthyroidism and liver disease can also affect serum ferritin concentrations, with values greater than 20,000 μg/L having been observed as a consequence of non-iron related disease (Finch *et al*., 1986).

Therefore, although ferritin is considered to accurately reflect total body iron deposits, this appears to only be true in the absence of inflammation or any other disease. Thus, transferrin saturation (TSat), calculated as the ratio of serum iron concentration to the total iron binding capacity, is often used in parallel to assess systemic iron status because this parameter is not readily affected by external factors not related to iron. When TSat exceeds 50%, iron overload is suspected and any values over 80% suggest high levels of NTBI with risk of organ damage. On the other hand, TSat < 16% is used as an indicator of iron deficiency (Anderson and Frazer, 2017).

1.5 IRON IN THE HEART

1.5.1 Iron homeostasis in the heart

Cardiomyocytes are known to express both ferroportin (FPN) and hepcidin, raising the possibility that the heart is capable of regulating cardiac iron handling locally, independent of systemic mechanisms. Indeed, using transgenic murine models where either FPN or hepcidin expression was altered specifically in the heart, Lakhal-Littleton *et al*. (2015 and 2016) showed that the expression of FPN and cardiomyocyte-derived hepcidin were required for the correct deposition of iron in cardiomyocytes and ultimately, healthy cardiac function. Importantly, cardiac-derived hepcidin/FPN interaction was independent of systemic iron homeostasis mechanisms and functioned autonomously at the level of cardiomyocytes. This suggests that the heart has mechanisms in place to protect it from becoming easily affected by derangements in systemic iron homeostasis.

1.5.2 Iron overload and cardiac disease

Much of the current literature revealing the importance of iron homeostasis in the heart is described within the context of iron overload. Cardiomyopathy is a common outcome following excess deposition of iron in the myocardium secondary to iron overload. It is the leading cause of death in HH, patients receiving chronic blood transfusion (β-thalassemia) or in those suffering from haemosiderosis (Gammella *et al.*, 2015b; Gujja *et al.*, 2010). The toxicity of excess iron in the heart is attributed to the iron-mediated generation of ROS, which initiates the pathologic development of fibrosis, cardiomyocyte apoptosis and ultimately, progression into heart failure (Gammella *et al*., 2015b).

The cardiotoxicity of iron has also been shown in mouse models by Lakhal-Littleton *et al.* (2015). Mice carrying a cardiac-specific deletion of FPN preferentially retained iron in the cardiomyocytes and developed fatal left ventricular dysfunction by three months of age. In comparison, a milder cardiac phenotype was developed in haemochromatosis mice generated by ubiquitous deletion of hepcidin. In these mice, despite iron overload in the total heart tissue, the iron was found outside of the cardiomyocyte due to excessive FPN activity. In addition to confirming role of iron in cardiotoxicity, these observations reveal that the site of iron deposition determines the extent of cardiac injury, with iron overload specifically in the cardiac myocytes being most detrimental to overall cardiac function.

1.5.3 Iron deficiency and cardiac disease

In humans, cardiac iron deficiency is the most common co-morbidity in heart failure and is associated with higher mortality rates (Anker *et al*., 2009; Jankowska *et al.*, 2013). In animals, severe iron deficiency is known to cause cardiomyopathy (Medeiros and Beard, 1998; Petering *et al*., 1990). Furthermore, mice lacking TfR1 in the heart develop lethal cardiomyopathy and die within the first two weeks of birth with cardiomegaly, poor cardiac function and energetic failure; this aggressive phenotype can be rescued by intensive iron therapy, underscoring the importance of iron balance in the heart (Xu *et al.*, 2015). However, the mechanisms by which iron deficiency leads to cardiac failure is still an area of active research.

1.6 INTERPLAY BETWEEN IRON AND OXYGEN HOMEOSTASIS

The relationship between iron and oxygen was initially observed within the context of the oxygen carrying capacity of the blood. In the last two decades, studies have revealed a relationship between oxygen and iron which goes beyond oxygen transport and storage. Thus, when discussing iron, oxygen must also be considered in parallel.

1.6.1 The hypoxia inducible factor and the oxygen sensing pathway

Central to the cell's oxygen sensing pathway is the transcription factor hypoxia inducible factor (HIF). HIF is known to regulate the expression of genes that are involved in a wide range of cellular functions such as erythropoiesis, angiogenesis and metabolism, as the cell adapts to changes in physiological oxygen levels (Figure 1.4) (Semenza, 2000).

HIF is a heterodimeric complex consisting of an oxygen sensitive α subunit and constitutive β subunit (van Wijk *et al*., 2010). Two main α subunit isoforms occur in mammalian systems – HIF-1α and HIF-2α – which share significant sequence and structural homology (Lee, 2008; Morris *et al*., 2009). In cells, HIF-1α mRNA is constitutively expressed and its stability is regulated in an oxygen-dependent manner by a family of three enzymes known as the prolyl hydroxylase domain proteins (PHD1, 2 and 3) (Semenza, 2000; van Wijk *et al.*, 2010). Under normoxic conditions, PHDs hydroxylate HIF-α on two prolines Pro402 and Pro564 of HIF-1α and Pro405 and Pro531 of HIF-2α (Lee, 2008).

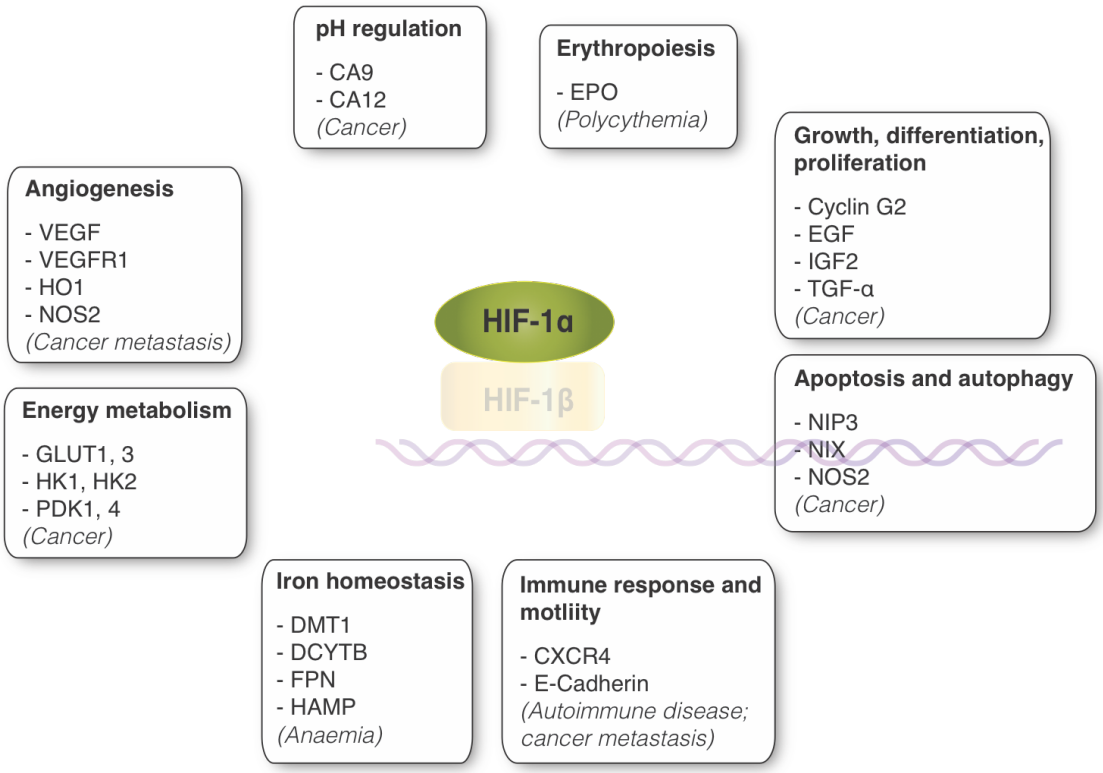


Figure 1.4 HIF target genes. Transcription factor HIF activates a broad range of genes. Relevant to this thesis are those genes related to iron homeostasis and energy metabolism.

This modification provides a recognition motif for the von Hippel Lindau tumor suppressor protein (VHL), a component of an E3 ubiquitin ligase complex, which targets HIF-α for degradation by the 26S proteasome (van Wijk *et al.*, 2010). Because the hydroxylation reaction catalysed by PHD utilises O_2 as a substrate and is inhibited by ROS generated under hypoxic conditions, the activity of PHDs is attenuated, HIF-α is stabilised and translocated to the nucleus. There, it heterodimerises with HIF-β and activates a broad range of genes involved in cellular response to hypoxia (Figure 1.5) (Lee *et al.*, 2006). This mechanism allows HIF-α levels to be highly responsive to changes in blood oxygen concentration.

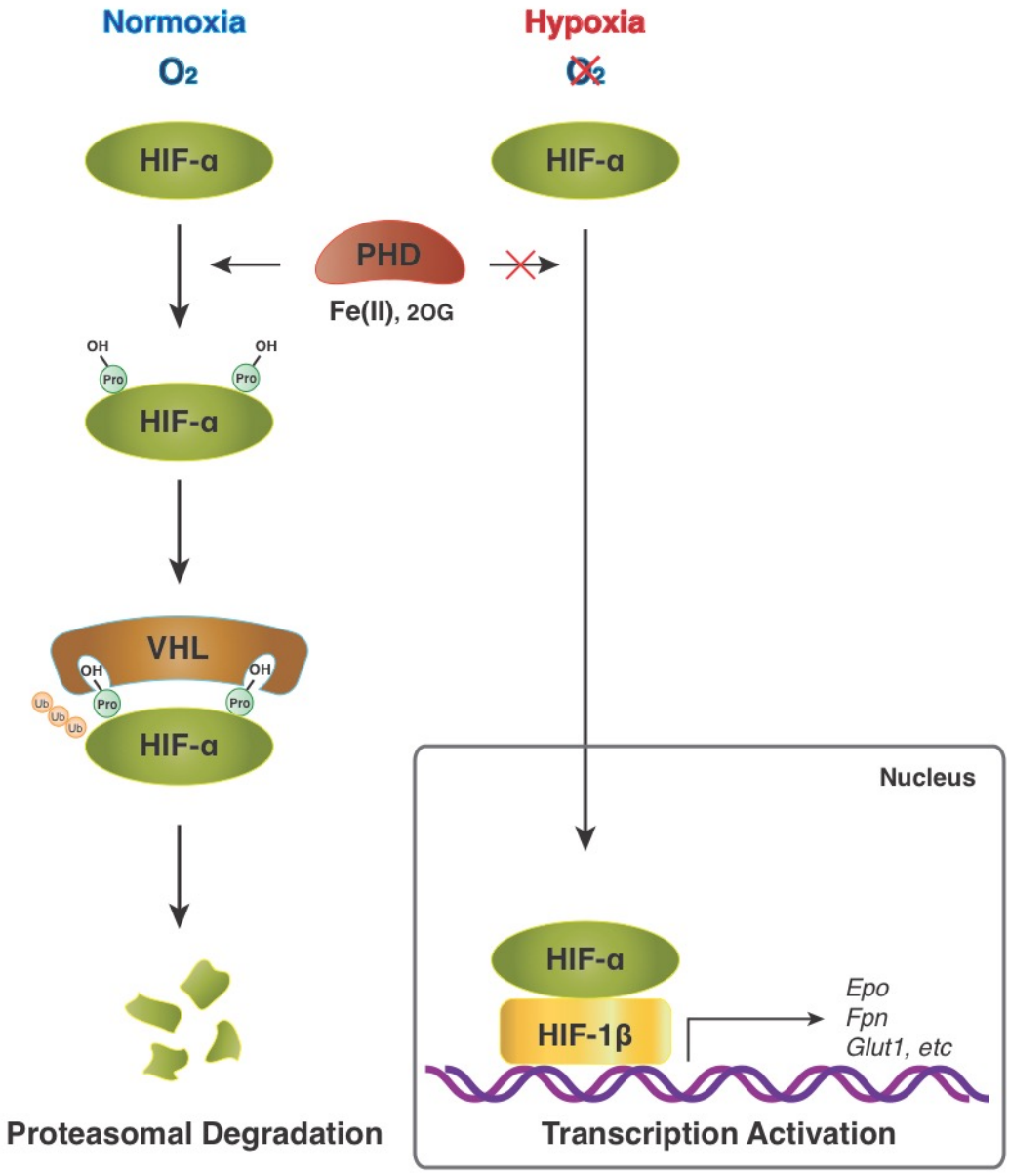


Figure 1.5 Post-translational regulation of HIF-α. The oxygen sensitive HIF-α subunit is regulated in an oxygen-dependent manner by the prolyl hydroxylase domain proteins PHDs. The degradations of HIF under normoxic conditions is mediated by the von Hippel Lindau (VHL) tumor suppressor protein. 2OG = 2-oxoglutarate; ub = ubiquitin.

Additionally, the regulation of HIF-1α by PHD2 is thought to be facilitated via the heat shock protein HSP90 pathway. The HSP90 co-chaperon protein p23 has been shown to bind to PHD2 via a PXLE (Pro-X-Leu-Glu) motif in the N-terminal region of PHD2 (Arsenault *et al.*, 2016; Song *et al.*, 2013). Given that HIF-1α is a client protein of HSP90, the proposed mechanism involves the recruitment of PHD2 to HSP90 via p23 to more efficiently hydroxylate HIF-1α under normoxic conditions.

HIF-2α is post-translationally regulated in a similar manner, but unlike HIF-1α, it is also regulated at the transcriptional level. The HIF-2α gene *Epas* is an IRE containing gene in its 5' UTR, thus its expression is regulated in an iron-dependent manner.

1.6.2 Hypoxia and iron homeostasis

Numerous lines of evidence exist showing that iron homeostasis is responsive to hypoxia. HIF mediates the transcription of many genes involved in a wide variety of biological processes, include a number of genes encoding for key players in the iron homeostasis pathway. The *Slc40a1, Dmt-1*, *Tfr1, Tmprss6* and *Dcytb* genes all contain the hypoxic responsive element (HRE), a recognition sequence for targeted HIF binding, in the promoter region and have been shown to be up-regulated in response to acute hypoxia and down-regulated in HIF-1α and HIF-2α knock-out models, both *in vitro* and in transgenic mice (Bianchi *et al.*, 1999; McKie *et al.*, 2001; Peyssonnaux *et al.*, 2007, 2008).

In addition, hypoxia also acts on regulating hepcidin by elevating the level of ERFE in the bone-marrow, which suppresses hepcidin (Kautz *et al*., 2015). Furthermore, hypoxia increases the expression of the prohormone convertase furin, the enzyme responsible for

the maturation of the hepcidin propeptide (Valore and Ganz, 2008). Furthermore, like TMPRSS6, furin is also known to cleave HJV, thus blunting the BMP/SMAD pathway and further suppressing the expression of hepcidin (Liu *et al.*, 2012).

1.6.3 Alternative links between oxygen and iron

The relationship between oxygen and iron goes beyond downstream effects of HIF. PHDs are members of the 2-oxoglutarate (2OG) and iron-dependent dioxygenase superfamily of enzymes. *In vitro*, iron chelation with desferrioxamine (DFO) attenuates PHD activity, stabilises HIF-1α and induces erythropoietin mRNA expression (Wang and Semenza, 1993). The relationship between iron availability and hypoxia has also been shown in humans. DFO infusion in healthy human volunteers resulted in an increase of erythropoietin in the serum under normoxic conditions in a dose-dependent manner in a similar time course to that of hypoxia (Ren *et al.*, 2000). Furthermore, clinical iron deficiency has been shown to disturb normal responses to hypoxia, as evidence by exaggerated pulmonary hypertension in response to acute hypoxic exposure (Frise *et al.*, 2016). Collectively, these studies provide evidence that PHDs are sensitive to intracellular iron availability and their activities can be modulated in an iron-dependent manner.

1.7 SUMMARY AND THESIS AIMS

Iron is a fundamental micronutrient which is essential for a wide range of biological processes. There is growing evidence that iron is also important in the heart and that perturbations in either systemic or cardiac iron homeostasis are detrimental to its function. Furthermore, sufficient evidence exists showing a causal relationship between iron deficiency and functional impairment of the heart, but mechanistic insight is still lacking. In light of this, the purpose of this thesis was to characterise the effects of iron deficiency on cardiac function and to gain mechanistic insight into how the former impairs the latter.

To achieve these objectives, both non-candidate and candidate-based studies were conducted and presented in this thesis as follows:

Chapter 3 introduces the mouse model and demonstrates that administration of an iron-deficient diet results in physiological iron deficiency. Furthermore, the effects of iron deficiency on cardiac function at the organ level is also shown.

Chapter 4 describes the findings of a study which investigated the effects of iron deficiency at the gene expression level using RNA-sequencing. This chapter provides evidence of profound alterations in the gene expression profile in the heart following the administration of an iron-deficient diet.

Target genes and pathways were identified following bioinformatics analysis, which led to the studies presented in Chapter 5 and 6. The collective aim of these two chapters was to gain mechanistic insight surrounding the alterations in cardiac function. Briefly, the study in **Chapter 5** investigates the effect of iron deficiency on cardiac metabolism. A study of the cardiac calcium signaling pathway is covered in **Chapter 6**.

Finally, **Chapter 7** draws together the final conclusions and proposals for future work.

CHAPTER 2:

ANIMAL MODEL AND GENERAL METHODS

2.1 CHAPTER OVERVIEW

This chapter will introduce the mouse models used throughout this thesis. It will also briefly describe the general experimental methods used in this thesis. Chapter-specific methods will be presented in the *Methods* section in each relevant chapter.

2.2 MOUSE MODEL

2.2.1 General animal housing and breeding

All animal usage in this thesis was in compliance with Home Office Guidance on the Operation of the Animals (Scientific Procedures) Act of 1986 (ASPA) and the University of Oxford institutional guidelines. All treatments administered to animals were approved by the Home Office under the Project License 30/3182. Mice were housed in individually ventilated cages (IVCs), with a minimum of 2 and maximum of 6 mice per cage at the University of Oxford Biomedical Services Building.

A total of 113 mice were used to generate the data presented in this thesis. An additional 67 mice were used for pilot experiments and refinement of experimental techniques.

2.2.2 Dietary model of systemic iron deficiency

All animals used in this study were male wild-type C57BL/6J mice. At the age of 3 weeks, mice were weaned onto either an iron-deficient (2-5 ppm iron, Teklad, TK99397; Envigo) or a matched iron-adjusted diet (200 ppm iron, Teklad, TK08713; Envigo). The duration of the diet varied depending on the study and is specified in the *Methods* section of each experimental chapter.

At the end of the study, animals were sacrificed by schedule 1 cervical dislocation or by terminal anaesthesia using vaporised isofluorane. Tissues were collected immediately, washed in ice-cold 1X phosphate buffered saline (PBS), snap frozen in liquid nitrogen, and stored in -80 °C for subsequent use.

2.3 EXPERIMENTAL METHODS

2.3.1 Frozen tissue preparation

Frozen tissues were crushed using a mortar and pestle over liquid nitrogen. Tissues were weighed and aliquoted separately for use in different assays and stored in -80 °C.

2.3.2 Adult primary cardiomyocyte isolation

Isolation and cannulation of the heart. Following schedule 1 cervical dislocation, the chest cavity was opened immediately to expose the heart. The mouse was moved to a microscope stage and the following steps were conducted under magnification. A suture was threaded under the aorta using a 105 mm micro-forceps. The aorta was cut and cannulated using a 23 G cannula. The heart was gently flushed with a syringe containing warm Tyrode perfusion solution containing (in mM): 130.0 NaCl, 5.6 KCl, 3.5 $MgCl_2$, 5.0 HEPES, 0.4 Na_2HPO_4, 10.0 Glucose and 20.0 Taurine and then mounted on a Langendorff apparatus (Figure 2.1).

Digestion and preparation of cardiac myocytes. The heart was first perfused with Tyrode perfusion solution. The tissue was then digested in 20 mL of digestion buffer: Tyrode perfusion solution supplemented with 0.1 mM $CaCl_2$ and either 1.0 mM liberase enzyme (Roche) or 1.0 mM collagenase type II (Worthington) and 0.1 mM protease (Sigma-Aldrich) for approximately 6-7 mins. Perfusion and digestion was carried out at 37 °C. Following digestion, the atria and vessels were removed and the remaining left and right ventricles were cut into small pieces. Cells were dissociated by careful mechanical disruption in 5 mL of digestion buffer at 37 °C. Cells were filtered through a 500 μm cell

strainer and enzymatic activity was quenched by adding 5 mL of 1% bovine serum albumin (BSA) in Tyrode perfusion buffer. The cells were then spun at 500 *g* for 3 mins and washed twice, once in Tyrode perfusion buffer containing 0.5 mM $CaCl_2$ and once in Tyrode perfusion buffer containing 1.0 mM $CaCl_2$. Cells were allowed to settle by gravity in between the two washes.

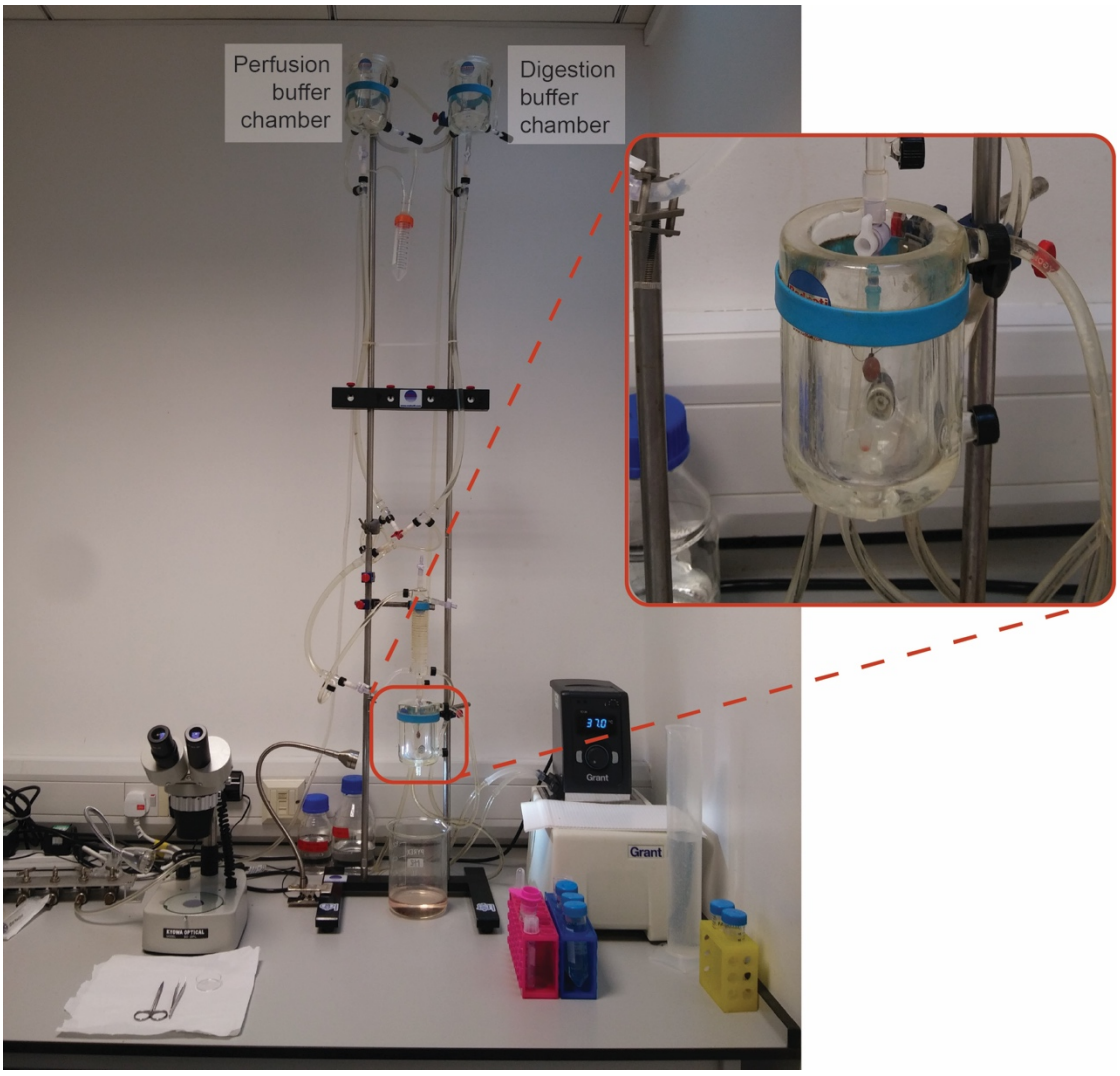


Figure 2.1 Langendorff perfusion rig for isolation of primary cardiomyocytes. Hearts were first perfused with a Tyrode perfusion buffer and then with digestion buffer. The protocol was carried out at 37 °C.

2.3.3 SDS-PAGE and Western blotting

Protein lysate preparation. Protein lysates were made by lysing approximately 20 mg of frozen mouse tissues in lysis buffer, sonicated at 4°C, and spun at 12,500 x *g* for 20 mins. The supernatant was collected and protein concentration was measured using either the Pierce BCA protein assay kit (Thermo Fisher) or Bradford assay (Sigma-Aldrich) following manufacturer's instructions.

SDS-PAGE and Western Blot. For SDS-PAGE, protein lysates were eluted in 10 μL of 2X Laemmli sample buffer and diluted in ddH_2O for a final volume of 25 μL. Samples were then heated to 95 °C for 5 mins, 20 μL loaded into the gel and subject to electrophoresis. Proteins on the gel were then transferred to a 0.2 μM PVDF membrane (Millipore) using a semi-dry transfer system (BioRad) at 15 V and 300 mAmp.

Western blot. The membrane was blocked for 1 h in 5% milk-PBS-0.05% Tween at room temperature. Primary antibody was applied and blocked overnight at 4 °C. The membrane was washed for 10 mins, 3 times, in PBS-0.05% Tween and blocked in HRP-conjugated secondary antibody for 30 mins at room temperature. After washing 3 times in PBS-0.05% Tween for a total of 30 mins, the membrane was exposed on film using a X-OMAT developer. Films were scanned and band densities were obtained using ImageJ (NIH Image). Protein intensities were normalised to the H3 nuclear loading control or the β-actin cytoplasmic loading control.

2.3.4 RNA extraction and cDNA synthesis

Total RNA was extracted from approximately 30 mg of snap frozen, crushed cardiac tissue using the RNeasy Fibrous Mini Kit (Qiagen), following manufacturer's instructions. Concentration of RNA was determined using the NanoDrop 2000. A total of 1 μg of RNA was reverse transcribed into cDNA using the Expand Reverse Transcriptase kit (Roche) and poly dT primers (Invitrogen). First, the RNA and poly dT primers were denatured at 65 °C for 10 mins. Then, reaction buffer (Roche), dNTP (Sigma-Aldrich), DTT (Roche), and reverse transcriptase (Roche) was added and incubated at 43 °C for 1 h. The cDNA was then diluted in RNase and DNase free water to a final concentration of 6.5 ng/μL.

2.3.5 Genomic DNA extraction

Genomic DNA (gDNA) was extracted from approximately 30 mg of snap frozen, crushed cardiac tissue using the DNeasy Blood and Tissue Kit (Qiagen), following manufacturer's instructions. Concentration of DNA was determined using the NanoDrop 2000. The gDNA was then diluted in RNase and DNase free water to a final concentration of 6.5 ng/μL.

2.3.6 Quantitative real-time PCR (qPCR)

Either Taqman or SYBR Green assay method was used for qPCR. All qPCR reactions were performed in 96-well plates and in either technical duplicates or triplicates, depending on the number of samples under investigation.

Gene expression. For quantification of mRNA, 25 μg of cDNA was used as template in duplex quantitative real-time PCR reactions. For Taqman assays, each well contained the

template, 0.5 μL of primer of interest, 0.5 μL of mouse β-actin housekeeper and 5 μL of the Taqman Fast Universal master mix (Life Technologies) in a 10 μL total reaction volume.

For SYBR Green assays, each well contained the template, 0.5 μL of each primer (concentration, primer dependent) and 5 μL PowerUp SYBR Green master mix (Life Technologies). The *Gapdh or Actb* gene was used as a housekeeper (*see* below, '*Selection of housekeeper*').

Analysis. First, the ΔC_T of each sample was determined by:

$$\Delta C_T^{sample} = C_T \text{ (gene of interest)} - C_T \text{ (housekeeper)}$$

To obtain the "expression level relative to controls," a mean ΔC_T (ΔC_T^{mean}) was obtained by averaging the ΔC_T of all control samples and the $\Delta\Delta C_T$ was obtained by:

$$\Delta\Delta C_T = \Delta C_T^{sample} - \Delta C_T^{mean}$$

The fold change was determined by:

$$\text{fold_change} = 2^{-\Delta\Delta CT}$$

Selection of housekeeper. For the selection of a housekeeper gene, the expression of ubiquitin C (*Ubc*), actin-β (*ActB*) and GAPDH (*Gapdh*), commonly used housekeeper genes, was first assessed using the data obtained by RNA-sequencing (Figure 2.2A). From these three genes, *Ubc* was eliminated as a candidate because its expression level compared between the iron-adjusted and iron-deficient was significantly different.

Next, the expression level of *ActB* and *Gapdh* was assessed by qPCR to validate that their expression was indeed not significantly altered between the two cohorts studied (Figure 2.2B). Having confirmed this, both *ActB* and *Gapdh* were deemed appropriate for use as housekeepers.

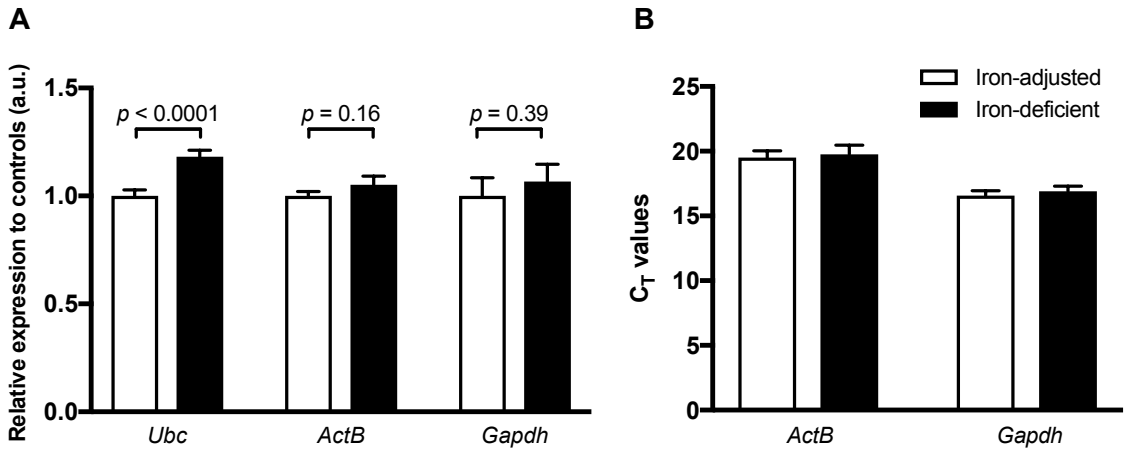


Figure 2.2 Selection of housekeeper gene for qPCR in mouse heart tissue. A) Gene expression assessed by RNA-sequencing. B) Validation of gene expression by qPCR. *Ubc* = Ubiquitin C, *ActB* = Actin-β, *Gapdh* = GAPDH. n = 10 hearts per cohort.

2.3.7 Statistical analysis

All values are shown in mean ± standard error of the mean (SEM). Depending on the data set or comparison, *p*-values were obtained using a two-tail unpaired student's *t*-test or a two-way ANOVA and post-hoc Sidak's or Tukey's multiple comparison's test. The statistical test used in each experiment is specified in each figure or table. *p*-values < 0.05 were deemed as indicating significant differences between groups.

CHAPTER 3:

PHYSIOLOGICAL CONSEQUENCES OF IRON DEFICIENCY

3.1 CHAPTER OVERVIEW

The objective of the experimental work described in this chapter was to determine the physiological consequences of dietary iron deficiency. Various indices were measured to determine the effects of an iron-deficient diet throughout the study. To assess the functional impact of dietary iron deprivation on the heart over time, mice were subject to cine-MR imaging weekly up to 12 weeks following the dietary intervention then again at 16, 20 and 24 weeks of diet. A group of animals were supplemented with iron in the form of intravenous ferric carboxymaltose to determine whether this ameliorates/reverses the physiological consequences of iron deficiency. The results of these studies demonstrate that mice become iron deficient through diet, and that their cardiac function shows modest impairment during the early stages of dietary iron restriction. Furthermore, both the iron deficiency and cardiac impairment were corrected by iron supplementation.

3.2 INTRODUCTION

3.2.1 Iron, iron deficiency and cardiac function

In the last two decades, there has been an active interest in the role of iron and iron deficiency in cardiovascular disease, particularly in the context of heart failure. Since the heart is one of the tissues with the highest metabolic demand in the body, it is very sensitive to changes in iron metabolism and any perturbations that may affect mitochondrial function, leading to abnormal energy production and utilization in the myocardium (Jankowska *et al.*, 2013; Zhabyeyev and Oudit, 2017). Both iron overload and iron deficiency impair normal cardiomyocyte activity and cause changes in the structure and overall function of the heart, contributing to the pathophysiology of heart failure (Cohen-Solal *et al*., 2014; Jankowska *et al.*, 2013).

3.2.2 Iron deficiency in chronic heart failure

Iron deficiency, in the presence or absence of anaemia, is a common co-morbidity in chronic heart failure (CHF) patients, affecting up to 50% of all heart failure (HF) patients and is associated with poor prognosis (Ebner and von Haehling, 2013). In humans, various studies have confirmed that iron deficiency can have negative effects on aerobic and endurance capacity, cognitive performance, emotions, fatigue and behaviour (Cohen-Solal *et al.*, 2014).

While the aetiology of iron deficiency in HF requires further investigation, some of the causes for iron deficiency in HF patients have been attributed to renal or bone marrow dysfunction, resistance to erythropoietin, gastrointestinal blood loss related to the use of

oral anticoagulants and other drugs, abnormal steroid metabolism, poor nutrition and malabsorption due to deranged iron transport system in the duodenal enterocytes (Cohen-Solal *et al.*, 2014; Jankowska *et al.*, 2013).

Furthermore, chronic inflammation and an augmented immune response are recognised as major contributors to functional iron deficiency in HF. One prominent feature of CHF is the activation of pro-inflammatory mediators such as NF-κB and tumor necrosis factors-α (TNF-α), both of which are considered important constituents towards the pathophysiology of HF (Jankowska *et al.*, 2006, 2013; Satoh *et al.*, 2008).

3.2.3 Iron supplementation in chronic heart failure

Due to the prevalence of iron deficiency in CHF patients, initial attempts to improve cardiac health used a combination of erythropoietin and intravenous (IV) iron sucrose. Following treatment, patients experienced improvements in both haemoglobin and left ventricular ejection fraction (LVEF) (von Haehling *et al.*, 2015). There is now overwhelming evidence that iron supplementation alone can be beneficial in iron deficient HF patients, irrespective of whether they have anaemia. In the past decade, intravenous iron supplementation (either iron sucrose or ferric carboxymaltose) in CHF patients has proved to be a positive treatment regime, with patients showing modest improvements in physiological symptoms and functional capacity compared to the cohort receiving a saline placebo (Anker *et al*., 2009; Bolger *et al*., 2006; Okonko *et al*., 2008; Ponikowski *et al*., 2015). Based on these observations, iron deficiency is currently thought to be a valid independent therapeutic target in the context of heart failure therapeutics (Anker *et al.*, 2009; Ebner and von Haehling, 2013).

Contrary to these findings, Lewis *et al.* (2017) found that a high oral iron supplementation did *not* improve haemoglobin levels and functional capacity in HF patients with iron deficiency, despite the similarities in HF aetiologies and baseline parameters of their volunteers compared to IV iron trial studies. This opens the possibility that IV iron, but not oral iron, may be an effective treatment in improving cardiac health in CHF patients. The different response between the two iron supplementation methods may be due to differences in iron absorption and distribution in the body.

3.2.4 Monitoring cardiac function in mice using magnetic resonance imaging

Magnetic resonance imaging (MRI) is commonly used to evaluate the cardiac function and morphology in humans and rodent models. The non-invasive nature of MRI makes it an ideal method for longitudinal studies aimed at monitoring structural and functional changes in the heart over the course of a treatment or in a genetic model (Tyler *et al.*, 2006). When combined with CINE imaging techniques, high-resolution images of the heart's anatomy can be obtained, in addition to functional parameters such as heart mass, ejection fraction and cardiac output more accurately and consistently than other methods capable of assessing cardiac parameters, such as 2D-echocardiography (Stuckey *et al.*, 2008; Tyler *et al.*, 2006).

Due to the small size of rodent hearts (compared to humans), high field strengths are necessary to increase signal-to-noise ratio (Stuckey *et al.*, 2008; Tyler *et al.*, 2006). In addition, gating strategies are required to compensate for high cardiac and respiratory rates (Stuckey *et al.*, 2008). The Department of Physiology, Anatomy and Genetics at the

University of Oxford is home to a 11.7 T vertical bore cine-MR system, custom-tailored for imaging of mouse hearts. This cine-MR system has been used throughout this chapter and the methods are outlined in the next section.

3.2.5 Study aims

Iron deficiency is the most common nutritional deficiency in the world. There is now a wealth of evidence supporting the importance of iron in the heart. Yet, the mechanisms by which iron plays a role in maintaining a healthy heart and the negative influence that iron deficiency exerts in HF models remain relatively unexplored. To begin to explore these questions, it is important to define precisely the nature and time course of heart failure in iron deficiency. Therefore, the aims of this study were to:

a) Establish a murine model of iron deficiency by dietary iron deprivation;

b) Investigate the effects of iron deprivation on cardiac morphology and function;

c) Test the hypothesis that iron supplementation ameliorates such effects.

3.3 METHODS

3.3.1 Mouse model

Mice used in this study were bred and provided for by the Biomedical Services at the University of Oxford. At the age of 3 weeks, animals were weaned on to either an iron-adjusted or iron-deficient diet. Blood samples were taken from the tail vein immediately prior to weaning to establish baseline blood haemoglobin concentration with the HemoCue (Radiometer) and again at the end of the week, every week throughout the duration of the experiment. The age and number of mice used in each experiment is specified in the relevant results section.

Mice were divided into the following cohorts:

- Cohort 1: Animals were kept for 24 weeks on the diet and underwent procedures as depicted in Figure 3.1A. Animals were culled on day 168 of diet.
- Cohort 2: Animals were kept on a diet for 6 weeks and culled on day 42 of diet. Body mass and haemoglobin were measured once at the end of the study.
- Cohort 3: Animals were kept on a diet for 9 weeks and culled on day 63 of diet. Body mass and haemoglobin were measured once at the end of the study.
- Cohort 4: Animals were kept for 5 weeks on the diet. At the beginning of week 4 (day 22) and week 5 (day 29), animals were intravenously administered either 15 mg/kg ferric carboxymaltose or an equivalent volume of saline. Additional procedures were conducted as depicted in Figure 3.1B. Animals were culled during the 6th week of diet, one animal per day (days 35-42 of diet).

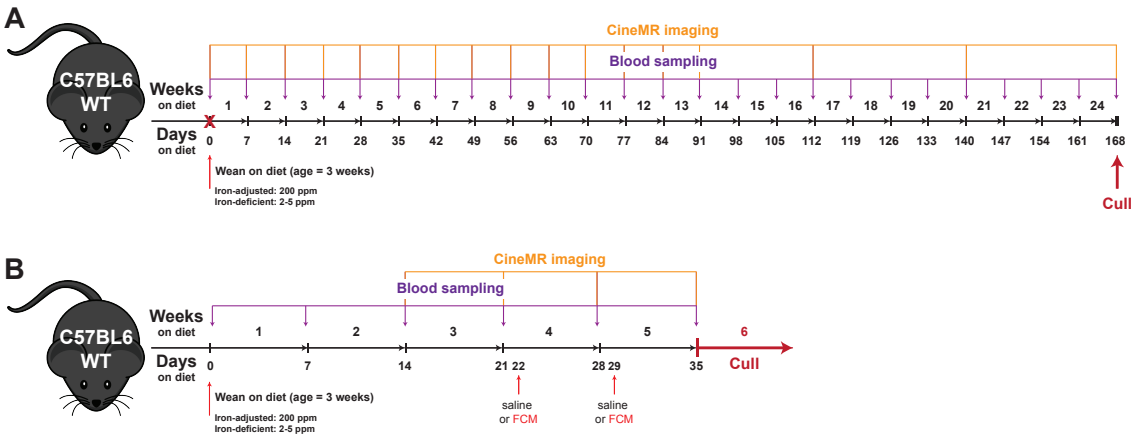


Figure 3.1 Schematic of the experimental mouse model A) For characterization of a mouse model of dietary iron-deficiency; B) For determination of the effect of iron supplementation on iron deficiency.

Mice were sacrificed and blood was collected for blood haemoglobin measurement and serum.

3.3.2 Blood sampling

Mice were placed in a heat box and warmed to 38 °C for 5 mins to encourage blood flow and then guided into a mouse restrainer. Approximately 10 μL of blood was collected from a tail vein using a 27 G needle and the blood haemoglobin concentration measured.

3.3.3 Quantitative PCR

Taqman probes (Life Technologies) for *Hamp* (Mm04231240) and *Fpn* (gene name *Slc40a1*, Mm01254822) were used for these assays. The qPCR reaction was run as described in Chapter 2, Section 2.3.6.

3.3.4 Cine-MR imaging

The methods in this section have been published in Tyler *et al.* (2006) and have been adapted below. The MRI set-up is shown in Figure 3.2.

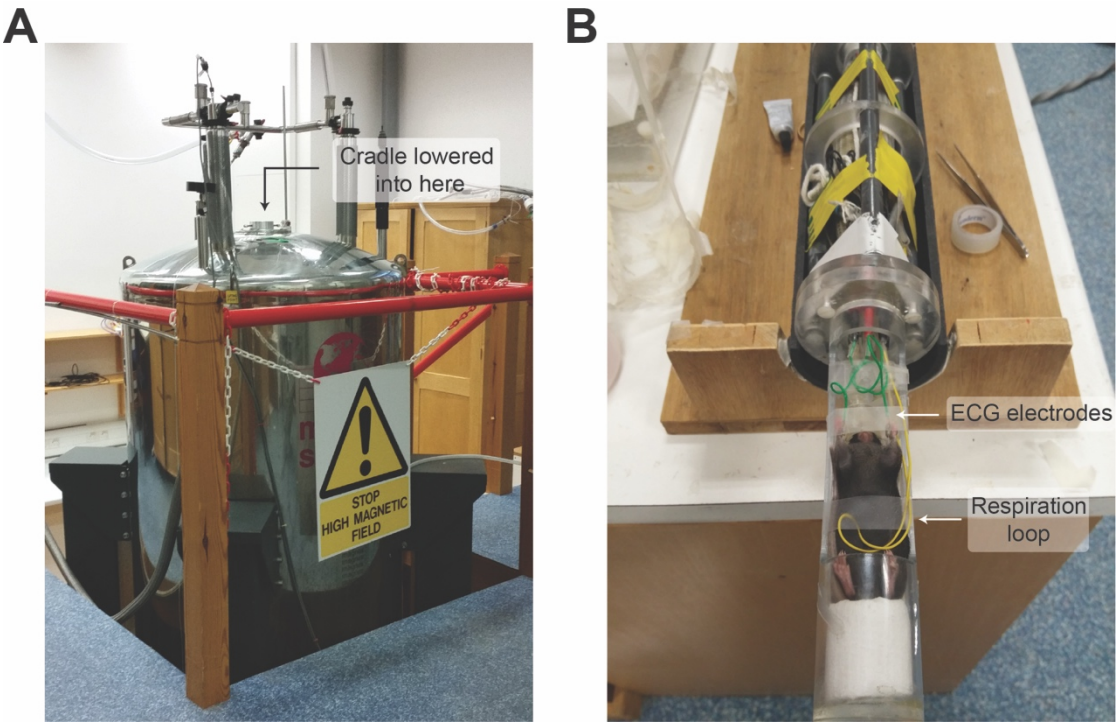


Figure 3.2 Cine-MRI setup. A) The vertical bore, 11.7 T MR system; B) Custom-built mouse cradle with mouse positioned, ready for scanning.

Imaging. Anaesthesia was initially induced in a chamber using 3% isoflurane in 100% oxygen. Mice were positioned supine in a purpose-built mouse cradle and maintained anaesthetised at 2% isoflurane in 1.5 L/min oxygen flow throughout the MRI scan. Temperature of the cradle was maintained at 35 °C via a warm air flow through a home-built heat-exchanger placed within the animal holder and above the coil in the magnet. When necessary, additional support for the body was provided with folded tissue paper.

ECG electrodes were inserted subcutaneously into the forepaws and a respiration loop taped across the chest and abdomen of the mouse with surgical tape. Heart and respiration signals were monitored using a custom-built physiological motion gating device. The cradle was lowered into a vertical-bore, 11.7 T (500 MHz) MR system with a 40 mm inner diameter birdcage coil (Rapid Biomedical, Würzburg, Germany) to transmit and receive the NMR signals.

Images were visualized using a Burker console running Paravision 2.1.1. Cardiac triggered and respiration-gated cine-FLASH images were acquired and for each animal, ten to eleven contiguous 1 mm thick, true short-axis images were obtained, covering the entire heart. Each *in vivo* protocol was performed in approximately 45 mins in the vertical position.

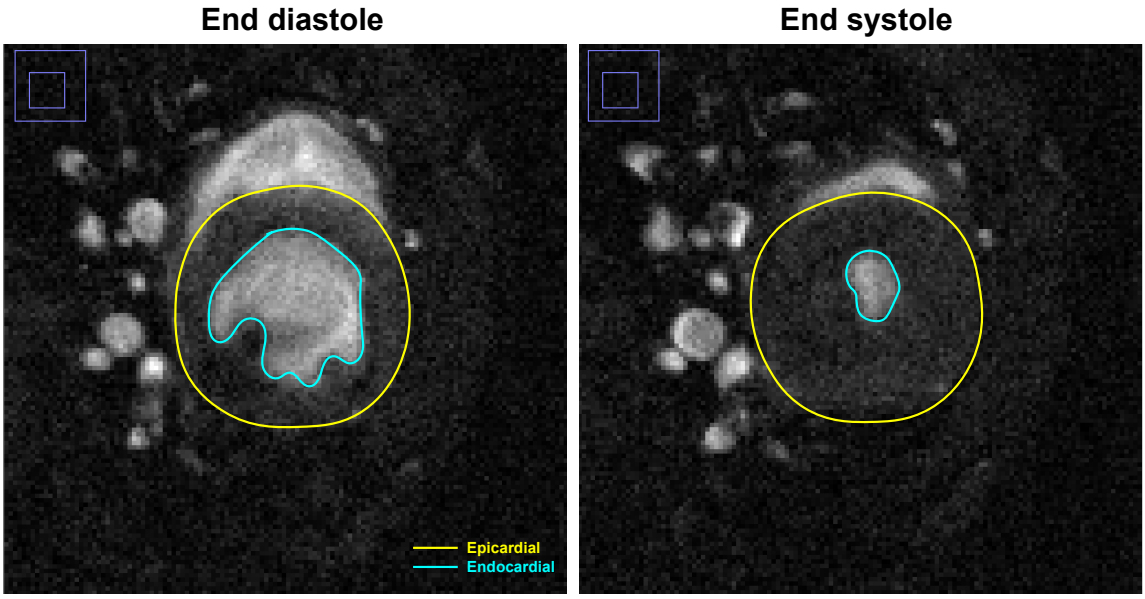


Figure 3.3 Cine-MRI analysis. For each 1 mm slice through the heart, the end diastole and end systole frames were selected according to maximal and minimal ventricular volumes. The epicardial and endocardial border was outlined for both the left and right ventricle. The border for left ventricle only is shown in this figure.

Analysis. Image analysis was performed using Fiji (NIH Image, Bethesda, MD). End-diastolic and end-systolic frames were selected according to maximal and minimal ventricular volumes (Figure 3.3). In both frames, the epicardial and endocardial border was outlined using the free-hand tool and a Wacom CTL-490DW-S drawing tablet.

Left and right ventricular mass (LV and RV, respectively) were obtained by multiplying the volume by the specific gravity of myocardial tissue (1.05 g/cm^3):

$$\text{LV or RV mass} = \left(\sum \text{V(epicardial)} - \sum \text{V(endocardial)}\right) \times 1.05$$

where: V = volume
$\sum$ = sum across entire heart

Based on end-diastolic and end-systolic volumes (EDV and ESV, respectively), parameters characterising cardiac function were calculated as follows:

Stroke volume (SV): $\mathrm{SV} = \mathrm{EDV} - \mathrm{ESV}$

Ejection fraction (EF): $\mathrm{EF} = \mathrm{SV}/\mathrm{EDV}$

Cardiac output (CO): $\mathrm{CO} = \mathrm{SV} \times \text{heart rate}$

3.3.5 Pentra chemical analysis

The ABX Pentra 400 (Horiba) was used to measure ferritin, transferrin, and iron in the serum of mice used in this thesis. Concentrations were automatically detected by the Pentra using the following reagent cassettes: Ferritin 2 CP (A11A01900; Horiba), Transferrin CP (A11A01926; Horiba) and Iron CP (A11A01637; Horiba). Each new cassette was calibrated prior to use using the calibration reagents Ferritin Cal (A11A01619; Horiba) for the ferritin cassette and Sp Cal (A11A01927; Horiba) for the transferrin and iron cassettes.

3.3.6 Isolation of primary cardiomyocytes

Primary cardiomyocytes were isolated from animals during the 6th week of diet using the liberase enzyme and as described in Chapter 2, Section 2.3.2.

3.3.7 Inductively coupled plasma-mass spectrometry

Microwave digestion. For determination of elemental metals in tissue samples, 5-50 mg of snap frozen tissue was suspended in 1 mL concentrated nitric acid (Sigma-Aldrich) and digested on a CEM SP-D80 Microwave Digestion System for 10 mins at 180 °C. For isolated cardiomyocyte samples, 150 μL of cell suspension from a whole heart isolation was weighed and then digested in 1 mL of nitric acid as described. Subsequently, 1 mL of digested sample was diluted in 49 mL of ultra-pure ddH_2O in a metal-free 50 mL

centrifuge tube. In addition, either 1 mL of nitric acid or 150 μL of 1.0 mM $CaCl_2$ Tyrode perfusion buffer in 1 mL nitric acid were microwave digested and submitted for inductively coupled plasma-mass spectrometry (ICP-MS) as blanks.

ICP-MS. Determination of tissue metal content was carried out on the Perkin Elmer 6100DRC quadrupole ICP-MS system. For calibrations, 0, 0.5, 1, 10, 20, and 100 ng/g iron was spiked into a selected sample. An external iron standard (ICPMS-68-A solution, High Purity Standards) was measured to validate the calibration. As an internal standard, 1 ng/g of rhodium was also spiked into each sample, including blanks and standards. Raw ICP-MS measurements were normalised to starting wet tissue mass.

3.3.8 Immunofluorescence

Preparation of cells. Isolated cardiomyocytes were plated on to laminin coated 8-well plates (Ibidi) and incubated at 37 °C for 2 hrs. Cells were fixed in ice-cold 4% paraformaldehyde for 20 mins at room temperature. Fixation was quenched with 1.0 mM glycine for 10 mins and the fixative washed 3 times with ice-cold PBS.

Immunofluorescence. Cells were permeabilized in 0.3% triton-X in PBS for 10 mins at room temperature, washed in PBS 3 times, and blocked in PBS supplemented with 3% donkey serum and 2% BSA for 1 hr at room temperature. Primary antibody was applied overnight at 4 °C in antibody dilution solution (PBS supplemented with 1% donkey serum and 1% BSA), washed 3 times in PBS and finally, secondary antibody was applied for 1 hr at room temperature in the dark. The nucleus was stained with DAPI for 10 mins at

room temperature. After washing, cells were preserved in PBS at 4 °C and in the dark until imaging. Cells were imaged on the Zeiss confocal microscope at 40 X-oil magnification.

The list of antibodies used for immunostaining are listed in Table 3.1.

Table 3.1 List of antibodies used in this chapter.

Antibody	Product code (Manufacturer)	Concentration
rb anti-ms MTP1 (FPN)	MTP11-A (alpha-Diagnostics Inc.)	1:50
dk anti-rb AlexaFluor 488	Ab150073 (Abcam)	1:5,000
DAPI	D1306 (Thermo Fisher)	1:10,000

rb = rabbit
ms = mouse
dk = donkey

3.4 RESULTS

3.4.1 Characterisation of a dietary model of iron deficiency

i) Effects on body mass and blood haemoglobin (Cohort 1)

C57Bl6 wild-type mice were weaned on to either an iron-adjusted (control) or iron-deficient diet and their body mass and blood haemoglobin concentration ([Hb]) were monitored weekly for 24 weeks. Immediately prior to weaning on to the respective diets (baseline or week 0 measurement), the average body mass of the iron-adjusted vs iron-deficient diet mice was not significantly different. Throughout this study, animals on an iron-deficient diet were numerically, but not significantly, underweight compared to the controls, according to a Sidak's multiple comparisons test following a two-way repeated measures ANOVA test (Figure 3.4A and Table 3.2).

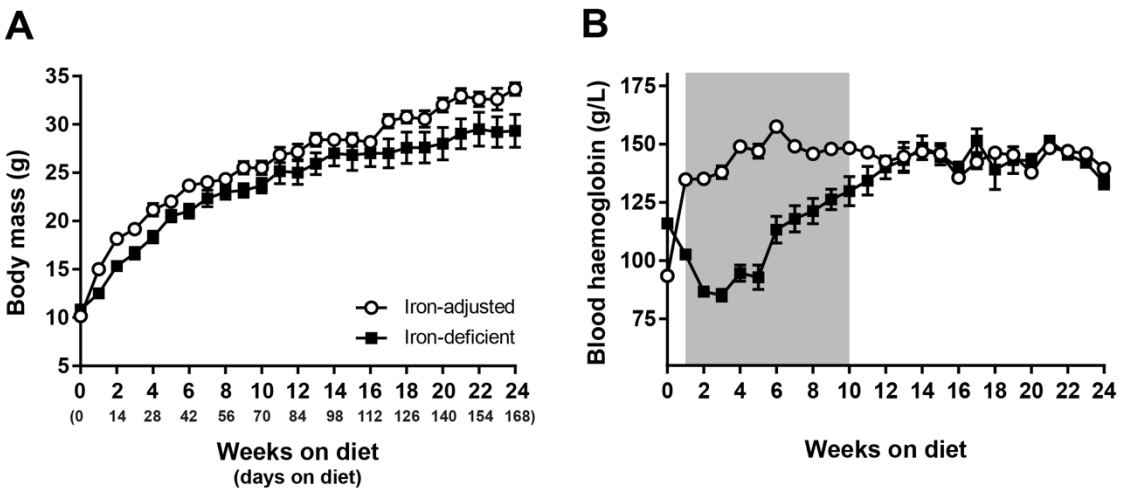


Figure 3.4 Body mass and blood haemoglobin concentration. A) Body mass and B) Blood haemoglobin concentration. Data plotted as mean ± SEM. Grey highlight region = statistically significant data-points ($p < 0.05$) according to a two-way ANOVA and post-hoc Sidak's multiple comparison's test; *see* Table 3.2. n = 6 mice per cohort.

Table 3.2 Body mass and blood haemoglobin concentration of mice on iron-adjusted or iron-deficient diets. Values represented as mean ± SEM. *p*-value determined by two-way ANOVA and post-hoc Sidak's multiple comparison's test. n = 6 mice per cohort.

	Body mass (g)			Haemoglobin (Hb)		
Weeks (days) on diet	**Iron-adjusted**	**Iron-deficient**	***p*-value**	**Iron-adjusted**	**Iron-deficient**	***p*-value**
0 (baseline)	10.2 ± 0.25	10.8 ± 0.25	> 0.9999	93.5 ± 1.66	116.0 ± 1.51	**0.0005**
1 (7)	15.0 ± 0.47	12.5 ± 0.46	0.8513	134.8 ± 1.78	102.7 ± 2.70	**< 0.0001**
2 (14)	18.2 ± 0.44	15.3 ± 0.46	0.6635	135.2 ± 2.08	86.7 ± 2.12	**< 0.0001**
3 (21)	19.2 ± 0.33	16.7 ± 0.50	0.8513	138.0 ± 1.78	85.2 ± 3.34	**< 0.0001**
4 (28)	21.2 ± 0.53	18.3 ± 0.50	0.6635	149.0 ± 1.96	94.7 ± 5.21	**< 0.0001**
5 (35)	22.0 ± 0.42	20.5 ± 0.51	0.9997	147.0 ± 2.92	92.8 ± 5.21	**< 0.0001**
6 (42)	23.7 ± 0.42	21.0 ± 0.73	0.7649	157.5 ± 2.17	113.3 ± 5.73	**< 0.0001**
7 (49)	24.0 ± 0.52	22.3 ± 0.84	0.9986	149.2 ± 1.69	118.0 ± 5.65	**< 0.0001**
8 (56)	24.3 ± 0.61	23.0 ± 0.77	> 0.9999	145.8 ± 2.36	121.3 ± 5.42	**< 0.0001**
9 (63)	25.5 ± 0.67	23.2 ± 0.70	0.9166	148.0 ± 1.93	126.3 ± 4.45	**0.0009**
10 (70)	25.5 ± 0.72	23.7 ± 0.76	0.9946	148.3 ± 0.99	129.8 ± 6.28	**0.0099**
11 (77)	26.8 ± 0.79	25.2 ± 1.30	0.9986	146.5 ± 1.34	134.3 ± 6.12	0.3811
12 (84)	27.2 ± 0.79	25.0 ± 1.24	0.9596	142.5 ± 2.39	140.0 ± 4.99	> 0.9999
13 (91)	28.4 ± 0.69	25.9 ± 1.12	0.8588	144.7 ± 6.17	143.2 ± 5.33	> 0.9999
14 (98)	28.4 ± 0.60	27.0 ± 1.32	> 0.9999	146.8 ± 0.95	148.5 ± 5.1	> 0.9999
15 (105)	28.4 ± 0.68	26.8 ± 1.62	0.9994	145.8 ± 3.43	145.7 ± 4.54	> 0.9999
16 (112)	28.2 ± 0.60	27.0 ± 1.39	> 0.9999	135.7 ± 1.12	139.7 ± 2.78	> 0.9999
17 (119)	30.3 ± 0.71	27.0 ± 1.51	0.3619	142.3 ± 2.91	151.5 ± 5.16	0.8633
18 (126)	30.8 ± 0.63	27.6 ± 1.65	0.4599	146.3 ± 0.76	139.2 ± 8.63	0.9892
19 (133)	30.6 ± 0.86	27.6 ± 1.62	0.5989	145.3 ± 2.01	143.2 ± 5.69	> 0.9999
20 (140)	32.0 ± 0.73	28.0 ± 1.69	0.1036	137.8 ± 1.25	143.0 ± 2.78	> 0.9999
21 (147)	33.0 ± 0.75	29.1 ± 1.57	0.1230	148.3 ± 1.31	151.5 ± 2.14	> 0.9999
22 (154)	32.6 ± 0.76	29.5 ± 1.76	0.4913	147.0 ± 2.00	145.5 ± 2.09	> 0.9999
23 (161)	32.6 ± 1.13	29.2 ± 1.59	0.3091	146.0 ± 2.34	142.0 ± 1.59	> 0.9999
24 (168)	33.7 ± 1.11	29.3 ± 1.71	**0.0499**	139.5 ± 2.11	133.7 ± 2.92	0.9994

[Hb] was significantly affected by diet. The [Hb] of the iron-deficient diet cohort was significantly lower than that of the controls throughout the first 10 weeks of diet (Figure 3.4B, highlighted region and Table 3.2). From the end of the 7th week of diet (day 49), the [Hb] of the animals on an iron-deficient diet began to recover in the absence of any experimental intervention, such that following 11 weeks of diet (day 77 onwards), [Hb] was no longer significantly different between the two treatment cohorts and remained comparable throughout the rest of the study.

ii) Effects on physiological iron status (Cohort 2)

For the assessment of iron status, serum ferritin (sFt), serum iron (sFe) and serum transferrin (sTf) were measured. Mice were sacrificed following 6 weeks of diet and their serum collected for biochemical analysis (Figure 3.5C-F and Table 3.3). As expected in iron deficiency, sFt and sFe levels were lower in the mice on an iron-deficient diet by 52% and 38% ($p < 0.0001$ and $p = 0.0002$), respectively, and sTf levels were elevated by 83% compared to the controls ($p < 0.0001$). TSat, approximated as the sFe/sTf ratio, was 63% lower in the iron-deficient diet cohort ($p < 0.0001$).

Furthermore, consistent with the results obtained from cohort 1, the [Hb] of this cohort of mice (cohort 2) on an iron-deficient diet was significantly decreased (Figure 3.5B). Notably, these animals on a low iron diet had significantly lower [Hb] values than those in cohort 1 (cohort 1 vs cohort 2 [Hb] (in g/L): 113.3 vs 52.5). In addition, unlike the cohort 1 animals, cohort 2 mice on an iron-deficient diet were also significantly underweight compared to the controls (Figure 3.5A), suggesting that a relationship exists between the degree of iron deficiency and the severity of the phenotype.

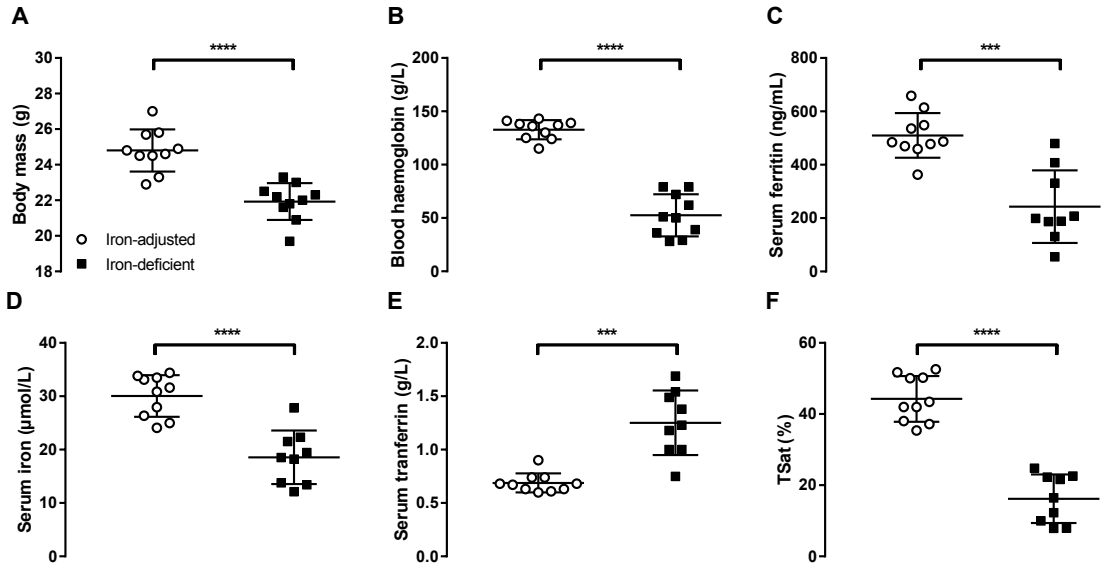


Figure 3.5 Various parameters to determine iron status following 6 weeks of diet. A) Body mass, B) Blood haemoglobin, C) Serum ferritin, D) Serum iron, E) Serum transferrin and F) Transferrin saturation (TSat). Data plotted as (top to bottom) third quartile, median and first quartile. *p*-value determined by two-tail unpaired student's *t*-test; *** $p < 0.001$, **** $p < 0.0001$. n = 10 mice per cohort per assay.

Table 3.3 Parameters measured for determination of iron status of mice on iron-adjusted or iron-deficient diets for 6, 9 and 24 weeks. Values represented as mean ± SEM. *p*-value determined by two-tail unpaired student's *t*-test. n = 10 mice (6 weeks) or 6 mice (9 and 24 weeks) per cohort.

	Body mass (g)	**Blood haemoglobin** (g/L)	**Serum ferritin** (ng/mL)	**Serum iron** (µmol/mL)	**Serum transferrin** (g/L)	**Transferrin saturation** (%)
6 weeks diet						
Iron-adjusted	24.8 ± 0.28	132.8 ± 2.84	509.8 ± 26.46	32.1 ± 2.49	0.69 ± 0.03	47.4 ± 4.29
Iron deficient	21.9 ± 0.33	52.5 ± 6.23	243.0 ± 45.36	18.6 ± 1.67	1.25 ± 0.10	16.2 ± 2.28
***p*-value**	**0.0099**	**< 0.0001**	**< 0.0001**	**0.0002**	**< 0.0001**	**< 0.0001**
9 weeks diet						
Iron-adjusted	24.4 ± 0.51	143.4 ± 5.85	489.7 ± 17. 33	24.9 ± 1.75	0.65 ± 0.01	38.6 ± 2.40
Iron deficient	19.8 ± 0.31	100.3 ± 13.40	166.8 ± 7.79	21.8 ± 4.70	1.05 ± 0.04	38.9 ± 5.22
***p*-value**	**0.0022**	**0.0041**	**< 0.0001**	0.8644	**< 0.0001**	**> 0.9999**
24 weeks diet						
Iron-adjusted	33.2 ± 1.11	139.5 ± 2.11	511.5 ± 19.88	20.9 ± 2.50	0.61 ± 0.01	34.4 ± 4.04
Iron deficient	29.3 ± 1.71	133.7 ± 2.92	325.6 ± 26.90	26.98 ± 2.51	0.72 ± 0.23	37.1 ± 2.70
***p*-value**	**0.0074**	0.9643	**0.0007**	0.3096	0.5027	0.9699

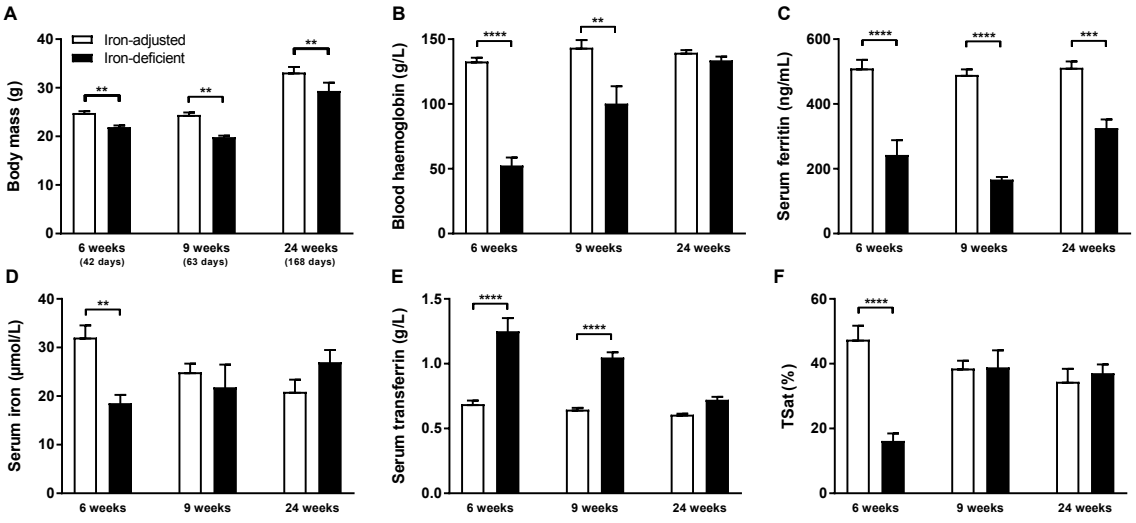


Figure 3.6 Serial measure of iron status following 6, 9 or 24 weeks of diet. A) Body mass, B) Blood haemoglobin concentration, C) Serum ferritin, D) Serum iron, E) Serum transferrin and F) Transferrin saturation (TSat). Data plotted as mean ± SEM. *p*-value determined by two-way ANOVA and post-hoc Sidak's multiple comparison's test; * $p < 0.05$, ** $p < 0.01$, *** $p < 0.001$, **** $p < 0.0001$. n = 10 mice (6 week diet) or 6 mice (9 and 24 week diet) per cohort per assay.

iii) Long-term consequence of an iron-deficient diet (Cohorts 1-3)

The [Hb] of mice on an iron-deficient diet increased over time despite continuous feeding on an iron-deficient diet, raising the possibility that these animals were no longer iron deficient. Therefore, to determine the long-term effect of an iron-deficient diet on physiological iron status, mice were sacrificed at two additional dietary time-points – 9 weeks (cohort 3) and 24 (cohort 1, end point) weeks of diet – and the various parameters were compared (Figure 3.6 and Table 3.3). For convenience, the data presented in Figure 3.5 has been adapted and reproduced in Figure 3.6.

At all three time-points, animals on an iron-deficient diet were significantly under-weight compared to the control animals. Furthermore, compared to the controls, average [Hb]

was decreased over 2-folds following 6 weeks of diet, decreased approximately 1.5-fold following 9 weeks of a deficient diet and was not significantly different following 24 weeks of diet. The time-dependent recovery of [Hb] to levels comparable to the controls was consistent with the patterns shown in Figure 3.4B.

Compared to controls, sFt concentration was significantly lower at all time-points in the iron deprived group. sFe was also significantly reduced following 6 weeks of dietary iron-deprivation, but increased over time, such that following 9 and 24 weeks of an iron-deficient diet, no difference in sFe levels were observed compared to the controls. The concentration of sTf was significantly higher in the iron-deficient cohort following 6 and 9 weeks of diet, but was no different to the controls following 24 weeks of diet. Finally, TSat was only decreased significantly following 6 weeks of an iron-deficient diet.

iv) Effect of iron supplementation on iron status of iron-deficient animals (Cohort 4)

To investigate the effect of iron supplementation on iron status, animals rendered iron deficient through dietary intervention were administered either 15 mg/kg of ferric carboxymaltose (FCM) or an equivalent volume of saline, intravenously, once on day 22 of diet and then again on day 29 of diet. The body mass and [Hb] were monitored weekly (Figure 3.7 and Table 3.4).

The body mass of animals on an iron-deficient diet, but not iron supplemented mice, became significantly lower than that of the controls following 4 weeks of diet and persisted through the 5th week of diet (Figure 3.7).

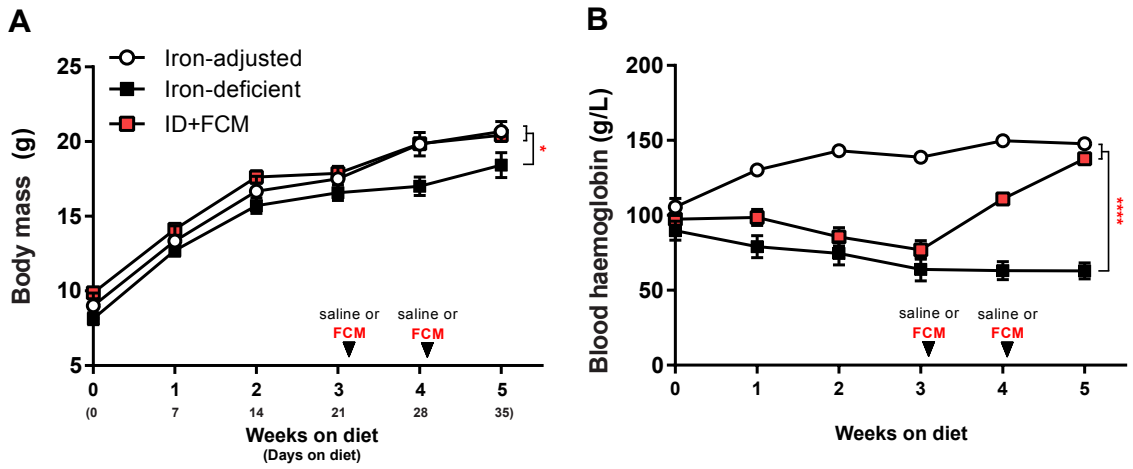


Figure 3.7 Body mass and blood haemoglobin concentration measurements. Body mass and B) Blood haemoglobin. ID+FCM = mice on iron-deficient diet receiving two doses of ferric carboxymaltose. ID+FCM = mice on iron-deficient diet receiving two doses of ferric carboxymaltose. Data plotted as mean ± SEM. *p*-value determined by a two-way ANOVA and post-hoc Tukey's multiple comparison's test; * $p < 0.05$, **** $p < 0.0001$. n = 10 mice per cohort per assay.

Table 3.4 Effect of iron supplementation on iron status. Values represented as mean ± SEM; *p*-value determined two-way ANOVA and post-hoc Tukey's multiple comparison's test. n = 10 mice per cohort.

	Iron-adjusted (1)	Iron-deficient (2)	ID+FCM (3)	*p*-value (1) vs (2)	*p*-value (1) vs (3)	*p*-value (2) vs (3)
Body mass (g)	20.7 ± 0.67	18.4 ± 0.84	20.4 ± 0.30	**0.0309**	0.9596	**0.0486**
Blood haemoglobin (g/L)	147.7 ± 3.04	63.6 ± 3.19	137.7 ± 2.67	**< 0.0001**	0.4990	**< 0.0001**
Serum ferritin (ng/mL)	529.7 ± 48.28	246.8 ± 26.15	563.9 ± 32.62	**< 0.0001**	0.6899	**< 0.0001**
Serum iron (µmol/mL)	32.36 ± 1.58	14.23 ± 2.13	32.97 ± 1.61	**0.0312**	0.4679	**0.0144**
Serum transferrin (g/L)	0.57 ± 0.04	0.97 ± 0.07	0.71 ± 0.03	**0.0014**	0.2583	**0.0021**
Transferrin saturation (%)	59.6 ± 5.25	14.90 ± 1.98	46.95 ± 2.46	**0.0326**	0.7692	**0.0002**

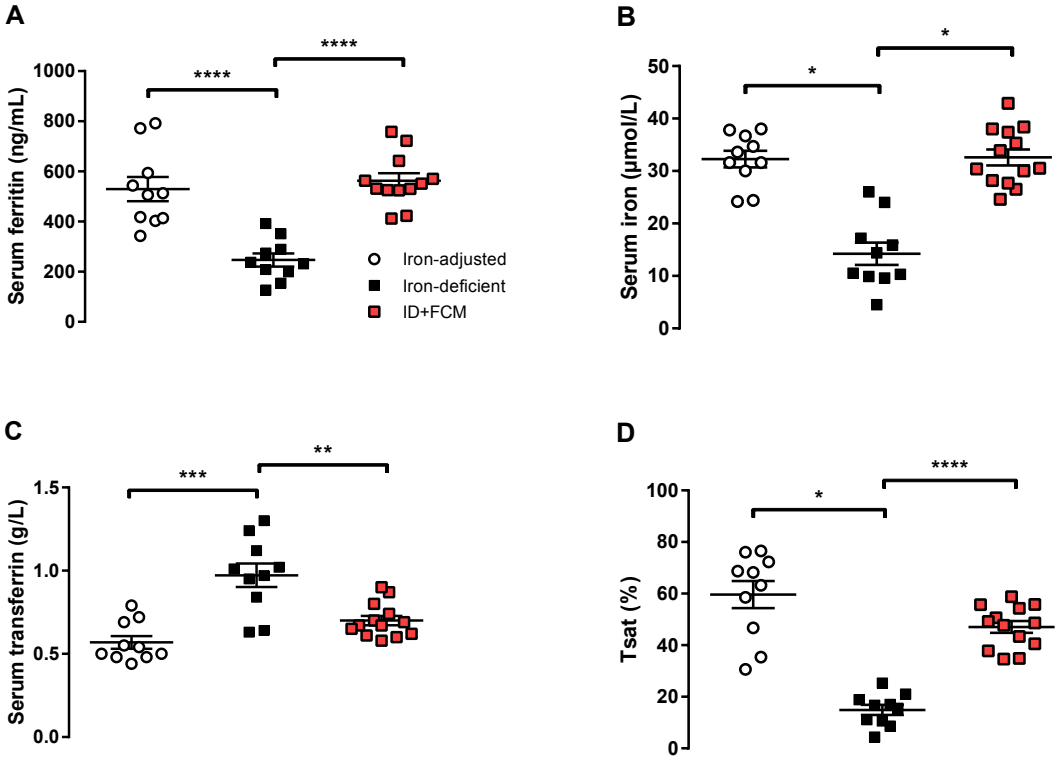


Figure 3.8 Measure of iron status following iron supplementation. A) Serum ferritin, B) Serum iron, C) Serum transferrin and D) Transferrin saturation were measured in mice following two weekly doses of either saline or ferric carboxymaltose. ID+FCM = mice on iron-deficient diet receiving two doses of ferric carboxymaltose. Data plotted as (top to bottom) third quartile, median and first quartile. *p*-value determined by a two-tail unpaired student's *t*-test; * $p < 0.05$, $p < 0.001$, **** $p < 0.0001$. n = 10-13 mice per cohort per assay.

Prior to administration of either saline or FCM at the beginning of week 4 of diet, all animals on an iron-deficient diet had significantly lower [Hb] than the controls. A week following the first injection (end of week 4), [Hb] of animals that received FCM (ID+FCM) increased from 75 to 111 g/L. A second dose of FCM further increased their haemoglobin to 137 g/L, a value that was significantly higher than that of mice on an iron-deficient diet ($p < 0.001$) and no longer significantly different than that of the control animals (147 g/L, $p = 0.4990$). On the other hand, the [Hb] of mice on an iron-deficient diet receiving saline

decreased from 72 to 63 g/L after the first injection and remained low (64 g/L) following the second injection (iron-adjusted vs iron-deficient: $p < 0.0001$; iron-deficient vs ID+FCM: $p < 0.0001$).

Animals were then sacrificed during the 6th week of diet and their serum was collected for analysis of iron status (Figure 3.8 and Table 3.4). Consistent with the results obtained from cohort 2 mice (Section 3.4.1.ii), mice on an iron-deficient diet had significantly lower levels of sFt and sFe concentration and significantly elevated levels of Tf in the serum, compared to mice on the control diet. Furthermore, compared to the iron-deficient cohort, ID+FCM mice had elevated sFt and sFe concentration and reduced sTf concentration; these values were comparable to those of the controls.

v) Determination of total elemental iron in tissues following an iron-deficient diet

Having established the effects of iron intervention on circulating iron indices, the effect of these treatments on tissue iron content was examined. Total elemental iron (Fe^{56}) in the heart, liver and spleen was measured by inductively coupled plasma-mass spectrometry (ICP-MS) (Figure 3.9). Compared to control animals, tissue iron content was decreased significantly in the livers and spleens of mice on a deficient diet by 2-fold and 4-fold, respectively (liver: $p < 0.0001$; spleen: $p < 0.0001$). FCM supplementation following 3 weeks of iron deprivation restored spleen iron stores to levels comparable to that of the controls ($p = 0.3620$); liver iron was approximately 140% of the controls ($p = 0.0002$). On the other hand, cardiac iron was unaltered following 6 weeks of an iron-deficient diet.

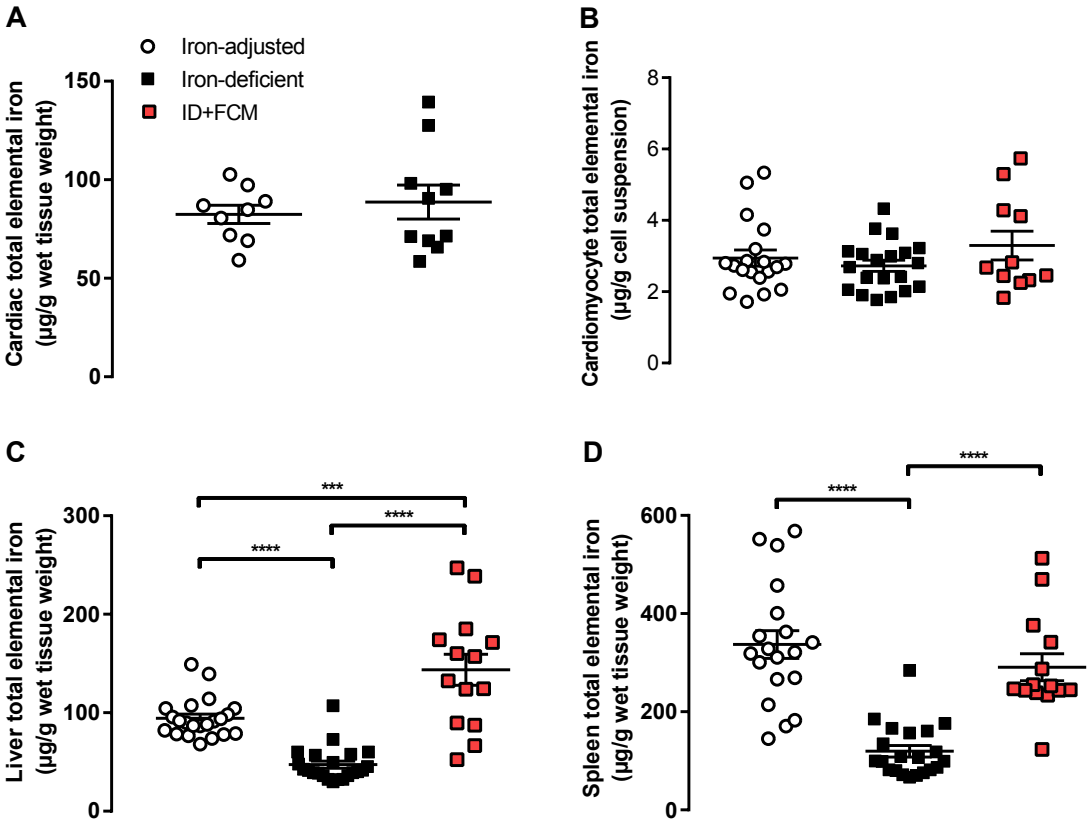


Figure 3.9 Measurement of total elemental iron by ICP-MS. A) Total heart tissue, B) Isolated primary cardiomyocytes, C) Liver and D) Spleen of iron-adjusted, iron-deficient and iron-deficient + FCM (ID+FCM) animals. Data plotted as (top to bottom) third quartile, median and first quartile. *p*-value determined by a two-tail unpaired student's *t*-test; * $p < 0.05$, *** $p < 0.001$, **** $p < 0.0001$. Number of animals used in this experiment can be found in Table 3.5.

When assessing iron content in total heart tissue, the measurement obtained is the total iron content of not only cardiomyocytes, but also fibroblasts, endothelial cells and white blood cells. To assess the iron content specifically in the muscle cells, cardiomyocytes were isolated and the iron content was measured only in the cardiac myocytes. Consistent with the values obtained in total tissue, the iron content in the myocytes was not altered by an iron-deficient diet (Figure 3.9B). Furthermore, supplementation of FCM had little impact on cardiomyocyte total iron stores (*see* Table 3.5).

Three other divalent metals – Mn^{55}, Cu^{63}, and Zn^{66} – were also measured (Table 3.5). Both Mn and Zn were significantly increased in the hearts and liver of mice on an iron-deficient diet. These changes could be due to an increase in the Zn/Mn transporter ZIP14, previously been shown to be up-regulated in iron-deficiency (Nam and Knutson, 2012). Furthermore, Mn transport could have been enhanced through the iron transporter DMT-1, which is also known to have an affinity for manganese (Fujishiro *et al.*, 2012).

The hearts, livers, and spleens of older animals were also analysed for total iron content (Figure 3.10). Compared to the controls, following 6 weeks of an iron-deficient diet, iron content in total heart tissue was unaltered, but it was decreased following 9 weeks and 24 weeks of diet. Liver and spleen iron content in the mice on an iron-deficient diet was significantly reduced following 6 weeks of an iron-deficient diet, and remained low throughout the study.

Furthermore, in the controls, all three organs accumulated more iron with age, such that mice at the 24 week time point had significantly larger iron stores than mice at the 6 week time point (iron-adjusted diet 6 week vs 24 week – heart: $p = 0.0066$; liver: $p = 0.0104$; spleen: $p < 0.0001$). In contrast, in the iron-deficient diet cohort, the level of iron in these three tissues was not altered significantly with age (iron-deficient diet 6 week vs 24 week – heart: $p > 0.9999$; liver: $p = 0.9992$; spleen: $p = 0.9994$).

Collectively, these results suggest that the provision of an iron-deficient diet prevents the time-dependent accumulation of iron otherwise seen in the control group. In the heart, this accounts for the significant difference in total iron following 9 and 24 weeks of diet, but not following 6 weeks of diet in the iron-deficient animals compared to the controls.

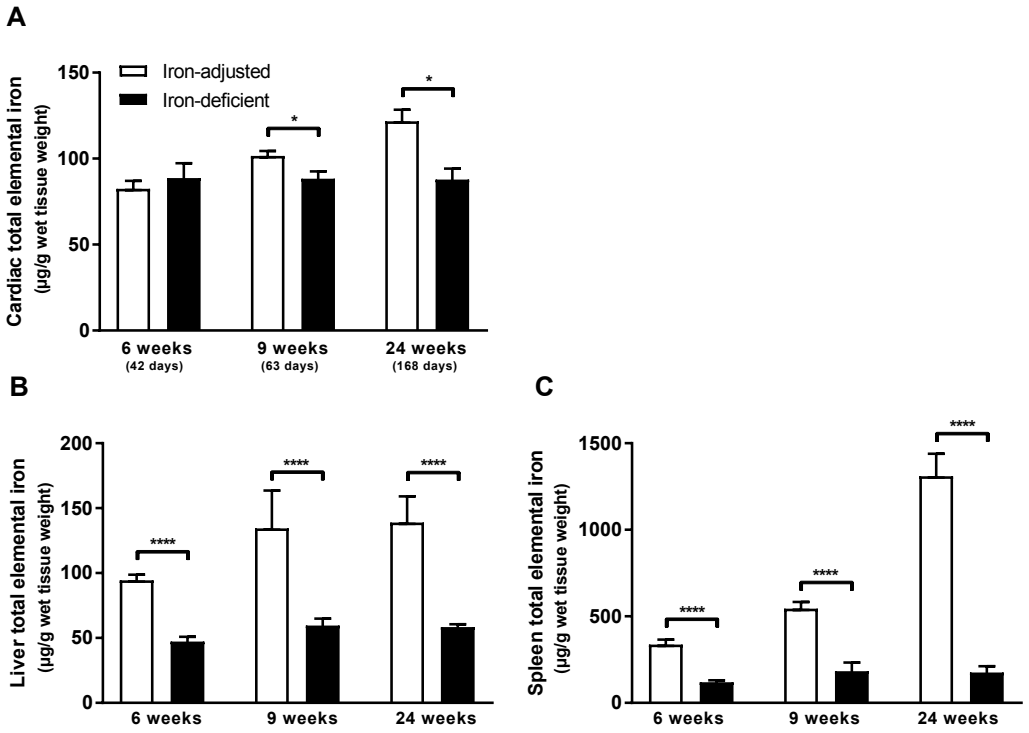


Figure 3.10 Determination of elemental iron following 6, 9 and 24 weeks of diet. A) Total heart tissue, B) Liver and C) Spleen of iron-adjusted and iron deficient animals. Data plotted as mean ± SEM. *p*-value determined by two-way ANOVA and post-hoc Sidak's multiple comparison test; * $p < 0.05$, **** $p < 0.0001$. n = 10 mice (6 weeks) and n = 6 mice (9 and 24 week).

Table 3.5 Total elemental iron measured by ICP-MS in heart, primary cardiomyocytes, liver and spleen following 6 weeks of diet. ID+FCM = iron-deficient + FCM. Data presented as mean ± SEM. *p*-value determined by a one-way ANOVA and post-hoc Tukey's multiple comparison's test; * $p < 0.05$, **** $p < 0.0001$.

(µg/g)	Mn 55	Cu 65	Zn 66	Fe 56	n
Total heart tissue					
Iron-adjusted	0.96 ± 0.73	9.4 ± 0.68	16.1 ± 0.69	90.3 ± 8.88	10
Iron deficient	1.25 ± 0.11 *	10.5 ± 0.87	19.9 ± 1.38 *	88.7 ± 8.59	10
Primary cardiomyocytes					
Iron-adjusted	Below DL	0.35 ± 0.01	0.70 ± 0.08	2.95 ± 0.23	19
Iron deficient	Below DL	0.36 ± 0.02	0.68 ± 0.06	2.73 ± 0.15	20
ID+FCM	Below DL	0.41 ± 0.06	0.72 ± 0.07	3.29 ± 0.40	12
Liver					
Iron-adjusted	0.89 ± 0.03	5.28 ± 0.20	25.7 ± 0.94	99.4 ± 4.24	30
Iron deficient	1.58 ± 0.09 ****	5.60 ± 0.23	29.0 ± 1.16 ****	55.2 ± 5.83 ****	31
ID+FCM	1.18 ± 0.07	4.96 ± 0.62	26.3 ± 1.81	143.6 ± 15.7	14
Spleen					
Iron-adjusted	0.50 ± 0.06	3.01 ± 0.19	31.3 ± 3.26	337.08 ± 28.4	20
Iron deficient	0.43 ± 0.05	3.29 ± 0.14	30.5 ± 0.14	119.5 ± 11.6 ****	21
ID+FCM	0.46 ± 0.05	3.81 ± 0.87	31.3 ± 2.11	290.7 ± 27.4	14

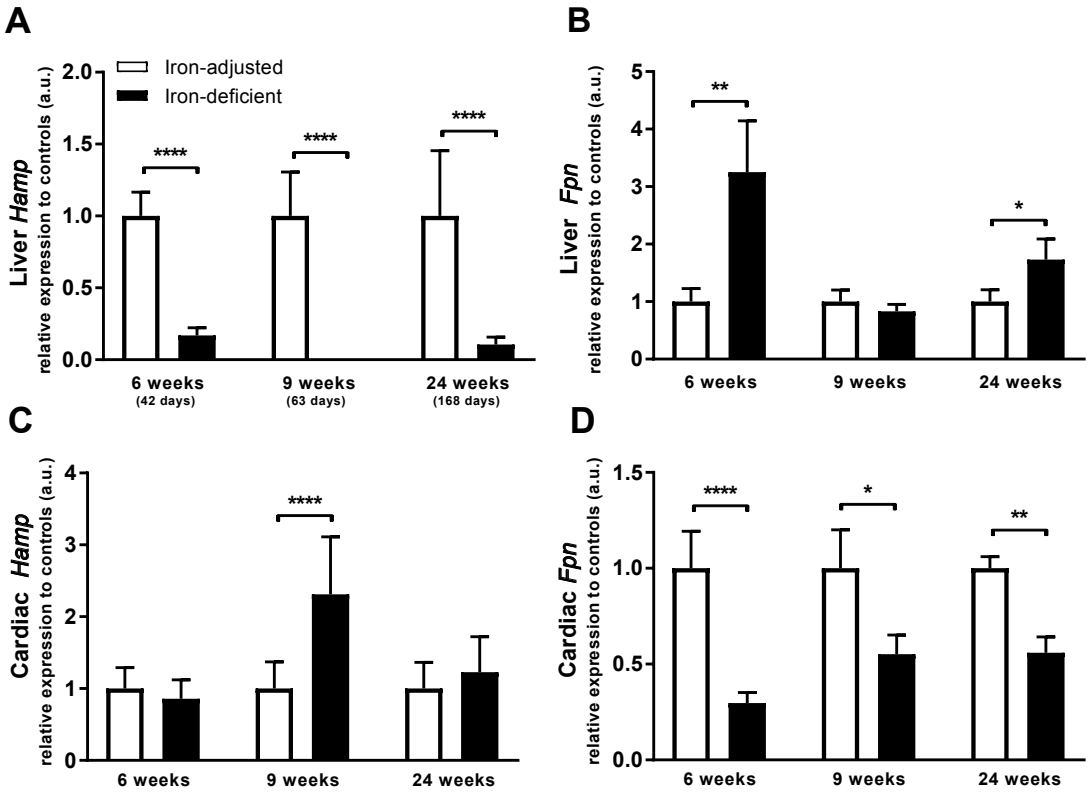


Figure 3.11 Real time qPCR comparison of *Hamp* and *Fpn* mRNA expression following 6 weeks, 9 weeks and 24 weeks of iron-deficient diet. *Hamp* gene expression in A) Heart and B) Liver. *Fpn* gene expression in C) Heart and D) Liver of animals on an iron-adjusted or iron-deficient diet. Data plotted as mean ± SEM. *p*-value determined by two-way ANOVA and post-hoc Sidak's multiple comparison test; * $p < 0.05$, ** $p < 0.01$, **** $p < 0.0001$. n = 9 (6 week) or 6 (9 and 24 week) per cohort.

vi) Effects of an iron-deficient diet on the hepcidin/FPN axis.

Iron homeostasis is tightly regulated by the hepcidin/FPN axis. Therefore, any perturbations in the bioavailability of iron is likely to elicit changes in the expression of hepcidin (*Hamp*) and ferroportin (*Fpn*), both at the mRNA and protein level.

The expression level of *Hamp* and *Fpn* genes was assessed using real-time quantitative PCR in both cardiac and liver tissues in animals maintained on diet for 6 weeks, 9 weeks and 24 weeks (Figure 3.11). At all 3 time-points, *Hamp* was decreased in the livers of iron

deprived animals compared to the controls; *Hamp* was most decreased following 9 weeks of diet. Liver *Fpn* was increased following 6 and 24 weeks of diet, but not 9 weeks of diet. In the heart, *Hamp* was only significantly increased following 9 weeks of iron-deficient diet and *Fpn* was decreased at all time-points.

Qualitatively, FPN at the protein level did not appear to be affected by an iron-deficient diet (Figure 3.12). Its distribution along the sarcolemma also appeared unchanged by diet.

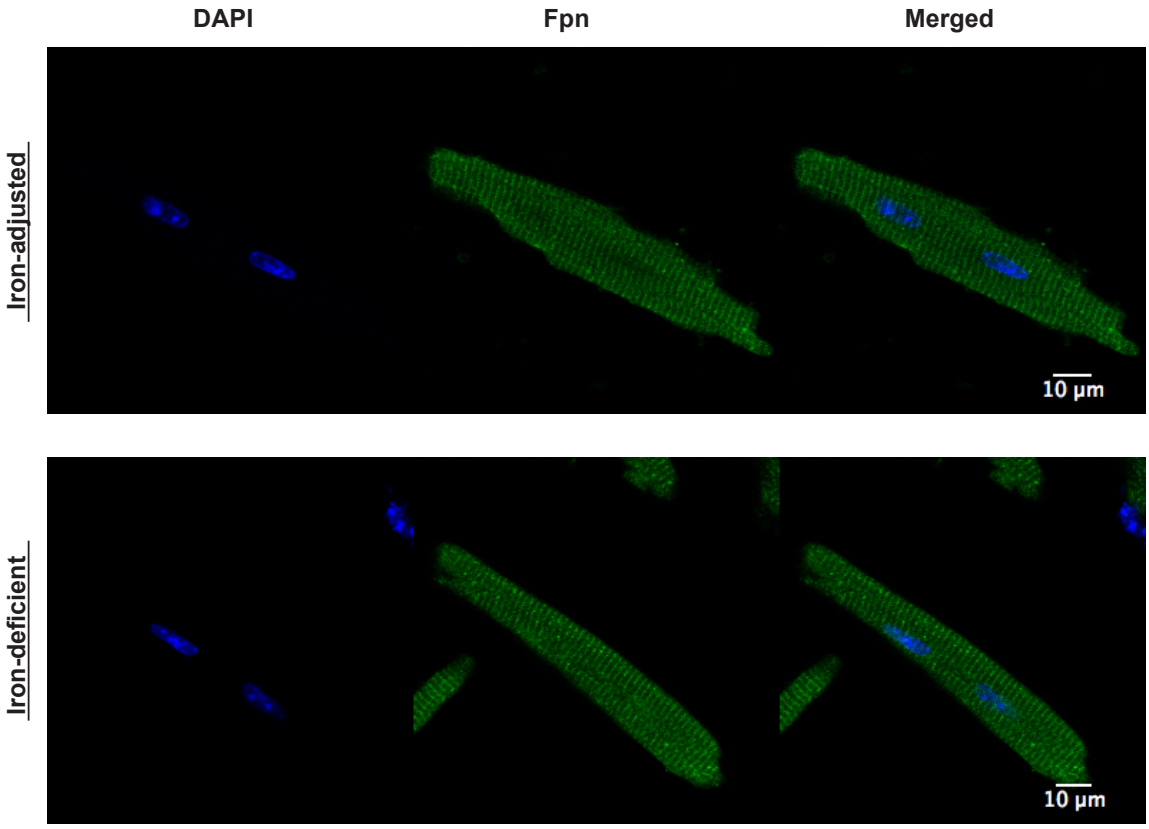


Figure 3.12 Immunofluorescence staining for FPN in isolated ventricular cardiomyocyte from a mouse on either an iron-adjusted or iron-deficient diet. Figure is a representative image from n = 3 mice and N = 4 or 5 cells per mouse.

3.4.2 Effects of iron deficiency on cardiac function

The work presented in Section 3.4.1 showed that an iron-deficient diet renders animals physiologically iron deficient. This deficiency appeared to be temporal, with reversal of the deficiency observed following long-term diet. Having established the nature and time course of changes in iron status in this mouse model, this section will explore how such changes affect cardiac function.

i) Serial measures of cardiac function during the course of dietary iron restriction (Cohort 1)

Cine-MRI was used to measure left and right ventricular function in mice on an iron-adjusted or iron-deficient diet. Scans were conducted once a week from the end of week 2 of diet (scan on day 14) until the end of week 12 of diet (scan on day 84) and again following 16, 20, and 24 weeks of diet. Representative cine-MR images at end diastole and end systole comparing an iron-adjusted vs iron-deficient mouse heart is shown in Figure 3.13A. A table of mean ± SEM for the measured parameters determined weekly can be found in Table 3.6.

The MRI results (Figure 3.13) show that cardiac function is impaired at an early stage of the dietary depletion of iron. Between weeks 2 and 4 of diet, heart-to-body mass ratio was higher in the iron-deficient group (Figure 3.13A). However, this difference was no longer observed from the end of the 5th week to the end of the 24th week of diet.

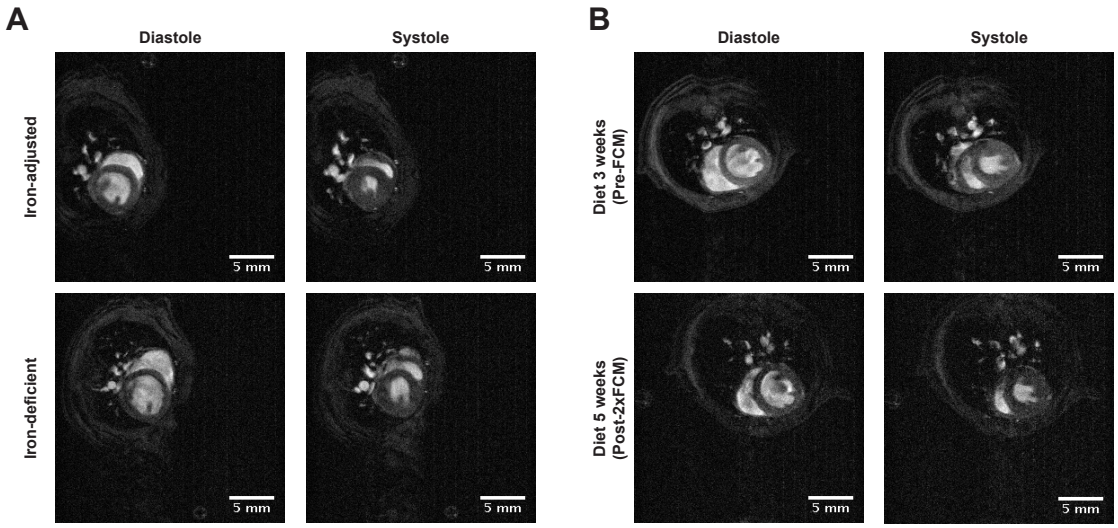


Figure 3.13 Assessment of cardiac function by cine-MRI. Representative images at end diastole and end systole for A) Iron-adjusted vs iron-deficient groups following 5 weeks of diet and B) Before and after 2 doses of FCM of the same mouse which was on an iron-deficient diet. n = 6 mice per cohort.

Left and right ventricular ejection fractions (LVEF and RVEF, respectively) were significantly reduced following 3 weeks of an iron-deficient diet and remained depressed until the end of the 8th week of diet (Figure 3.14B and C). Despite differences in ejection fraction, the underlying differences in end-diastolic, end-systolic and stroke volumes did not reach significance (Figure 3.14D-I). Interestingly, at 9-10 weeks of diet, LVEF and RVEF were no longer different in the iron deprived group compared to the controls.

Septal wall, LV and RV free wall thickness were not significantly different between the two groups (Figure 3.14J-L).

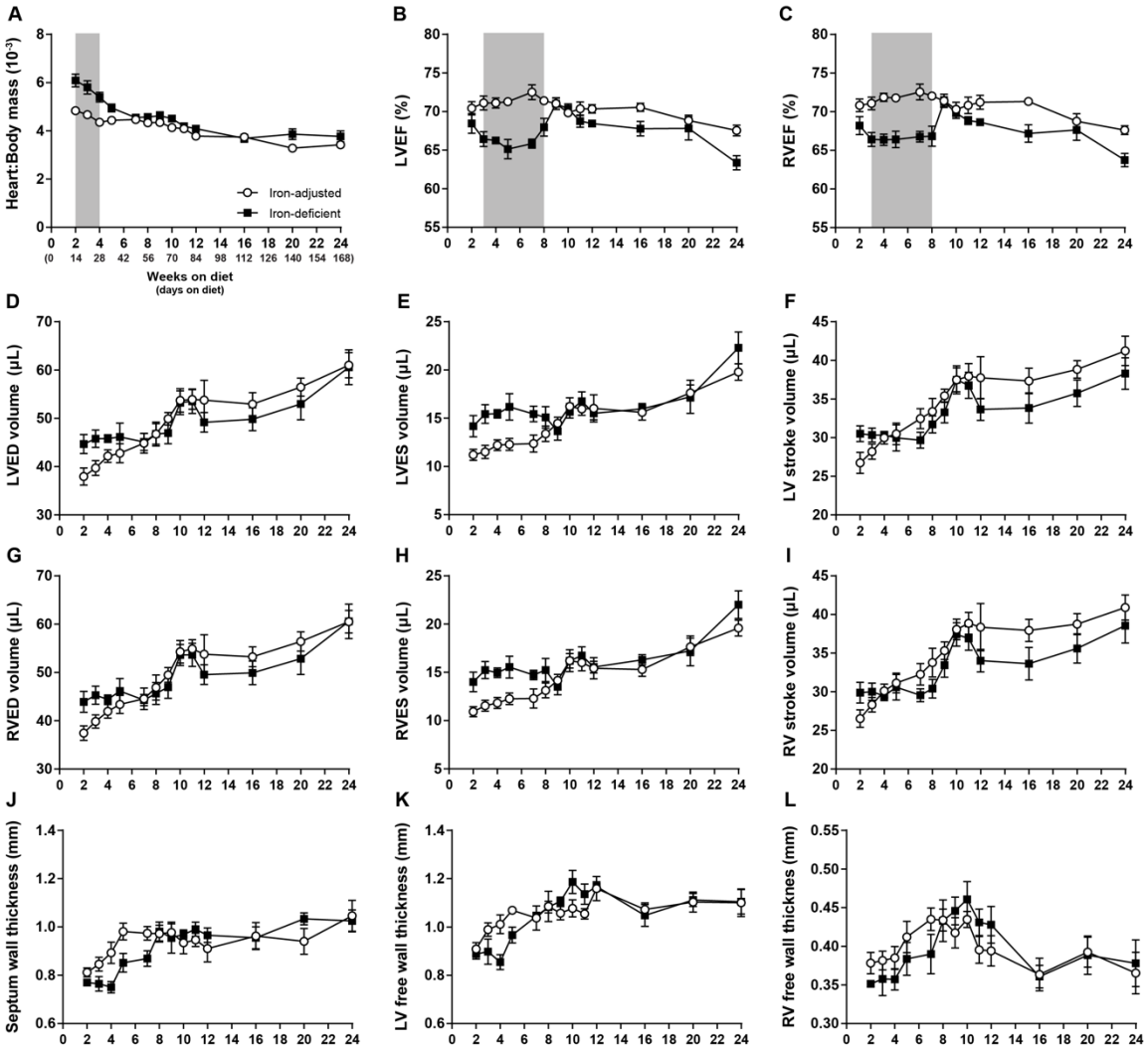


Figure 3.14 Assessment of cardiac function over long-term dietary intervention. A) Heart-to-body mass ratio, B and C) Left and right ventricular ejection fraction, D-I) Left and right ventricular volumes at end diastole and end systole and stroke volumes, J-L) Wall thickness. Data plotted as mean ± SEM. Grey highlight represents statistically significant data according to a two-way ANOVA and post-hoc Tukey's multiple comparison's test. n = 6 mice per cohort.

Table 3.6 Serial measure of *in vivo* cardiac function assessed by cine-MRI. *p*-value determined by a two-way ANOVA and post-hoc Tukey's multiple comparison's test. n = 6 mice per cohort.

Weeks on diet	2 weeks			3 weeks			4 weeks		
	Iron-adjusted	Iron-deficient	*p*-value	Iron-adjusted	Iron-deficient	*p*-value	Iron-adjusted	Iron-deficient	*p*-value
Heart:body mass ($\bullet 10^{-3}$)	4.84 ± 0.12	6.09 ± 0.26	**< 0.0001**	4.67 ± 0.12	5.80 ± 0.28	**< 0.0001**	4.36 ± 0.09	5.39 ± 0.20	**< 0.0001**
LVED volume (µL)	37.9 ± 1.78	44.7 ± 1.98	0.4333	39.7 ± 1.53	45.8 ± 1.81	0.5967	42.2 ± 1.30	45.8 ± 0.82	0.9846
LVES volume (µL)	11.2 ± 0.56	14.2 ± 1.10	0.3216	11.5 ± 0.68	15.4 ± 0.97	0.0521	12.2 ± 0.56	15.5 ± 0.44	0.2002
RVED volume (µL)	37.5 ± 1.49	43.9 ± 2.18	0.4682	39.9 ± 1.37	45.3 ± 1.87	0.7305	41.9 ± 1.41	44.4 ± 0.93	0.9995
RVES volume (µL)	10.9 ± 0.52	14.0 ± 1.01	0.1892	11.5 ± 0.58	15.2 ± 0.88	0.0511	11.8 ± 0.57	15.0 ± 0.51	0.1744
LV stroke volume (µL)	26.7 ± 1.36	30.5 ± 1.02	0.6590	28.2 ± 0.97	30.3 ± 0.90	0.9932	30.0 ± 0.82	30.3 ± 0.46	> 0.9999
RV stroke volume (µL)	26.5 ± 1.12	29.9 ± 1.35	0.9236	28.3 ± 0.94	30.0 ± 1.11	0.9994	30.1 ± 0.88	29.5 ± 0.61	> 0.9999
LVEF (%)	70.4 ± 0.86	68.5 ± 1.27	0.7504	71.1 ± 0.90	66.4 ± 0.97	**0.0016**	71.1 ± 0.65	66.3 ± 0.48	**0.0009**
RVEF (%)	70.8 ± 0.81	68.2 ± 1.16	0.3372	71.1 ± 0.81	66.4 ± 0.90	**0.0022**	71.9 ± 0.52	66.4 ± 0.73	**0.0002**
Septum wall thickness in diastole (mm)	0.812 ± 0.02	0.770 ± 0.01	0.9996	0.846 ± 0.03	0.764 ± 0.03	0.8740	0.893 ± 0.04	0.750 ± 0.02	0.1430
LV free wall thickness in diastole (mm)	0.908 ± 0.03	0.888 ± 0.02	> 0.9999	0.989 ± 0.03	0.898 ± 0.05	0.6921	1.011 ± 0.04	0.854 ± 0.03	**0.0459**
RV free wall thickness in diastole (mm)	0.378 ± 0.01	0.351 ± 0.00	0.9949	0.381 ± 0.01	0.358 ± 0.02	0.9985	0.385 ± 0.01	0.357 ± 0.01	0.9932
Average heart rate (bpm)	479 ± 19	508 ± 6	0.2001	463 ± 13	473 ± 15	0.6257	487 ± 11	498 ± 15	0.5662
Cardiac output (mL/min)	12.7 ± 0.48	15.5 ± 0.60	0.1764	13.0 ± 0.48	14.3 ± 0.37	0.9802	14.6 ± 0.27	15.1 ± 0.62	> 0.9999

Table 3.6 *continued*

Weeks on diet	5 weeks			7 weeks			8 weeks		
	Iron-adjusted	Iron-deficient	*p*-value	Iron-adjusted	Iron-deficient	*p*-value	Iron-adjusted	Iron-deficient	*p*-value
Heart:body mass ($\bullet 10^{-3}$)	4.44 ± 0.14	4.95 ± 0.16	0.2223	4.47 ± 0.08	4.55 ± 0.13	> 0.9999	4.33 ± 0.14	4.57 ± 0.13	0.9829
LVED volume (µL)	42.8 ± 1.97	46.1 ± 2.88	0.9919	44.9 ± 2.03	45.1 ± 1.77	> 0.9999	46.8 ± 2.47	46.8 ± 2.13	> 0.9999
LVES volume (µL)	12.3 ± 0.62	16.2 ± 1.36	0.0588	12.4 ± 0.88	15.4 ± 0.80	0.2777	13.4 ± 0.81	15.1 ± 1.13	0.9529
RVED volume (µL)	43.4 ± 1.88	46.1 ± 2.62	0.9986	44.6 ± 2.24	44.3 ± 1.17	> 0.9999	46.9 ± 2.61	45.6 ± 2.27	> 0.9999
RVES volume (µL)	12.3 ± 0.60	15.5 ± 1.14	0.1270	12.3 ± 0.99	14.7 ± 0.49	0.5379	13.1 ± 0.77	15.2 ± 1.20	0.7323
LV stroke volume (µL)	30.5 ± 1.39	30.0 ± 1.69	> 0.9999	32.5 ± 1.29	29.7 ± 1.03	0.9381	33.4 ± 1.70	31.7 ± 1.10	0.9994
RV stroke volume (µL)	31.1 ± 1.29	30.6 ± 1.66	> 0.9999	32.3 ± 1.39	29.6 ± 0.84	0.9579	33.8 ± 1.87	30.4 ± 1.21	0.8222
LVEF (%)	71.3 ± 0.49	65.1 ± 1.25	**< 0.0001**	72.5 ± 0.96	65.8 ± 0.58	**<0.0001**	71.4 ± 0.45	68.0 ± 1.14	0.0522
RVEF (%)	71.8 ± 0.25	66.4 ± 1.06	**0.0002**	72.6 ± 1.02	66.8 ± 0.69	**< 0.0001**	72.0 ± 0.31	66.8 ± 1.30	**0.0004**
Septum wall thickness in diastole (mm)	0.981 ± 0.03	0.852 ± 0.04	0.2495	0.974 ± 0.03	0.869 ± 0.03	0.5628	0.972 ± 0.03	0.981 ± 0.04	> 0.9999
LV free wall thickness in diastole (mm)	1.069 ± 0.01	0.967 ± 0.03	0.5248	1.037 ± 0.05	1.045 ± 0.02	> 0.9999	1.085 ± 0.06	1.082 ± 0.02	> 0.9999
RV free wall thickness in diastole (mm)	0.412 ± 0.02	0.384 ± 0.02	0.9920	0.435 ± 0.01	0.390 ± 0.03	0.7748	0.434 ± 0.01	0.433 ± 0.03	> 0.9999
Average heart rate (bpm)	484 ± 25	500 ± 26	0.6663	459 ± 10	473 ± 18	0.5129	455 ± 10	489 ± 20	0.1637
Cardiac output (mL/min)	14.7 ± 0.71	14.9 ± 0.81	> 0.9999	14.9 ± 0.49	14.1 ± 0.95	0.9999	15.2 ± 0.88	15.5 ± 0.69	> 0.9999

Table 3.6 *continued*

Weeks on diet	9 weeks			10 weeks			11 weeks		
	Iron-adjusted	Iron-deficient	*p*-value	Iron-adjusted	Iron-deficient	*p*-value	Iron-adjusted	Iron-deficient	*p*-value
Heart:body mass (• 10^{-3})	4.35 ± 0.07	4.62 ± 0.17	0.9547	4.14 ± 0.08	4.51 ± 0.13	0.7017	4.09 ± 0.07	4.19 ± 0.15	> 0.9999
LVED volume (µL)	49.9 ± 1.32	46.9 ± 2.23	0.9974	53.7 ± 2.42	53.3 ± 2.47	> 0.9999	53.9 ± 2.05	53.5 ± 2.53	> 0.9999
LVES volume (µL)	14.5 ± 0.64	13.7 ± 0.94	> 0.9999	16.2 ± 0.89	15.8 ± 0.76	> 0.9999	16.0 ± 0.66	16.8 ± 0.99	> 0.9999
RVED volume (µL)	49.5 ± 1.55	47.0 ± 2.31	0.9994	54.3 ± 2.35	53.6 ± 2.16	> 0.9999	54.9 ± 1.90	53.7 ± 2.39	> 0.9999
RVES volume (µL)	14.2 ± 0.64	13.5 ± 0.84	> 0.9999	16.2 ± 1.13	16.2 ± 0.76	> 0.9999	16.0 ± 0.85	16.7 ± 0.91	> 0.9999
LV stroke volume (µL)	35.4 ± 0.86	33.3 ± 1.36	0.9925	37.5 ± 1.55	37.5 ± 1.83	> 0.9999	38.0 ± 1.65	36.8 ± 1.69	> 0.9999
RV stroke volume (µL)	35.3 ± 1.16	33.4 ± 1.55	0.9984	38.1 ± 1.34	37.4 ± 1.53	> 0.9999	38.9 ± 1.42	36.9 ± 1.52	0.9974
LVEF (%)	71.0 ± 0.76	71.0 ± 0.72	> 0.9999	69.9 ± 0.39	70.4 ± 0.63	> 0.9999	70.4 ± 0.89	68.8 ± 0.79	0.9229
RVEF (%)	71.4 ± 0.86	71.3 ± 0.64	> 0.9999	70.3 ± 0.92	69.8 ± 0.68	> 0.9999	70.8 ± 1.07	68.8 ± 0.50	0.7460
Septum wall thickness in diastole (mm)	0.977 ± 0.04	0.955 ± 0.06	> 0.9999	0.935 ± 0.05	0.969 ± 0.02	> 0.9999	0.946 ± 0.03	0.990 ± 0.03	0.9994
LV free wall thickness in diastole (mm)	1.057 ± 0.03	1.106 ± 0.02	0.9996	1.077 ± 0.04	1.186 ± 0.05	0.4177	1.055 ± 0.02	1.136 ± 0.04	0.8299
RV free wall thickness in diastole (mm)	0.418 ± 0.02	0.446 ± 0.02	0.9920	0.435 ± 0.01	0.461 ± 0.02	0.9962	0.395 ± 0.02	0.431 ± 0.02	0.9470
Average heart rate (bpm)	456 ± 8	479 ± 18	0.3041	486 ± 15	505 ± 16	0.4183	492 ± 19	507 ± 16	0.5714
Cardiac output (mL/min)	16.2 ± 0.43	15.9 ± 0.73	> 0.9999	18.2 ± 1.02	18.9 ± 0.94	> 0.9999	18.6 ± 0.58	18.6 ± 0.74	> 0.9999

Table 3.6 *continued*

Weeks on diet	12 weeks			16 weeks			20 weeks		
	Iron-adjusted	Iron-deficient	*p*-value	Iron-adjusted	Iron-deficient	*p*-value	Iron-adjusted	Iron-deficient	*p*-value
Heart:body mass ($\bullet 10^{-3}$)	3.78 ± 0.08	4.09 ± 0.14	0.8908	3.74 ± 0.10	3.69 ± 0.16	> 0.99999	3.29 ± 0.12	3.87 ± 0.22	0.1035
LVED volume (µL)	53.8 ± 4.10	49.2 ± 2.05	0.9027	52.9 ± 2.37	49.8 ± 2.37	0.9958	56.5 ± 1.88	53.0 ± 3.29	0.9888
LVES volume (µL)	16.0 ± 1.40	15.5 ± 0.67	> 0.9999	15.6 ± 0.80	16.0 ± 0.55	> 0.99999	17.6 ± 0.85	17.2 ± 1.72	> 0.9999
RVED volume (µL)	53.8 ± 4.05	49.6 ± 2.03	0.9369	53.2 ± 2.08	49.9 ± 2.44	0.9911	56.4 ± 2.02	52.8 ± 3.28	0.9834
RVES volume (µL)	15.4 ± 1.11	15.5 ± 0.61	> 0.9999	15.3 ± 0.70	16.3 ± 0.54	0.9994	17.6 ± 0.90	17.2 ± 1.55	> 0.9999
LV stroke volume (µL)	37.8 ± 2.73	33.7 ± 1.42	0.5319	37.3 ± 1.64	33.8 ± 1.95	0.7575	38.8 ± 1.13	35.8 ± 1.71	0.8825
RV stroke volume (µL)	38.4 ± 3.06	34.0 ± 1.46	0.4759	37.9 ± 1.43	33.6 ± 2.12	0.4847	38.8 ± 1.36	35.6 ± 1.91	0.8821
LVEF (%)	70.3 ± 0.55	68.4 ± 0.39	0.7834	70.5 ± 0.54	67.8 ± 0.94	0.2417	68.8 ± 0.69	67.8 ± 1.51	0.9985
RVEF (%)	71.2 ± 0.90	68.6 ± 0.36	0.3575	71.3 ± 0.43	67.2 ± 1.12	**0.0101**	68.8 ± 0.98	67.6 ± 1.34	0.9961
Septum wall thickness in diastole (mm)	0.910 ± 0.06	0.966 ± 0.03	> 0.9999	0.962 ± 0.06	0.955 ± 0.05	0.7426	0.941 ± 0.05	1.033 ± 0.03	> 0.9999
LV free wall thickness in diastole (mm)	1.159 ± 0.05	1.168 ± 0.02	> 0.9999	1.072 ± 0.03	1.047 ± 0.05	> 0.99999	1.103 ± 0.04	1.111 ± 0.03	> 0.9999
RV free wall thickness in diastole (mm)	0.394 ± 0.02	0.428 ± 0.02	0.9644	0.363 ± 0.02	0.361 ± 0.01	> 0.99999	0.393 ± 0.02	0.389 ± 0.02	> 0.9999
Average heart rate (bpm)	486 ± 15	549 ± 16	0.0159	520 ± 18	528 ± 14	0.7313	471 ± 16	489 ± 18	0.4710
Cardiac output (mL/min)	18.2 ± 1.07	18.5 ± 0.86	> 0.9999	19.3 ± 0.57	17.9 ± 1.12	0.9473	18.2 ± 0.50	17.5 ± 1.22	> 0.9999

Table 3.6 *continued*

Weeks on diet	24 weeks		
	Iron-adjusted	Iron-deficient	*p*-value
Heart:body mass (• 10^{-3})	3.42 ± 0.15	3.77 ± 0.23	0.7948
LVED volume (µL)	61.0 ± 2.63	60.6 ± 3.60	> 0.9999
LVES volume (µL)	19.8 ± 0.87	22.3 ± 1.64	0.5813
RVED volume (µL)	60.5 ± 2.33	60.6 ± 3.58	> 0.9999
RVES volume (µL)	19.6 ± 0.82	22.0 ± 1.44	0.5488
LV stroke volume (µL)	41.2 ± 1.90	38.3 ± 2.04	0.9102
RV stroke volume (µL)	40.9 ± 1.62	38.6 ± 2.24	0.9876
LVEF (%)	67.6 ± 0.70	63.4 ± 0.93	**0.0068**
RVEF (%)	67.6 ± 0.58	63.7 ± 0.85	**0.0212**
Septum wall thickness in diastole (mm)	1.046 ± 0.06	1.025 ± 0.05	0.7903
LV free wall thickness in diastole (mm)	1.100 ± 0.06	1.104 ± 0.05	> 0.9999
RV free wall thickness in diastole (mm)	0.365 ± 0.03	0.378 ± 0.03	> 0.9999
Average heart rate (bpm)	484 ± 12	493 ± 22	0.7352
Cardiac output (mL/min)	19.9 ± 0.58	19.0 ± 1.57	0.9990

ii) Effect of iron supplementation on cardiac function (Cohort 4)

The results in section 3.4.1.iv showed that in iron-deprived animals, iron supplementation with FCM corrected their iron status towards the control (iron-adjusted) state. To determine whether iron supplementation also had an effect on cardiac function, animals were MRI scanned before and after FCM supplementation (Figure 3.15; *see* Table 3.7 for *p*-values).

Several notable alterations in cardiac function were observed. The LVEF and RVEF were improved following a single dose of iron (LVEF 10% increase, $p = 0.0002$; RVEF 8% increase, $p = 0.0052$). A second dose of iron fully restored EF levels to control levels, whilst the EF of time-matched iron-deficient animals that did not receive FCM remained reduced at 60% (compared to 72% and 70%, iron-adjusted controls and ID+FCM, respectively).

At 3 weeks of diet, prior to the administration of either saline or FCM, animals on an iron-deficient diet and the ID+FCM group had higher LV and RV end-systolic volume by at least 20% compared to the controls (LV: $p < 0.0001$ and $p = 0.0009$; RV: $p = 0.0012$ and $p = 0.0091$, respectively).

Furthermore, the following trends were observed. After administration of the first dose of saline, the end-systolic volume in the hearts of mice on an iron-deficient diet increased by 10% compared to the previous week and continued to be elevated after the second dose the following week. On the other hand, in the hearts of animals receiving FCM supplementation, end-systolic volume was reduced by 10% after the first dose, and by

another 5% after the second dose of FCM compared to the previous week. The magnitude of changes occurring each week was not large enough to reach statistical significance.

At the end of the study, the average systolic volume in the FCM group was significantly (or near significant) above the iron-adjusted controls (LV: $p = 0.0260$; RV: $p = 0.0725$). Finally, following two doses of FCM, animals had significantly higher stroke volume compared to controls (LV: $p = 0.0133$; RV: $p = 0.0048$).

Compared to the control mice, iron-deprived animals receiving saline had thinner LV wall following the first and second dose of saline ($p = 0.0280$ and $p = 0.0471$). In iron supplemented animals, LV free wall was significantly thicker after one dose of FCM and further thickened after a second dose (vs iron-adjusted: $p = 0.9872$ and $p = 0.0007$; vs iron-deficient: $p = 0.0140$ and $p < 0.0001$). Finally, following 2 doses of supplementation, the RV free wall were significantly thickened in the ID+FCM animals compared to both groups receiving saline (vs iron-adjusted: $p = 0.0031$; vs iron-deficient: $p = 0.0087$). Unlike cohort 1, discussed in Section 3.4.2.i., in the mice in cohort 2, these parameters did reach statistical significance.

Representative cine-MR images at end diastole and end systole comparing before and after two doses of FCM in the same mouse is shown in Figure 3.13B.

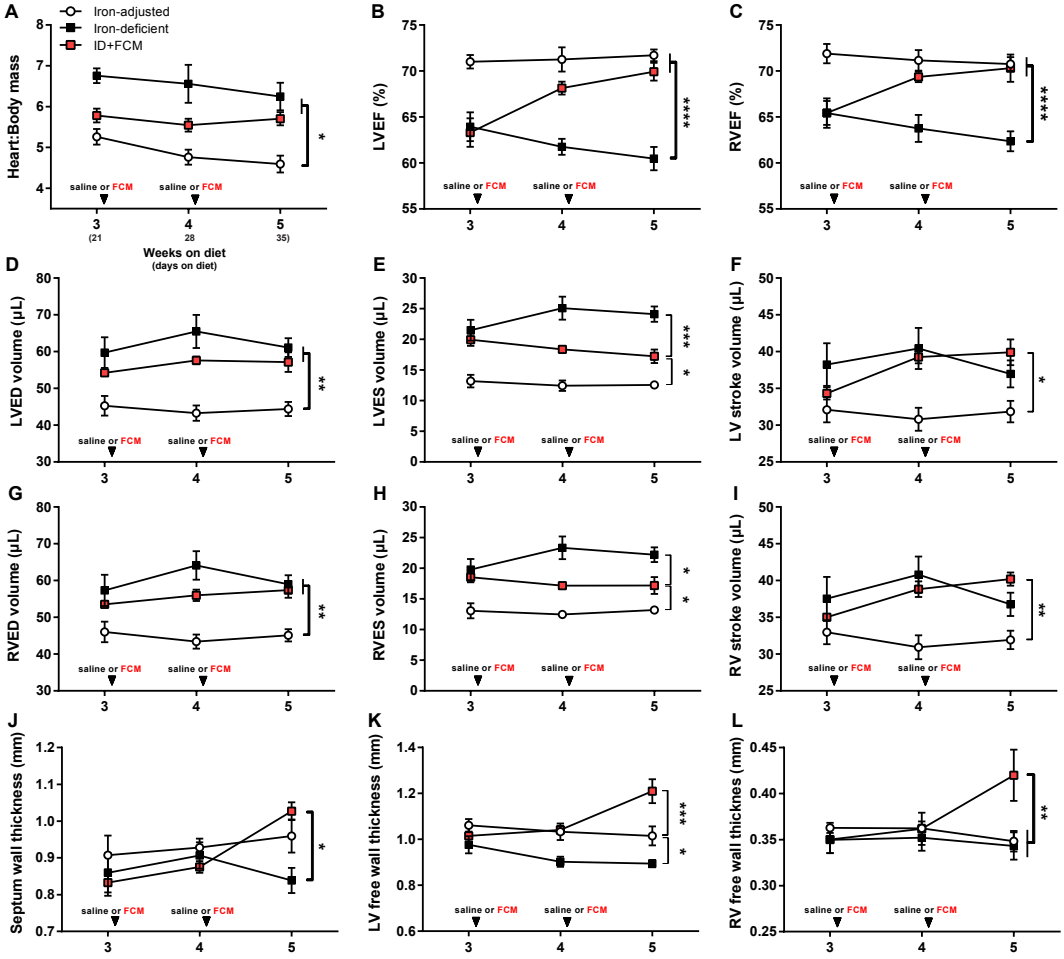


Figure 3.15 Cardiac function parameters following iron supplementation. A) Heart-to-body mass ratio, B and C) Left and right ventricular ejection fraction, D-I) Left and right ventricular volumes at end diastole and end systole and stroke volumes, J-L) Wall thickness, as measured by cine-MRI. Data plotted as mean ± SEM. *p*-value determined at 5 week of diet by a multiple two-tail, unpaired student's *t*-test; * $p < 0.05$, **** $p < 0.0001$. n = 6 mice for iron-adjusted and iron-deficient and n = 7 mice for ID+FCM cohort.

Table 3.7 Effect of iron supplementation on *in vivo* cardiac function. *p*-value determined by a two-way ANOVA and post-hoc Tukey's multiple comparison's test. n = 6 mice per cohort.

Weeks on diet	3 weeks											
	Iron-adjusted + saline (1)			Iron-deficient + saline (2)			Iron-deficient + FCM (3)			*p*-value (1) vs (2)	*p*-value (1) vs (3)	*p*-value (2) vs (3)
Heart:body mass (• 10^{-3})	5.26	±	0.47	6.61	±	0.44	5.62	±	0.20	**0.0004**	0.3334	**0.0208**
LVED volume (µL)	45.3	±	6.58	59.2	±	10.37	54.6	±	1.65	**0.0023**	0.0790	0.3451
LVES volume (µL)	13.2	±	2.50	21.3	±	4.43	20.5	±	2.47	**< 0.0001**	**0.0009**	0.6262
RVED volume (µL)	46.0	±	6.82	57.3	±	10.13	53.7	±	1.00	**0.0123**	0.1281	0.5587
RVES volume (µL)	13.1	±	3.02	19.8	±	4.55	19.4	±	1.58	**0.0012**	**0.0091**	0.7444
LV stroke volume (µL)	32.1	±	4.18	37.8	±	7.11	34.1	±	2.10	0.0741	0.6988	0.3050
RV stroke volume (µL)	33.0	±	3.98	37.5	±	6.93	34.4	±	1.25	0.1726	0.6957	0.5501
LVEF (%)	71.0	±	1.80	63.9	±	4.12	62.5	±	4.02	**0.0020**	**< 0.0001**	0.9710
RVEF (%)	71.9	±	2.58	65.4	±	4.42	64.0	±	2.58	**0.0018**	**0.0019**	> 0.9999
Septum wall thickness in diastole (mm)	0.908	±	0.13	0.844	±	0.13	0.837	±	0.11	0.6488	0.3540	0.8623
LV free wall thickness in diastole (mm)	1.061	±	0.07	0.977	±	0.01	0.971	±	0.07	0.2089	0.6198	0.6976
RV free wall thickness in diastole (mm)	0.363	±	0.13	0.350	±	0.01	0.340	±	0.03	0.8415	0.8510	0.9998
Average heart rate (bpm)	494	±	70	499	±	46	490	±	37	0.8873	0.9374	0.9124
Cardiac output (mL/min)	15.7	±	1.62	18.9	±	3.87	16.7	±	1.50	0.0809	0.1490	0.2685

Table 3.7 *continued*

Weeks on diet	4 weeks								
	Iron-adjusted + saline (1)	Iron-deficient + saline (2)	Iron-deficient + FCM (3)	*p*-value (1) vs (2)	*p*-value (1) vs (3)	*p*-value (2) vs (3)
Heart:body mass (• 10^{-3})	4.76 ± 0.45	6.56 ± 1.23	5.55 ± 0.42	**< 0.0001**	0.0928	**0.0160**
LVED volume (µL)	43.3 ± 5.14	65.5 ± 4.52	57.6 ± 2.77	**<0.0001**	**0.0024**	0.1161
LVES volume (µL)	12.4 ± 2.11	25.1 ± 4.96	18.4 ± 1.33	**< 0.0001**	**0.0039**	**0.0006**
RVED volume (µL)	43.4 ± 4.72	64.1 ± 10.34	56.0 ± 4.06	**< 0.0001**	**0.0047**	0.0756
RVES volume (µL)	12.5 ± 1.42	23.3 ± 0.93	17.2 ± 1.60	**< 0.0001**	**0.0292**	**0.0020**
LV stroke volume (µL)	30.8 ± 3.81	40.4 ± 7.39	39.3 ± 2.30	**0.0027**	**0.0091**	0.8985
RV stroke volume (µL)	30.9 ± 4.01	40.8 ± 6.49	38.8 ± 2.83	**0.0007**	**0.0073**	0.6906
LVEF (%)	71.3 ± 3.24	61.8 ± 2.30	68.1 ± 1.87	**< 0.0001**	0.7179	**0.0002**
RVEF (%)	71.2 ± 2.73	63.8 ± 3.88	69.4 ± 1.52	**0.0003**	0.6768	**0.0052**
Septum wall thickness in diastole (mm)	0.928 ± 0.06	0.889 ± 0.11	0.875 ± 0.04	0.9144	0.5932	0.8211
LV free wall thickness in diastole (mm)	1.033 ± 0.09	0.902 ± 0.06	1.041 ± 0.05	**0.0280**	0.9872	**0.0140**
RV free wall thickness in diastole (mm)	0.362 ± 0.02	0.352 ± 0.04	0.369 ± 0.04	0.9017	0.9028	0.9998
Average heart rate (bpm)	526 ± 30	490 ± 35	494 ± 36	0.0716	0.1047	0.8437
Cardiac output (mL/min)	16.2 ± 1.96	19.7 ± 3.34	19.4 ± 1.85	**0.0391**	**0.0125**	0.8118

Table 3.7 *continued*

Weeks on diet	5 weeks					
	Iron-adjusted + saline (1)	Iron-deficient + saline (2)	Iron-deficient + FCM (3)	*p*-value (1) vs (2)	*p*-value (1) vs (3)	*p*-value (2) vs (3)
Heart:body mass (• 10^{-3})	4.59 ± 0.51	6.25 ± 0.89	5.70 ± 0.46	**0.0001**	**0.0105**	**0.2762**
LVED volume (µL)	44.4 ± 4.74	61.1 ± 6.80	57.6 ± 7.10	**0.0004**	**0.0076**	0.5730
LVES volume (µL)	12.6 ± 1.41	24.1 ± 3.29	17.1 ± 3.14	**< 0.0001**	**0.0260**	**0.0004**
RVED volume (µL)	45.1 ± 4.10	59.0 ± 6.49	57.2 ± 5.38	**0.0018**	**0.0060**	0.8999
RVES volume (µL)	13.2 ± 1.45	22.2 ± 3.16	16.9 ± 3.72	**< 0.0001**	**0.0425**	**0.0133**
LV stroke volume (µL)	31.8 ± 3.57	37.0 ± 4.75	40.5 ± 4.51	0.1575	**0.0133**	0.5090
RV stroke volume (µL)	31.9 ± 3.06	36.8 ± 4.22	40.3 ± 2.29	0.1380	**0.0048**	0.3348
LVEF (%)	71.7 ± 1.55	60.5 ± 3.20	70.4 ± 2.78	**< 0.0001**	0.6364	**< 0.0001**
RVEF (%)	70.8 ± 1.86	62.4 ± 2.88	70.6 ± 4.12	**< 0.0001**	0.9925	**< 0.0001**
Septum wall thickness in diastole (mm)	0.960 ± 0.11	0.820 ± 0.05	1.027 ± 0.07	0.0730	0.4275	**0.0018**
LV free wall thickness in diastole (mm)	1.015 ± 0.10	0.894 ± 0.04	1.210 ± 0.14	0.0471	**0.0007**	**< 0.0001**
RV free wall thickness in diastole (mm)	0.348 ± 0.03	0.343 ± 0.04	0.419 ± 0.08	0.9726	**0.0031**	**0.0087**
Average heart rate (bpm)	463 ± 20	563 ± 39	512 ± 53	**0.0002**	**0.0408**	0.0556
Cardiac output (mL/min)	14.7 ± 1.58	20.7 ± 2.09	20.6 ± 1.58	**0.0001**	**0.0001**	0.9301

3.5 DISCUSSION

3.5.1 Validation of a mouse model of iron deficiency through diet

i) Abnormal body mass and haemoglobin due to an iron-deficient diet

An adequate supply of iron is crucial for mammalian growth and development; iron deficiency in growing mammals can result in impaired growth (Frazer *et al.*, 2016; Lozoff, 2007). Consistent with our current understanding of the importance of iron in growth and development, mice on an iron-deficient diet consistently weighed less than their age-matched controls, despite being weaned at a similar body mass.

One notable difference was haemoglobin measurements prior to the dietary intervention. In cohort 1, the longitudinal study which monitored the mice over 24 weeks of diet, animals weaned onto the deficient diet had an average [Hb] that was significantly higher than the mice weaned onto the adjusted diet immediately prior to beginning the diets (p = 0.0005). This may be due to an unintended difference in the nursing conditions during the suckling period. Prior to weaning onto their respective diets, animals weaned onto the iron-adjusted diet were nursed by a pregnant mother whereas the mice weaned onto the deficient diet were housed with a non-pregnant mother. Because pregnancy affects iron handling in the body, diverting iron to the gestating foetus, it is possible that the milk of the pregnant mouse contained less iron than it normally would if the she was not pregnant. Alternatively, litters could have been born with different iron endowment, due to receiving different amounts of iron during the gestation. This could be due to differences in litter size or starting maternal iron stores. Because this information was obtained retrospectively, it was not possible to analyse the iron status of the mothers.

Interestingly, the haemoglobin of the control mice increased approximately 50% from the baseline measurement within the first week of weaning onto the iron-adjusted diet, and this was maintained relatively unchanged through the 24 weeks on the diet. This phenomenon could be explained by a change in diet upon weaning. The iron content of rodent breast milk is relatively low, between 7-16 ppm (Ezekiel and Morgan, 1963; Kaldor and Ezekiel, 1962). To meet the necessary iron demands, suckling mice are more efficient at absorbing dietary iron than weaned mice. More than 80% of iron is absorbed in the intestine during the suckling period, which then decreases to around 10-20% upon weaning onto a solid diet, which contains 200 ppm iron (Frazer *et al.*, 2016). Despite its superior ability to extract iron from its diet, the suckling mouse will absorb only 5-13 ppm of iron from the mother's milk, whereas a weaned mouse will have the possibility to absorb up to 40 ppm iron. A 4 to 8-fold increase in iron bioavailability would then allow for increased erythropoiesis, thus elevating haemoglobin during the first week after weaning.

Upon weaning onto an iron-deficient diet, mice are subject to a 4 to 8-fold reduction in iron availability in the diet, but the haemoglobin of these animals decreased by only 14% following one week of diet from baseline, a modest decrease compared to the increase observed in the controls. This is most likely due to the release of iron from stores in the liver, spleen and bone marrow gained during gestation and suckling period. Indeed, following 6 weeks of deficient diet, the iron content in the liver is only half and spleen is only a quarter of what was measured in the control mice.

From week 7 of diet onwards, the [Hb] of the iron deficient group began to increase in the absence of any other intervention. By the end of week 11 of diet, the [Hb] in this group was no longer different to that of the control group. This observation may have a developmental explanation. Mice typically undergo a growth spurt during the first 7-10 weeks after birth. The end of the 6th week of diet coincides with the end of this rapid growing period, as the mice would be 9 weeks old by then. Therefore, it is possible that the slowing of growth is accompanied by a decreased demand for iron, meaning that iron could be re-distributed for red blood cell production. Alternatively, it may also be possible that with deprivation of iron over the long term, mice develop an adaptive mechanism allowing the animals to draw what little iron is present in the nominally iron-deficient diet more efficiently.

ii) Serum and tissue iron status and cellular iron homeostasis

For the determination of iron status, ferritin, iron and transferrin concentrations were measured in the serum of all animals used in this chapter. Clinically, the presence of iron deficiency can be assessed by using a combination of measured levels of blood haemoglobin, serum ferritin (in parallel with levels of C-reactive protein) and TSat. Furthermore, iron deficiency is considered severe when anaemia is present in addition to iron deficiency. The current standard for the determination of iron deficiency in humans (at least in clinical studies) is defined as serum ferritin < 100 ng/mL (absolute iron deficiency) or 100-300 ng/mL with TSat < 20% (functional iron deficiency) (McDonagh and Macdougall, 2015). Since applying these clinical standards directly to rodents was not deemed to be appropriate, in this study, iron deficiency was determined by directly

comparing the measured biomarkers in the animals on an iron-adjusted vs iron-deficient diet. Furthermore, the severity of iron deficiency was assessed by the degree of difference in the measured parameters, collectively, between the two cohorts (i.e. the bigger the difference in values and statistical significance, the greater the iron deficient the animal was considered to be).

The serum indices of all animals fed an iron-deficient diet were significantly altered in the direction expected in iron deficiency. In addition, due to their low haemoglobin following 6 weeks of diet, the animals should also be considered anaemic at this time point.

To further characterise the effects of an iron-deficient diet on physiological iron status, total elemental iron was measured in the hearts, livers and spleens of all mice used in this study. Livers and spleens of all animals on an iron-deficient diet were depleted of iron. Interestingly, despite the highly depleted state of liver and spleen iron stores, in addition to other measured parameters pointing to severe iron-deficiency anaemia, the amount of total iron in the heart remained unchanged following 6 weeks of diet. Furthermore, consistent with previously reported response to iron deficiency, hepatic *Hamp* was decreased and *Fpn* was increased significantly in the animals on an iron-deficient diet. On the other hand, cardiac *Fpn* mRNA was decreased significantly at the 6 week time-point.

Qualitatively, the expression of FPN at the protein level did not appear to be affected by the diet. A more quantitative assay would be required to validate this result (i.e. by ELISA). Finally, cardiac *Hamp* was unchanged at this time-point of diet. The lack of a coordinated hepcidin/FPN response to minimise iron extrusion from the cardiac tissue suggests a situation in which cellular iron availability in the heart remains unaltered despite systemic

iron deficiency. This being said, a redistribution of the pool of labile vs stored iron within the cardiac tissue cannot be excluded.

iii) Iron supplementation rescues iron status

Supplementation of iron through an intravenous route was effective in rescuing the effects of an iron-deficient diet on body mass and all measured parameters of iron status. Of note, previously iron-deficient animals receiving FCM supplementation had significantly higher levels of total iron in the liver (iron-adjusted vs ID+FCM (in μg/g): 99.4 vs 143.6). This is not surprising, since it has been previously shown in patients that intravenously administered FCM is rapidly cleared from the circulation and primarily distributed to the bone marrow, liver and spleen (Lyseng-Williamson and Keating, 2009).

iv) Implications of the current study

First, consistent with previous findings by Lakhal-Littleton *et al*. (2015, 2016), the results in this study suggest that there are cardiac-specific mechanisms to maintain iron status in the heart, which is independent of systemic signals. Interestingly, whereas Lakhal-Littleton *et al*. found that 6 weeks of an iron-deficient diet decreased *Hamp* mRNA expression in the heart, in the current study, *Hamp* expression did not change following 6 weeks of diet and increased significantly following 9 weeks of diet. This inconsistency could be attributable to a difference in the degree of iron deficiency. However, the iron status of the animals was not provided by the authors and therefore, a comparison could not be made at this point.

Second, the data presented here provides further insight into our current understanding of the handling and prioritization of iron metabolism in tissues. In humans, when iron availability is scarce, the body mobilizes iron stores, first from the liver, spleen and macrophages, then from skeletal muscles and the intestines and finally from the heart and the brain (Neu, 2008). This allows for the prioritisation of the use of iron for red blood cell production and thus, maintain oxygen transport throughout the body (von Haehling *et al.*, 2015; Neu, 2008; Polin *et al.*, 2011).

In humans, this may certainly be true. In sheep, prioritisation of iron for erythropoiesis over the brain has also been shown (Zamora *et al.*, 2016). However, in rodents, there is some evidence that cardio-protection of iron stores occurs during iron deficiency. Using a spectroscopic technique called Mössbauer spectroscopy to measure iron content of tissues, Wofford *et al.* (2017) were able to show that, in both adult and young mice (up to 3 weeks old) made iron deficient by through administration of low iron diet, the hearts contained normal or even higher iron levels when compared to the hearts of control animals, demonstrating that iron content of the heart is protected despite systemic iron deficiency. However, the study did not report the degree of iron deficiency of the animals and the iron content of other organs, such as the liver and the spleen, thus the iron status of these animals remain rather ambiguous. Therefore, a large-scale systematic study monitoring the impact of iron deficiency on iron status, both circulating and in tissues, in a murine model does not exist, despite this model being frequently used to study various aspects of iron deficiency.

Contrary to our understanding of iron prioritisation in humans and consistent with Wofford *et al*. (2017), the findings in the present study suggest that haemoglobin is, in fact, affected prior to the loss of iron in the heart. In other words, iron-deficiency anaemia is presented *before* cardiac iron deficiency, raising the possibility that the heart, as one of the most critical organs in the body, possesses mechanisms to protect itself from iron depletion when total body iron is low. In fact, this may very well be achieved through the cardiomyocyte-derived hepcidin/FPN axis. Given this phenomenon, it is conceivable that other critical tissues, such as the brain, also possess this autonomous iron regulatory mechanisms to protect its iron stores during low iron states.

Finally, the iron status of the animals on an iron-deficient diet improved, surprisingly, over time in the absence of any experimental intervention. This observation is evidence that, at least in a murine model, there may exist an adaptive mechanism allowing the animals to maximise the uptake of resources under scarce conditions. This thesis does not attempt to answer whether such a mechanism exists in all mammals or the phenomenon is simply due to the robustness of mouse physiology. It does, however, demonstrate that iron deficiency and associated phenotype are lost over time and that care must be taken when selecting the lengths of dietary treatment in subsequent experiments.

3.5.2 Iron deficiency and iron supplementation on cardiac function

i) Iron deficiency alters cardiac function

Several key findings were demonstrated in this study. First, abnormalities in cardiac function were observed following an iron-deficient diet, and these occurred as early as 2 weeks on the diet (Figure 3.14). A modest deterioration in ejection fraction persisted

throughout the first 8 weeks of diet. This dysfunction, however, was reversible, as the heart function of the iron deficient animals began to improve following 7 weeks of diet and returned to levels comparable to that of the controls in all the parameters measured during week 9 and 10 of diet. Interestingly, the initial progressive decrease in LV and RV EFs coincided with a decrease in haemoglobin of the iron-deficient animals during the early weeks of diet. Similarly, increases in EF and in haemoglobin were observed concurrently, raising the possibilities that: 1) cardiac remodelling may occur sometime during weeks 7 and 10 to compensate for the early dysfunction and 2) this change may be possible, in part, by increased erythropoiesis. An increase in haemoglobin could help increase oxygen delivery to the heart, which in turn, may improve cellular function. The latter is further supported by the observation where iron supplementation in previously iron-deficient mice, which resulted in an increase in [Hb] (Figure 3.8), also led to a restoration of cardiac function (assessed as ejection fraction) (Figure 3.15).

Second, in cohort 4, a decrease in ejection fraction between weeks 3 and 5 of diet was accompanied by a significant increase in heart mass relative to body mass (Figure 3.15A). Following 5 weeks of diet, the septal and LV walls were significantly thinner in the iron deprived animals. Such structural remodelling would allow for a larger chamber volume; in turn, a larger ventricular volume could serve to increase pressure within the ventricles such that less effort is required to eject a larger volume of blood required to sustain normal circulation. Consistent with this, the LV and RV volumes at end diastole in the iron-deficient animals were larger than that of the controls (Figure 3.15D and G). Nevertheless, ejection fraction in the iron-deficient animals was still lower compared to the controls.

Notably, cardiac dysfunction was present even in the absence of iron deficiency in heart tissue as measured by ICP-MS (Figure 3.9), implying that systemic iron deficiency is sufficient to cause alterations in cardiac function. Given that cardiac function is impaired at the 5-7 week time point, but not at the 9 week time point, despite clear indications of iron deficiency in both cases, this alteration in cardiac performance may be a consequence of anaemia, rather than iron deficiency itself, which arises from the iron deficiency at the 5-7 week time point but which is no longer pronounced at the 9 week time point.

ii) Iron supplementation improves cardiac dysfunction

In cohort 4, iron supplementation was given to a group of mice on an iron-deficient diet, after verification of iron deficiency (by haemoglobin, Figure 3.8) and cardiac dysfunction (by cine-MRI, Figure 3.15). Supplementation of iron had positive effects on heart function, namely, raising the ejection fraction to levels comparable to that of the control animals. It did not, however, restore many of the other functional parameters measured in this study. For instance, end-diastolic and end-systolic volumes remained elevated in the iron supplemented animals compared to the controls and stroke volume was increased significantly, beyond that of the iron-deficient cohort. In addition, chamber walls were thicker following iron supplementation, with changes first significant in the left ventricular free wall after the first dose of iron, and then the right ventricular free wall after the second dose of iron.

These results suggest that iron supplementation does not reverse the altered heart to conditions comparable to the controls. These changes also do not resemble the changes that occur during weeks 9 and 10 of an iron-deficient diet (observed in cohort 1), during

which all functional parameters were restored to levels comparable to the controls. Rather, iron supplementation appears to have induced a different response. Whereas the hearts of iron-deficient mice exhibited characteristics of dilated cardiomyopathy, the hearts of iron-deficient mice supplemented with iron resembled a hypertrophic-like response.

This observation suggests that iron may activate a compensatory mechanism to restore cardiac function rather than reversing the adverse effects of iron deficiency. In support of this hypothesis, a persistent increase in heart rate and cardiac output was observed in the iron-supplemented group compared to the control group (Table 3.6), raising the possibility that restoration of ejection fraction in these animals is due to sympathetic stimulation. Alternatively, ejection fraction could have been restored through increasing venous returns (which would increase end-diastolic volume, contractile force and stroke volume), consistent with the principles of Frank-Starling law. The mechanistic pathway and how iron is involved in evoking such response will not be further explored in this thesis.

iii) Ageing reduces cardiac efficiency

Finally, ageing is known to bring about several structural and functional changes in the heart. In both humans and in mice, ageing commonly results in thickening of the interventricular septum wall but not the LV free wall, with or without an increase in left ventricular or total heart mass (Betsuyaku *et al.*, 2002; Oxenham and Sharpe, 2003; Strait and Lakatta, 2012). Functionally, systolic function is preserved with age. Consistent with these previous findings, in the present study, a thickening of the septal wall without a change in total heart mass, and a marginal reduction in systolic function (4% reduction in LVEF and no change in cardiac output) was observed in the ageing control mice.

3.5.3 Limitations of the current study

One major difficulty of this study was the variation observed in batches of mice on the iron-deficient diet. Other than body mass, which was discussed in the previous section, different groups of mice had different average [Hb] at the same time point despite being on an identical iron-deficient diet. For instance, following 5 weeks of diet, cohort 1 mice had an average haemoglobin of 92.8 g/L (Section 3.4.1.i, Table 3.2) whereas cohort 2 mice had an average of 62.9 g/L (Section 3.4.1.iv, Figure 3.3). One possible explanation for this observation could be that cohort 1 mice were more iron replete (and/or had larger iron stores) at birth or prior to weaning than cohort 2 mice. Indeed, comparing the [Hb] at baseline (the only dataset available for comparison at baseline), the first cohort of animals had a [Hb] of 116.0 g/L and the second cohort was 91.1 g/L. However, in the absence of more robust measurement of iron status, such as serum parameters or total liver iron measurement by ICP-MS, this remains a hypothesis. More broadly speaking, each animal is different and behaves differently; therefore, a considerable degree of batch-to-batch variation is expected to be observed, especially in animals fed an iron-deficient diet.

Similar variations were noted when assessing cardiac function. For instance, at the 5 week time point, the chamber wall thickness appeared to be different between the iron-deficient and controls in cohort 1 mice, but this difference did not reach statistical significance. Yet, cohort 2 animals, these parameters did reach statistical significance. Again, these variations could be a consequence of the degree of iron deficiency, as cohort 1 iron-deficient animals were less iron deficient than cohort 2 iron-deficient animals.

3.6 CONCLUSIONS

The study presented in this chapter was carried out to fulfil two main objectives. First, to establish a viable model of iron deficiency in mice through dietary intervention and second, should this treatment be successful, to explore the effect of iron deficiency and iron supplementation on cardiac function. The results from section 3.4.1 collectively confirm that feeding an iron-deficient diet is an effective method of inducing rapid systemic iron deficiency (and anaemia), but not cardiac iron deficiency, in mice; instead it appears as though iron deficiency impedes the age-dependent accumulation of iron otherwise seen in control mice. Further, this phenotype could be easily rescued by iron supplementation.

In terms of cardiac function, the results from section 3.4.2 suggest that iron deficiency is detrimental to normal cardiac function and that IV iron supplementation following iron deficiency can rescue deteriorated function (assessed by ejection fraction). However, it is important to note that the improvement in ejection fraction was likely not due to restoration of cardiac function but through a different compensatory mechanism evoked by iron supplementation.

Based on the two studies presented in this chapter, a 6 week dietary time-point was selected as appropriate for many of the experiments presented in subsequent chapter.

CHAPTER 4:

CONSEQUENCES OF IRON DEFICIENCY ON THE CARDIAC GENE EXPRESSION

4.1 CHAPTER OVERVIEW

This chapter explores the consequence of an iron-deficient diet on cardiac gene expression. mRNA obtained from the hearts of animals on 6 weeks of iron-adjusted or deficient diet were submitted for high-throughput sequencing. The resulting data were analysed for differential gene expression and differentially regulated pathways. Results showed that the gene expression landscape is significantly altered following an iron-deficient diet. Furthermore, Gene Ontology and pathway analyses revealed that many of the genome-wide changes are likely downstream of a response to stress and external stimuli. Finally, iron deficiency altered the methylation state of histone H3K9 and H3K36, implicating a contribution of epigenetics in altering the transcriptional profile of iron deficiency.

4.2 INTRODUCTION

4.2.1 Genomic basis of cardiac remodelling in heart failure

Heart failure (HF) is a complex clinical syndrome that results from impairment in the structure or function of the heart which interferes with the filling or ejection of the blood from the ventricles (Buonocore and Wallace, 2014). Cardiac remodelling occurs during pathological conditions and is largely a response of the cardiomyocytes to biomechanical stress, such as pressure or volume overload, circulating hormones or cytokines and reactive oxygen species (Dirkx *et al*., 2013). In response to stress, a signaling cascade is activated, which typically leads to transcriptional reprogramming and subsequent alterations in cardiac gene expression (Marín-García and Akhmedov, 2015).

Different types of HF have unique gene expression signatures (Liu *et al*., 2015), but common to most HF pathologies is the reactivation of foetal genes such as atrial natriuretic factor (ANF), brain natriuretic protein (BNP) and β-myosin heavy chain (β-MHC) in the adult heart (Mathiyalagan *et al.*, 2014). Although foetal gene reprogramming is regarded as an adaptive response to stress, the chronic or aberrant up-regulation of foetal genes can become maladaptive and is believed to play a causative role in the pathological cardiac remodelling process (Dirkx *et al.*, 2013). This is further supported by the evidence that foetal gene expression often decreases in heart failure patients upon pharmacological or mechanical treatment (Blaxall *et al*., 2003; Lowes *et al*., 2002).

4.2.2 Epigenetic basis of cardiac remodelling

Epigenetics refers to a set of mechanisms that influence gene expression without altering the DNA sequence but are nonetheless heritable from one generation of cells to another (Berezin, 2016; Papait *et al*., 2013a). Epigenetic regulation is based on different molecular mechanisms which act to dynamically modulate chromatin structure to influence its accessibility for transcription and expression of genes (Berezin, 2016).

In the last decade, it has become clear that epigenetic mechanisms play a key role in governing the gene expression changes underlying the development and progression of heart failure (Papait *et al.*, 2013a). Of the many mechanisms that regulate the epigenetic landscape, both histone acetylation and methylation have been implicated in the pathophysiology of heart failure. In this thesis, methylation is investigated due to its relevance in iron homeostasis.

i) Histone methylation in heart failure

Alterations in histone methylation are known to occur as a pathology of heart failure, but the exact role it plays in the context of the disease is still unclear (Table 4.1). Kaneda *et al.* (2009) identified dynamic, genome-wide changes in the histone H3K4 and H3K9 tri-methylation states in both failing human hearts and rat models of LV hypertrophy. Also, locus-specific alterations in histone methyl marks were found to correlate with changes in transcript abundance in pressure-overload mouse cardiomyocytes (Di Salvo and Haldar, 2014; Papait *et al.*, 2013b). However, it remains to be determined whether changes in methylation state contribute to the initiation and development of the disease or whether they are merely associated with the diseased state.

Considering the former, some progress has been made in recent years. The loss of the repressive marks di- and tri-methyl H3K9 at the promoter of *Anf* and *Bnp* has been observed in diseased hearts, raising the possibility that this particular epigenetic modification may be directly linked to the re-programming of foetal gene (Hohl *et al.*, 2013; Papait *et al.*, 2015). Furthermore, in mice, the loss of H3K4me3, via *loss-of-function* of the histone methylase PTIP, was associated with an inability to up-regulate foetal genes and a blunted hypertrophic phenotype was observed in response to cardiac injury (Stein *et al.*, 2011). This implicates histone methylation as epigenetic regulators that are sufficient to cause the development and progression of cardiac disease by altering the transcriptional profile of cardiomyocytes.

ii) Histone demethylases in heart failure

The methylation state of histones is dynamically regulated by histone methyltransferases and histone demethylases (KDMs) (Grunstein, 1990; Zhang and Reinberg, 2001). Several KDMs have been shown to promote the hypertrophic response (Table 4.1). Mice overexpressing cardiac KDM4A show an exacerbated hypertrophic phenotype whereas knock-out of KDM4A blunts this pathological response (Zhang *et al.*, 2011). The hypertrophic phenotype was a consequence of up-regulation of the four-and-a-half LIM domain 1 (FHL1) protein, a biomechanical sensor in the heart, which was under the transcriptional control of the KDM4A target histone mark H3K9me3.

KDM3A and KDM4B have also been found to be overexpressed in the failing heart and their up-regulation correlates positively with increased *Anp* and *Bnp* expression *(Hohl et al.*, 2013).

Table 4.1 Epigenetic modulations associated with heart disease.

Disease state	Methylation state	Gene locus	KDM implicated	References
Heart failure	H3K4me3 K3K9me3	Genome-wide study	–	Kaneda *et al.*, 2009
Pressure overload	Global	Genome-wide study	–	Papait *et al.*, 2013b
Cardiac specific PTIP knock-out mouse	Global H3K4me3	*Kcnip2* ↓	–	Stein *et al.*, 2011
Cardiac hypertrophy	H3K9me3	*Fhl1* ↑	KDM4A ↑	Zhang *et al.*, 2011
Cardiomyopathy	H3K9me2/3	*Anf* ↑ *Bnp* ↑	KDM3A ↑ KDM4A ↑ KDM4B ↑	Hohl *et al.*, 2013

4.2.3 Link between histone methylation and iron homeostasis

Histone methylations are particularly relevant in iron deficiency because all KDMs (except KDM1) are members of the iron-dependent dioxygenase superfamily of enzymes. Much like the HIF regulators PHDs, the activity of these enzymes can be down-regulated *in vitro* by chelation of iron using DFO (Whetstine *et al.*, 2006). However, whereas reduction of PHD activity (based on readouts downstream of HIF activation) in iron deficiency has been shown in both humans and in animals, the function of KDMs has not been explored *in vivo* in iron deficiency. Thus, it has yet to be determined whether the activity of KDMs can also be attenuated in settings of reduced iron levels which are physiologically relevant (and achievable).

Considering a situation where the activity of KDMs is indeed affected by the degree of iron deficiency achieved in this study, it is possible to postulate that histone methylation patterns may be altered, ultimately affecting gene expression. For this reason, this chapter proposes to investigate the effect of iron deficiency on gene expression rather than its effect on global protein expression.

4.2.4 RNA-sequencing

Studying the molecular constituents of cells and the functional elements of the genome is an essential step towards understanding the underlying cause and development of disease (Wang *et al.*, 2009). Accordingly, in recent years, transcriptomics, the study of the sum of the complete set of transcripts in an organism, has become an active area of research and several technologies have been developed for this purpose, all of which utilise either a hybridization- or sequence-based approach (Wang *et al.*, 2009).

The sequence-based approach has many advantages over hybridization-based methods. Unlike the latter, sequence-based technology does not require, and is therefore not limited to, an existing knowledge of the genomic sequence, allowing for unbiased interrogation of the transcriptome under investigation (Behjati and Tarpey, 2013; Wang *et al.*, 2009). Furthermore, because the sequence-based method directly determines the DNA sequence, this approach produces very low background noise and therefore is sensitive for lowly-expressed genes. In addition, it is also not limited by saturation of signals from highly-expressed genes (Wang *et al.*, 2009; Zhao *et al.*, 2014). These two features give the sequence-based approach a very large dynamic range of expression levels which cannot be achieved using hybridization-based methods.

RNA-sequencing (RNA-seq, also known as whole transcriptome shotgun sequencing, WTSS) is the most recent sequence-based sequencing technique that relies on the recently-developed deep-sequencing, or next generation sequencing (NGS), technology (Wang *et al.*, 2009). Therefore, this method is the first high-throughput sequencing-based method that allows for the large-scale interrogation of entire transcriptomes in a quantitative and

accurate manner (Wang *et al.*, 2009). Given the strengths of RNA-seq, this method was chosen as the principle method in carrying out the aims of this chapter.

4.2.5 Study aims

There is no doubt that alterations in gene expression and epigenetic regulation occur during pathological cardiac remodelling. As presented in Chapter 3, a change in cardiac function was observed following the administration of an iron-deficient diet for 6 weeks. This raises the possibility that changes in gene expression may have occurred in the impaired hearts. Therefore, the aim of this study was to utilise RNA-sequencing technology to understand the impact of an iron-deficient diet on the cardiac gene expression in a hypothesis-free approach, to explore the cardiac genomic signature created by iron deficiency and to identify differentially regulated processes for follow-up functional studies.

4.3 METHODS

4.3.1 Mouse model

The mice used in this section correspond to cohort 2 described in Chapter 2.

4.3.2 RNA-sequencing

RNA extraction. Total RNA was extracted from 30 mg of crushed, frozen heart tissues. Prior to submitting samples for library preparation and sequencing, RNA concentration was measured by Qubit using the RNA Broad Range Assay Kit and RNA quality was assessed using the Agilent 2200 RNA TapeStation, following manufacturer's instructions.

Library preparation. mRNA was selected from total RNA a by poly-(A) selection before conversion to cDNA. The second strand cDNA synthesis incorporated dUTP, ends were repaired, A-tailed and adapter-ligated. Prior to amplification, samples underwent fractionation by uridine digestion.

Sequencing. High-throughput sequencing was carried out on the Illumina HiSeq 4000. A total of 20 samples were submitted for sequencing across 2 lanes (10 samples per lane). Each lane received approximately 240 million pair-ended reads (24 million reads per sample). Raw reads were 75 base-pairs (bp) in length.

Library preparation and sequencing was carried out by the Oxford Genomics Centre, Wellcome Trust Centre for Human Genetics, University of Oxford.

Analysis. The analysis pipeline is detailed in Section 4.4.2 of this chapter.

4.3.3 SDS-PAGE and Western blot

Approximately 30 mg of crushed, frozen heart tissue was prepared in ice-cold 8 M urea lysis buffer (in mM, unless otherwise specified): 8 M urea, 1% glycerol, 1% SDS, 5 DTT, 10 Tris pH 6.8 and supplemented with complete protease inhibitor cocktail. Samples were sonicated to clear the chromatin and protein concentration was measured using the BCA Protein Assay (Thermo Fisher) and a 9-point BSA standard following manufacturer's instructions. For SDS-PAGE, 100 μg of sample lysate was run on a 15% gel. The gel was transferred onto a 0.2 μM PVDF for 40 mins.

The antibodies used for western blotting are listed in Table 4.2.

Table 4.2 List of antibodies used in this chapter

Antibody	Product code (Manufacturer)	Concentration
rb-H3K4me1	ab8895 (Abcam)	1:5,000
rb-H3K4me2	ab7766 (Abcam)	1:5,000
rb-H3K4me3	ab8580 (Abcam)	1:5,000
rb-H3K9me1	ab9045 (Abcam)	1:5,000
rb-H3K9me2	ab1220 (Abcam)	1:1,000
rb-H3K9me3	ab8898 (Abcam)	1:2,000
rb-H3K36me1	ab9048 (Abcam)	1:2,000
rb-H3K36me2	ab9049 (Abcam)	1:2,000
rb-H3K36me3	ab9050 (Abcam)	1:1,000
rb-H3 (nuclear loading control)	ab1791 (Abcam)	1:10,000
gt-anti rb-HRP	sc-2030 (Santa Cruz)	1:10,000

rb = rabbit
gt = goat

4.3.4 qPCR

SYBR Green quantitative PCR was performed on cDNA made from mRNA obtained from total heart tissue. *Gapdh* was used as the housekeeping gene. Primers were used at 500 nM concentration, except for *Kdm4a* and *Gapdh*, which were used at 300 nM concentration. The list of primers can be found in Table 4.3.

Table 4.3 List of primers used in this chapter.

Primer	Sequence	Concentration
Kdm4a	F – GAACAGCACGTTGATGAGTGGA R – TGCCGAAGTAAAGGTAGGGGG	300 nM
Kdm4b	F – AGGGACTTCAACAGATATGTGGC R – GATGTCATCATACGTCTGCCG	500 nM
Kdm4c	F – TGGAGAGTCCCCTAAATCCCA R – CCTTGGCAAGACCTGCTCG	500 nM
Kdm4d	F – CAGAGGCCATCAATTTTGCCA R – TTTCCACAGTTCATATCGCTCAG	500 nM
Kdm5a	F – CACAGACCCGCTGAGTTTTAT R – CTTCACAGGCAAATGGAGGTT	500 nM
Kdm5b	F – CTGGGAAGAGTTCGCGGAC R – CGCGGGGTGAAATGAAGTTTAT	500 nM
Kdm5c	F – GAGGCCCAGACAAGAGTGAAA R – TTGGGAATCTTTAAGGATGAGCC	500 nM
Kdm5d	F – CCAGGATCTGACGACTTTCTACC R – TTCTCCGCAATGGGTCTGATT	500 nM
Gapdh	F – GGCACAGTCAAGGCTGAGAATG R – ATGGTGGTGAAGACGCCCAGTA	300 nM

4.4 RESULTS

4.4.1 Assessment of RNA quality prior to sequencing

The quality of the extracted RNA was assessed prior to sequencing using an RNA TapeStation (Figure 4.1). Quality of RNA can be assessed by measuring the RNA integrity number (RIN), which is the ratio of the 28S to 18S subunits of ribosomal RNA (rRNA).

RIN is on a scale of 0-10, where 10 is excellent quality. Typically, RIN > 7.0 is accepted as good quality RNA in most tissue samples. In muscle samples, due to the fibrous nature of the tissue (which makes RNA extraction more difficult), RIN > 6.0 is considered acceptable for the purposes of NGS. In this chapter, all 20 samples submitted for RNA-sequencing had a RIN > 6.0, with only two samples being below 7.0.

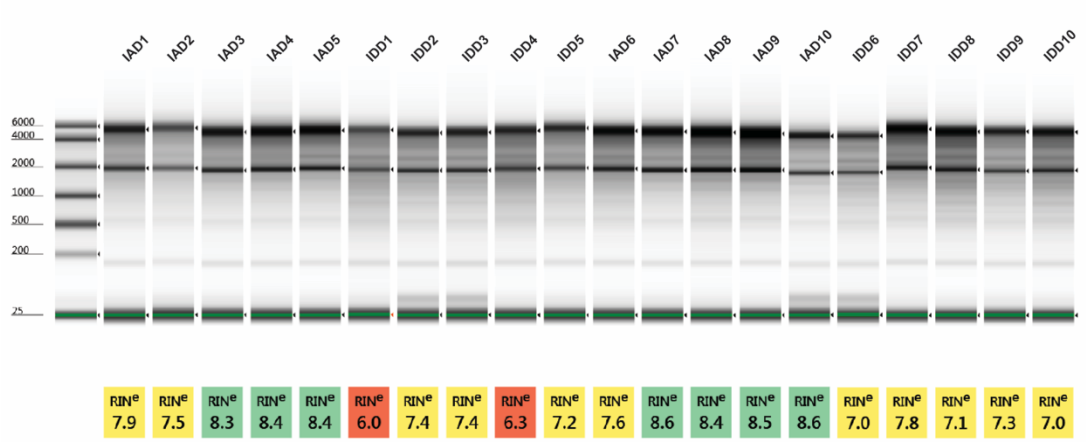


Figure 4.1 Assessment of RNA integrity. RNA integrity number (RIN) is determined by evaluating the 28S to 18S rRNA ratio. RIN is on a scale of 0-10, where 10 is excellent quality. Top arrow = 28S, bottom arrow = 18S. IAD = Iron-adjusted diet; IDD = Iron-deficient diet.

4.4.2 The analysis pipeline

The mRNA of ten iron-adjusted and ten iron-deficient hearts were subject to next generation sequencing on an Illumina HiSeq 4000 platform. A flowchart of the RNA-seq analysis used in this chapter is shown Figure 4.2.

The quality of the raw reads (*fastq* format) was checked using FASTQC, a web-based quality control tool (Simon, 2010). Using the aligner software Spliced Transcripts Alignment to a Reference (STAR), the reads were aligned to the mouse reference genome *mm10* (Dobin *et al.*, 2013). Next, PCR duplicates were removed using the sequence alignment/map (SAM) tools (Li *et al*., 2009). To generate a table of sequenced genes, the FeatureCounts tool (Liao *et al*., 2014) was used to count the number of mapped raw reads. The final output file was a table of mapped genes with the corresponding number of reads counted in *.txt* format. This process was conducted on a UNIX platform via remote access to an account with the Computational Biology Research Group (CBRG) at the University of Oxford. A total of 23,420 unique sequences were identified in the raw read counts.

Subsequent analysis for differential gene expression was carried out in RStudio. First, lowly expressed genes (counts per million, cpm < 1) were removed. The remaining 13,590 raw counts were normalised to library size, to account for differences in gene length. A PCA plot was generated to visualize sample distribution. Differential gene expression was performed using both DESeq2 (Love *et al*., 2014) and EdgeR (McCarthy *et al.*, 2012; Robinson *et al.*, 2010), Gene Ontology using REVIGO (Supek *et al*., 2011) and identification of differentially regulated pathways using the Generally Applicable Gene Set

Enrichment (GAGE) (Luo *et al.*, 2009) and PathView (Luo and Brouwer, 2013) Bioconductor packages.

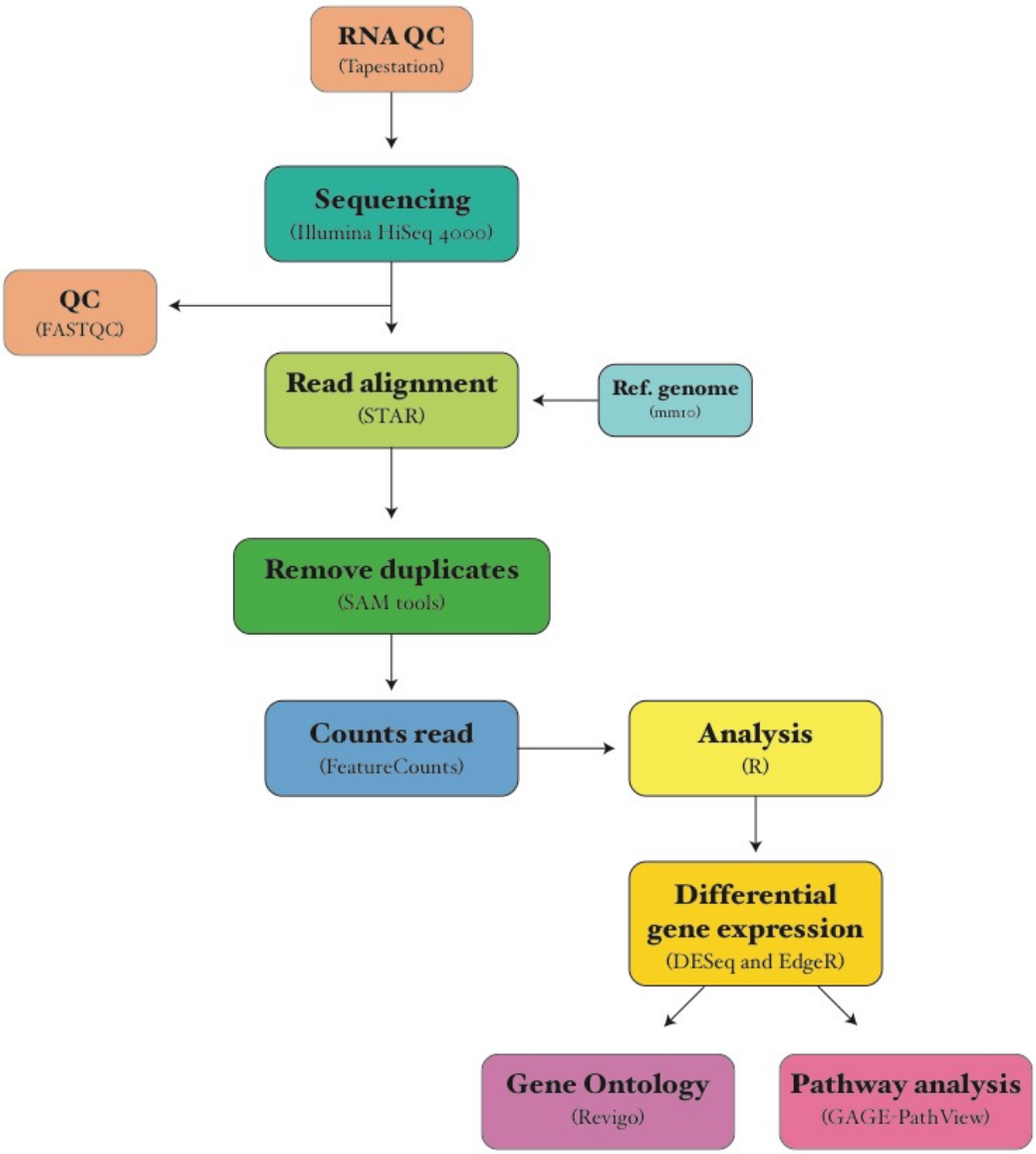


Figure 4.2 The analysis pipeline. 'Read alignment', 'remove duplicates', 'counts read' steps were conducted on a UNIX platform. 'Analysis' (differential gene expression, Gene Ontology, pathway analysis) were carried out in R.

4.4.3 Determination of variation in dataset: Principal component analysis and cluster dendrogram

Principal component analysis (PCA) is a statistical procedure that is used to emphasize variation between samples and to bring out strong patterns that may exist in any given dataset. The output of the analysis is a plot in which one can easily visualize similarities and differences between samples (Ringnér, 2008). The mathematical algorithm that is employed in this analysis reduces the dimensionality of the dataset while identifying directions of maximal variation in the data. This direction is called principal component (PC) and there can be up to one less PCs as the number of samples in the dataset (Ringnér, 2008).

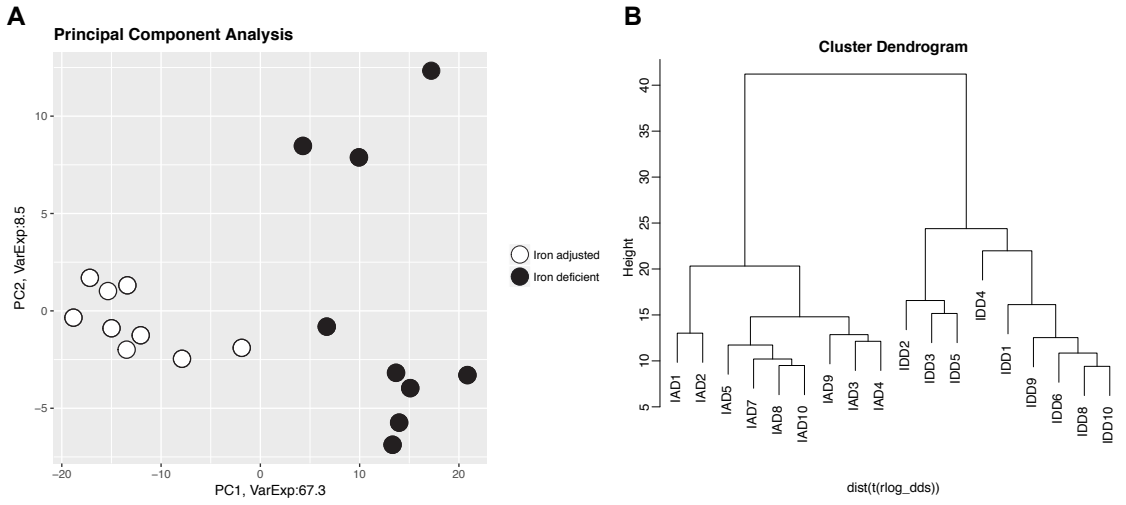


Figure 4.3 Visual representation of the dataset. A) Principal component analysis plot showing sources of variation within the dataset submitted for RNA-seq. n=9 biological replicates in each group. B) Cluster dendrogram showing clustering of iron-adjusted (IAD) and iron-deficient (IDD). Height = $\log_2$(counts normalised to library size)

The PCA plot in Figure 4.3A shows two distinct clusters, one made up entirely of iron-adjusted samples and the other, iron-deficient samples. As expected, the principle source of variation is across PC1, accounting for 67.3% of all identified variation between the samples within each respective group. Across PC2, an 8.5% variation is observed between the samples within the two diet groups.

The cluster dendrogram, as seen in Figure 4.3B, is a visual representation of the distance between samples, where the y-axis (height) represents the closeness or "similarity" of the data points to each other. Consistent with the PCA plot, the dendrogram, generated using the Bioconductor package DESeq2, also shows that the iron-adjusted and iron-deficient samples cluster into two distinct clades are divided based on dietary treatment. Furthermore, the distance between the two diet groups is large, suggesting that the difference in the gene expression profiles of iron-adjusted and iron-deficient samples is large.

One sample in each group, IAD6 and IDD7, were removed from subsequent analysis because they clustered in the incorrect groups (not shown). The reason for this incorrect clustering is unclear since neither the RIN scores nor the number of mapped reads, two parameters which could affect the quality of the data, were significantly different in these two samples compared to the rest of the samples.

4.4.4 Differential gene expression analysis using DESeq2 and EdgeR

The analysis for differentially expressed (DE) genes was performed using DESeq2 and EdgeR, which separately identified 6,232 and 6,095 DE genes, respectively, with a *p*-value < 0.01 and $\log_2$ fold-change > 0.58 (at least 1.5-fold greater or less change in expression). Given that nearly 50% of all mapped reads were deemed differentially expressed by DESeq

and EdgeR, stringency of DE gene selection was increased by selecting only those genes which were differentially expressed in both analyses. This reduced the number of DE genes to 1,569 common or overlapping genes. Of these DE genes, approximately 22% were up-regulated and 78% were down-regulated in the iron-deficient group compared to the control (iron-adjusted) group (Figure 4.4).

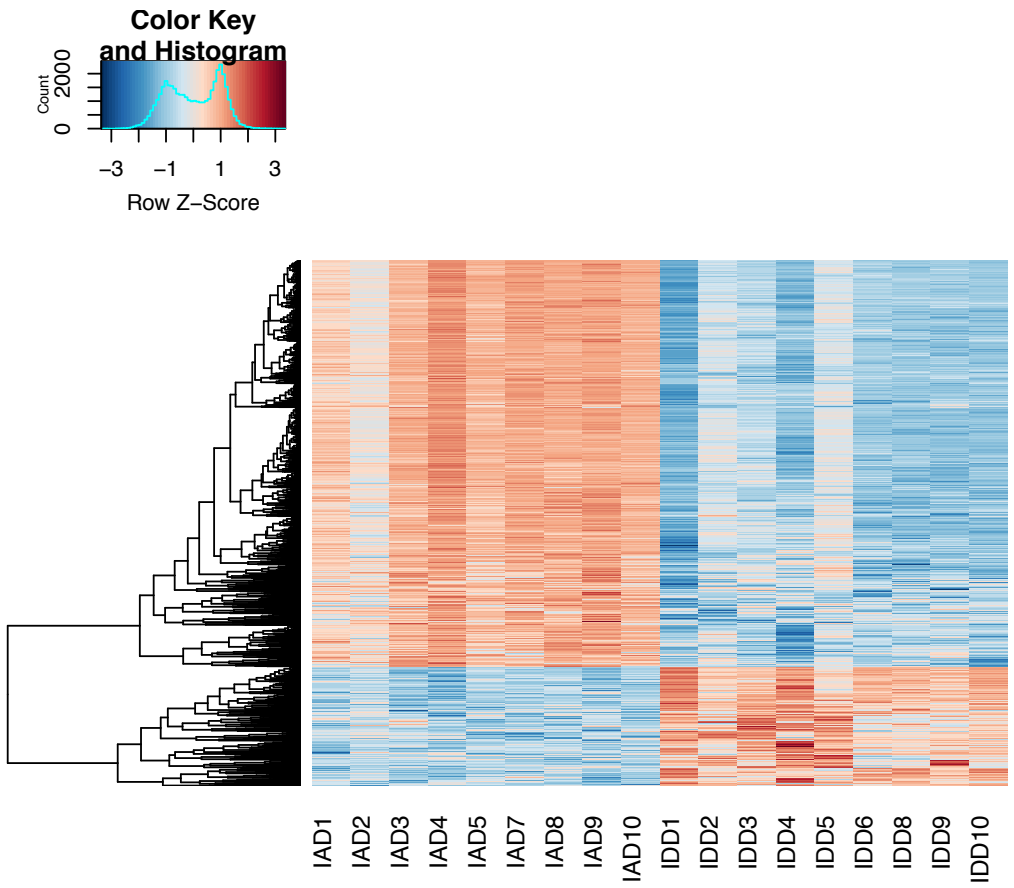


Figure 4.4 Hierarchical heat map of differentially expressed genes in iron-adjusted (IAD) or iron-deficient (IDD) conditions. Approximately 22% up-regulated (orange) and 78% down-regulated (blue) genes. Figure created using R software heatmap.2 function of gplots package (http://www.r-project.org/).

4.4.5 Gene Ontology enrichment using REVIGO

To gain a better understanding of the biological response elicited by an iron-deficient diet, Gene Ontology (GO) analysis was performed on the DE gene dataset using REVIGO, a web-based tool that identifies statistically significant ontology terms between experimental groups. The top up- and down-regulated biological process, cellular component, and molecular function can be found in Table 4.4.

A systemic deficiency of an essential micronutrient such as iron is expected to be a major physiological stressor, thus predicted to evoke a stress response. Not surprisingly, over-represented, up-regulated biological processes were associated with *response to stress* (GO:0006950) and *regulation of response to external stimulus* (GO:0032101). Cellular components related to the *extracellular region* (GO:0005576) and *plasma membrane* (GO:0005886), and *cytokine* (GO:0005125) and *cytokine receptor* (GO:0004896) activities under molecular function were also found to be up-regulated in the hearts of animals on an iron-deficient diet. These are consistent with a general stress response given that the cell's extracellular region plays a key role in promoting cell signaling, thereby modulating the cell's behaviour in response to its surrounding (Jorgensen and Is, 2014).

Cellular adaptation to stress is likely to involve transcriptional and post-translational mechanisms to modulate gene and protein expression. This is clearly the case in the animal model used in this chapter, evidenced by the vast number of DE genes. To further support the previous statements, properties related to nuclear components and transcription/ translation activity were over-represented in the down-regulated GO terms.

4.4.6 Differentially regulated KEGG pathways using GAGE and visualized with PathView

To understand better the relationship between the GO themes and to visualise these changes in terms of biological pathways, the data was further analysed to determine key pathways that were differentially regulated in iron deficiency (Table 4.5). The Bioconductor package GAGE and PathView were used to identify differentially regulated pathways within the Kyoto Encyclopedia of Genes and Genomes (KEGG) database.

Consistent with the GO terms, many of the differentially regulated pathways were related to processes involving gene and protein expression, signaling cascades, and cell-cell communications. More interestingly, two metabolic pathways, *oxidative phosphorylation* (mmu00190) and *pyruvate metabolism* (mmu00620), and the *calcium signaling* pathway were also differentially affected, implicating perturbations in cardiac energetics and contractility. These will be discussed further in the *Discussion* section.

Table 4.4 Over-represented GO terms in the hearts of mice on an iron-deficient diet compared to control mice on an iron-adjusted diet.

	Up-regulated			Down-regulated		
Biological process	**GO term**	**Description**	***p*-value**	**GO term**	**Description**	***p*-value**
	GO:0009611	response to wounding	0.00002	GO:0034654	nucleobase-containing compound biosynthetic process	0.00005
	GO:0007596	blood coagulation	0.00003	GO:0006464	cellular protein modification process	0.00010
	GO:0006952	defence response	0.00007	GO:0043412	macromolecule modification	0.00013
	GO:0002376	immune system process	0.00015	GO:0018130	heterocycle biosynthetic process	0.00014
	GO:0006955	immune response	0.00017	GO:0019438	aromatic compound biosynthetic process	0.00016
	GO:0001775	cell activation	0.00035	GO:1901362	organic cyclic compound biosynthetic process	0.00030
	GO:0006954	inflammatory response	0.00043	GO:0006366	transcription from RNA polymerase II promoter	0.00032
	GO:0006950	response to stress	0.00114	GO:0006357	regulation of transcription from RNA polymerase II promoter	0.00067
	GO:0007159	leukocyte cell-cell adhesion	0.00189	GO:0006793	phosphorus metabolic process	0.00068
	GO:0050878	regulation of body fluid levels	0.00293	GO:0006796	phosphate-containing compound metabolic process	0.00072
	GO:0032101	regulation of response to external stimulus	0.00551	GO:0045893	positive regulation of transcription, DNA-templated	0.00120
Cellular compartment	**GO term**	**Description**	***p*-value**	**GO term**	**Description**	***p*-value**
	GO:0005576	extracellular region	0.00107	GO:0000785	chromatin	0.01947
	GO:0005615	extracellular space	0.00412	GO:0034702	ion channel complex	0.02113
	GO:0031225	anchored component of membrane	0.01056	GO:0031981	nuclear lumen	0.02291
	GO:0030141	secretory granule	0.01529	GO:0044463	cell projection part	0.02444
	GO:0071944	cell periphery	0.03858	GO:0005794	Golgi apparatus	0.03354
	GO:0005886	plasma membrane	0.04079	GO:0005694	chromosome	0.03487
Molecular function	**GO term**	**Description**	***p*-value**	**GO term**	**Description**	***p*-value**
	GO:0008236	serine-type peptidase activity	0.00688	GO:0005524	ATP binding	0.00005
	GO:0017171	serine hydrolase activity	0.00688	GO:0008270	zinc ion binding	0.00030
	GO:0004866	endopeptidase inhibitor activity	0.02110	GO:0016773	phosphotransferase activity, alcohol group as acceptor	0.00042
	GO:0005125	cytokine activity	0.02481	GO:0003677	DNA binding	0.00049
	GO:0031406	carboxylic acid binding	0.02518	GO:0003676	nucleic acid binding	0.00089
	GO:0005198	structural molecule activity	0.02547	GO:0016772	transferase activity, transferring phosphorus-containing groups	0.00115
	GO:0016853	isomerase activity	0.02850	GO:1901265	nucleoside phosphate binding	0.00200
	GO:0004896	cytokine receptor activity	0.04777	GO:0016740	transferase activity	0.00407

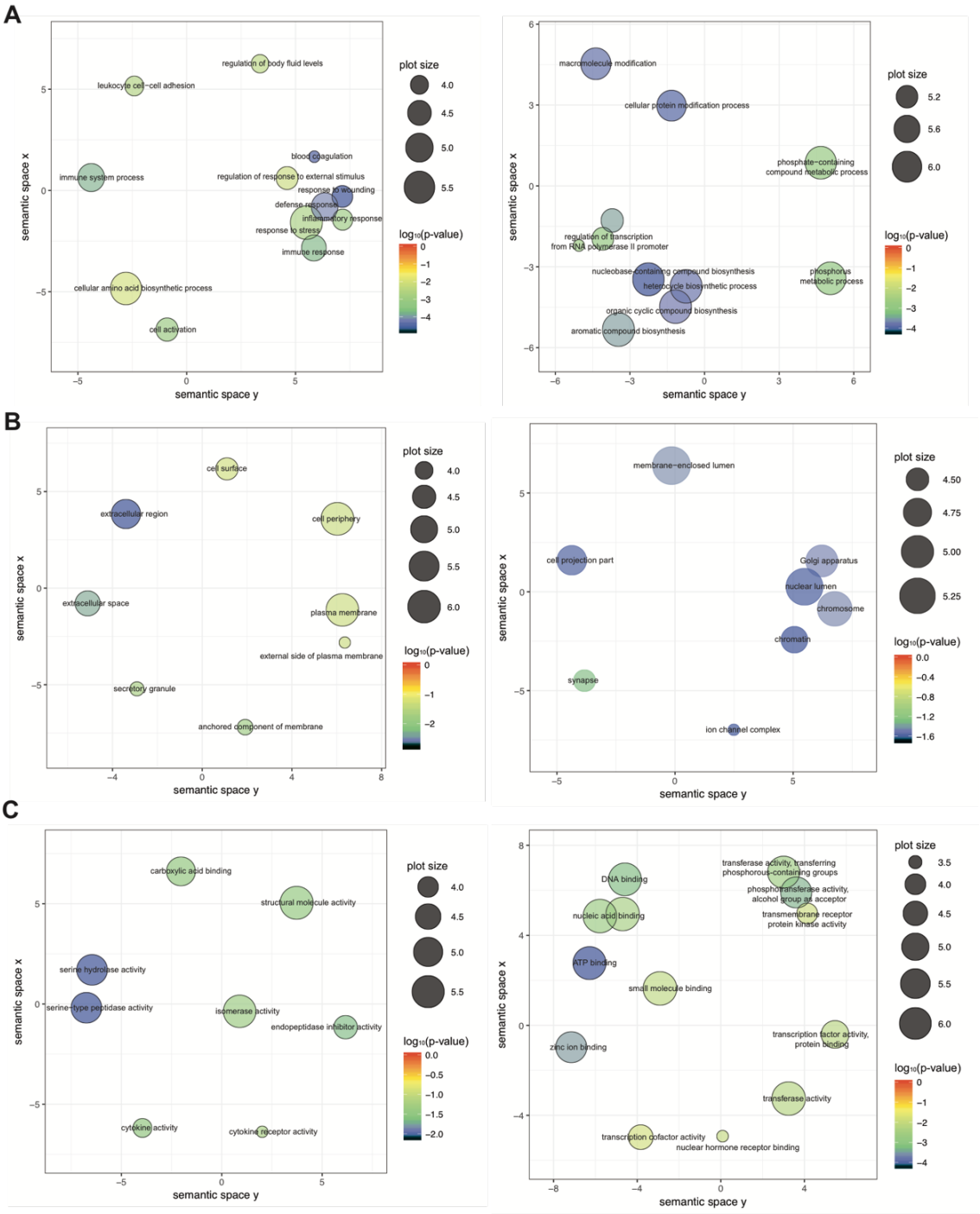


Figure 4.5 Visual representation of GO terms. (left) Up-regulated; (right) Down-regulated. A) Biological process; B) Cellular component; C) Molecular function. GO terms are represented in a two-dimensional space referred to as "semantic space," which represents the semantic similarities of each identified GO term to each other; the units in the semantic space themselves do not have any intrinsic meaning. Circle size indicates the frequency of the GO term annotated in the database (i.e. the more specific the term, the smaller the circle) (Supek *et al.*, 2011).

Table 4.5 Differentially regulated pathways in the hearts of mice on an iron-deficient diet compared to controls on an iron-adjusted diet.

KEGG Pathway	Description	*p*-value
mmu03010	Ribosome	0.00000
mmu00190	Oxidative phosphorylation	0.00001
mmu03050	Proteasome	0.00010
mmu00970	Aminoacyl-tRNA biosynthesis	0.00289
mmu04012	ErbB signaling pathway	0.00220
mmu04310	Wnt signaling pathway	0.00312
mmu04070	Phosphatidylinositol signaling system	0.00342
mmu00480	Glutathione metabolism	0.00465
mmu03030	DNA replication	0.00566
mmu04020	Calcium signaling pathway	0.00631
mmu03040	Spliceosome	0.00601
mmu00520	Amino sugar and nucleotide sugar metabolism	0.00790
mmu04270	Vascular smooth muscle contraction	0.01094
mmu00240	Pyrimidine metabolism	0.01188
mmu04910	Insulin signaling pathway	0.01434
mmu04520	Adherens junction	0.01544
mmu04510	Focal adhesion	0.01845
mmu00620	Pyruvate metabolism	0.01989
mmu04540	Gap junction	0.02941
mmu04010	MAPK signaling pathway	0.02941

4.4.7 Effect of an iron-deficient diet on genes involved in iron homeostasis

Given that the GO and pathway analysis did not identify differential regulation of processes involved in iron homeostasis, the expression level was investigated in a selection of iron-related genes, whose expression is sensitive to iron bioavailability, using the raw counts table generated using FeaturesCount (Figure 4.6). Where the expression of genes encoding for DMT1 (*Slc11a2)*, DCYTB (*Cybrd1)*, TfR1 (*Tfrc)* and hepcidin (*Hamp*) were not significantly different in the controls vs iron-deficient hearts, the expression of FPN (*Slc40a1*) and hephaestin (*Heph*) was significantly reduced. The former is consistent with the qPCR results presented in Chapter 3 (*see* Figure 3.11D). Furthermore, the expression of ferritin heavy chain (*Fth1*) and light chain (*Ftl1*) was significantly enhanced in the iron-deficient hearts compared to the controls, which may suggest increased effort in the heart to store intracellular iron in response to systemic iron deficiency as a mechanism of cardio-protection against loss of cardiac iron.

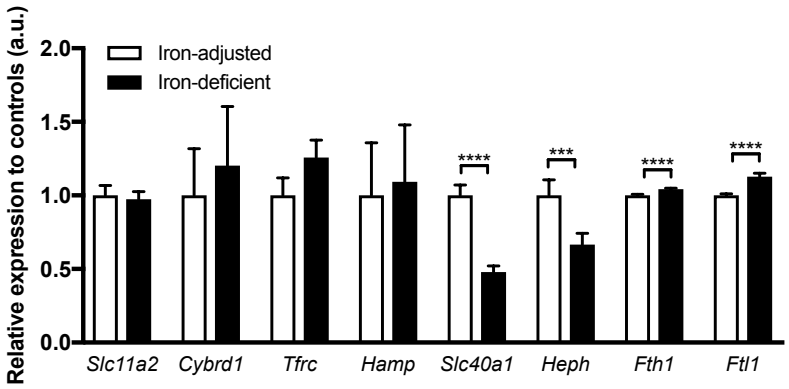


Figure 4.6 Gene expression of iron-sensitive proteins involved in iron homeostasis. Raw counts averaged and normalised to expression of controls. *Slc11a2* = DMT1, *Cybrd1* = DCYTB, *Tfrc* = Transferrin receptor 1, *Hamp* = Hepcidin, *Slc40a1* = FPN, *Heph* = Hephaesin, *Fth1* = Ferritin heavy chain, *Ftl1* = Ferritin light chain. Data plotted as mean ± SEM. *p*-value determined by a two-tail, unpaired student's *t*-test; *** $p > 0.001$, **** $p > 0.0001$. n = 9 mice per cohort.

4.4.8 Effect of an iron-deficient diet on epigenetic regulation: histone methylation

Post-translational methylation of histone tails contributes towards the regulation of gene expression. As discussed in the introduction of this chapter, the histone marks H3K4 and H3K9 have been linked to the pathology of heart disease. The previous sections found that gene expression was certainly affected by an iron-deficient diet, but the question remained as to whether physiological iron deficiency also affects gene expression at the epigenetic level. To address this question, the histone marks H3K4, H3K9 and H3K36 were probed for by western blot (Figure 4.7A). A general up-regulation in methylation state was observed in the hearts of animals on an iron-deficient diet, with significant increases in H3K4me1, H3K9me3, H3K36me1 and H3K36me3; the level of H3K4me3 was similar in the two cohorts.

To determine whether the differences in histone methylation pattern were due to a difference in demethylase expression, the gene expression of the H3K9 and H3K36 tri-methyl demethylases, KDM4s was investigated. In the hearts of iron-deficient animals, *Kdm4a*, the most abundantly expressed KDM transcript (Figure 4.7C), was not altered, *Kdm4b* was increased and *Kdm4c* was decreased with the administration of an iron-deficient diet (Figure 4.7B). *Kdm5a-d*, the demethylases for H3K4, were found to be down-regulated in the hearts of the iron-deficient group. Assessment of KDM protein expression by western blot proved to be technically difficult. Therefore, this information was not acquired in this thesis.

Further to regulation at the transcriptional and post-translational level, the activity of demethylase can also be modulated by nuclear targeting (Kamikawa and Donohoe, 2014). In addition, it is also known that KDM homologues are functionally redundant (Schofield and Hausinger, 2015), thus it is difficult to predict the impact of alterations in mRNA expression on histone methylation status. Methylation is also acted upon by methyltransferases, which adds another layer of complexity. Therefore, a mechanistic interpretation is difficult at this stage.

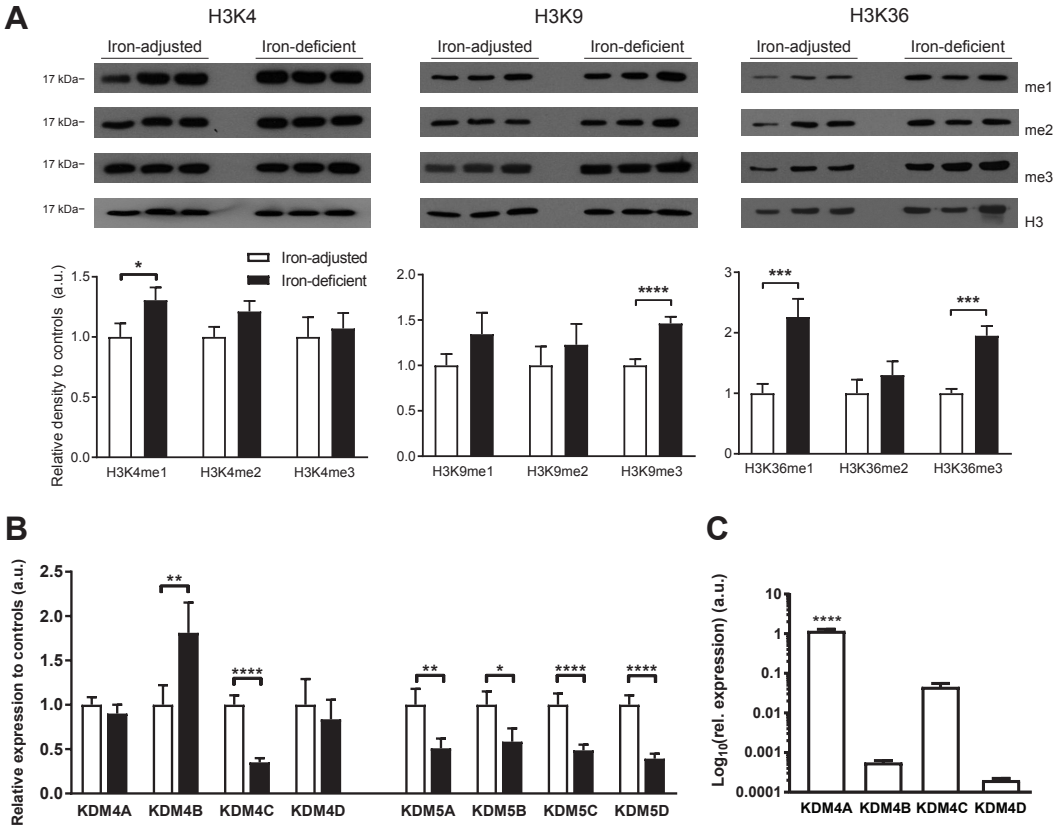


Figure 4.7 Histone H3 methylation marks. A) (top) Western blot of histone marks H3K4, H3K9 and H3K36 and (bottom) calculated band density, normalised to the H3 nuclear loading control; B) Relative expression of KDM4 and KDM5 enzymes at the mRNA level, relative to the controls; C) Expression of KDM4s relative to KDM4A in wild-type C57Bl6 mice. Data plotted as mean ± SEM. *p*-value determined by a two-tail, unpaired student's *t*-test; * $p > 0.05$, ** $p > 0.01$, *** $p > 0.001$, **** $p > 0.0001$. For western blot, n = 3 mice per cohort; for qPCR, n = 9 mice per cohort.

4.5 DISCUSSION

4.5.1 An iron-deficient diet leads to epigenetic alterations

The RNA-sequencing data presented in this chapter provided the first insight into the changes in gene expression that occurs in the hearts as a result of an iron-deficient diet.

A striking observation was the distinct segregation of the genomic footprint in the iron-adjusted vs iron-deficient samples. Both the PCA and cluster dendrogram showed a clear separation between the two cohorts. Of note, as previously mentioned, one sample in each group, IAD6 and IDD7, clustered in the incorrect group. The reason for this incorrect clustering is unclear, since neither the RIN scores (IAD6 RIN – 7.6; IAD7 RIN – 7.0) was significantly lower, nor the number of mapped reads was different than the rest of the samples. Nevertheless, overall, this analysis revealed that the administration of an iron-deficient diet alone leads to large-scale genetic reprogramming.

Changes in gene expression result from the cumulative contribution of many different factors, one of which is histone modification. In this thesis, histone methylation was a particularly interesting target of study since KDM family of demethylases are iron-dependent enzymes. In the heart, KDM4A has previously been shown to promote the hypertrophic response via up-regulation of the four-and-a-half LIM domain (FHL) gene expression (Zhang *et al*., 2011). Furthermore, in patients suffering from hypertrophic cardiomyopathy, an enhanced expression of KDM4A has been detected, implicating this demethylase as a causative factor in heart disease (Zhang *et al.*, 2011).

In this chapter, the mRNA expression of cardiac KDM4A was not altered following the administration of an iron-deficient diet. Furthermore, the tri-methylation state of its preferred substrates H3K9 and H3K36 was also enhanced in the hearts of iron-deficient animals. Given a background of unchanged total cardiac iron, the findings presented in this chapter raises the possibility that changes in iron handling within the cardiomyocyte may have been affected. For instance, it is possible that the pool of labile iron has decreased and thus affecting the function of KDM4A.

That being said, the level of tri-methyl H3K4 was not significantly different in the hearts of iron-deficient animals compared to the controls. This result challenges the hypothesis that the function of KDM4A is affected due to a change in labile iron availability in the heart. Tri-methyl H3K4 is a target substrate for the KDM5 demethylase family, which, like KDM4s, are iron-dependent enzymes. If there was a general lack of iron availability, it is likely that the function of both enzymes would have been affected, thus an increase in all methylation states should have been observed. Furthermore, at the transcript level, the expression all four KDM5 isoforms was decreased significantly in the hearts of iron-deficient animals, which may have further impact at the functional level. That tri-methyl H3K4 was unaffected, together with the observation that gene expression of the various KDM isoforms were altered differently, suggests that the changes in methylation state may be a targeted response to distinct and specific gene sets in response to stress or injury rather than a global, genome-wide alteration as a result of impaired enzyme function.

Finally, the observed methylation states would have also been affected by the action of methylases, but it remains to be shown what their exact contributions are. Further

experiments would be required to clarify the mechanisms by which the methylation state was altered in the hearts of iron-deficient animals. Nevertheless, these results collectively show that epigenetic mechanisms are altered and implicate histone modifications in the differential regulation of the transcriptome following an iron-deficient diet.

4.5.2 Iron-deficiency leads to differential regulation of stress-responsive processes and pathways

From the results presented in this chapter, it is evident that an iron-deficient diet has elicited numerous responses in the hearts of these animals. However, many of the observed changes have a common upstream effector, a response to stress and external stimuli (Table 4.4, Biological Processes). While it is recognised that different stressors evoke different cellular responses, common responses also exist and are collectively known as the environmental stress response (ESR). The regulation of gene expression (chromatin structure, transcriptional regulation, mRNA stability and translation) is a major component of ESR. Other ESRs include alterations in metabolism, protein homeostasis, cytoskeletal (or extracellular) organization, trafficking of transport vesicles and modification of enzymatic activity (de Nadal *et al*., 2011), all of which were observed to be differentially regulated in the hearts of iron-deficient mice.

Primarily, the cell's mechanism of evoking the stress response is through signal transduction pathways that involve stress-activated protein kinases. Accordingly, ErbB, Wnt and MAPK were among the most differentially regulated pathways in the hearts of iron-deficient animals. In heart disease, these pathways are known to play an important role in regulating the pathological hypertrophic response (Özcelik *et al.*, 2002).

4.5.3 Systemic iron-deficiency does not appear to evoke a response involving the cardiac iron homeostasis pathway

Given the nature of the experimental design used in this study, one would expect that the iron homeostasis pathway be affected following an iron-deficient diet. However, in the animals used in this study, this pathway was not identified as differentially regulated. The lack of a coordinated, differential response of the iron homeostasis pathway is not surprising, given that total cardiac iron was not found to be different in animals on an iron-deficient diet (*see* Chapter 3, Figure 3.9 and Table 3.4).

4.5.4 Limitations of the current study

The animal model used in this chapter was selected based on two criteria: 1) the animals were rendered iron deficient and 2) their cardiac function at that time point was compromised. Based on this, a 6 week dietary time point was selected to carry forth the study presented in this chapter. Due to the length of the dietary treatment, the transcriptional changes observed in this chapter are likely to be adaptations to chronic iron deficiency (or changes downstream of altered cardiac function) rather than responses to an acute lack of iron bioavailability. The result was a very complex data set with nearly 1,570 genes which were differentially regulated and hundreds of significantly affected pathways. The complexity of the data, together with the design of the animal model, therefore, has made it difficult to decipher which changes were direct effects of iron deficiency and which ones were secondary to iron deficiency, such as long term adaptive response.

A second limitation is that the RNA submitted for RNA-seq were obtained from total heart tissues rather than isolated cardiomyocytes. Even though cardiomyocytes occupy

approximately 75% of the myocardial tissue volume, they only account for 30-40% of cell number (Camelliti *et al.*, 2005). Therefore, the samples would have been "contaminated" with RNA from other cells that make up the heart, such as fibroblasts and endothelial cells, as well as from red and white blood cells. While some of the identified processes and pathways (i.e. metabolism) can be more convincingly attributed to cardiomyocytes than others, for events such as *immune-response* or *regulation of transcription*, the source from which the signal derives remains rather ambiguous. An ideal solution to this would be to utilise RNA obtained from isolated cardiomyocytes. However, the isolation process inevitably results in cell death, which would lower the quality of the RNA beyond what is acceptable for RNA-seq standards.

A final limitation of this chapter is that RNA-seq does not provide functional information related to cellular function, since proteomic remodelling may not necessarily follow alterations in gene expression. Therefore, it is difficult to speculate the effects of differential gene regulation at the functional level. For this, a separate functional study would be required to determine the physiological relevance of any given differentially regulated process.

4.5.5 Selection of pathways for functional studies

Following 6 weeks of diet, a decrease in cardiac performance was observed in the iron-deficient animals, which suggests that cardiac remodelling has occurred. Amidst a strong response to stress, particularly interesting findings were the differential regulation of metabolism and the calcium signaling pathway (Figure 4.8-4.11). These will be discussed briefly below and further developed in Chapters 5 and 6 of this thesis.

i) Alterations in metabolic pathways

Metabolism is a requirement for cardiac function. Previous studies have shown an increase in the gene expression of subunits of the electron transport chain complexes in early pressure-overload cardiac hypertrophy mouse models as well as in aortic constriction rat models (Rosca *et al.*, 2013). Consistent with the literature, many of the genes in the *oxidative phosphorylation* pathway were up-regulated in the hearts of iron-deficient animals. Finally, an increase in the *pyruvate metabolism* pathway suggests a possible switch in metabolic substrate preference from fatty acid to glucose, a phenomenon that is common to the pathophysiology of heart failure.

Chapter 5 will explore the effects of an iron-deficient diet on metabolism at the physiological and functional level.

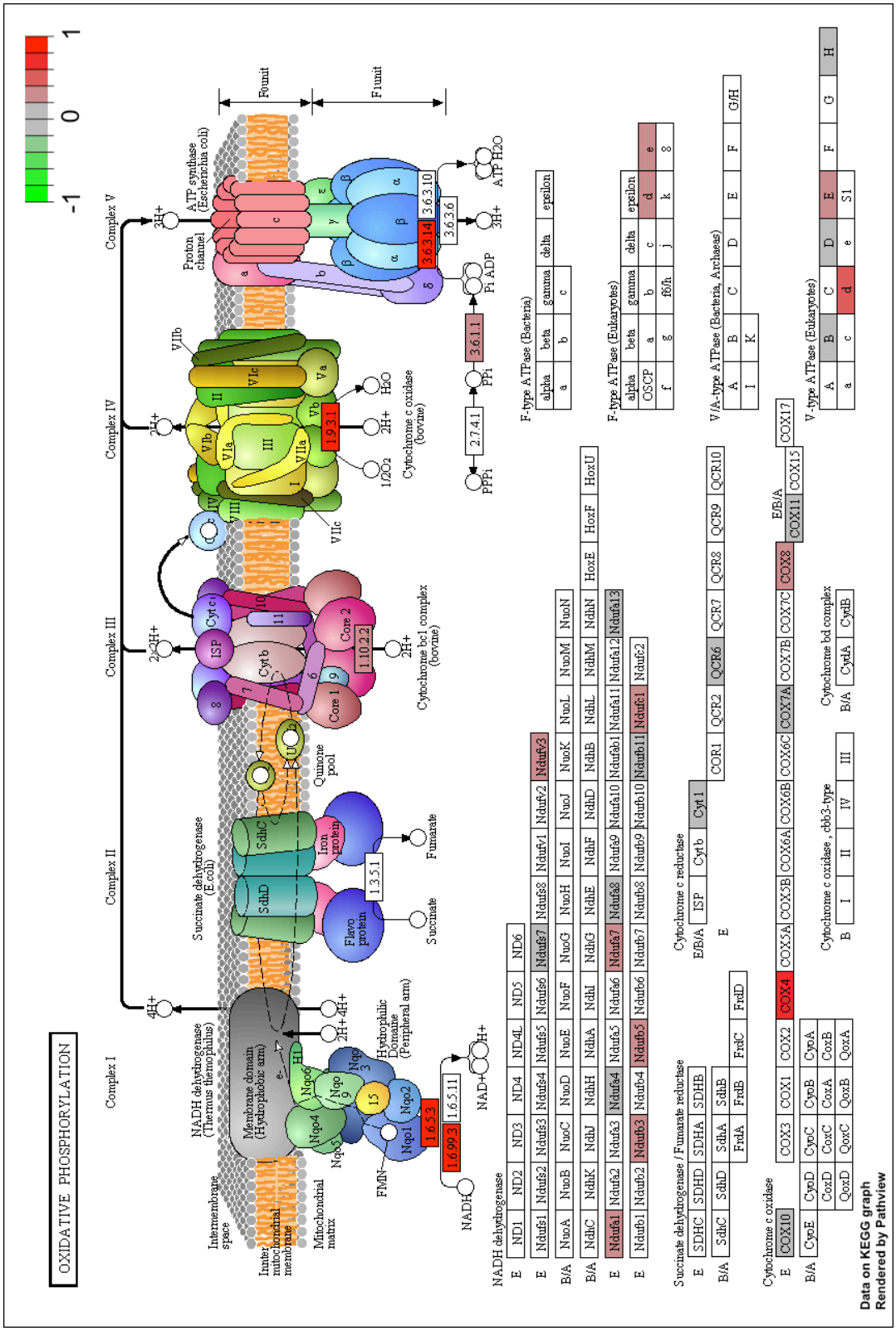


Figure 4.8 Differential regulation of cardiac oxidative phosphorylation. Green = down-regulated and red = up-regulated in the hearts of iron-deficient animals compared to controls.

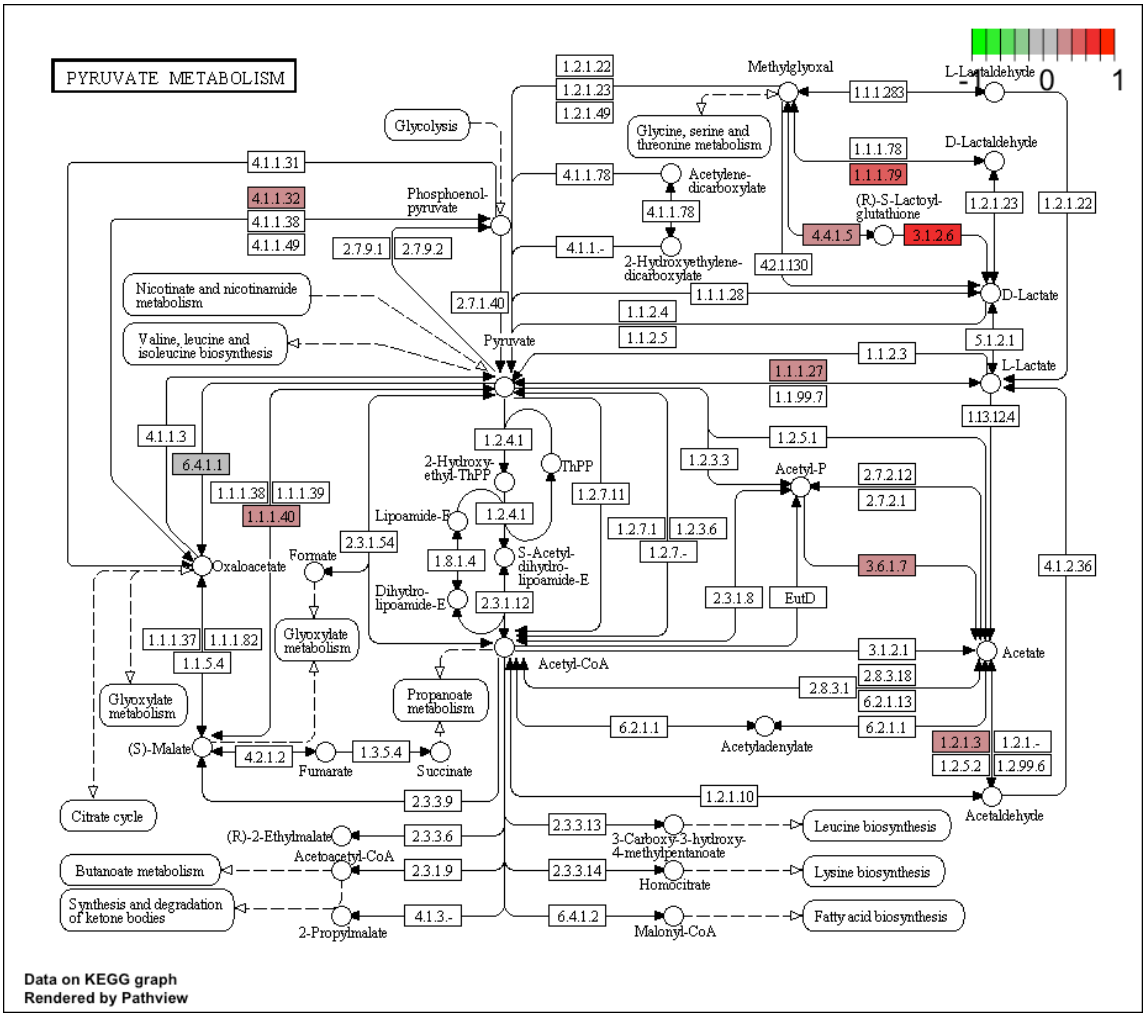


Figure 4.9 Differential regulation of cardiac pyruvate metabolism. Green = down-regulated and red = up-regulated in the hearts of iron-deficient animals compared to controls.

ii) Differential regulation in the calcium signaling pathway

Calcium is required for cardiac contraction and a derangement in calcium homeostasis in the heart leads to impairment in contractility and eventual deterioration of cardiac health. In terms of gene expression of calcium handling proteins, the current literature has yet to agree. Borlak and Thum (2003) found that in end-stage heart failure patients, the expression of the L-type calcium channel (Ca_v1, also known as LTCC), ryanodine receptor 2 (RYR2), sodium/calcium exchanger (NCX) genes were found to be repressed. In contrast, Soltysinska *et al*. (2009) found that these three genes were up-regulated in similar a patient cohort. In both cases, the sarco/endoplasmic reticulum calcium-ATPase (SERCA) gene was found to be down-regulated. In the study presented in this chapter, the Ca_v1, RYR2 and NCX genes were significantly down-regulated in the hearts of iron-deficient animals and the expression for SERCA was not found to be differentially regulated. The disagreements in previously reported results, as well as the observations made in this chapter, highlight the heterogeneity and complexity of heart disease.

Although a consensus is yet to be reached regarding the gene expression profile of calcium-handling proteins in the diseased state, an alteration in their expression is often accompanied by a change in calcium handling kinetics. Therefore, it is possible to postulate that, in the animal model used in this thesis, the differential regulation of calcium genes may result in abnormal signaling in the heart and may contribute to the impairment of heart function. Additional studies would be required to assess the physiological effects of the differential regulation of the key players in the calcium signaling pathway. This will be explored in Chapter 6.

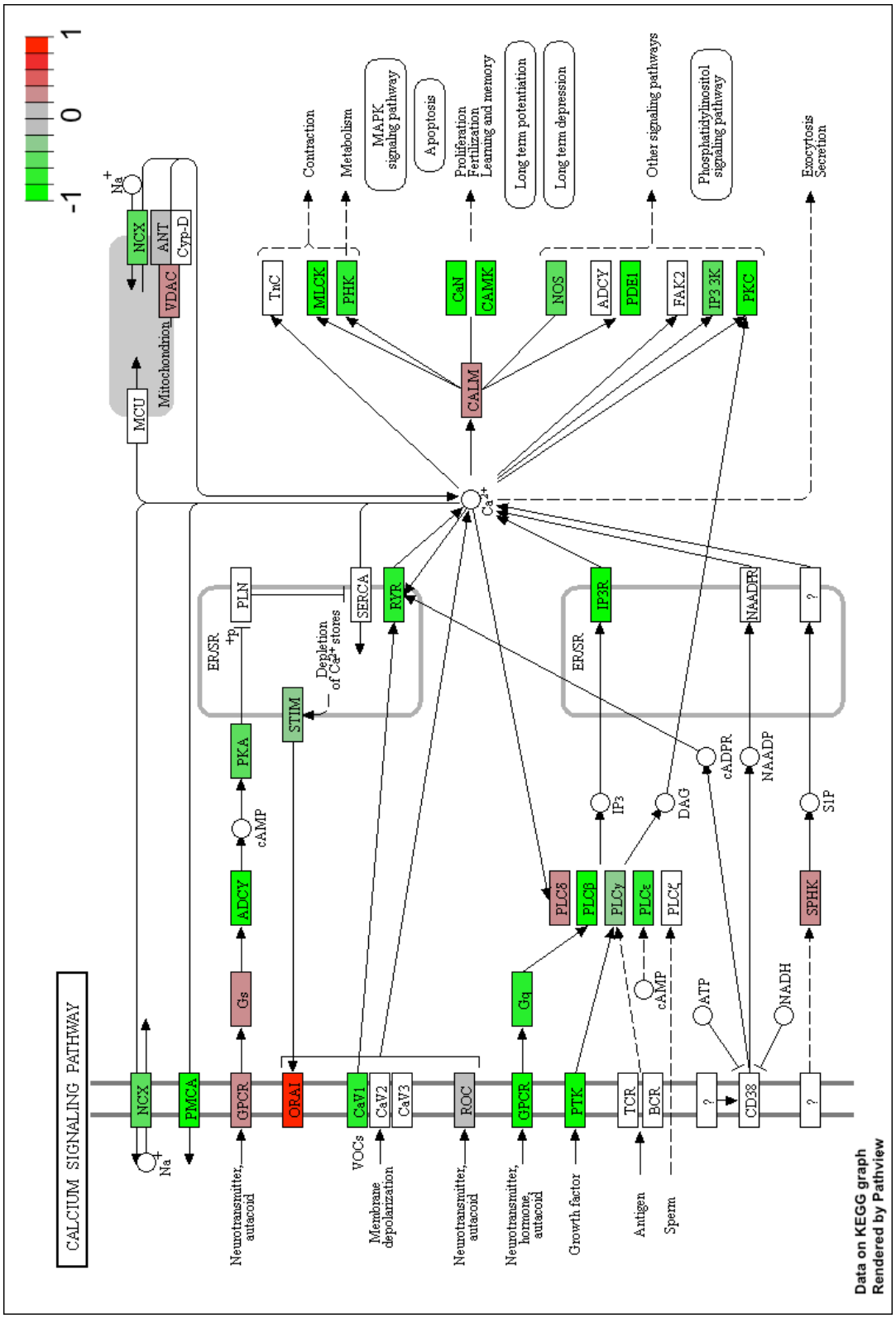


Figure 4.10 Differential regulation of the calcium signaling pathway. Green = down-regulated and red = up-regulated in the hearts of iron-deficient animals compared to controls.

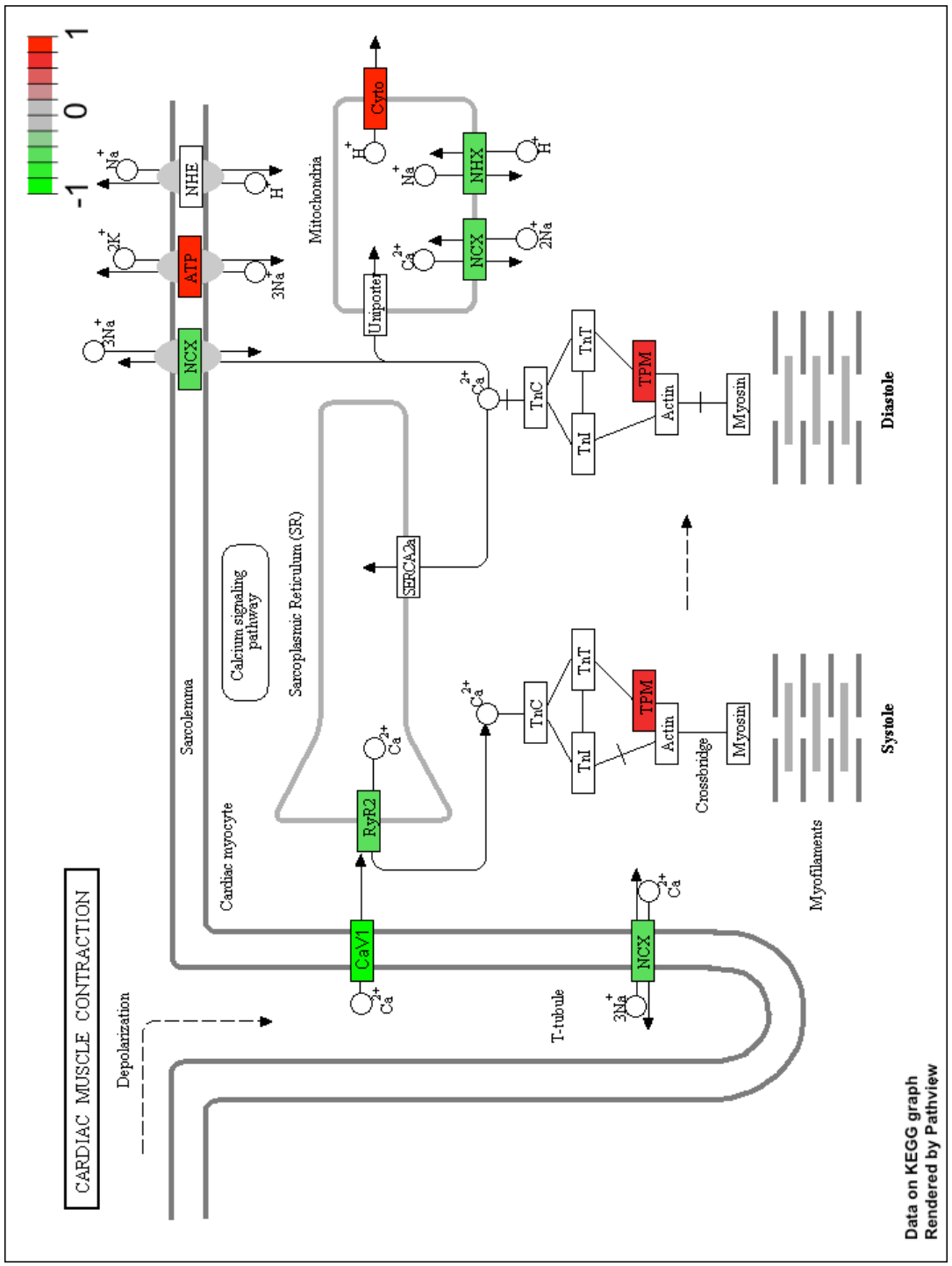


Figure 4.11 Calcium signaling in the context of cardiac muscle contraction. Green = down-regulated and red = up-regulated in the hearts of iron-deficient animals compared to controls.

4.6 CONCLUSIONS

The study of transcriptomes is an important and useful approach in understanding the aetiology of a disease. Using RNA-seq and a non-target based approach, the transcriptome of the hearts of iron-deficient animals were compared to that of the control. The resulting data has provided invaluable insight into the cardiac gene expression signature of iron deficiency. Perhaps the most interesting finding was that iron deficiency through diet is sufficient to produce a unique genomic footprint in the heart. Furthermore, many of the genome-wide alterations were consistent with a general stress response. The histone methylation state was also shown to be altered with an iron-deficient diet, implicating epigenetic regulation in the alteration of the transcriptome in this animal model. Finally, two differentially regulated pathways (metabolism and calcium signaling) were selected for follow-up functional studies to investigate the physiological significance of the findings presented in this chapter.

CHAPTER 5:

EFFECTS OF IRON DEFICIENCY ON CARDIAC METABOLISM

5.1 CHAPTER OVERVIEW

In Chapter 4, the *pyruvate metabolism* and *oxidative phosphorylation* pathways were identified as differentially regulated in the hearts of mice on an iron-deficient diet. Based on this evidence, the study presented in this chapter aimed to investigate the effects of an iron-deficient diet on cardiac metabolism. For this purpose, animals were administered an iron-deficient diet for 6, 9 or 24 weeks. First, their metabolic profile was studied *in vivo* using a hyperpolarised [1-^{13}C]pyruvate MRS technique. Then, various aspects of metabolism were studied *ex vivo*, such as assessment of the gene expression of metabolic proteins and enzyme activity assays using spectroscopic methods. The results showed that cardiac metabolism is affected in iron deficiency; these alterations were consistent within the context of physiological iron status and cardiac function described in Chapter 3.

5.2 INTRODUCTION

5.2.1 Energy metabolism in the heart

The heart is an organ of high metabolic demand. In an adult human, the heart requires approximately 15 to 20 times its own weight in ATP in one day (about 6 kg per day) to maintain normal function (Kolwicz *et al.*, 2013; Noordali *et al.*, 2017). Accordingly, the cardiac metabolic pathway is optimised to maximise efficiency and energy production in a tightly regulated process.

The heart is capable of using a range of energy substrates, ranging from carbohydrates, lipids, amino acids to ketone bodies for ATP production (Kolwicz *et al.*, 2013). The primary fuels for the generation of ATP in the mitochondria are fatty acyl-coenzyme A and pyruvate, which are metabolites of fatty acid and carbohydrates (mostly glucose), respectively. In the healthy, mature heart, approximately 60-80% of ATP production is attributable to fatty acids, 15-30% to glucose and the remainder to lactate, ketone bodies and amino acids (van Bilsen *et al.*, 2004; Jaswal *et al.*, 2011; Noordali *et al.*, 2017). Finally, 95% of the ATP is produced by oxidative phosphorylation in the mitochondria. The remaining 5% is derived from glycolysis and to a lesser extent, the citric acid cycle (TCA) (Kolwicz and Tian, 2011).

5.2.2 Fatty acid metabolism in the heart

i) Fatty acids: The major energy source in the heart

Fatty acids (FA) are the preferred metabolic substrates in the adult myocardium. Free FA in the blood are taken up into the cardiomyocyte through the transport protein FA-

translocase (FAT/CD36) and accessory protein FA-binding protein (Doenst *et al.*, 2013). Once in the cytosol, free FAs are esterified to fatty acyl-coenzyme A (CoA). For transport into the mitochondrial intermembrane space, fatty acyl-CoA is first converted into long-chain fatty acylcarnitines by a mitochondrial outer membrane enzyme carnitine palmitoyltransferase (CPT) 1. Next, the acylcarnitine is converted back to acyl-CoA by CPT2 before being translocated into the mitochondrial matrix. Finally, acyl-CoA undergoes β-oxidation to generate acetyl-CoA, which enters the TCA cycle. The reaction also produces reduced nicotinamide adenine dinucleotide (NADH) and reduced flavin adenine dinucleotide ($FADH_2$), co-enzymes which are oxidised during oxidative phosphorylation to generate ATP.

ii) Regulation of fatty acid metabolism

One important factor regulating the rate of FA oxidation is the intracellular level of malonyl-CoA, which acts as an endogenous inhibitor of CPT1, the rate limiting enzyme in the β-oxidation pathway (Dyck and Lopaschuk, 2002). The consequence of high levels of malonyl-CoA is a reduction of mitochondrial FA oxidation.

The level of malonyl-CoA is determined by energy demand and its rates of synthesis and degradation. Malonyl-CoA is an intermediate of *de novo* FA synthesis, and is produced by the carboxylation of acetyl-CoA by the acetyl-CoA carboxylase (ACC). In turn, ACC is regulated by the 5'-AMP activated protein kinase (AMPK), a kinase which modulates the activity of a number of metabolic enzymes involved in regulating both FA and glucose metabolism (Dyck and Lopaschuk, 2002; Jaswal *et al.*, 2011). AMPK is activated under conditions of high metabolic demand (i.e. when AMP/ATP ratio becomes high) (van

Bilsen *et al*., 2004). The subsequent AMPK-dependent phosphorylation of ACC inhibits its activity, reducing the synthesis of malonyl-CoA and promoting β-oxidation (Jaswal *et al.*, 2011).

In addition to regulation by malonyl-CoA, the overall rate of FA metabolism and utilization in the myocardium is also influenced by the activities of the enzymes involved in the β-oxidation pathway. Many of the enzymes involved in the metabolism of FA, for example, acyl-CoA dehydrogenase and 3-hydroxyacyl-CoA dehydrogenase, are regulated by levels of their own metabolic products such as NADH, FADH and acetyl-CoA (Jaswal *et al.*, 2011).

Finally, the rate of β-oxidation is further regulated by circulating free FA concentration in the plasma. Increase in the activity of the sympathetic nervous system elevates the rate of adipose tissue lipolysis, which raises the levels of free FA in the plasma. This increases the availability of circulating free FA to the heart, thereby stimulating uptake into the myocardium (Jaswal *et al*., 2011).

5.2.3 Glucose metabolism in the heart: Regulation of glucose metabolism through glycolysis

Glycolysis represents the major pathway in glucose use. This pathway consists of an energy investment phase and an energy payoff phase. The products of glycolysis are 2 pyruvate, 2 NADH and a net of 2 ATP per one molecule of glucose.

The flux through glycolysis is regulated at multiple levels along the pathway. The first regulatory step involves the supply of glucose, either by breakdown of existing glycogen

stores or by uptake of exogenous glucose (Depre *et al.*, 1998). Glucose transport from the blood into the cardiomyocyte is facilitated by its diffusion across the membrane via glucose transporters (GLUTs) and is a rate limiting step of the initiation of glycolysis. In the heart, GLUT1 and GLUT4 are the two major isoforms expressed. GLUT1 mediates insulin-independent glucose uptake and is responsible for maintaining basal level of glucose transport (Shao and Tian, 2015). GLUT4 mediates glucose uptake in an insulin-sensitive manner and accordingly, its expression is altered in response to blood insulin levels (Kolwicz and Tian, 2011). Once in the cytosol, glucose is rapidly and irreversibly phosphorylated by hexokinases (HKs) to glucose 6-phosphate, which can either be metabolised via glycolysis or stored as glycogen. This phosphorylation traps glucose in the cell for further metabolism, because only free glucose, but not phosphorylated glucose, can diffuse through the glucose transporters.

The phosphorylation of fructose 6-phosphate to fructose 1,6-bisphosphate commits glucose to glycolysis. Phosphofructokinase (PFK; muscle isoform PFKM), the enzyme which catalyses this reaction, is perhaps the most important control element in the glycolytic pathway (Berg *et al.*, 2002). As the enzyme that catalyses a rate limiting step in glycolysis, PFK sets the pace of glucose metabolism. Furthermore, its function is allosterically inhibited by high levels of ATP whereas it is enhanced by high levels of AMP (Berg *et al.*, 2002; Jaswal *et al.*, 2011). Finally, the activity of PFK is also inhibited by acidic pH, which would occur in the event of excess lactic acid accumulation due to anaerobic respiration (Berg *et al.*, 2002). Of note, the inhibition of PFK also leads to the inhibition of HKs, as the latter are regulated by levels of glucose-6-phosphate.

Pyruvate kinase catalyses the third irreversible and final step of glycolysis, and controls the outflow from this pathway (Berg *et al.*, 2002). The enzyme converts phosphoenolpyruvate to pyruvate, along with one molecule of ATP. This reaction is a committed step leading to either oxidative phosphorylation of pyruvate or its metabolism by anaerobic respiration (Jurica *et al.*, 1998).

5.2.4 The metabolic fate of pyruvate

i) Pyruvate to acetyl-CoA

Pyruvate, the end-product of glycolysis, can be metabolised further to either acetyl-CoA, lactate or alanine (*see* Figure 5.3 schematic). Under aerobic conditions, most of the pyruvate is carried into the mitochondria where it is decarboxylated and oxidised into acetyl-CoA by the enzyme pyruvate dehydrogenase (PDH) (Depre *et al.*, 1998).

Both FA oxidation and pyruvate metabolism contribute acetyl-CoA as substrate for the TCA cycle. The aim of the TCA cycle is to produce NADH and $FADH_2$ for the generation of ATP during oxidative phosphorylation (Fernie *et al.*, 2004). These reducing equivalents donate electrons which are passed via four electron transport chain (ETC) complexes to oxygen, the ultimate electron acceptor. This process simultaneously translocates protons into the inter-membrane space of the mitochondria and the resultant proton motive force is used to drive the ATP synthase for generation of ATP (Fernie *et al.*, 2004; Lodish *et al.*, 2000).

ii) Pyruvate to lactate

When oxygen supply to the heart is decreased or inadequate, glycolysis becomes a very important source of ATP (Jaswal *et al.*, 2011). Several mechanisms exist to divert metabolic flux towards the anaerobic pathway. Hypoxia, and the consequent stabilization of the hypoxia inducible factor (HIF), increases the expression of the lactate dehydrogenase (LDH) enzyme, which mediates the reduction of pyruvate to lactate. Furthermore, PDH activity is inhibited by the up-regulation of the HIF-target enzyme pyruvate dehydrogenase kinase (PDK), thereby decreasing the supply of acetyl-CoA to the TCA cycle.

Additionally, aerobic respiration is restricted further at the FA level. The malonyl-CoA decarboxylase (MCD) is under the transcriptional control of the transcription factor peroxisome proliferator activated receptor-α (PPARα), which is down-regulated in hypoxia. A decrease in MCD results in an increase in malonyl-CoA accumulation, which inhibits FA metabolism and further production of acetyl-CoA.

A 16-carbon FA, such as palmitic acid, is capable of generating approximately 129 ATPs. On the other hand, a single molecule of glucose generates 26-30 ATPs or 2 ATPs when metabolised to lactate. Although a shift in substrate preference towards glucose may initially be an adaptive response to altered cellular environment (i.e. workload or hormones), a chronic decline in FA oxidation may not be fully compensated for by an increase in glucose oxidation, thereby imposing a burden on the ATP generating capacity in the myocardium (van Bilsen *et al*., 2004). This is particularly relevant in the context of cardiac pathology, as will be discussed in the next section.

iii) Pyruvate to alanine

The third metabolic fate of pyruvate is its conversion to alanine. In a process known as the Cahill cycle, pyruvate is transaminated to alanine by the enzyme alanine aminotransferase (ALAT1). Alanine is then released into circulation, taken up by the liver where it is converted back to glucose (Taegtmeyer *et al.*, 1977).

5.2.5 Metabolic state in the diseased heart

Perturbations in metabolism are recognised as an integral feature of heart failure. Significant changes in cardiac metabolism and impairment of energetic status have been shown to contribute to the development and progression of myocardial injury (Noordali *et al.*, 2017).

There is a wealth of evidence showing that the pathological remodelling of the heart is accompanied by a shift in substrate preference away from FAs to glucose (van Bilsen *et al.*, 2004; Kolwicz *et al*., 2013). Since the amount of ATP produced through glycolysis is substantially less than that produced through β-oxidation, chronic down-regulation of FA metabolism would predict that the failing myocardium is chronically energy starved. This phenomenon was first reported by Herrmann and Decherd in 1939, where they observed a significant reduction in creatine in the failing myocardium. This observation was further developed by Neubauer (2007), who described the failing heart as an "engine out of fuel," asserting that altered energetics played a crucial role in the mechanism and progression of left ventricular dysfunction and ultimately heart failure. Indeed, it has been observed in the both humans and animal models, a 30% reduction in ATP in the failing myocardium compared to a healthy heart (Ingwall, 2009a). This reduction in metabolic reserve is likely

to cause disruptions in normal cardiac processes, such as contractility, which is a major ATP consuming pathway in the cardiac myocytes.

Several studies have suggested that the enhancement of glycolysis in the failing heart may be related to changes in the expression of genes encoding for proteins involved in substrate transport and metabolism (van Bilsen *et al*., 2004). A down-regulation of the PPARα-mediated transcription of FA oxidation enzymes and mitochondrial biogenesis has been observed in parallel to a decrease in β-oxidation (Kolwicz *et al*., 2013). Similarly, the activity and distribution of the glycolytic enzymes HK and LDH have been found to be altered in the hypertrophied myocardium (van Bilsen *et al*., 2004; Taegtmeyer and Overturf, 1988). Additionally, hypertrophy and heart failure were associated with a reduction in the expression of *Glut4* and an increase of *Glut1*, possibly as part of the fetal gene reprogramming which occurs during pathological remodelling of the heart (Shao and Tian, 2015).

Furthermore, in rat models of transaortic constriction, severe end-stage heart failure was accompanied by a depression in overall oxidative metabolism (Bugger *et al.*, 2010; Jaswal *et al.*, 2011). Clinically, in the hearts of patients with dilated cardiomyopathy, a reduction in the rates of both FA uptake from the plasma and β-oxidation were decreased and the rate of glucose uptake and lactate synthesis was increased (Jaswal *et al.*, 2011; Neglia *et al*., 2007).

5.2.6 Mitochondrial structural damage and metabolic dysfunction

A chronic shift in metabolism can cause deleterious changes in mitochondrial structure. Accumulation of FA due to a reduction in β-oxidation and build-up of protons following lactate oxidation can alter cellular pH. Oxidative stress follows the acidification of the cellular environment and promotes the production of reactive oxygen species which damage both the mitochondrial membrane and important mitochondrial proteins (Noordali *et al*., 2017). Mitochondrial deformities are often observed in heart failure, with electron tomography showing an overall disarray in structure and decrease in cristae surface (Rosca *et al*., 2013). These structural abnormalities are typically accompanied by a decrease in oxidative capacity of the heart, which, in a continuous feedback loop, exacerbate mitochondrial failure (Jaswal *et al*., 2011; Rosca *et al*., 2013).

5.2.7 Metabolism in altered iron status

Iron is a functional component of various metabolic enzymes, raising the possibility that iron status and metabolism may be interconnected. Oexle *et al.*, (1999) investigated the effects of an altered iron status on metabolism in the human K-562 bone marrow cell line. Iron depletion, induced by treatment of cells with the iron chelator desferrioxamine (DFO), resulted in a decrease in the activities of TCA enzymes citrate synthase, isocitric dehydrogenase, succinate dehydrogenase and aconitase. In particular, the activity of aconitase was decreased via a translational mechanism involving the iron regulatory protein (IRP) pathway, whereby the conversion of IRP1 to aconitase is inhibited by a reduction in iron bioavailability (*see* Chapter 1, Figure 1.3).

Furthermore, iron depletion led to a reduction in the formation of NADH by the TCA cycle. Consequently, a decrease in mitochondrial oxygen consumption and ATP production via the oxidative phosphorylation was reported. In addition, a significant increase in glucose uptake from the blood, enhanced glycolysis and increased lactate formation was observed in the presence of DFO. By contrast, iron supplementation had the opposite effect, increasing oxidative metabolism and decreasing glucose uptake and downstream glycolytic pathway, thus revealing a relationship between iron homeostasis and cellular energy metabolism.

5.2.8 Magnetic resonance spectroscopy and dynamic nuclear polarization

The assessment of the metabolic profile of the heart is an important first step in understanding the alterations in cardiac energetics that occur in the pathological state. This approach also provides new insight for diagnosis and treatment of the disease.

For nearly a century, spectroscopic techniques have been used to determine enzyme activities or metabolite concentration in crude tissue lysates (Dodd *et al.*, 2013). The advent of technologies such as ^{1}H-nuclear magnetic resonance (NMR), gas chromatography-mass spectrometry (MS) and liquid chromatograpy-MS have enabled researchers to detect metabolite concentrations at the millimolar to sub-picomolar levels in a sample. In addition, the use of ^{13}C magnetic resonance spectroscopy (MRS) has made it possible to label and observe the metabolism of an extensive range of metabolites. However, traditional ^{13}C MRS is inherently insensitive and is limited by the low signal-to-noise ratio when imaging is attempted *in vivo* (Dodd *et al.*, 2013; Le Page *et al.*, 2016;

Miller *et al.*, 2016). Thus, the technique has been mostly used in *ex vivo* perfused heart models.

Furthermore, although these methods provide valuable metabolomic insight, they are limited in that they require the collection of tissues from animals, terminating the experiment at specific time points. Therefore, serial measurements aimed at monitoring the progression of disease are not possible.

The above limitation can be circumvented by using a hyperpolarization technique coupled with MRS, which increases the sensitivity of the MR spectra by more than 10,000-fold that of traditional ^{13}C MRS (Dodd *et al.*, 2013; Le Page *et al.*, 2016; Schroeder *et al.*, 2011). Hyperpolarised ^{13}C-labelled compounds, via dynamic nuclear polarization (DNP), can be injected *in vivo* and their metabolism can be visualised in real-time.

One example of a routinely used DNP hyperpolarised molecule is the [1-^{13}C]pyruvate. As previously discussed, pyruvate can be acted upon by three enzymes: PDH, LDH and alanine aminotransferase (ALAT). The transfer of ^{13}C to bicarbonate represent the flux through PDH and the transfer of ^{13}C to lactate and alanine provides a measure of the balance between anaerobic glycolysis and glucose oxidation (Dodd *et al.*, 2013; Le Page *et al.*, 2016; Miller *et al.*, 2016).

The Department of Physiology, Anatomy and Genetics at the University of Oxford is home to a high resolution 7 T MRS system, custom-tailored for imaging of mouse hearts. This MRS system has been used this chapter for *in vivo* metabolomics work and the methods are outlined in the *Methods* section of this chapter.

5.2.9 Study aims

Metabolic remodelling is a well-established pathology of the diseased heart. Given that an impairment of cardiac function was observed following an iron-deficient diet, it is possible to postulate that metabolic perturbations may have occurred in the heart of iron-deficient mice. In addition, RNA-seq analysis identified a differential regulation in various metabolic pathways in the 6 week model of iron deficiency. Therefore, the aim of this chapter was to gain insight into the effects of an iron-deficient diet on cardiac energetics. To achieve this aim, the metabolic state of the iron-deficient mouse model was studied using a combination of spectroscopic and hyperpolarised MRS techniques.

5.3 METHODS

5.3.1 Animal model

Mice used in this study correspond to cohorts 2, 3 and 1 (6 week, 9 week and 24 week on diet, respectively) described in Chapter 3. At each time-point, six iron-adjusted and six iron-deficient were MRI scanned as described in Section 5.3.3.

5.3.2 Blood sampling

At the 6, 9 and 24 week time point, approximately 0.6 μL of blood was sampled from the tail vein for measurement of blood glucose concentration using the FreeStyle Optimum blood glucose meter. Blood samples were collected between 7 a.m. and 8 a.m. in the fed state to reduce fluctuations in blood glucose concentrations due to feeding vs fasting.

5.3.3 Dynamic Nuclear Polarization (DNP)-hyperpolarised-$^{13}C_1$ MRS

The methods in this section have been published in Dodd *et al.*, (2013) and have been adapted below. The MRS system and position of animal are shown in Figure 5.1.

Animal handling. All scans were performed between 7 a.m. and 1 p.m., during the early absorptive state (fed state). Anaesthesia was initially induced at 3% isoflurane in a 2 L/min flow of 4:1 oxygen:nitrous oxide mixture. A catheter with a 32 G needle was inserted into the tail vein for intravenous infusion of hyperpolarised solutions. The animal was then placed into a home-built animal cradle and body temperature was maintained via a warm air flow through a home-built heat-exchanger placed on either side of the animal. A circular custom-built ^{13}C RF surface transmit/receive coil with a 10 mm radius was placed

on the chest over the heart and secured with surgical tape. ECG probes were inserted into each forepaw and monitored throughout the experiment.

Pyruvate polarization and dissolution. Approximately 40 mg of [1-^{13}C] pyruvic acid doped with 15 mM trityl radical (OXO63, Oxford Instruments) and 3 μL Dotarem (1:50 dilution) (Guerbet), was hyperpolarised in a General Electric Protoype Polarizer (GE Healthcare) with 45 mins of microwave irradiation. The sample was then dissolved for 20 mins in a pressurised and heated alkaline solution, containing 60 mM sodium hydroxide and 247 mM EDTA dipotassium salt (Sigma-Aldrich). This yielded an 80 mM solution of hyperpolarised sodium [1-^{13}C]pyruvate with a polarization of approximately 30% at physiological pH and temperature.

Hyperpolarised ^{13}C MRS protocol. The sensitivity profile of the RF coil was previously tested in Dodd *et al.* (2013). For scanning, the mouse was positioned in a 7 T (300 MHz) horizontal bore MR scanner interfaced to a direct-drive console (Varian Inc). Using a 72 mm ^{1}H volume transmit/receive RF coil (Rapid Biomedical), a 3-plane FLASH localizer image was obtained to confirm the location of the heart at the magnet isocenter. A fiducial marker containing water, positioned on top of the ^{13}C RF coil, was used to ensure the correct position of the ^{13}C RF coil over the heart. Using the ^{1}H volume coil, an ECG-gated shim was used to reduce the proton linewidth to approximate 150 Hz.

Following dissolution, 150 μL of hyperpolarised pyruvate was injected over 10 secs into the mouse, followed by a 50 μL flush of heparinized saline to clear the delivery line. Sixty individual ECG-gated ^{13}C MR pulse-acquire cardiac spectra were acquired over 2 mins following injection. The frequency was centred on the C_1 pyruvate resonance.

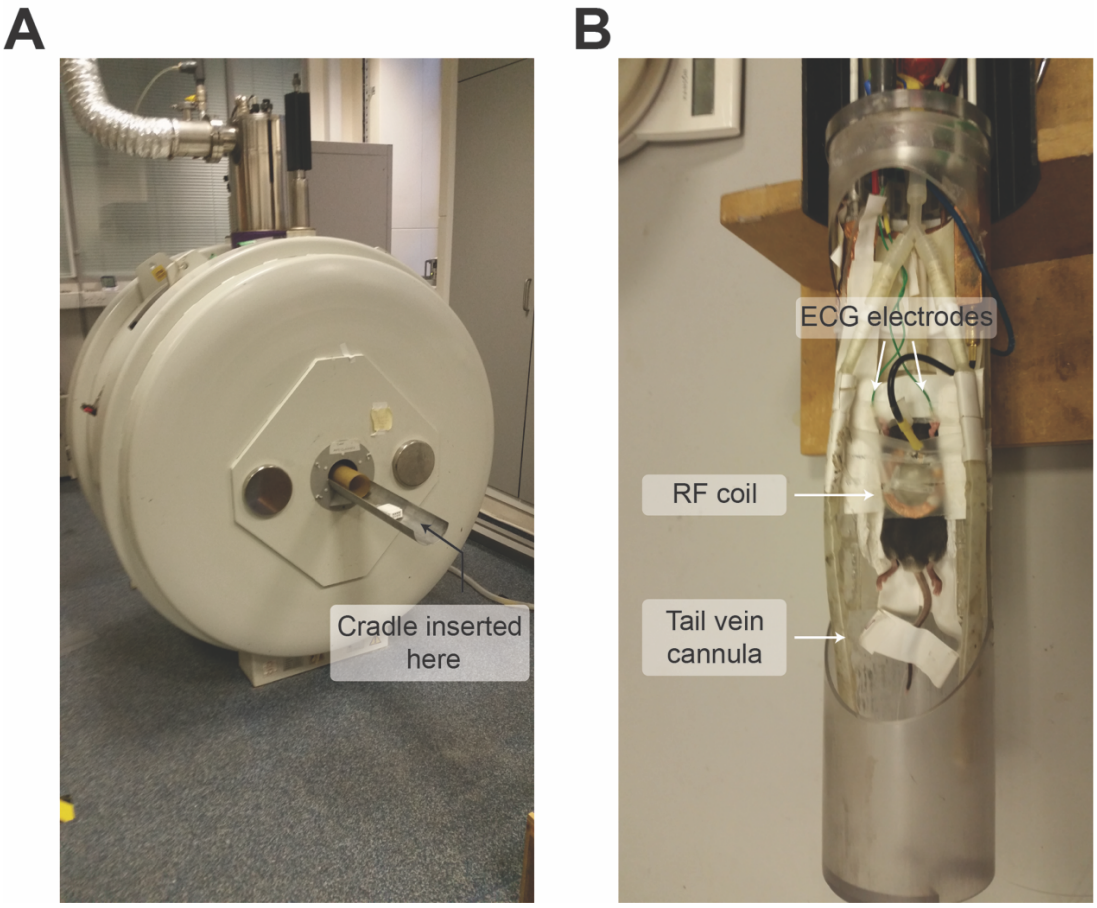


Figure 5.1 Hyperpolarised DNP MRS setup. A) The horizontal bore, high resolution 7 T MR system; B) Custom-built mouse cradle with mouse positioned, ready for scanning.

Analysis. ^{13}C spectra were analysed using the AMARES algorithm in the jMRUI software package. Spectra were DC offset-corrected based on the last half of acquired points. A kinetic model was obtained by quantification of the peak areas of [1-^{13}C]pyruvate, [1-^{13}C]lactate, [1-^{13}C]alanine and [1-^{13}C]bicarbonate at each time point and normalised to the peak area of [1-^{13}C]pyruvate.

5.3.4 Quantitative real-time PCR

Preparation of template. Genomic DNA (gDNA) or total RNA was extracted from frozen cardiac tissue using the Qiagen DNA Extraction kit or the RNeasy mini kit, respectively, following manufacturer's instructions.

Mitochondrial copy number assay. Mitochondrial (mt) copy number was determined as a ratio of mtDNA:gDNA. The mt primer is located within the *Nd4* gene in the mitochondrial genome, which encodes for the NADH dehydrogenase 4 protein. The genomic primer was designed to span the exon-intron junction of the β-actin genomic sequence. The qPCR reaction was run in a 10 μL total reaction mixture containing 20 ng gDNA template, 0.5 μl of each primer (stock 10 μM) and 5 μL of PowerUp SYBR Green Master Mix (Life Technologies). The primer sequences used in this assay can be found in Table 6.1.

qPCR for metabolic HIF target genes. The following Taqman probes were used for these assays: *Hk2* (Mm00443385), *Glut1* (Mm00441480), *Glut4* (Mm00436615), *Pdk1* (Mm00554300), *Pdk4* (Mm01166879), *Ldha* (Mm01612132), *Alat1* (Mm00805379) and *Pfkm* (Mm01309576). β-actin was used as the housekeeper gene.

SYBR Green qPCR was conducted for the detection of *Eno1* and *Gapdh* gene expression. The primer sequence used in this assay can be found in Table 5.1.

Table 5.1 List of primers used in this chapter.

Primer	Sequence	Concentration
mtDNA	F – CCAACTACGAACGGATCCACA R – TGATTGAAGGGGGTAGAGCTAGA	300 nM
gDNA	F – TAGGGTCCGGGCCTCGAT R – TGTCTCGGTTACTAGGCCTGC	300 nM
Eno1	F – TGCGTCCACTGGCATCTAC R – CAGAGCAGGCGCAATAGTTTTA	500 nM
Actb	F – CGTGAAAAGATGACCCAGATCA R – TGGTACGACCAGAGGCATACAG	500 nM

5.3.5 Measurement of serum free fatty acid concentration

To determine the free fatty acid concentration in the serum, the Free Fatty Acid Quantification Assay Kit (Colorimetric/Fluorometric) kit was used (ab65341, Abcam) following manufacturer's instructions for colorimetric measurement. The assay was conducted in technical duplicates.

5.3.6 Western blot

Protein lysate was prepared from crushed, frozen heart tissue using 8 M urea lysis buffer supplemented with complete protease inhibitor. The tissues were sonicated to clear the chromatin and protein concentration was measure using the BCA Protein Assay (Thermo Fisher) and a 9-point BSA standard, following manufacturer's instructions.

For SDS-PAGE, 100 μg of protein lysate was loaded onto a 12% gel. The gel was transferred onto a PVDF membrane for 1.5 h. The antibodies used for western blotting are listed in Table 6.2. HIF-2α antibody was obtained from the Ratcliffe group at the Francis Crick Institute.

Table 5.2 List of antibodies used in this chapter.

Antibody	Product code (Manufacturer)	Concentration
rb-COX4	NB110-39115 (Novus Biological)	1:1,000
ms-COX4 isoform 2	H00084701-M01 (Novus Biological)	1:500
rb-HIF-1α	NB100-479 (Novus Biological)	1:1,000
ms-HIF-2α	Ab190b (un-purified mouse sera)	1:5
ms-β-actin	NB100-74340 (Novus Biological)	1:4,000
gt-anti ms-HRP	sc-2031 (Santa Cruz)	1:10,000
gt-anti rb-HRP	sc-2030 (Santa Cruz)	1:10,000

ms = mouse
rb = rabbit
gt = goat

5.3.7 Mitochondrial complex assays

The methods in this section are published in Lakhal-Littleton *et al.*, (2016) and have been reproduced, with permission, below.

Preparation of homogenates. Approximately 10 mg of frozen, crushed tissues were suspended in 200 µL of ice-cold KME buffer (in mM): 100.0 KCl, 50.0 Mops, 0.5 EGTA and pH 7.4 at room temperature with NaOH. Samples were homogenized by rupturing with a TissueRuptor (Qiagen) over ice and used immediately to measure the activities of mitochondrial complexes I, II, III, and IV. Protein concentration was measured using the BCA Protein Assay (Thermo Fisher), following manufacturer's instructions.

Mitochondrial complex I assay. Mitochondrial complex I activity was measured as the rate of NADH oxidation at 340 nm and 30 °C using a spectrophotometer. The assay buffer contained the following (in mM, unless otherwise specified): 25.0 potassium phosphate

pH 7.2, 5.0 $MgCl_2$, 0.13 NADH (MP Biomedicals, LLP), 3.65 antimycin A (Santa Cruz), 65 μM coenzyme Q1 (Sigma-Aldrich) and 250 mg fatty acid free BSA (Sigma-Aldrich). The reaction was carried out in 1 mL assay buffer supplemented with 20 μL of protein lysate and read for 1 min at 340 nm against a blank containing ddH_2O. As a negative control, 200 μM of rotenone (Sigma-Aldrich) was added to a new reaction and the inhibited rate measured for 1 min. The activity of complex I was determined by dividing the gradient of the absorbance change over the extinction coefficient (6810 $nmol \cdot min^{-1}$) and expressed in $nmol \cdot min^{-1} \cdot mg\ protein^{-1}$.

Mitochondrial complex II assay. Mitochondrial complex II activity was measured as the rate of succinate-dependent reduction of dichlorophenolindophenol (DCIP) at 600 nm and 30 °C using a spectrophotometer. The assay buffer contained the following (in mM): 25.0 potassium phosphate pH 7.2, 5.0 $MgCl_2$, and 2.0 sodium succinate dibasic hexahydrate (Sigma-Aldrich). The reaction was carried out in 985 μL of assay buffer supplemented by 10 μL of buffer containing 365 μM antimycin, 50 μM DCIP (Sigma-Aldrich) and 500 μM rotenone, followed by addition of 65 μM CoQ_1 and 20 μL protein lysate and read for 2 mins at 600 nm against a blank containing ddH_2O. As a negative control, 200 μM of sodium malonate (Sigma-Aldrich) was added to a new reaction and the inhibited rate measured for 2 mins. The activity of complex II was determined by dividing the gradient of the absorbance change over the extinction coefficient (21000 $nmol \cdot min^{-1}$) and expressed in $nmol \cdot min^{-1} \cdot mg\ protein^{-1}$.

Mitochondrial complex III assay. Mitochondrial complex III activity was measured as the rate of reduction of cytochrome c^{3+} at 550 nm and 30 °C using a spectrophotometer and reduced ubiquinol as an electron acceptor.

Preparation of reduced ubiquinol. Ubiquinol was prepared as follows: 10 mg of decylubiquinone (Sigma-Aldrich) was dissolved in 312.5 µL absolute ethanol to give a final concentration of 100 mM. An aliquot of 100 µL decylubiquinone working solution was further diluted in 900 µL ethanol and acidified to pH 2 with a 6 M HCl solution. The pH was checked with a pH indicator paper. The ubiquinone was then reduced with a pinch of sodium borohydrate (Sigma-Aldrich) and 1 mL of ddH_2O was added to stop the reaction. Excess sodium borohydrate was allowed to settle and the sample centrifuged briefly to separate the sodium borohydrate precipitate from the reduced ubiquinol. Using a pH indicator paper, the pH of the ubiquinol was verified to be at pH 2 before using in the activity assay.

Activity assay. The assay buffer contained the following (in mM, unless otherwise specified): 50.0 potassium phosphate pH 7.2, 3.0 sodium azide (Sigma-Aldrich), 1.5 µM rotenone, and 50 µM cytochrome c from bovine heart (Sigma-Aldrich). The reaction was carried in 1 mL of assay buffer, supplemented with 5 µL reduced ubiquinol and 20 µL protein lysate and read for 1 min at 550 nm against a blank containing ddH_2O. As a negative control, 200 µM of antimycin A was added to a new reaction and the inhibited rate measured for 1 min. The activity of complex III was determined by dividing the gradient of the absorbance change over the extinction coefficient (19100 $nmol \cdot min^{-1}$) and expressed in $nmol \cdot min^{-1} \cdot mg\ protein^{-1}$.

Mitochondrial complex IV assay. Mitochondrial complex IV activity was measured as the rate of oxidation of cytochrome c^{2+} at 550 nm and 30 °C using a spectrophotometer.

Preparation of reduced cytochrome c^{2+}. Preparation of the dialysis tubing was as follows: a dialysis tubing (Visking 7000/1) of appropriate length was hydrated for 30 mins in 1 L ddH_2O supplemented with 20 g sodium carbonate and 0.372 g EDTA at 80 °C. A solution of 100 mg of cytochrome c from bovine heart and 10 mg sodium ascorbate dissolved in 10 mL potassium phosphate (0.1 M, pH 7.0) was added to the tubing and dialysed against 1 L of 0.1 M potassium phosphate buffer for 24 hrs at 4 °C. The phosphate buffer was exchanged 3 times, every 8 hrs. The redox state of the synthesized reduced cytochrome c was verified by measuring the absorbance spectra between wavelengths of 500 and 600 nM, in the presence or absence of 100 µM potassium ferricyanide (Sigma-Aldrich) and compared against the oxidised cytochrome c.

Activity assay. The assay buffer contained 10 mM potassium phosphate pH 7.0 and 0.5 µM reduced cytochrome c. The reaction was carried out in 1 mL assay buffer supplemented with 5 µL protein lysate and read for 3 mins at 550 nm against a blank of assay buffer supplemented by 100 µM potassium ferricyanide. As a negative control, 10 µM of sodium azide was added to a new reaction and the inhibited rate measure for 3 mins. The first-order rate constant (k) was calculated as previously described (Brooks *et al.*, 2000). Briefly, the natural logarithm was taken for the absorbance at the time points t = 0, 60, 120, 180 seconds and the difference for each pair of time points determined (t(60)-t(0), t(120)-t(60), t(180)-t(120)). The average of these differences were taken to be k and the activity expressed in $k \cdot min^{-1} \cdot mg\ protein^{-1}$.

Aconitase assay. Aconitase activity was measured as the rate of isomerization of cis-aconitic acid to isocitrate at 240 nm and 37 °C using a spectrophotometer. The reaction was carried out in 1 mL assay buffer containing 50 mM Tris-HCl, pH 7.5 with NaOH supplemented with 200 μM cis-aconitic acid solution and 5 μL protein lysate in a quartz cuvette and read for 2 mins at 240 nm against a blank containing ddH_2O. The activity of aconitase was determined by dividing the gradient of the absorbance change over the extinction coefficient (3600 $nmol \cdot min^{-1}$) and expressed in $nmol \cdot min^{-1} \cdot mg\ protein^{-1}$.

5.3.8 Transmission electron microscopy (TEM)

Primary fixation. Fresh tissues or isolated cardiomyocytes were fixed in 2.5% glutaraldehyde made in 1X PBS, overnight at 4 °C. The fixative was removed and replaced with a 0.25% glutaraldehyde solution and kept at 4 °C until further processing.

Secondary and tertiary fixation. Tissues were rinsed 5 times in 1X PBS, 15 mins each wash, then fixed in 1% osmium tetroxide (OsO_4; TAAB Laboratories) in 1X PBS at 4 °C for 2 hrs with gentle rotation. Samples were rinsed 5 times in ddH_2O, 15 mins each wash and fixed in 0.2% uranyl acetate (Agar Scientific) overnight at 4 °C in the dark. Samples were washed once in ddH_2O for 10 min.

Preparation of specimen and embedding. For dehydration of specimen, samples were washed, for 15 mins at 4 °C, in 30%, 50%, 70%, 80%, 90% and 95% EtOH. Samples were then incubated 3 times in 100% dry EtOH at 4 °C, 30 mins each incubation step. For resin infiltration, samples were incubated in 2:1 100% dry EtOH:TAAB TLV resin (TAAB Laboratories) for 2 hrs, 1:1 100% dry EtOH:TAAB TLV resin for 3 hrs and 1:2 100% dry

EtOH:TAAB TLV resin for 2 hrs with gentle rotation. Samples were then incubated in 100% TAAB TLV resin for 48 hrs at room temperature. During this time, the resin was changed every 8 hrs.

Tissue pieces were transferred to Beem capsules filled with fresh 100% TAAB TLV resin and polymerized overnight at 60 °C.

Sectioning. Samples were sectioned on the Leica UC7 ultramicrotome. Resin blocks were faced-up using a glass knife in preparation for ultra-thin sectioning. For ultra-thin sectioning, 90 nm thin sections were cut using a diamond knife (Diatome) and transferred to a 200 mesh Cu grid (TAAB Laboratories). Between 4 and 6 sections were cut per sample block.

Transmission Electron Imaging (TEM). Prior to imaging, grids were post-stained with Reynold's lead citrate for 5 mins, and washed 3 times in ddH_2O and air-dried overnight.

TEM imaging was performed at 120 kV on the FEI Tecnai 12 and images acquired using the Gatan OneView CMOS camera with Digital Micrograph 3.0 software.

5.4 RESULTS

5.4.1 Acquisition of [1-C^{13}]pyruvate spectra in the *in vivo* mouse heart

To gain insight into the metabolic state of the heart following an iron-deficient diet, the fate of pyruvate was examined *in vivo* using hyperpolarised MRS on live mice.

A typical set of spectra from a control fed mouse is shown in Figure 5.2. Each spectra shows the injected [1-C^{13}]pyruvate along with [1-C^{13}]lactate, [1-C^{13}]alanine and [1-C^{13}]bicarbonate with 1 second temporal resolution (Figure 5.2A). [1-C^{13}]pyruvate hydrate can also be visualised in the NMR spectra, but it is not metabolically active and is spontaneously formed under physiological pH of the injection solution (Golman *et al.*, 2006).

Bicarbonate is the product of the conversion of CO_2 by the carbonic anhydrase (Ca9) enzyme. CO_2 is produced as a by-product of the decarboxylation of pyruvate to acetyl-CoA by PDH (*see* Figure 5.3 schematic). Due to the low signal-to-noise ratio of the $^{13}CO_2$ peak and a rapid exchange into [1-C^{13}]bicarbonate, $^{13}CO_2$ is difficult to visualize in the NMR spectra. Therefore, the flux through PDH is instead assessed as the rate of ^{13}C label transfer from pyruvate to bicarbonate (Figure 5.3C).

Similarly, the conversion of pyruvate to lactate and alanine was assessed as the rate of ^{13}C label transfer from pyruvate to lactate and alanine, respectively. Of note, because lactate dehydrogenase is an equilibrium enzyme, lactate production is increased in when pyruvate concentration levels that exceed the catalytic capacity of PDH (Heigenhauser and Parolin, 1999). For this reason, the rate of ^{13}C incorporation to lactate appears to be 10-fold greater

than that of bicarbonate, but is not a reflection of the endogenous metabolic profile of the heart.

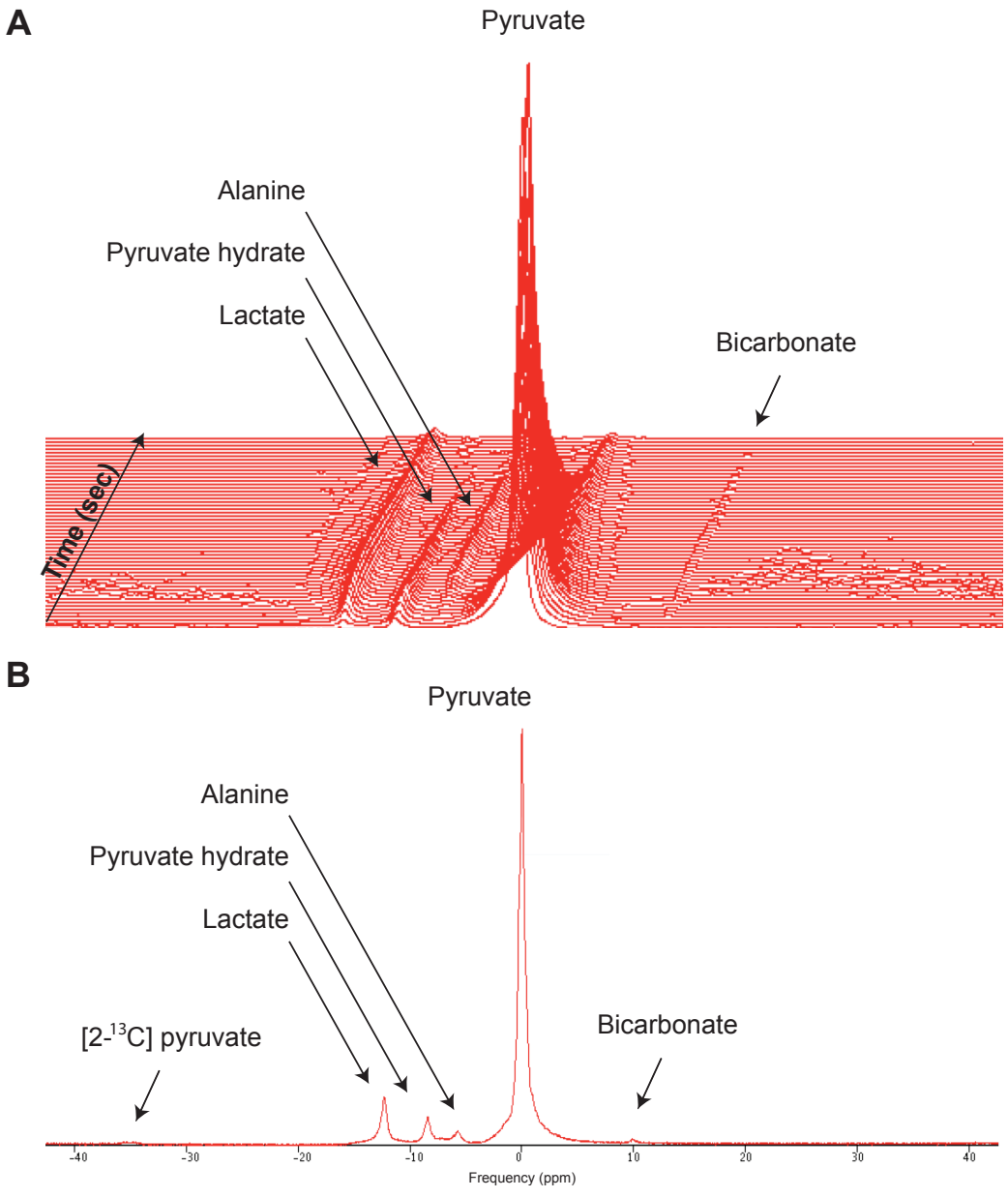


Figure 5.2 Example mouse spectra of [^{13}C]pyruvate. A) Example spectra in a fed mouse on an iron-adjusted diet for 24 weeks. Every line represents 1 sec; B) Summed spectrum of 30 individual spectra from a fed mouse on an iron-adjusted diet for 24 weeks.

The ^{13}C incorporation kinetics to each of the three products of pyruvate was determined in the following way. First, an average time course was fitted to the peak areas of pyruvate, lactate, alanine and bicarbonate. Then, the curves were normalised to the peak pyruvate signal intensity to account for any differences in the initial polarization, injection volume and coil sensitivity. The incorporation kinetics were calculated based on the function of best fit to the time course and was obtained utilising an Excel solver sheet which was written by Dr Michael S. Dodd, Department of Physiology, Anatomy and Genetics, University of Oxford.

5.4.2 *In vivo* cardiac metabolism using hyperpolarised magnetic resonance spectroscopy

In the mice, ^{13}C label incorporation to bicarbonate was reduced by 72% and 55% following 6 and 9 weeks of diet (p = 0.04197 and 0.0409, respectively), but significantly increased by 44% following 24 weeks of diet (p = 0.0454). This suggests that at the first two time points, the activity of PDH may be reduced and at the 24 week time point, its activity is enhanced in the iron-deficient animals.

On the other hand, the conversion of pyruvate to lactate was significantly decreased in the iron-deficient animals following 6 and 9 weeks of diet compared to the iron-adjusted controls (45% and 62%, p= 0.0486 and p = 0.0460, respectively) and remained unchanged following 24 weeks of diet (p = 0.9506) (Figure 5.3B). The ratio of the ^{13}C incorporation kinetics of lactate and bicarbonate (Figure 5.3D) was significantly increased in the first two time points and significantly decreased at the 24 week time point (p = 0.0063, p = 0.0058 and p = 0.0059, respectively) indicating that in the earlier two time points, the

energetic state of the iron-deficient mice may have a preference for anaerobic metabolism. In contrast, aerobic metabolism appears to be favoured at the 24 week time point.

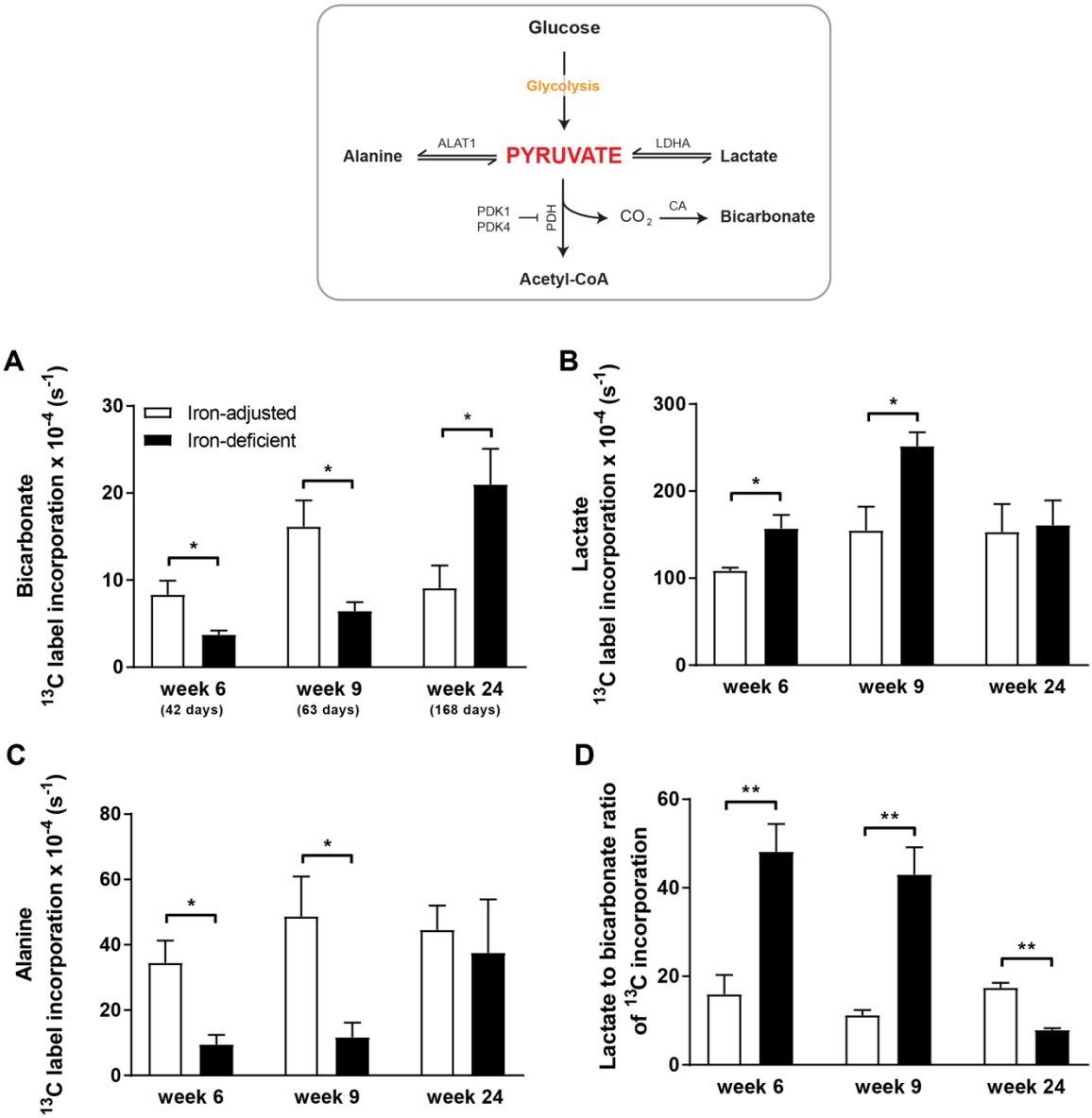


Figure 5.3 Fate of hyperpolarised pyruvate metabolism in iron-adjusted and iron-deficient mice. (top) Schematic of the metabolic fate of pyruvate; ^{13}C label incorporation into A) Bicarbonate, B) Lactate and C) Alanine. *x*-axis represents weeks (days) on diet. Data plotted as mean ± SEM. *p*-value determined by a two-tail, unpaired student's *t*-test; * $p < 0.05$. n = 5 or 6 mice per cohort.

Finally, the ^{13}C incorporation to alanine was decreased in the iron-deficient animals following 6 and 9 weeks of diet compared to the iron-adjusted controls (72% and 76%, $p = 0.0266$ and $p = 0.0490$, respectively) but not different following 24 weeks of diet ($p = 0.7110$) (Figure 5.3C). The formation of alanine from pyruvate is thought to be an alternative pathway of pyruvate metabolism which reduces its conversion to lactate (Piacentino *et al.*, 2003). Thus, a reduction in alanine formation is consistent with the observed increase in lactate formation at the 6 and 9 week time point.

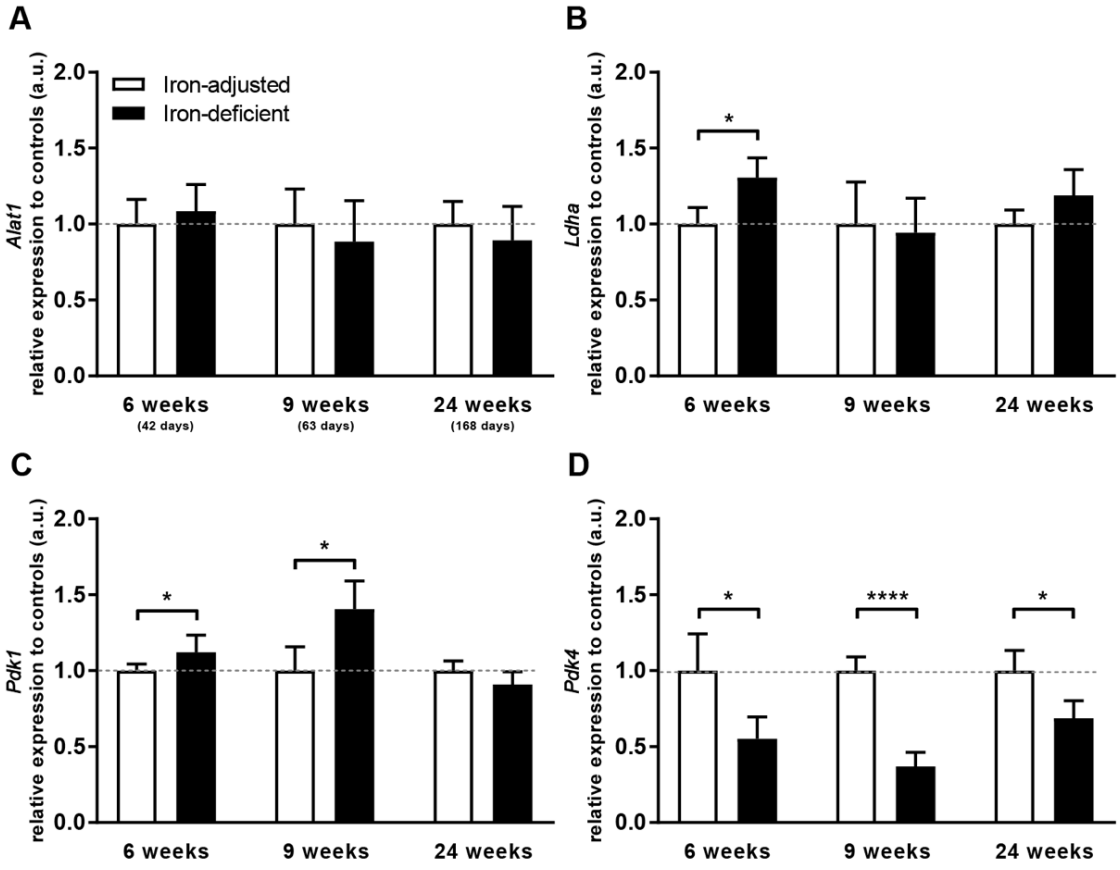


Figure 5.4 Gene expression of enzymes catalysing the conversion of pyruvate. Relative gene expressions of A) Alanine aminotransferase (*Alat1*), B) Lactate dehydrogenase A (*Ldha*), C and D) Pyruvate dehydrogenase kinase 1 (*Pdk1*) and 4 (*Pdk4*). x-axis represents weeks (days) on diet. Data plotted as mean ± SEM. *p*-value determined by a two-tailed, unpaired student's *t*-test; * $p < 0.05$, **** $p < 0.0001$. n = 9 mice (6 weeks) and 6 mice (9 and 24 weeks) per cohort.

5.4.3 Assessment of the gene expression of pyruvate-handling enzymes

To assess whether the observed alterations in pyruvate metabolism were attributable to changes in key metabolic enzymes that regulate the fate of pyruvate, the gene expression of *Alat1*, *Ldha, Pdk1* and *Pdk4* was assessed by qPCR (Figure 5.4 and *see* Figure 5.3 schematic).

The expression of *Alat1* was not altered at any of the time points surveyed. *Ldha* was up-regulated in the iron-deficient animals following 6 weeks of diet. *Pdk1* was up-regulated and *Pdk4* was down-regulated at the 6 and 9 week time point. Furthermore, *Pdk4* remained down-regulated following 24 weeks of diet. Both *Ldha* and *Pdk1* are HIF-target genes and *Pdk4* is a target of PPARα, which is down-regulated by HIF. These alterations in gene expression suggest HIF-stabilization.

5.4.4 Effect of systemic iron deficiency on HIF

The expression of additional HIF-target genes was assessed to further validate the presence of HIF (Figure 5.5). The HIF-target genes *Glut1* and *Eno1* were significantly up-regulated following 6 and 9 weeks of diet at the gene expression level, whereas the expression of *Glut4* and *Pfkm*, which are not under HIF regulation, remained unaltered by administration of an iron-deficient diet. At the 24 week time point, the only changes observed were a reduction in *Glut1* and an increase in *Glut4* expression.

Together with the apparent preference for anaerobic metabolism observed in Section 5.4.2, these results collectively implicate an active HIF presence in the hearts of iron-deficient mice at the 6 and 9 week time points.

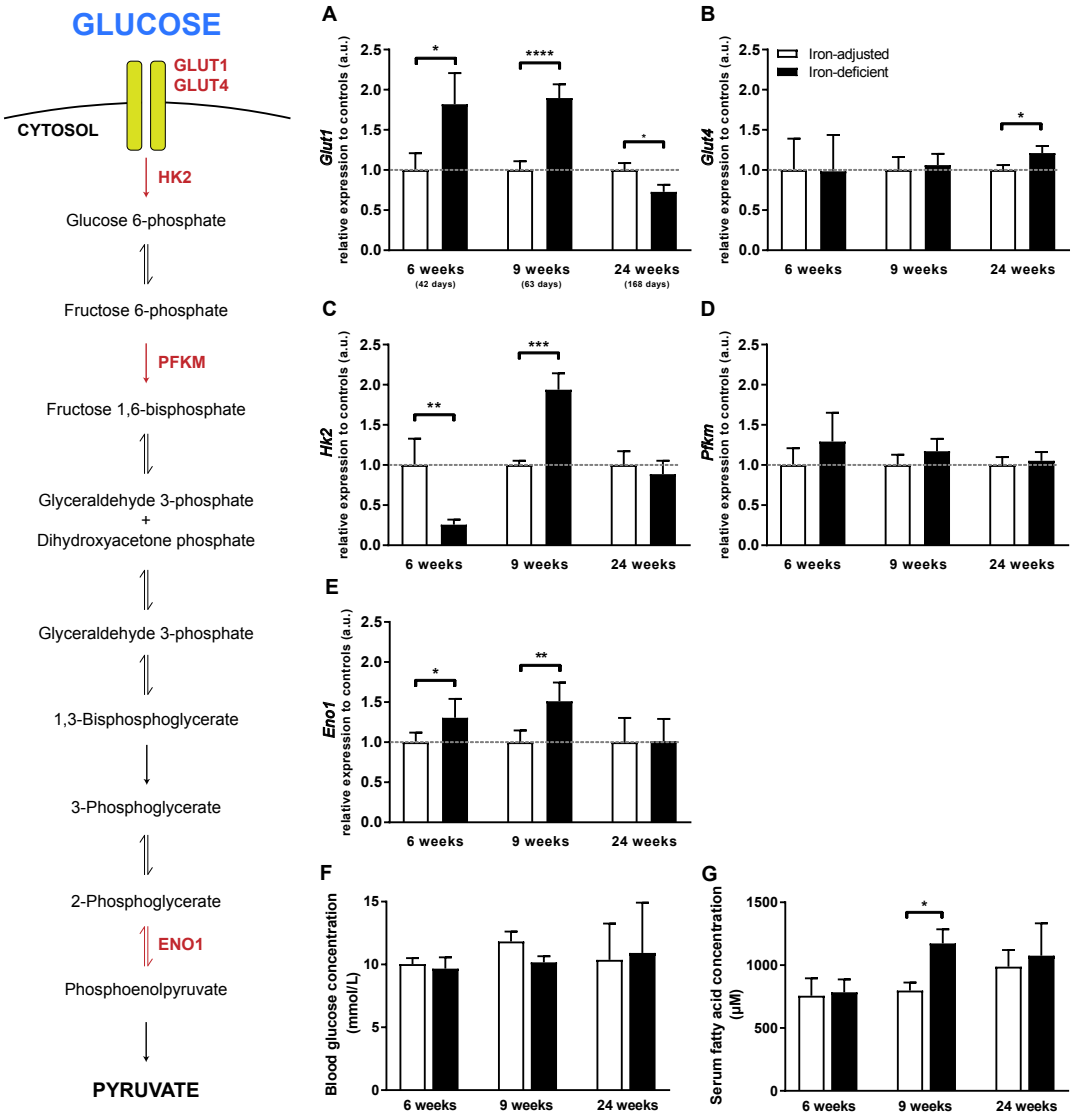


Figure 5.5 Gene expression of various glycolytic enzymes. (left) Schematic of glycolysis, starting from transport of blood glucose in the cytosol. A and B) Glucose transporter 1 (*Glut1*) and 4 (*Glut4*); C) Hexokinase 2 (*Hk2*); D) Phosphofructokinase, muscle (*Pfkm*); E) Enolase 1 (*Eno1*). Data plotted as mean ± SEM. *p*-value determined by a two-tailed, unpaired student's *t*-test; * $p < 0.05$, ** $p < 0.01$, **** $p < 0.0001$. n = 9 mice per cohort (6 week diet) and n = 6 mice per cohort (9 and 24 week diet).

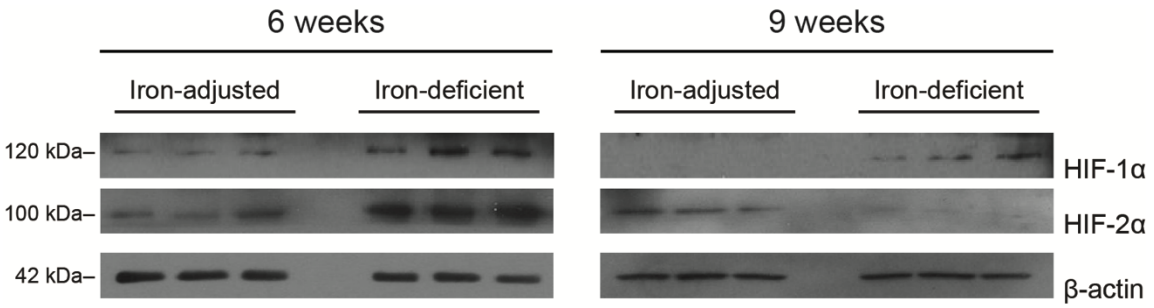


Figure 5.6 HIF-α protein expression. Protein expression of HIF-1α and HIF-2α following (left) 6 weeks or (right) 9 weeks of diet. β-actin was used as a loading control. n = 3 mice per cohort.

5.4.5 Effect of an iron-deficient diet on HIF-α protein expression

Having observed a general up-regulation of HIF-target genes, the expression of HIF-α at the protein level was investigated at the 6 week and 9 week time point (Figure 5.6). Consistent with the notion of enhanced HIF-α activity, HIF-1α was up-regulated in the iron-deficient animals at both time points. HIF-2α was up-regulated at the 6 week time point and down-regulated at the 9 week time point.

As discussed in Chapter 1, Section 1.6, HIF-1α is constitutively expressed and its stability is regulated in an oxygen- and iron-dependent manner at the post-translational level. The HIF-2α protein is post-translationally regulated in the same way, but unlike HIF-1α, HIF-2α is further regulated at the post-transcriptional (pre-translational) level in an iron-dependent manner by iron response proteins (IRPs). The HIF-2α mRNA contains a 5'-UTR iron response element (IRE), which functions as a translational repressor when intracellular iron levels are low (*see* Chapter 1, Figure 1.3). Reduced HIF-2α expression in the iron-deficient animals following 9 weeks of diet compared to the controls is expected

in light of the findings in Chapter 3, Section 3.4.1.v (*see* Figure 3.10), where a significant decrease in total cardiac iron was observed in the iron-deficient animals compared to the controls.

Importantly, the western blots in Figure 5.6 confirm an increase in HIF-α at the protein level, which is consistent with the observed apparent HIF stability, as determined by an up-regulation of HIF-target genes (Section 5.4.3 and 5.4.4).

5.4.6 Effect of systemic iron deficiency on circulating glucose and fatty acid concentration

An anaerobic metabolic profile would predict an increase in glucose usage and a decrease in FA oxidation. These processes are likely to have an effect on circulating levels of glucose and fatty acid concentration. Therefore, these parameters were measured in the animals studied in this chapter (Figure 5.5F and G). Blood glucose concentration was not altered by administration of an iron-deficient diet. However, following 9 weeks of diet, serum free FA concentration was significantly increased in the iron-deficient animals. Since FA uptake and β-oxidation is, in part, directly regulated by serum FA concentration, this implies an increase in FA uptake in the hearts of iron-deficient animals.

5.4.7 Effect on an iron-deficient diet on aerobic respiration: Oxidative phosphorylation

The healthy heart obtains 95% of its ATP through oxidative phosphorylation. However, because this process consumes large amounts of oxygen, this pathway is not favoured under conditions of low oxygen availability. Evidence presented in the previous sections

suggests that the hearts of iron-deficient animals may be hypoxic following 6 and 9 weeks of diet. Consistent with this, anaerobic respiration was up-regulated in the iron-deficient cohort. Together, these predict a down-regulation of oxidative metabolism.

To assess the effect of an iron-deficient diet on oxidative phosphorylation, total cardiac homogenates were used to determine the activity of each of the four ETC complexes (I-IV) and total aconitase *ex vivo* (Figure 5.7). Following 6 weeks of diet, the activity of complex I and total aconitase was down-regulated in the hearts of iron-deficient animals. Following 9 weeks of diet, a reduction in complex I and III activity and up-regulation of complex IV activity was observed in the iron-deficient group. Finally, complex III activity was enhanced in the iron-deficient cohort following 24 weeks of diet. The perturbations in the activities in oxidative phosphorylation and aconitase could not be attributed to changes in mitochondrial number (Figure 5.7F).

An increase in complex IV activity at the 9 week time-point was an interesting finding. One of the components of complex IV is the cytochrome oxidase subunit 4 (COX4), which exists as two isoforms. In the normal heart, COX4-1 is ubiquitously expressed. However, under conditions of limited oxygen availability, COX4-2 overexpression has been observed and thought to provide a mechanism to maximise the efficiency of respiration in hypoxic conditions (Fukuda *et al.*, 2007). Thus, this isoform switch is considered a critical adaptation to hypoxia.

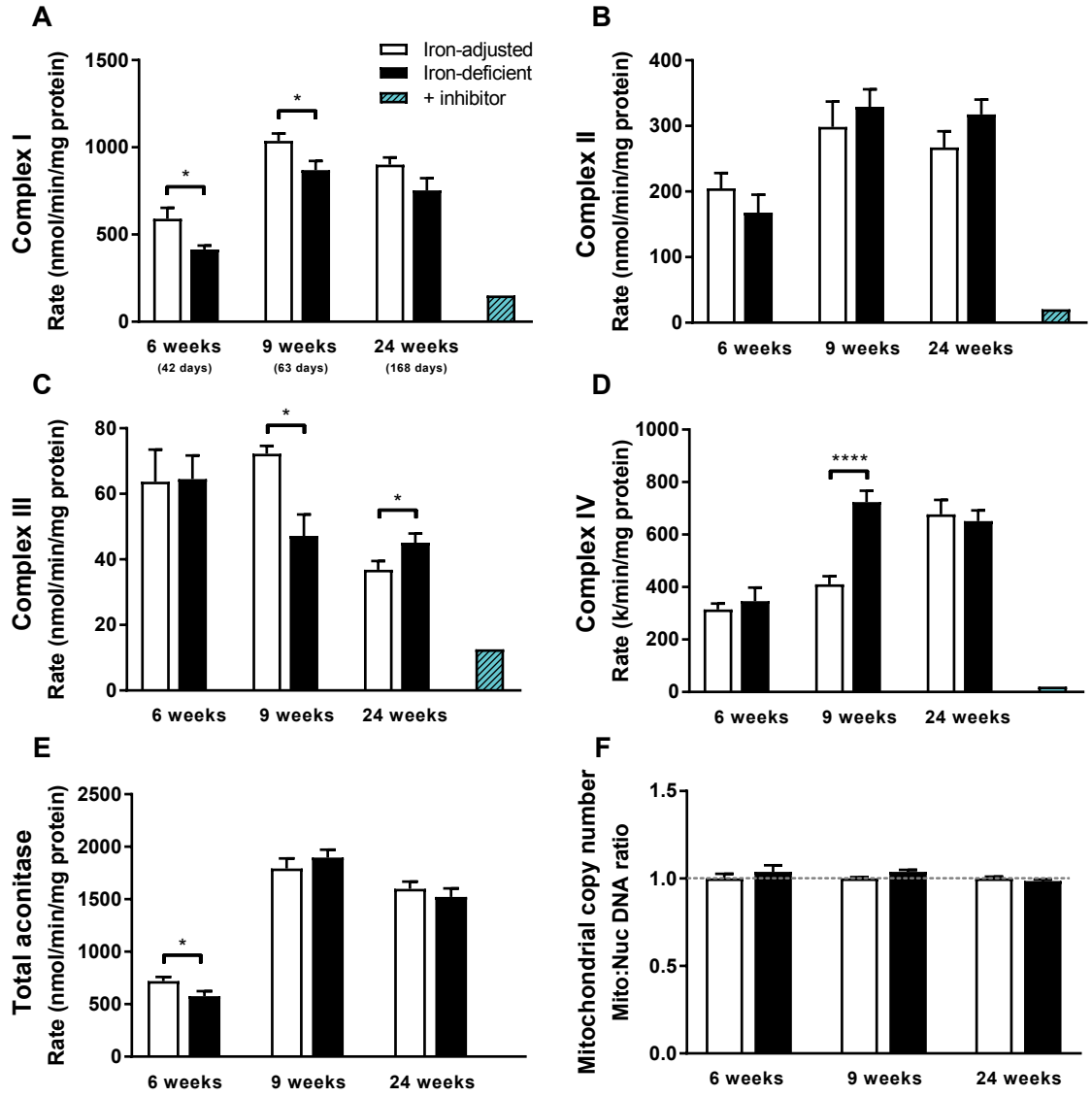


Figure 5.7 Assessment of OXPHOS complex activity in total protein lysate. The activities of A-D) Complex I, II, III and IV and E) Total aconitase (mitochondrial and cytosolic) were measure spectroscopically in the presence of excess substrate relevant to each complex; F) Mitochondrial (Mito) to nuclear (Nuc) DNA ratio as a measurement of mitochondrial abundance. Weeks (days) on diet. Data plotted as mean ± SEM. *p*-value determined by a two-tailed, unpaired student's *t*-test; * $p < 0.05$, **** $p < 0.0001$. n = 6 mice per cohort.

To investigate whether this was true in the mouse model used in this chapter, the expression of COX4 was investigated (Figure 5.8A and B). Following the administration of an iron-deficient diet for 6 and 9 weeks, the gene expression of *Cox4-2* was increased significantly, where the expression of *Cox4-1* was significantly reduced only after 9 weeks on the diet. No differences were observed at the 24 week time point.

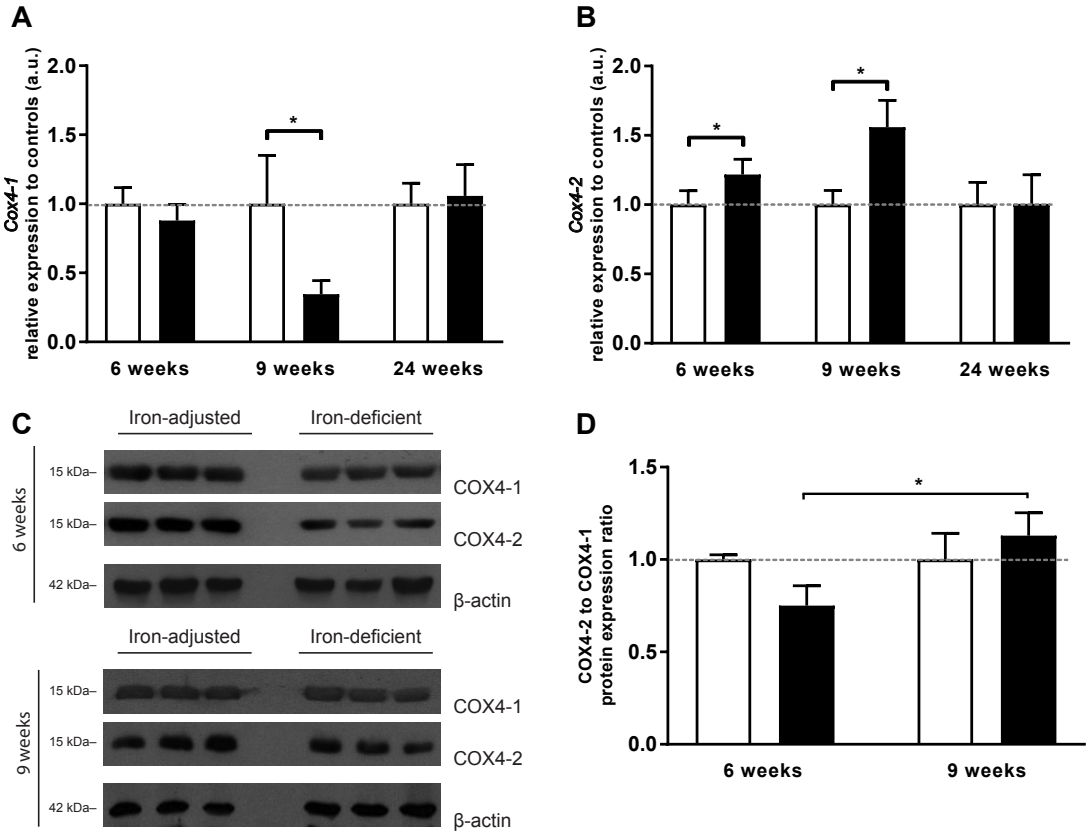


Figure 5.8 Assessment of the expression of COX4. The relative gene expression of A) COX4 isoform 1 and B) COX4 isoform 2 following 6, 9 and 24 weeks of diet. C) Protein expression of COX4-1 and COX4-2 and D) Ratio of COX4-2 to COX4-1 protein expression following 6 and 9 weeks of diet. Data plotted as mean ± SEM. *p*-value determined by a two-tailed, unpaired student's *t*-test; * $p < 0.05$. n = 6 mice per cohort for A and B; n = 3 mice per cohort for C and D.

At the protein expression level, a significant increase in the COX4-2/COX4-1 ratio was observed in the iron-deficient animals at the 9 week time point compared to the 6 week time point. An increase in the fraction of the more active COX4 isoform would be consistent with an increase in the rate of complex IV, which was observed in Figure 6.6D. Furthermore, the expression of *Cox4-2* is regulated in a HIF-dependent manner (Fukuda *et al.*, 2007), which is also consistent with evidence of HIF presence found in Section 5.4.3, 5.4.4 and 5.4.5.

5.4.8 Effect on an iron-deficient diet on mitochondrial morphology

The association of mitochondrial structural damage in metabolic dysfunction and impairment has been well documented. Particularly relevant, Lakhal-Littleton *et al.* (2016) observed mitochondrial deformities along with metabolic alterations in a transgenic mouse model in which the hearts were deficient of iron. To determine whether this was also true in the mice used this study, transmission electron microscopy (TEM) was used to examine mitochondrial structure in isolated cardiomyocytes (6 weeks of diet) and whole cardiac tissue (9 and 24 weeks of diet). No obvious morphological changes were observed at any of the time points surveyed (Figure 5.9).

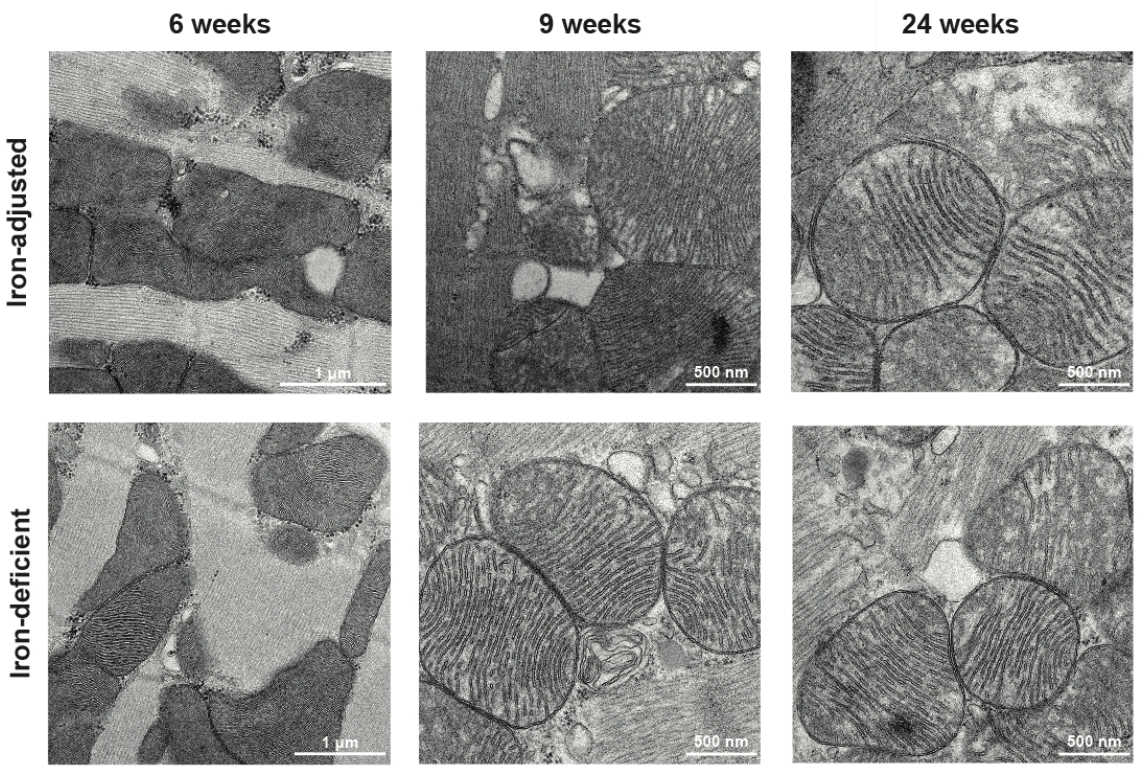


Figure 5.9 Representative electron micrograph of either primary cardiomyocytes (6 week diet) or whole heart tissue (9 and 24 week diet) obtained from iron-adjusted or iron-deficient animals.

5.5 DISCUSSION

The aim of this study was to determine the effects of iron deficiency on cardiac metabolism. The major finding in this chapter was evidence of a switch in metabolic substrate preference occurring following 6 weeks of an iron-deficient diet; this switch was likely a hypoxia-driven effect, as evidence by an up-regulation of HIF-α at the protein level in iron-deficiency (Figure 5.6). Importantly, perturbations in metabolism were observed in the absence of obvious mitochondrial structural abnormalities (Figure 5.9) and difference in mitochondrial number (Figure 5.7F).

5.5.1 Summary of iron status of animals used in this study.

Before discussing the results presented in this chapter, it would be useful to reiterate some of the significant findings made in Chapter 3 which are relevant to the discussion for this chapter (Table 5.3):

1. The 6 week time point correspond to Cohort 2 animals.
    a. Mice on an iron-deficient diet had a blood haemoglobin concentration ([Hb]) of 52.5g /L ± 6.2 and mice on an iron-adjusted diet had a [Hb] of 132.8 g/L ± 2.8, rendering the former iron-deficient and also anaemic;
    b. Serum ferritin and serum iron was decreased and serum transferrin was increased in the iron-deficient animals compared to the controls. Transferrin saturation was also significantly lower in the iron-deficient animals;
    c. No difference in cardiac total elemental iron was observed in these mice.

Table 5.3 Measure of iron status of mice on iron-adjusted or iron-deficient diets for 6, 9 and 24 weeks. Values represented as mean ± SEM. *p*-value determined by two-tail unpaired student's *t*-test. n = 10 mice (6 weeks) or 6 mice (9 and 24 weeks) per cohort.

	Blood haemoglobin (g/L)	Serum ferritin (ng/mL)	Serum iron (µmol/mL)	Serum transferrin (g/L)	Transferrin saturation (%)	Total cardiac iron (µg/g)
Cohort 2: 6 weeks diet						
Iron-adjusted	132.8 ± 2.84	509.8 ± 26.46	32.1 ± 2.49	0.69 ± 0.03	47.4 ± 4.29	90.3 ± 8.88
Iron deficient	52.5 ± 6.23	243.0 ± 45.36	18.6 ± 1.67	1.25 ± 0.10	16.2 ± 2.28	88.7 ± 8.59
***p*-value**	**< 0.0001**	**< 0.0001**	**0.0002**	**< 0.0001**	**< 0.0001**	0.9002
Cohort 3: 9 weeks diet						
Iron-adjusted	143.4 ± 5.85	489.7 ± 17. 33	24.9 ± 1.75	0.65 ± 0.01	38.6 ± 2.40	101.6 ± 2.84
Iron deficient	100.3 ± 13.4	166.8 ± 7.79	21.8 ± 4.70	1.05 ± 0.04	38.9 ± 5.22	88.3 ± 4.24
***p*-value**	**0.0041**	**< 0.0001**	0.8644	**< 0.0001**	**> 0.9999**	**0.0370**
Cohort 1: 24 weeks diet						
Iron-adjusted	139.5 ± 2.11	511.5 ± 19.88	20.9 ± 2.50	0.61 ± 0.01	34.4 ± 4.04	121.7 ± 6.78
Iron deficient	133.7 ± 2.92	325.6 ± 26.90	26.98 ± 2.51	0.72 ± 0.23	37.1 ± 2.70	87.9 ± 6.27
***p*-value**	0.9643	**0.0007**	0.3096	0.5027	0.9699	**0.0064**

2. The 9 week time point correspond to Cohort 3 animals.
    a. Mice on an iron-deficient diet had a [Hb] of 100.3 g/L ± 13.4 and mice on an iron-adjusted diet had a [Hb] of 143.4 g/L ± 5.9, rendering the former iron-deficient but the anaemia in these mice was less pronounced;
    b. Serum ferritin was reduced and serum transferrin was elevated in the iron-deficient animals;
    c. Iron-deficient animals had reduced cardiac total elemental iron compared to the control mice.
3. The 24 week time point correspond to Cohort 24 animals.
    a. Mice on an iron-deficient diet had a [Hb] of 133.7 g/L ± 2.9 and mice on an iron-adjusted diet had a [Hb] of 139.5 g/L ± 2.1.
    b. Serum ferritin was significantly reduced in the animals on an iron-deficient diet, but all other serum indices were no different to the controls;

c. Cardiac, liver and spleen total elemental iron were significantly reduced in the animals on an iron-deficient diet compared to the control mice;
d. In this cohort, the iron deficiency was less pronounced and difficult to definitely conclude that the animals on an iron-deficient diet were iron deficient.

5.5.2 Cohort 2: Metabolic switch in iron-deficient animals is likely a consequence of anaemia caused by iron deficiency

Consistent with the findings by Oexle *et al.*, (1999) in iron-deficient bone marrow cells, at the 6 week time point, an increase in pyruvate flux to lactate, along with a decrease in flux through PDH, was observed in the hearts of iron-deficient animals. Although not shown experimentally, given these results, it is possible to postulate that the TCA cycle is also reduced in the iron-deficient hearts. Collectively, these findings suggest that these hearts have switched to anaerobic respiration for ATP production.

Mechanistically, hypoxia is likely to play a role in driving this metabolic switch. Iron-deficient animals were anaemic, which would predict a general impairment of oxygen delivery to tissues. Consistent with a hypothesis that the cardiac tissue is hypoxic, the HIF-target genes (*Ldha*, *Pdk1*, *Glut1*, *Eno1* and *Cox4-2*), but genes which are not targets of HIF (*Glut4*, *Pfkm* and *Alat1*) remained unchanged. These finds are a strong indicator of HIF stabilization. In addition, *Pdk4*, a target of PPARα (which is down-regulated by HIF), was down-regulated, further implicating HIF. Interestingly, *Hk2*, which is also a HIF-target gene, was significantly down-regulated.

In addition, the activities of complex I of the ETC and total aconitase were reduced in the hearts of iron-deficient animals. These changes were observed against a background of unchanged mitochondrial numbers (Figure 5.6F). This is consistent with the observations made by Lakhal-Littleton *et al.*, (2016) in transgenic mice which were iron-deficient specifically in the cardiomyocytes. However, when considering a direct effect of iron on the function of these oxidative complexes, the results of this study provide little evidence that their activities were compromised as a consequence iron loss. First, total iron was not significantly reduced in the hearts and cardiomyocytes of iron-deficient animals at this time point. Second, complex III and complex IV are also iron-containing complexes but their activities were not affected by iron deficiency. A direct inhibition of the enzymes' activities by hypoxia is also unlikely since the assays were conducted under normoxic conditions. Therefore, a more likely explanation would be that an intrinsic property, or properties, of complex I and aconitase may have been altered as part of an adaptive (or maladaptive) response to chronic hypoxia and independent of iron.

A metabolism based solely on anaerobic glycolysis is unlikely to be able to produce the necessary ATP to meet the demands of the heart for normal function (van Bilsen *et al.*, 2004). Therefore, reduced energetic status in the heart is expected. Much like Neubauer's (2007) "engine out of fuel" hypothesis of the failing heart, the reduction in energy output observed in the hearts of iron-deficient animals would explain and is consistent with the reduced ejection fraction in the iron-deficient animals observed in Chapter 3. However, additional experiments would be required to determine whether total ATP output is reduced in iron deficiency.

Of final note, it appears, however, that anaemia, and impaired oxygen delivery, alone cannot explain either the alterations in cardiac energetics or the cardiac dysfunction observed here and in Chapter 3, respectively. Anaemia can be caused by other nutritional deficiencies, such as vitamin B_{12} and folate deficiency. But, according to our current understanding of HF, these are not recognised as a significantly prevalent comorbidity in HF and no convincing evidence exists that these deficiencies pose an additional burden on left/right ventricular function and patient outcome (Wal *et al.*, 2015). This is much unlike anaemia of iron deficiency, which is recognised as an important comorbidity in HF patients and whose detrimental effects on overall cardiac function has been confirmed and reiterated many times in literature. In addition, recent studies have also revealed that vitamin D deficiency, which can also cause anaemia, is also associated with heart failure risks (Agarwal *et al*., 2011; Cioffi *et al*., 2010; Porto *et al*., 2018). The variable impact of anaemia of different origins on cardiac health suggests that the cause of anaemia is important in determining its effects on heart function rather than simply impaired oxygen delivery alone.

5.5.3 Cohort 3: Metabolic state is likely a combination of oxidative and anaerobic respiration

The cardiac function of iron-deficient animals at this time point had returned to normal (*see* Chapter 3, Figure 3.14). Since normal cardiac function cannot be sustained on anaerobic respiration alone, it is possible to postulate that the hearts of iron-deficient animals may be relying on oxidative metabolism for energy production. Given that the animals in this cohort were iron deficient but not anaemic, this lends support to the

aforementioned hypothesis. Furthermore, free FA concentrations in the serum was increased in the iron-deficient animals following 9 weeks of diet (Figure 5.5G), which is known to promote FA uptake and β-oxidation in the heart (Jaswal *et al.*, 2011).

However, similar to the 6 week time point, many of the results obtained at the 9 week time point are evidence of HIF activity, which is seemingly inconsistent with the above discussion. This conundrum can be addressed by considering the iron-dependence of HIF regulation. A HIF response can be evoked by a deficiency of iron under normoxic conditions, by inhibiting the activity of PHDs (Wang and Semenza, 1993). Therefore, HIF stabilization at this time point is likely not due to a lack of oxygen, but rather a lack of iron, since the hearts of iron-deficient animals had reduced total iron content compared to the controls (Table 5.2). This statement is strengthened by the observation that HIF-1α but not HIF-2α was up-regulated in the hearts of iron-deficient animals (Figure 5.6). Indeed, a deficiency of iron would result in impaired PHD activity, thus inhibiting HIF-1α degradation. However, for HIF-2α, its protein expression is expected to be reduced since its translation would be inhibited by regulation by IRPs.

Further support for HIF stability arising from cardiac iron deficiency can be found in the ETC complex activities. Complex I and complex III require Fe-S clusters for activity and a reduction in iron bioavailability may impinge on Fe-S cluster synthesis. A deficiency of Fe-S cluster would explain the reduction in the activities of complex I and III (Figure 5.7A and C).

The activity of complex IV, also an Fe-S cluster containing complex, was enhanced in the iron-deficient animals. This enhancement can be explained by the hypoxia-driven up-

regulation of COX4-2 expression. At the gene expression level, *Cox4-2* was up-regulated and this effect was evident at the protein level in cohort 3 animals when compared to cohort 2 iron-deficient animals (Figure 5.7D). Because COX4-2 is the more active isoform (Fukuda *et al.*, 2007), an increase in complex IV activity is consistent with an increase in the fraction of COX4-2 to COX4-1 incorporation to the complex IV structure. However, the functional relevance of this isoform switch is uncertain due to limitations of the experimental setup, which will be discussed in the next paragraph.

Although the reduction in the ETC complex I and III activities are in accordance with what can be expected in conditions of tissue iron deficiency, this is in conflict with the need for oxidative respiration, which would be required to sustain normal cardiac function. This seemingly inconsistent finding may not reflect true physiology of the cell. In order to study the activity of individual complexes and enzymes, these activity assays were conducted *in vitro* in the presence of excess substrates of a single complex and with inhibitors of the other complexes.

Therefore, one major limitation arises from this experimental set-up: the maximal rate observed *in vitro* may not be a true reflection of the maximal rate that can be achieved *in vivo*. In other words, because each complex was taken out of its biological context, this eliminated the possibility to study the interdependence of each complex to one other and to the mitochondrial/cellular environment. Therefore, given the results obtained, it is not possible to conclude how these alterations affect the final ATP output *in vivo*. Further experiments would be required to assess the physiological relevance of the alterations observed spectroscopically *in vitro*. For these reasons, in relating spectroscopic results to

the overall energetics of the heart, a reduction in the activities of the ETC complexes may have little functional impact and a capacity for aerobic respiration comparable to the controls may be achievable in the iron-deficient animals.

Finally, in addition to a HIF effect acting on PDH (through an increase in PDK1), the increase in the flux of pyruvate to lactate could be further promoted by an increased FA oxidation (Figure 5.3C). The final product of FA oxidation is acetyl-CoA, an endogenous inhibitor of PDH (Gray *et al.*, 2014). Inhibition of PDH arising from an increase in β-oxidation would subsequently force pyruvate to be metabolised to lactate. This would explain why cohort 3 animals had a larger lactate flux than cohort 2 animals (when normalised to the controls: cohort 3: 1.62 vs cohort 2: 1.44).

Importantly, the results obtained from cohort 3 demonstrate that iron deficiency, in the absence of anaemia, is sufficient to cause perturbations to the normal metabolic pathway. Although in this study, the metabolic profile that arises from iron deficiency did not have a negative functional impact, chronic up-regulation of lactate metabolism can become pathological. Pyruvate metabolism to lactate generates protons. Intracellular acidosis arising from accumulation of protons can impair various cellular processes, including those involved in cardiomyocyte contractility, and promote cardiomyocyte apoptosis (Jaswal *et al.*, 2011; Noordali *et al.*, 2017). This effect is most pronounced and relevant in ischaemia, where restricted blood flow increases the generation of lactate through anaerobic respiration but unable to clear the resulting protons (Jaswal *et al.*, 2011).

In light of these findings, it would be of interest to measure blood lactate concentration and intracellular pH of cardiomyocytes in the animals used in this chapter.

5.5.4 Cohort 1: A metabolism driven by glucose oxidation?

Aerobic oxidation of glucose appears to be enhanced, as evidence by the significant increase in bicarbonate flux in the iron-deficient animals compared to the controls (Figure 5.3A). However, the underlying mechanism remains elusive, since no coordinated alterations were observed in at this time point. Nevertheless, one certainty is that metabolic state of animals on an iron-deficient diet is no longer acted on by HIF, as evidenced by the lack of up-regulation of HIF-target gene expression.

Interestingly, the activities of complex I, III and IV in the iron-deficient animals were no different than that of the controls, despite a significant reduction in cardiac total iron content (Figure 5.6 and Table 5.2). This is in contrast to the observations made in cohort 3. However, closer examination of the results revealed the following. Comparing iron-deficient animals in cohort 3 (9 weeks) and cohort 1 (24 weeks), the activities of these complexes are comparable at the two different time points. On the other hand, in the control animals, a reduction in the activities of the complex I and III and an increase in complex IV activity is observed in cohort 1 compared to cohort 3. Consequently, when comparing between diet groups at the 24 week time point, the activities of ETC complexes appear to no longer be significant. Within the constraints of the experiments conducted in this study, it is not possible to explain why the activities of ETC complexes are sustained in iron deficiency over time but altered in the control animals.

5.5.5 Limitations of the current study

In addition to the limitations of the spectroscopic enzyme activity assays discussed in Section 5.5.3, another limitation of the study was the inability to control the nutritional

status of the animals. Metabolism is sensitive to nutrient availability, which fluctuates daily depending on whether the animal is in a fed or fasted state. In this chapter, the assumption was that, because mice are nocturnal animals, they feed during the night and fast during the day, thus mornings were considered the "absorptive state" and all experiments were conducted in the morning rather than afternoons. However, it would be incorrect to assume that all animals have fed at the same time prior to experimentation and thus, are in a similar nutritional state at the time of the experiment. A variation in the feeding behaviour and consequent nutritional status would explain the wide variation which was observed in the some of the measured results.

5.6 CONCLUSIONS

The aim of this chapter was to determine the effects of iron deficiency on cardiac energetics. The results presented in this chapter led to two important findings. First, a switch in metabolism towards an increased glycolytic mechanism which was likely hypoxia-driven arising from anaemia at the 6 week time point. This observation predicts a reduction in energetic output which would be consistent with the observed impaired ejection fraction in these mice. Second, the results at the 9 week time point describe a metabolic state which combines oxidative phosphorylation and anaerobic respiration. The underlying mechanism likely involves an increase in tissue oxygenation, due to an increase in blood haemoglobin concentration, and HIF stabilization, as a consequence of tissue iron deficiency. These results predict an energetic output which can sustain normal cardiac function, as was observed by cine-MRI.

In summary, the results presented in this chapter emphasise that maintenance of metabolic homeostasis is essential in supporting cardiac performance. Importantly, the effects of anaemia in metabolic output is profound, but iron deficiency in the absence of anaemia is also sufficient to cause perturbations in cardiac metabolism which may be detrimental to cardiac function in disease settings.

CHAPTER 6:

EFFECTS OF IRON DEFICIENCY ON CARDIAC CALCIUM SIGNALING

6.1 CHAPTER OVERVIEW

In Chapter 4, the Ca^{2+} signaling pathway was identified as being differentially regulated in the heart of mice on an iron-deficient diet. Based on this finding, the purpose of this study was to explore the physiological consequences of an iron-deficient diet as well as iron supplementation on cardiac Ca^{2+} signaling. Primary cardiac myocytes were obtained from mice on either an iron-adjusted or an iron-deficient diet having received either FCM supplementation or saline. Fluorescence Ca^{2+} imaging and patch clamp electrophysiology experiments were conducted on isolated cardiomyocytes. Results showed that, in the myocytes of mice on an iron-deficient diet, diastolic Ca^{2+} levels were elevated and the amplitude of electrically-evoked Ca^{2+} transients (CaTs) was decreased; both changes could be reversed by FCM supplementation. The perturbations in CaT amplitude were not due to a change in the size of the myocyte's Ca^{2+} store (sarcoplasmic reticulum) but likely a change in fractional release.

6.2 INTRODUCTION

6.2.1 Calcium in the heart

Cardiac muscle converts electric activation (excitation) at the membrane into a mechanical force response (contraction) (Eisner *et al*., 2017; Landstrom *et al*., 2017). The coupling between excitation and contraction (EC) involves Ca^{2+} signals (electrically evoked Ca^{2+} transients, CaTs) that arise from a carefully orchestrated activation of Ca^{2+}-handling proteins in the cardiomyocyte (Figure 6.1).

During systole, each action potential is triggered by an influx of Na^+ ions through the voltage-gated Na^+ channel ($Na_v1.5$). Na^+ current depolarizes the membrane, which evokes an influx of Ca^{2+} through the voltage-activated L-type Ca^{2+} channel (LTCCs). This initial Ca^{2+} influx triggers a much larger Ca^{2+} release from the sarcoplasmic reticulum (SR) through the Ca^{2+}-sensitive ryanodine receptor (RyR2) in a process known as Ca^{2+}-induced Ca^{2+}-release (CICR). As free cytoplasmic [Ca^{2+}] rises, it binds to cardiac troponin C and activates the contractile apparatus (Crossman *et al.*, 2017; Eisner *et al*., 2017).

For relaxation to occur, cytoplasmic [Ca^{2+}] must return to diastolic levels. This is achieved partly by the re-uptake of Ca^{2+} back into the SR by the SR Ca^{2+}-ATPase (SERCA) and partly export into the extracellular space by the Na^+/Ca^{2+}-exchanger (NCX) and a smaller contribution from a sarcolemmal Ca^{2+} ATPase (PMCA) (Eisner *et al.*, 2017). In ventricular cardiomyocytes, PMCA tends to play a minor role and was not investigated in detail in this chapter. The amplitude of the CaT is determined by the amount of Ca^{2+} released from the SR and cytoplasmic buffering power, and correlates with the strength of contraction (inotropy) (Landstrom *et al.*, 2017).

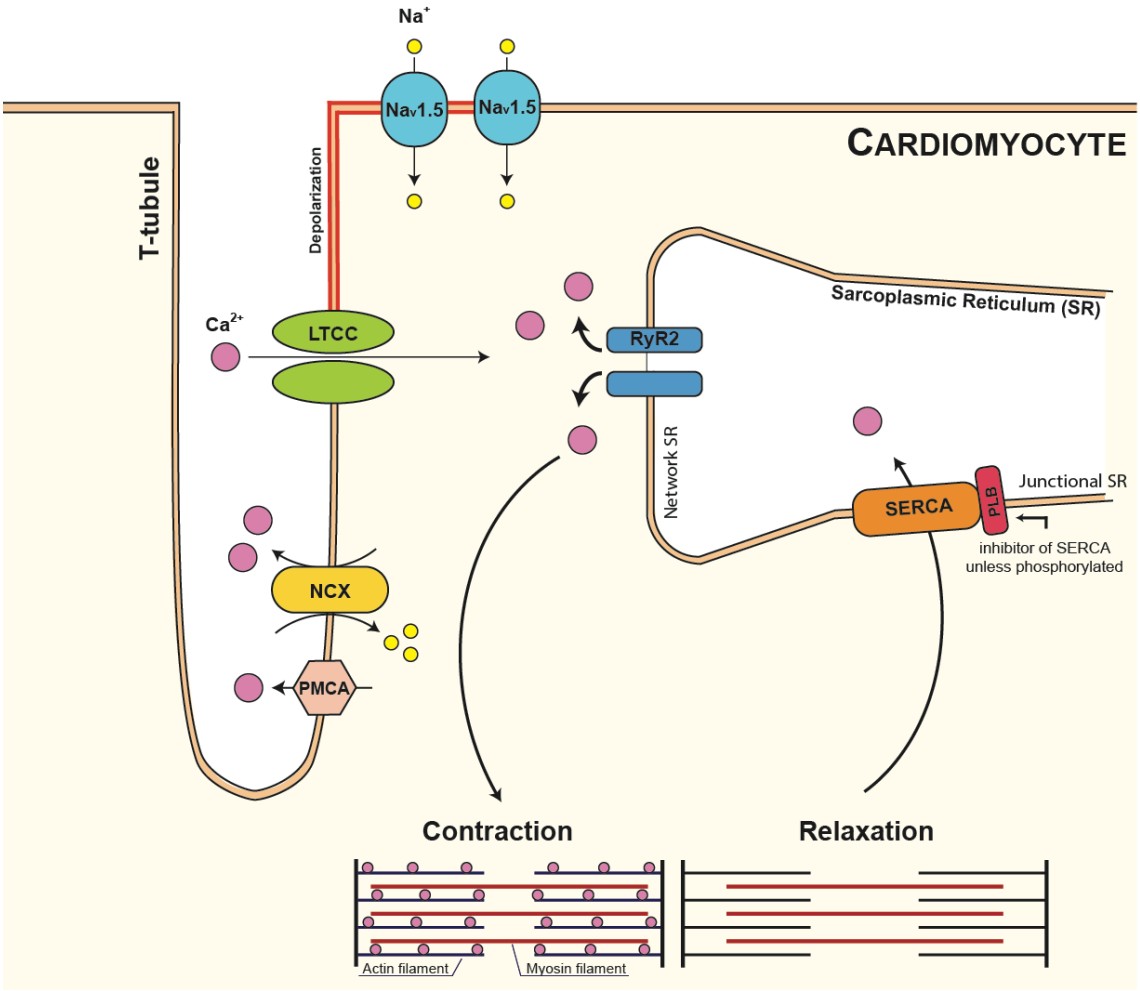


Figure 6.1 Ca^{2+} signaling pathway in the cardiac couplon. In EC coupling, influx of Na^{+} depolarizes the membrane. A small amount of Ca^{2+} enters the cell through the LTCC, leading to a larger Ca^{2+} release from SR Ca^{2+} stores through the RyR2 (known as CICR). During diastole, Ca^{2+} is either sequestered back into the SR by SERCA or extruded into the extracellular space through NCX/PMCA.

EC coupling takes place in discrete units called couplons, which are organised around transverse tubules (t-tubules) (Hong and Shaw, 2017). In mature ventricular myocytes, cardiac t-tubules are highly branched invaginations on the plasma membrane that contain microdomains rich in ion channels and signaling molecules that participate in the EC coupling event (Crossman *et al.*, 2017). These structures penetrate deep into the myocyte,

forming complex network of invaginations that facilitate a fast and uniform delivery of signal to achieve synchronous contraction across the entire cell (Crossman *et al.*, 2017; Hong and Shaw, 2017). As a result, a typical CaT can reach its peak Ca^{2+} within less than 100 ms, which is twice as fast as it would take if the cell were to rely on Ca^{2+} diffusion alone (Crocini *et al*., 2014; Crossman *et al*., 2017).

6.2.2 Regulation of intracellular Ca^{2+} handling

The process of EC coupling relies on the coordination of many different Ca^{2+} transport processes in order to generate stable signals over time, as expected for a healthy heart at steady-state. Moreover, these processes must have the capacity to become up- or down-regulated as may be required by the heart's inotropic state. This section will provide a summary on the various components that contribute to Ca^{2+} signaling required for a contracting heart.

i) Biophysical properties of Ca^{2+}-handling channels and transporters

Since Ca^{2+} influx and efflux can work against each other, the CaT time course is very sensitive to the overall regulatory status. Furthermore, many physiological and pathological changes involve several concurrent changes in transport activity, often producing non-intuitive effects on CaT properties, such as baseline (diastolic), rise-time, peak amplitude and relaxation.

The activities of LTCC, RyR2, SERCA and NCX depend on their expression, targeting to specific microdomains and post-translational modifications, such as phosphorylation.

Acutely, changes in phosphorylation are commonly exploited physiologically regulating cardiac output (Catterall, 2015; Landstrom *et al*., 2017). In one example, when the heart is stressed and cardiac demand is increased, the activation of β-adrenoreceptors causes a rise in the concentration of the second messenger cyclic adenosine monophosphate (cAMP) and subsequent activation of the cAMP-dependent protein kinase A (PKA) (Landstrom *et al*., 2017). The downstream targets of PKA-mediated phosphorylation include LTCC, RyR2, and the regulatory proteins of SERCA, phospholamban (PLN) and sarcolipin (SLN) (Landstrom *et al*., 2017; Taur and Frishman, 2005). In a similar manner, the activity of NCX can be increased by phosphorylation by protein kinase C (PKC), the latter which is activated, in part, by rise in cytoplasmic [Ca^{2+}] (Ghigo *et al*., 2017). Finally, channel activity can be reduced by dephosphorylation of these channels and accessory proteins by phosphoprotein phosphatases (PPs) such as PP1 and PP2A (Ather *et al*., 2013; Catterall, 2015).

The levels of these proteins are also regulated at the transcriptional level. LTCC is known to autoregulate its own transcription in a Ca^{2+}-dependent manner, whereby the C-terminus of the channel encodes a transcription factor (Gomez-Ospina *et al.*, 2006; Naranjo and Mellström, 2012). Similarly, Ca^{2+} also up-regulates the expression of the SERCA gene *Atp2a2*; this regulation involves the calciuneurin/NFAT signaling pathway (Naranjo and Mellström, 2012). Less is known about the transcriptional regulation of RyR2 and NCX.

The major biophysical properties of the four channels explored in this chapter relate to (Crossman *et al*., 2017; Eisner *et al*., 2017; Ghigo *et al*., 2017; Landstrom *et al*., 2017; Naranjo and Mellström, 2012):

- Ca^{2+} current carried by LTCC, which depends on:
  - Channel number (determined by gene expression and protein targeting);
  - Single channel conductance;
  - Open probability (a function of various post-translational factors, including phosphorylation);
  - Membrane voltage (determined by the stage of the action potential);
  - Reversal potential (set by the Nernst potential);
  - Inactivation kinetics (a voltage and Ca^{2+}-dependent process).
- Ca^{2+} release via RyR channels, which depends on:
  - Channel number;
  - Single channel conductance;
  - Open probability (including leakiness);
  - Coupling to LTCC channels and SR Ca^{2+} load.
- Ca^{2+} re-uptake by SERCA, which depends on:
  - Pump number;
  - ATP/ADP ratio that drives the ATPase activity;
  - Apparent Ca^{2+} affinity;
  - Diffusive coupling to the site of Ca^{2+} release;
  - State of its endogenous inhibitor PLN.
- Ca^{2+} transport by NCX, which depends on:
  - Carrier number;
  - Thermodynamic driving forces (including membrane potential, Na^{+} and Ca^{2+} gradients);
  - Apparent Ca^{2+} affinity.

ii) Structural and spatial considerations: The dyad

The process of CICR depends on the activity of LTCC and RyR channels, as well as the diffusive coupling between these proteins (Taur and Frishman, 2005). Studies indicate that RyR2 channels are activated by a localized increase in cytoplasmic [Ca^{2+}] in its vicinity rather than by a global rise in [Ca^{2+}] (Taur and Frishman, 2005). Therefore, the rise in cytoplasmic [Ca^{2+}] is highly dependent on the structural relationship between junctional SR (the sub-compartment of the SR that harbours RyR channels) and t-tubule membranes (Eisner *et al*., 2017). Clusters of RyR2 on the SR membrane and LTCCs, expressed along the t-tubules, are found at a distance of 15 nm of each other, and together, they form what is known as the dyad (Eisner *et al*., 2017; Taur and Frishman, 2005).

Because the primary purpose of the dyad is to facilitate the initiation of CaTs, loss of dyad coupling, either by loss of t-tubules (de-tubulation), changes in SR morphology or changes in channel expression and/or activity, results in a reduction in the synchronicity and amplitude of CaTs (Eisner *et al*., 2017).

Another structural consideration is the coupling between junctional SR, where Ca^{2+} is released through RyR channels, and network SR, into which Ca^{2+} is sequestered by SERCA pumps (Jorgensen *et al.*, 1993). Diffusive delays would affect the CaT recovery time course.

iii) Ca^{2+} leaks and flux balance

An imbalance in Ca^{2+} fluxes resulting in a net gain or net loss of total cellular Ca^{2+} leads to changes in the amplitude of CaTs and contractility and may result in instability over

time (i.e. arrhythmias). Therefore, a steady state requires that the amount of Ca^{2+} entering the cell must equal the amount of Ca^{2+} leaving the cell (Eisner *et al.*, 2017). Mathematically, this means that at steady state, the ratio of LTCC-dependent Ca^{2+} entry to SR Ca^{2+} release must equal the ratio of fluxes carried by NCX+PMCA and SERCA. One example that affects flux balance is diastolic Ca^{2+} leak, which reduces the amount of Ca^{2+} available for release in response to electrical excitation. Ca^{2+} leaks are events involving spontaneous opening of a single RyR2 channel in the absence of LTCC driven Ca^{2+} stimulus (Sato and Bers, 2011). This increases the $[Ca^{2+}]$ locally, inducing the opening of a cluster of RyR2 channels in what is referred to as a "Ca spark" and may propagate further as a Ca^{2+} wave (Eisner *et al.*, 2017; Sato and Bers, 2011). While not all Ca leaks lead to a Ca wave, a major effect of both events is a decrease in SR Ca^{2+} content and amplitude of any subsequent CaTs.

iv) Ca^{2+} buffering

Cytoplasmic Ca^{2+} can be buffered by two types of processes. The first is by molecules that bind Ca^{2+} passively and reversibly, thereby reducing the amplitude of $[Ca^{2+}]$ events but restricting the mobility of Ca^{2+} ions in the cytoplasm. In fact, restricted diffusion is essential for microdomain signaling to take place in dyads, and a certain degree of buffering, facilitated by Ca diffusivity, is needed for coupling between consecutive steps in EC coupling (Rosenbaum, 2002; Schwaller, 2010).

The effects of Ca^{2+} buffering depends greatly on the binding and de-binding kinetics of the buffer (Eisner *et al.*, 2017). In the presence of a fast buffer, any given Ca^{2+} flux will produce a smaller change in $[Ca^{2+}]$ and therefore decrease the amplitude of CaTs and slow

decay time. On the other hand, a slow Ca buffer is unlikely to affect CaT amplitude, but may affect diastolic [Ca^{2+}] (Eisner *et al*., 2017). Because of their capacity to alter the dynamics of CaTs, Ca buffers play an important role in determining the rate of relaxation during diastole (Eisner *et al.*, 2017).

A second, active form of buffering involves the mitochondria. It has been suggested (although not without controversy) that the mitochondria dynamically take up Ca^{2+} during the CaT and then release Ca^{2+} in diastole. This uptake is proposed to take place through the mitochondrial calcium uniporter MCU down the steep electrical gradient (-180 mV (Drago *et al*., 2012). The reverse process involves the mitochondrial Na^+/Ca^{2+}-exchanger mNCE and the mitochondrial Na^+/H^+ exchanger mNHE (Kohlhaas and Maack, 2013; Maack *et al*., 2006). Again, the effect of mitochondrial buffering is to restrict the amplitude of CaTs, but may also influence diastolic Ca^{2+} levels.

6.2.3 Ca^{2+} handling in cardiovascular disease and heart failure

As described above, EC coupling is a tightly regulated event which relies on the fine coordination of many different factors. Perturbations in any one of the functional, structural or spatial processes involved can therefore cause substantial effects on cardiac contraction. In fact, alterations in the four Ca^{2+}-handling proteins are associated with cardiac disorders and heart failure (HF) (Zou *et al*., 2011).

i) Ryanodine receptor in heart failure

The contributions of deranged RyR2 function is well established in HF. A hyper-phosphorylated state results in enhanced diastolic Ca^{2+} leaks from the SR and partial

depletion of SR stores. The physiological consequences of this are reduced EC coupling, raised diastolic pressure and compromised contractile force (Ather *et al*., 2013; Zou *et al.*, 2011). Furthermore, Ca leaks and Ca sparks are a natural occurrence, but when the frequency of these events increase, as it would with RyR2 hyper-phosphorylation, this can trigger a Ca wave in the myocytes that contribute to arrhythmias, such as in delayed after-depolarizations (Opie, 2004). RyR2 channels are often found to be hyper-phosphorylated in diseased states and have been implicated in the pathogenesis of HF and ventricular arrhythmias (Dobrev and Wehrens, 2014). Finally, some RyR channels may become structurally uncoupled from the dyad, in which case they cannot not contribute to effective contraction and are dubbed rogue RyR channels (Xie *et al.*, 2010)

ii) SERCA in heart failure

Where RyR2 channels releases Ca^{2+} from the SR to the cytosol, the primary function of SERCA is to remove cytoplasmic Ca^{2+} and replenish the SR. Therefore, SERCA activity controls the rate of CaT recovery and refilling of the SR (Eisner *et al.*, 2017). Impairments in SERCA, either due to decrease in expression or activity, result in decreased SR Ca^{2+} load and reduced CICR and is a hallmark characteristic of HF (Ather *et al.*, 2013).

SERCA activity is directly regulated by accessory proteins PLN and SLN, both of which have been implicated in the pathogenesis of HF (Ather *et al.*, 2013). In mouse models, a cardiomyocyte-specific overexpression of PLN or SLN resulted in impairment of cardiac contractility and development of ventricular hypertrophy (Asahi *et al.*, 2003; Ather *et al.*, 2013). Both phenomena were attributed to reduced amplitude and increased recovery time of CaTs (Asahi *et al.*, 2003). On the other hand, inhibition of PLN or SLN delayed the

progression of cardiac remodelling and dysfunction in HF models (Ather *et al*., 2013). However, constitutively active SERCA was also detrimental to the heart, where ablation of either regulatory proteins resulted in cardiac hypertrophy and decreased contractility (Shanmugam *et al*., 2011). The latter finding emphasises the notion that an up-regulation of Ca^{2+} pumps can be as deleterious to cardiac performance as a down-regulation of their function.

Furthermore, since SERCA pumps are directly coupled to ATP hydrolysis, their activity is subservient to the ATP/ADP and phosphocreatine (PCr)/ATP ratios, which tend to be reduced in the diseased state (Periasamy *et al*., 2008). In the hearts of animal models of severe heart failure, [ATP] and [PCr] are reduced by up to 30% and 60%, respectively, compared to normal myocardium (Ingwall, 2009b; Periasamy et al., 2008).

iii) L-type Ca^{2+} channel in heart failure

Although there is overwhelming evidence that LTCC is involved in the pathophysiology of HF, its exact role in the pathology and disease progression remains rather elusive and contradictory. Many studies have reported an unaltered or down-regulated LTCC activity in HF, while others have demonstrated an increase in whole-cell LTCC current in hypertrophy and HF (Ather *et al.*, 2013; Bodi *et al.*, 2005). Furthermore, Schröder *et al.* (1998) showed an enhanced LTCC activity at the level of the single-channel in failing human hearts, against a background of unaltered whole-cell current density. Finally, studies conducted on mice showed that a constitutively active LTCC leads to cardiomyopathy and cardiomyocyte death (Nakayama *et al.*, 2007) and a partial knock-

out of the channel results in reduced LTCC current, leaky RyR2 and severe hypertrophy of the heart (Goonasekera *et al.*, 2012).

iv) NCX in heart failure

Less is known about the role of NCX in the context of cardiac disease. Compensatory up-regulation of NCX expression and activity has been observed in conditions of reduced SERCA activity (Ather *et al.*, 2013). However, a chronic up-regulation of this channel can become maladaptive. Because NCX does not replenish the SR, eventual run-down of SR Ca^{2+} stores and diminished CICR is observed when NCX activity is raised (Ather *et al*., 2013; Dewenter *et al*., 2017). Furthermore, when intracellular [Na^{+}] is high, as is often observed in HF, the inward current by NCX may be reduced or even reversed, thus contributing to Ca^{2+} overload and arrhythmias (Dewenter *et al*., 2017).

6.2.4 Cardiac Ca^{2+} and iron handling

A physiological relationship between Ca^{2+}-handling proteins and iron homeostasis in the heart exists through the LTCC. Although the primary function of LTCC is to transport Ca^{2+} across the membrane, there is also evidence that iron can be transported through these channels under conditions of systemic iron overload (Otto-Duessel *et al.*, 2011; Wongjaikam *et al.*, 2017). The LTCC, therefore, provides an alternative route for cardiac iron loading, independent of the canonical iron transport pathway.

However, the effect of iron deficiency on cardiac calcium homeostasis is still relatively unknown. A first attempt to understand the effect of iron deficiency on Ca^{2+} signaling has been made by Goldstein *et al.* (1996). The authors reported decreased LTCC current,

shortened action potential, and reduced contractile force in the ventricular myocytes of rats on an iron-deficient diet compared to controls. However, this 1996 study only explored L-type current, thus a complete insight into the effect of iron deficiency on Ca^{2+} handling kinetics is still lacking.

6.2.5 Study aims

Ca^{2+} signaling is fundamental to the beating heart. In Chapter 4, the RNA-seq study suggested that an iron-deficient diet may affect the cardiac calcium signaling pathway. The aim of this chapter, therefore, was to study the impact of an iron-deficient diet on cardiac Ca^{2+} handling and to propose a mechanism by which alterations in Ca^{2+} homeostasis may occur.

6.3 METHODS

6.3.1 Mouse model

Cohort 4 mice were used for the experiments described in this chapter. The time line of the animal model, which was originally shown in Figure 3.1B, has been adapted and is shown in Figure 6.2. Two groups of male C57B6 mice were weaned onto an iron-adjusted and two groups onto an iron-deficient diet at the age of 3 weeks. At the beginning of the 4th week of diet and then again the following week (days 22 and 29 of diet), animals were intravenously administered either 15 mg/kg of FCM or an equivalent volume of saline, for a total of 2 injections. Animals were culled during the 6th week of diet, one animal per day, for experiments.

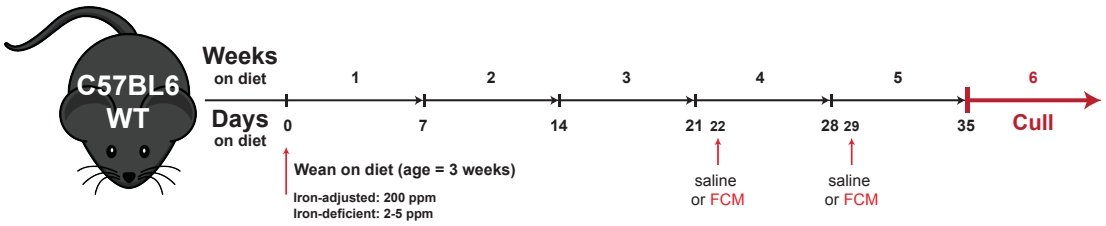


Figure 6.2 Time line of animal model. Animals were weaned on to an iron-adjusted or iron-deficient diet at 3 weeks of age. At the beginning of 4th and 5th week, animals received an intravenous injection of either FCM or saline. Mice were culled during the 6th week of diet.

6.3.2 qPCR

SYBR Green quantitative PCR was performed on cDNA made from mRNA obtained from total heart tissue. *Gapdh* was used as the internal house-keeping gene, and 300 nM of primer was used for the reaction. The list of primers can be found in Table 6.1.

Table 6.1 List of primers used in this chapter.

Primer	Sequence	Concentration
Ryr2	F – CGAGGATGAGATCCAGTTCC R – CAAATCCTTCTGCTGCCAAG	500 nM
Cacna1c	F – AGCAAGAACCACTGCGGAT R – GAAGAAATGCAGCAACAGCC	500 nM
Slc8a1	F – TTGAGGACACCTGTGGAGAG R – GGGGCTCTCCAATCTCAAT	500 nM
Atp2a2	F – GGGCAAAGTGTATCGACAGG R – TCAGCAGGAACTTTGTCACC	500 nM
Gapdh	F – GGCACAGTCAAGGCTGAGAATG R – ATGGTGGTGAAGACGCCCAGTA	300 nM

6.3.3 Western blot

Cell lysate was prepared from crushed, frozen heart tissue using RIPA buffer (in mM unless otherwise specified): 150.0 NaCl, 50.0 Tris (pH 8.0), 1% Triton-X, 0.5% sodium deoxycholate, 0.1% SDS supplemented with complete protease inhibitor. The tissues were mechanically disrupted using the TissueRuptor (Qiagen). Total protein concentration was measured using the Bradford Assay (Sigma) and calibrated using a 9-point BSA standard, following manufacturer's instructions.

For SDS-PAGE, 100 μg of protein lysate was loaded onto a 4-18% gradient gel (BioRad) (for most proteins) or a 10% gel (for RyR2 blotting only). The gel was transferred onto a PVDF membrane for 3 h using an SDS-free transfer buffer (10% MeOH in 1X running buffer). The antibodies used for western blotting are listed in Table 6.2.

Table 6.2 List of antibodies used in this chapter.

Antibody	Product code (Manufacturer)	Concentration
rb-RyR2	MA3-916 (Thermo Fisher)	1:1,000
rb-$Ca_v1.2$	ab84814 (Abcam)	1:500
ms-SERCA	NB300-581 (Novus Biological)	1:2,000
ms-NCX	R3F1 (Swant)	1:2,000
ms-PLN	A010-14 (Badrilla)	1:2,000
rb-ser16-PLN	A010-12 (Badrilla)	1:2,000
rb-thr16-PLN	A010-13 (Badrilla)	1:2,000
ms-β-actin	NB100-74340 (Novus Biological)	1:4,000
gt-anti ms-HRP	sc-2031 (Santa Cruz)	1:10,000
gt-anti rb-HRP	sc-2030 (Santa Cruz)	1:10,000

ms = mouse
rb = rabbit
gt = goat

6.3.4 Adult primary cardiomyocyte isolation

Primary cardiomyocytes were isolated as described in Chapter 2, Section 2.3.2. During the experiments, cells were kept in suspension in Tyrode perfusion buffer supplemented with 1.0 mM $CaCl_2$ at room temperature.

6.3.5 Whole-cell voltage clamp

Voltage clamp. Primary cardiomyocytes were plated onto a Perspex chamber mounted on an Olympus IX73 microscope. All patch clamp experiments were conducted at room temperature using the Axopatch200B patch clamp amplifier (Axon Instruments). Patch electrodes were prepared from soft glass micropipettes (1.5 mm OD x 1.16 mm ID; Harvard Instruments) pulled on a horizontal puller (Sutter Instruments). Electrodes had a

tip resistance of 1-1.5 MΩ when filled with the pipette solution, which contained (in mM): 5.0 NaCl, 120.0 CsCl, 1.0 $MgCl_2$, 3.0 $CaCl_2$, 10.0 TEA-Cl, 5.0 Mg-ATP, 1.0 Na_2-GTP, 5.0 phosphocreatine tris, 5.0 BAPTA and 10.0 HEPES at pH 7.2 with CsOH at room temperature.

The recorded currents (I_{LTCC}) were filtered at 10 kHz through a 4-pole low-pass Bessel filter and digitized at 10 kHz. The experiments were controlled using the pClamp software (Axon Instruments). Current recordings were performed in the following bath solution (in mM): 135.0 NaCl, 5.4 CsCl, 1.0 $MgCl_2$, 1.8 $CaCl_2$, 5.0 4-aminopyridine (4-AP), 10.0 HEPES, and 10.0 glucose at pH 7.4 with NaOH at room temperature. Under these conditions, current through K^+ conductance was minimized.

Currents were measured by means of whole-cell recording. L-type Ca^{2+} current was reported as the amplitude of the inward component of the recorded membrane current. The membrane was first held at -80 mV for 100 ms. Next, a depolarizing voltage was applied at -40 mV for 100 ms to inactivate voltage-gated sodium channels. Finally, a 12-step voltage was applied from -40 mV to +70 mV in 10 mV increments, each step lasting 300 ms, to determine the current-voltage relationship for the Ca^{2+} current. The voltage protocol can be found in Figure 6.3.

Analysis. The Clampfit software was used to analyse the data. For each voltage step, the peak current and area were extracted and raw values were normalised to capacitance.

6.3.6 Ca^{2+} imaging

Ratiometic imaging of electrically-evoked and caffeine-evoked CaTs using FuraRed. Primary cardiomyocytes were loaded with the membrane-permeant acetoxymethyl (AM) ester of FuraRed (10 μM), a ratiometric Ca^{2+} dye (excitation 435 nm and 490 nm, emission 637 nm and 657 nm; Life Technologies) at room temperature. After 10 mins, cells were plated onto a poly-L-lysine covered Perspex chamber mounted on an Olympus IX73 microscope and superfused in Tyrode imaging buffer (in mM): 135.0 NaCl, 4.5 KCl, 1.0 $CaCl_2$, 1.0 $MgCl_2$, 20.0 HEPES, 11.0 Glucose, 1.0 Probenicid at 37 °C. Myocytes were field-stimulated using the DS2A isolated constant voltage stimulator (Digitimer) at 2 Hz with 5 ms pulse duration and a voltage, determined empirically, that paced cells. Pacing continued for at least 10 cycles to attain a constant systolic amplitude. In the first protocol (Figure 6.3A), the stimulator was turned off for 2-3 secs and a 10 mM caffeine-containing solution was applied rapidly in the vicinity of a cell via a glass pipette.

In a second protocol (Figure 6.3B), caffeine application was delayed to 120 s after pacing. During this delay, SR load may decrease because of diastolic leaks. Therefore, this protocol interrogates the degree of diastolic SR Ca^{2+} leak.

Imaging was conducted at 2 ms exposure duration and 8-pixel binning using the optiMOS CMOS camera (Qimaging). Dual wavelength excitation was controlled through the Multistream (Cairn), driven by the CMOS camera trigger.

Analysis. Post-imaging analysis was conducted in ImageJ using custom-written macros. First, a background region of the image was selected and its time-average was subtracted from the whole image. Then, the cell was selected and its fluorescence signal, measured

at 490 and 435 nm, was ratioed using a custom-written script in MATLAB to extract the following information:

- Systolic and diastolic ratios were determined as the peak and nadir of the average of at least 3 consecutive CaTs;
- Resting Ca^{2+} was determined from the interval after the last electrically-evoked CaT and before caffeine application;
- SR load was estimated from the peak amplitude of the caffeine-evoked cytoplasmic $[Ca^{2+}]$ response;
- Recovery was quantified in terms of the time constant (τ) of an exponential curve, fitted to the decay phase of the CaT (approximates inversely SERCA activity) or caffeine-evoked response (approximates inversely NCX activity).

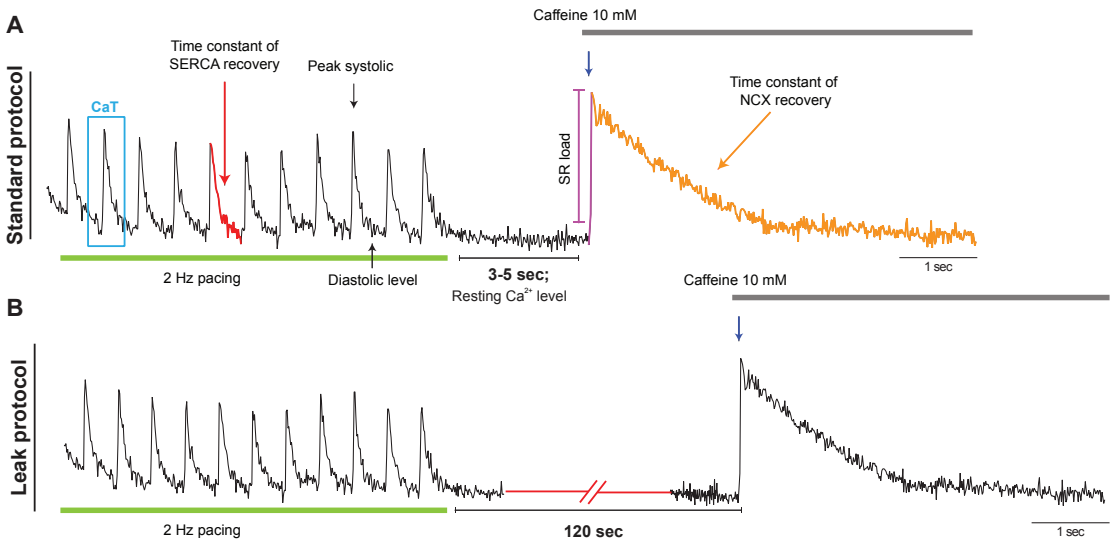


Figure 6.3 Ca^{2+} imaging protocols. A) Standard protocol, where caffeine was applied 2-3 secs after stimulus was turned off; B) Leak protocol, cells were left quiescent for 120 secs before application of caffeine.

Fast non-ratiometic Ca^{2+} imaging with Fluo-3 in line scan mode. Primary cardiomyocytes were AM-loaded with 18 μM Fluo-3AM (excitation at 488 nm, emission at > 520 nm; Life Technologies) at room temperature for 4 mins, plated onto a poly-L-lysine covered Perspex chamber mounted on a Zeiss confocal imaging microscope and superfused in Tyrode imaging buffer at 37 °C. Cells were electrically stimulated using the DS2A constant isolated voltage stimulator (Digitimer) at 5 ms duration and a 2 Hz field-stimulus. CaTs were imaged in line scan mode, with an acquisition rate of 1 line per 0.9 ms, which allowed accurate resolution of the upstroke of the CaT.

Analysis. Post-imaging analysis was conducted in MATLAB using a custom-written script. An average of at least 3 transients, normalised to the starting level (i.e. F/F_0 pseudo-ratio) was used to extract the following information:

- Peak systolic level, expressed as a ratio to its diastolic level (F_{sys}/F_0);
- Slope of CaT rise (a readout of CICR coupling);
- Time constant of the CaT decay (τ).

6.4 RESULTS

6.4.1 Validation of RNA-sequencing data by qPCR

Consistent with the RNA-sequencing data presented in Chapter 4, the expression of the RyR2, LTCC and NCX genes (*Ryr2*, *Cacna1c* and *Slc8a1*, respectively) were decreased in the iron-deficient hearts. No significant difference was observed for the expression of the SERCA gene (*Atp2a2*) by qPCR (Figure 6.4).

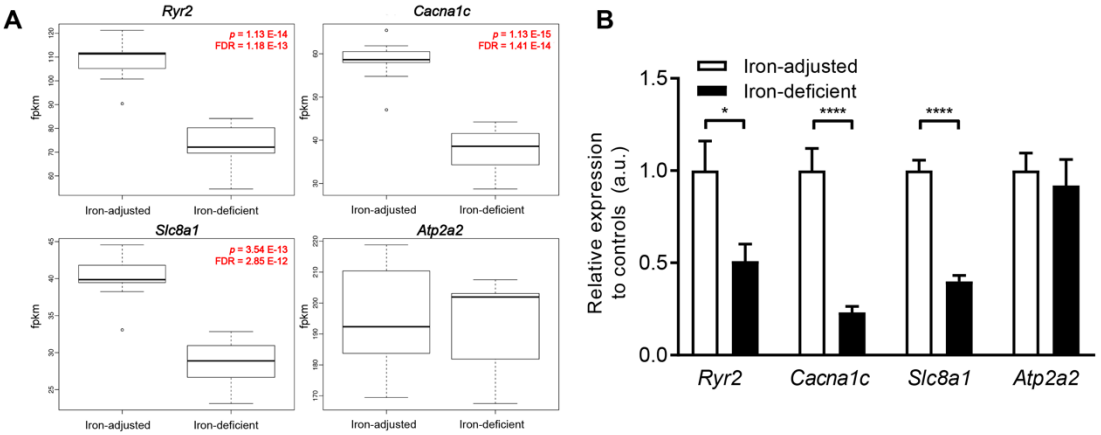


Figure 6.4 Validation of RNA-seq gene expression by qPCR. Gene expression determined by A) RNA-seq and B) qPCR from total heart tissue. Boxplot represents (from top to bottom) maximum, third quartile, median, first quartile and minimum; histogram represents mean ± SEM. FDR = false discovery rate; fpkm = fragments per kilobase of transcript per million. *p*-value was determined using a two-tail, unpaired student's *t*-test; * $p < 0.05$, **** $p < 0.0001$. n = 9 mice per cohort.

6.4.2 Western blot analyses of Ca^{2+}-handling proteins

At the protein level, RyR2 was significantly decreased by 2-fold in the hearts of iron-deficient animals (Figure 6.5), which is expected to decrease the fractional Ca^{2+} release from the SR and a fall in CaT amplitude.

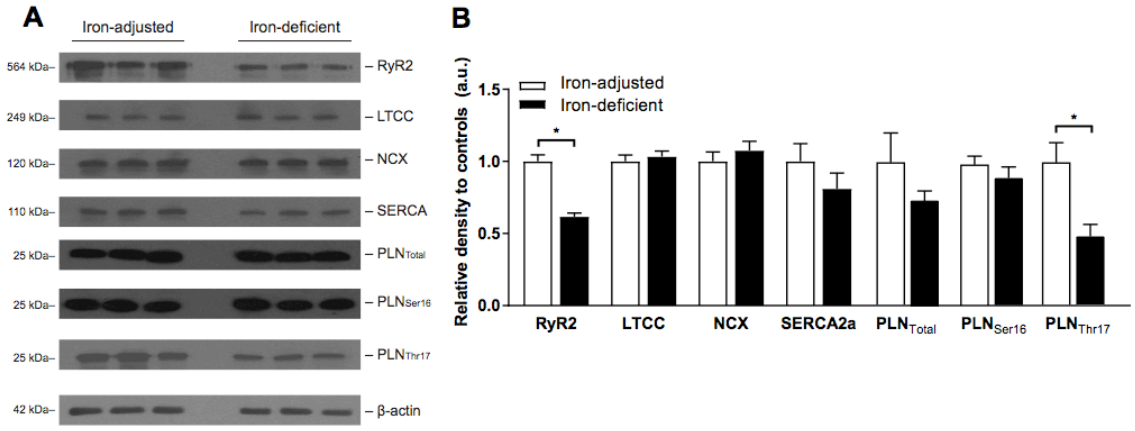


Figure 6.5 Ca^{2+} channel protein expression comparison between iron-adjusted and iron-deficient hearts. A) Western blot of RyR2, LTCC, NCX, SERCA and PLN phosphorylated states; B) Band density normalised to the loading control β-actin and plotted as mean ± SEM. Data plotted as mean ± SEM. *p*-value determined by a two-tail, unpaired student's *t*-test; * $p < 0.05$, ** $p < 0.01$, **** $p < 0.0001$. n = 3 mouse hearts per cohort.

Furthermore, neither SERCA protein levels nor total phospholamban (PLN_{Total}), an endogenous inhibitor of SERCA, and its Ser16 phosphorylation state (PLN_{Ser16}) was unaltered; however, PLN phosphorylation at Thr17 (PLN_{Thr17}) was decreased by nearly 2-fold in the iron-deficient group compared to the controls. Functionally, this predicts increased inhibition of SERCA activity by PLN.

6.4.3 Effect of an iron-deficient diet on L-type Ca^{2+} channel current

Ca^{2+} influx through the LTCC is the first step in the Ca^{2+} signaling pathway. Whole-cell voltage-clamp was used to determine L-type Ca^{2+} channel current (I_{LTCC}) in the cardiac myocytes of animals on either an iron-adjusted (control) or iron-deficient diet, with or without FCM supplementation, using a protocol that blocks K^+ conductances and Na^+ current (Figure 6.6). A group of animals on an iron-adjusted diet supplemented with FCM (IA+FCM) was included as an additional control to assess any effects of FCM that were independent of iron status. No significant differences were found in I_{LTCC} density, peak

current or total Ca^{2+} influx across the four treatment groups. This finding is in agreement with LTCC protein levels determined by western blot (Figure 6.5).

6.4.4 Effect of an iron-deficient diet on membrane capacitance

Capacitance, a measure of sarcolemmal surface area, was not significantly altered, indicating that myocytes had not been detubulated, as often happens in failing hearts (Figure 6.6D). Since capacitance is an indirect measure of t-tubule structure, immunofluorescent staining of cardiomyocyte membrane using membrane dyes such as 8-ANNEPS or FluoVolt, would be helpful in visualising t-tubule structure. However, this was not further pursued since electron micrograph analysis did not reveal any striking alterations in t-tubule morphology in the cardiomyocytes (*see* Chapter 5, Figure 5.9).

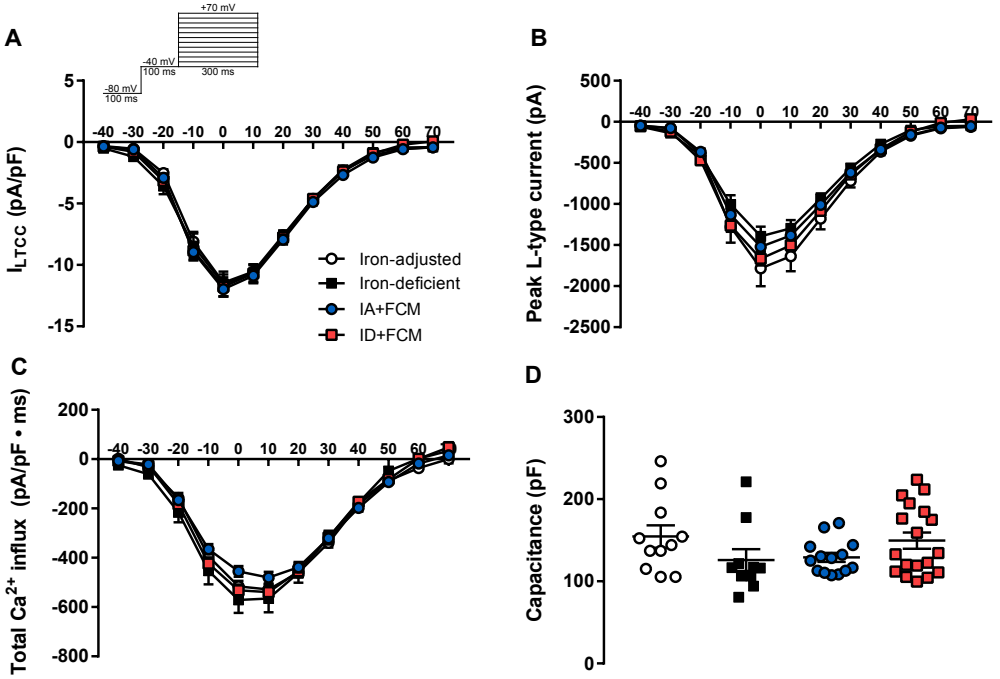


Figure 6.6 L-type Ca^{2+} channel electrophysiology. A) L-type current density, normalised to capacitance, and voltage protocol; B) Peak L-type current; C) Total Ca^{2+} influx; D) Membrane capacitance. Data plotted as (top to bottom) third quartile, median and first quartile. n = 4-6 mice per cohort and N >3 myocytes from single animal.

6.4.5 Effect of an iron-deficient diet on Ca^{2+} transients

Live-cell ratiometric imaging of cardiomyocytes was conducted using FuraRed (Figure 6.7). Calcium transients (CaT) were evoked electrically by field stimulation at 2 Hz. Diastolic Ca^{2+} level was significantly elevated in iron deficiency, whereas systolic [Ca^{2+}] was not different. Consequently, CaT amplitude was significantly reduced in animals on an iron-deficient diet (Figure 6.7D-F). Strikingly, these alterations were reversed upon correction of iron deficiency by FCM supplementation.

6.4.6 Effect of an iron-deficient diet on SR Ca^{2+} stores

To assess SR Ca^{2+} content, cells were exposed to 10 mM caffeine, a ryanodine receptor agonist, which evokes a rapid emptying of the SR Ca^{2+} store (Figure 6.3A). Total SR Ca^{2+} content was inferred from the difference between the peak cytoplasmic [Ca^{2+}] response to caffeine and resting [Ca^{2+}]. This measure was not different between the four treatment groups, indicating that SR load was likely to be unaltered, unless cytoplasmic Ca^{2+} buffering was different between the groups (higher buffering would reduce the magnitude of the cytoplasmic [Ca^{2+}] response to SR emptying).

Previous studies have suggested that some forms of HF are linked to leaky RyR2 channels which result in a partial dissipation of the SR store (Respress *et al*., 2012). To assess the 'leakiness' of the SR store, cells were first electrically paced to fill the SR with Ca^{2+} and then left quiescent for 120 secs before exposure to 10 mM caffeine (Figure 6.3B). During this quiescent period, leaky RyR2 channels would be expected to gradually reduce the size of the SR Ca^{2+} store. Thus, a substantial leak would have measurably reduced caffeine-evoked Ca^{2+} release. However, the cytoplasmic [Ca^{2+}] response to caffeine was not different between the four experimental groups (Figure 6.7G, striped bars), and was also

not different to the response to an immediate caffeine exposure (3-5 s delay after pacing, solid bars). Thus, myocytes isolated from iron-deficient animals were not significantly leakier than the controls.

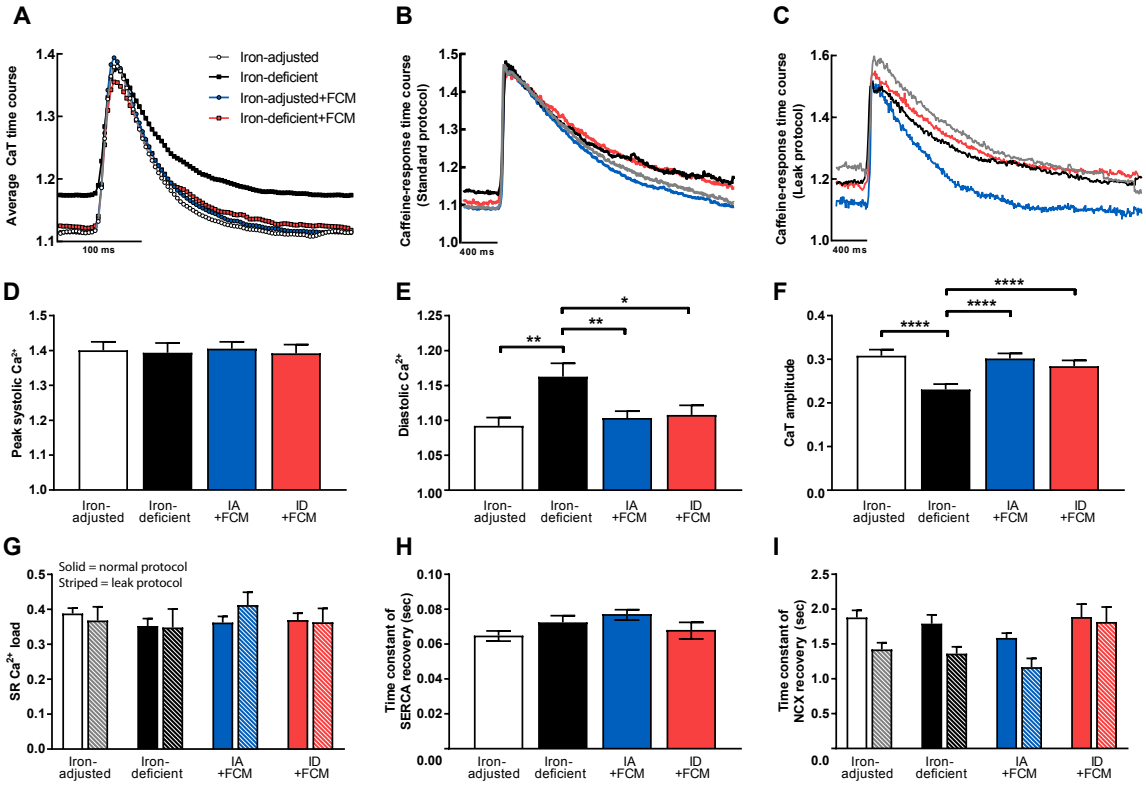


Figure 6.7 CaT imaging of live cardiomyocytes loaded with FuraRed. Cells were paced at 2 Hz field stimulus. A) Average CaT time course; B) and C) Average caffeine-response time course following standard or leak protocol; D) Peak systolic Ca^{2+} (490/435 ratio); E) Diastolic Ca^{2+}(490/435 nm ratio); F) CaT amplitude (difference in ratio); G) SR Ca^{2+} load; H) Time constant of SERCA recovery; I) Time constant of NCX recovery. Data plotted as mean ± SEM. IA+FCM = mice on iron-adjusted diet supplemented with FCM; ID+FCM = mice on iron-deficient diet supplemented with FCM. *p*-value determined by either a one-way ANOVA and post-hoc Tukey's multiple comparison test or a two-way ANOVA and post-hoc Sidak's multiple comparison test; * $p < 0.05$, ** $p < 0.01$, **** $p < 0.0001$. n = 4 mice per cohort and N > 10 myocytes from single animal.

6.4.7 Effect of an iron-deficient diet on NCX and SERCA activity

Ca^{2+} recovery from a CaT is driven primarily by SERCA, therefore the time constant of this process is an inverse estimate of SERCA activity. In contrast, SERCA activity is unable to contribute towards Ca^{2+} recovery during caffeine exposure because the SR is short-circuited by open RyR channels. Instead, the recovery during caffeine exposure is primarily due to NCX activity, thus its time constant is an inverse readout of NCX activity.

There was no significant effect of an iron-deficient diet on time constants related to SERCA and NCX activity (Figure 6.7G and I). However, time constant is a simplistic descriptor of activity, and these results cannot exclude a more subtle shift in the Ca^{2+}-dependence of SERCA and/or NCX activity.

6.4.8 Effect of an iron-deficient diet on LTCC-RyR coupling

The image-capture rate of FuraRed, due to alternating between two excitation wavelengths, is inherently slow, and therefore it is not possible to accurately resolve rapid events, such as the rising phase of the CaT, a read out of LTCC-RyR coupling. To increase temporal resolution, the CaTs were measured in parallel using Fluo-3 (single excitation dye) in line-scan mode (approximately 1.0 linescan/ms) on a confocal system.

Consistent with the data obtained using FuraRed, the CaT amplitude (peak CaT) was significantly reduced in the myocytes obtained from hearts of iron-deficient animals (Figure 6.8B). Furthermore, the rate of $[Ca^{2+}]$ rise during the CaT (Figure 6.8C) and the time to 50% recovery of the CaT (Figure 6.8D) remained unchanged across the four groups, the latter which was in agreement with the data collected with FuraRed (*see* Figure 6.7H).

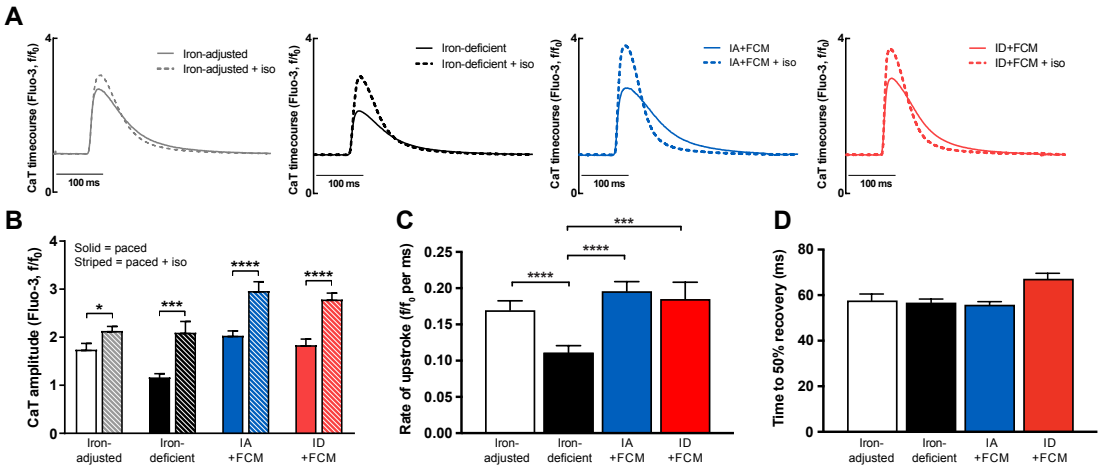


Figure 6.8 CaT imaging of live cardiomyocytes loaded with Fluo-3 dye and confocal line scan. Cells were paced at 2 Hz field stimulus. A) Average CaT amplitude for iron-adjusted, iron-deficient, IA+FCM and ID+FCM (left to right); B) Maximum amplitude reached during CaT; C) Rate of CaT upstroke D) Time to 50% recovery of CaT. Data plotted as mean ± SEM. *p*-value determined by a two-way ANOVA and post-hoc Sidak's multiple comparison test; * $p < 0.05$, ** $p < 0.01$, *** $p < 0.001$, **** $p < 0.0001$. n = 3 biological replicates and N > 10 myocytes from single animal.

6.4.9 Effect of an iron-deficient diet on isoprenaline-stimulated CaTs

To assess Ca^{2+}-handling kinetics under a stress condition, the cardiac myocytes were exposed to 100 nM of the β-adrenoreceptor agonist isoprenaline (iso). Consistent with existing literature, a rise in CaT amplitude and faster relaxation was observed in all four treatment groups in response to acute treatment with isoprenaline (Figure 6.8A, compare solid vs dotted line) (Ginsburg and Bers, 2004). Importantly, in the iron-deficient group, the CaT amplitude was raised to levels comparable to the controls, suggesting that the adrenergic cascade remained intact with iron deficiency.

6.5 DISCUSSION

The aim of the present study was to determine the effects of an iron-deficient diet on Ca^{2+} signaling in the heart, and to gain a mechanistic understanding of the underlying effects. Two major findings were presented in this chapter. First, higher diastolic Ca^{2+} level and smaller CaT amplitude were observed in the cardiomyocytes of animals on an iron-deficient diet. Second, the observed changes could be reversed by FCM supplementation in mice. Figures 6.9 and 6.10 summarizes the results presented in this chapter.

6.5.1 An iron-deficient diet affects diastolic [Ca^{2+}] and CaT amplitude

Compared to the controls, cardiomyocytes of iron-deficient animals had an elevated diastolic [Ca^{2+}] in the absence of any significant change in peak systolic [Ca^{2+}]. Consequently, a decrease in CaT amplitude was observed. As there was no significant change in SR Ca^{2+} load or SERCA activity (Figure 6.7G and H), the effect on CaT amplitude is likely to be due to a decrease in fractional release. Reduced fractional release was not due to a change in trigger Ca^{2+} carried by L-type current as this was unaltered in iron-deficient animals (Figure 6.6A). The surface area of the cardiomyocytes, measured as capacitance, was also not significantly different in the two cohorts, indicative of no significant loss of t-tubule (which may otherwise decrease LTCC-RyR2 coupling and reduce SR Ca^{2+} release) in the iron-deficient group (Figure 6.6D). That being said, decreased CaT amplitude may be due to a rise in Ca^{2+} buffering power, which was not determined in this series of experiments.

Reduced fractional release could also be relate to the activity of RyR channels and/or their coupling to LTCC. The rate of [Ca^{2+}]-rise reported by Fluo-3 during a CaT was unchanged

in iron deficiency, arguing that the onset of CICR was similar to control levels (Figure 6.8D).

Western blot analysis did find a significant decrease in RyR2 protein (Figure 6.4) in iron deficiency which may explain the decrease in fractional release. Thus, reduced fractional SR release could be due to slower Ca^{2+} release from RyR channels beyond the initial trigger period. Reduced RyR density could result in weaker diffusive coupling between the nearest RyR2 channels. Additional experiments would be required to test this hypothesis.

Changes in diastolic [Ca^{2+}] are likely to involve a re-adjustment of the balance of Ca^{2+}-handling fluxes, and may involve changes in the activity of several proteins, buffering properties and/or structural alterations.

At the level of protein expression, SERCA was not significantly affected but PLN was significantly decreased in iron deficiency (Figure 6.5). However, there was no difference in the fraction of phosphorylated PLN at Ser16 and Thr17 between iron-deficient and control animals. Under normal conditions, PLN expression exceeds SERCA by approximately 2.5-fold and only about 40% of SERCA is inhibited by PLN (MacLennan and Kranias, 2003). Therefore, it is difficult to predict the functional consequences of an apparent modest decrease in PLN to SERCA ratio. However, when reviewing the study in its entirety, it appears that a decrease in PLN may not have a prominent functional impact of SERCA activity, which is consistent with the comparable time constant of CaT recovery (Figure 6.7I and Figure 6.8D). Collectively, the rise in diastolic Ca^{2+} level is unlikely to be a result of changes in PLN protein expression and its phosphorylation state.

An elevation of diastolic [Ca^{2+}] can be due to leaky RyRs, impaired Ca^{2+} clearance from cytoplasm by SERCA and/or NCX activity, or incomplete buffering by mitochondria (Figure 6.11A and B) (Eisner *et al*., 2017; Periasamy and Janssen, 2008). In this study, RyR2 were not significantly leakier in the iron-deficient animals compared to the controls (Figure 6.7G). Furthermore, the time constant of recovery by SERCA and NCX were not different in iron deficiency (Figure 6.7 H and I). However, this does not preclude the possibility of more subtle alterations that affect the Ca^{2+}-activation curve of these proteins. For example, a right-shift in the activation of either SERCA or NCX would result slower clearance of cytoplasmic Ca^{2+}, thus raising diastolic [Ca^{2+}] (Figure 6.11A). This could be interrogated by biophysical kinetics analysis (mathematical modelling) using the already acquired time constant data.

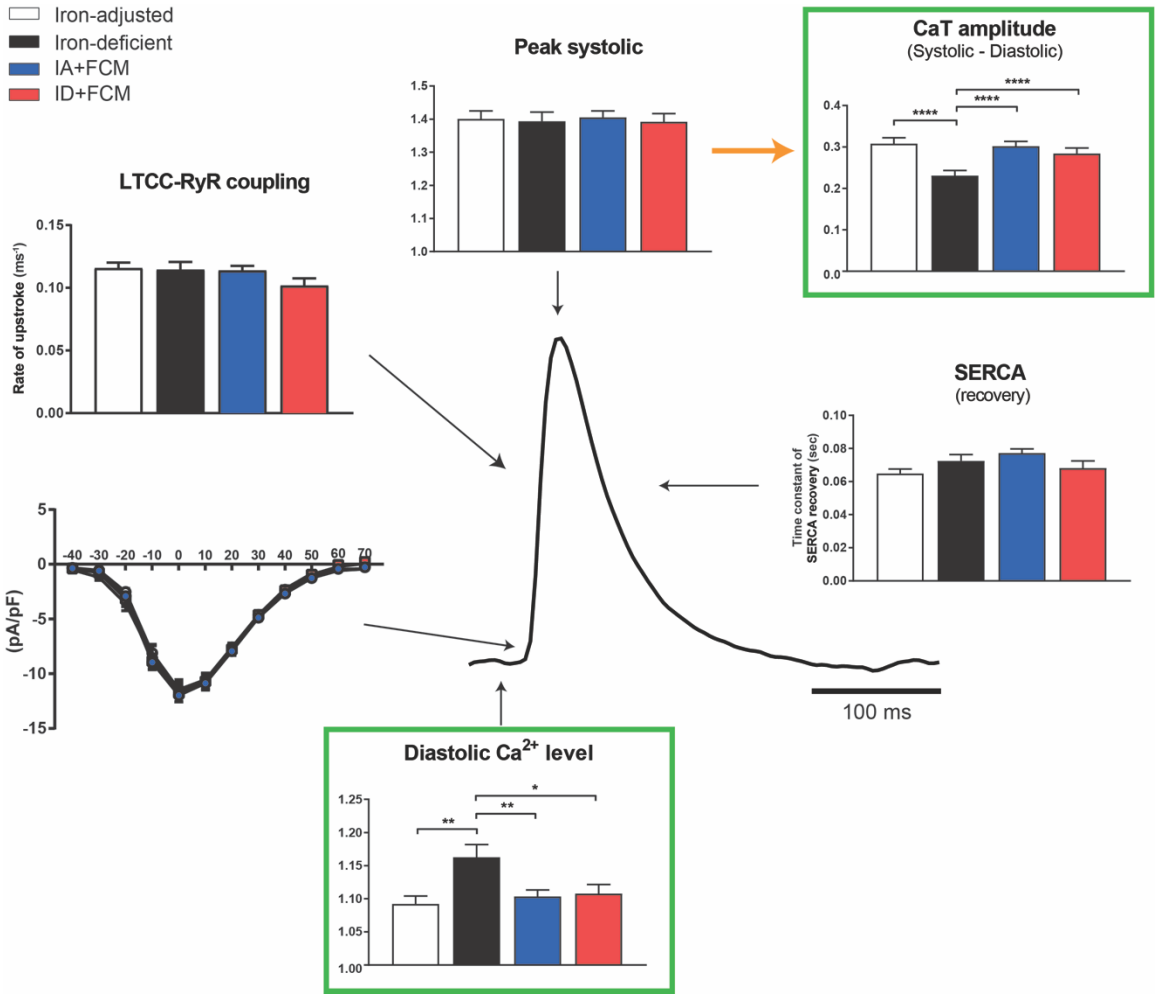


Figure 6.9 Summary of results involving CaTs. Components that make up a typical CaT was investigated: (clockwise) Diastolic Ca^{2+} level, L-type Ca^{2+} current, gain of CICR, peak systolic Ca^{2+} level and time constant of recovery of SERCA. CaT amplitude was calculated as the difference between peak systolic and diastolic Ca^{2+} level. Significant differences in diastolic Ca^{2+} level and CaT amplitude were observed between the iron-adjusted and iron-deficient group.

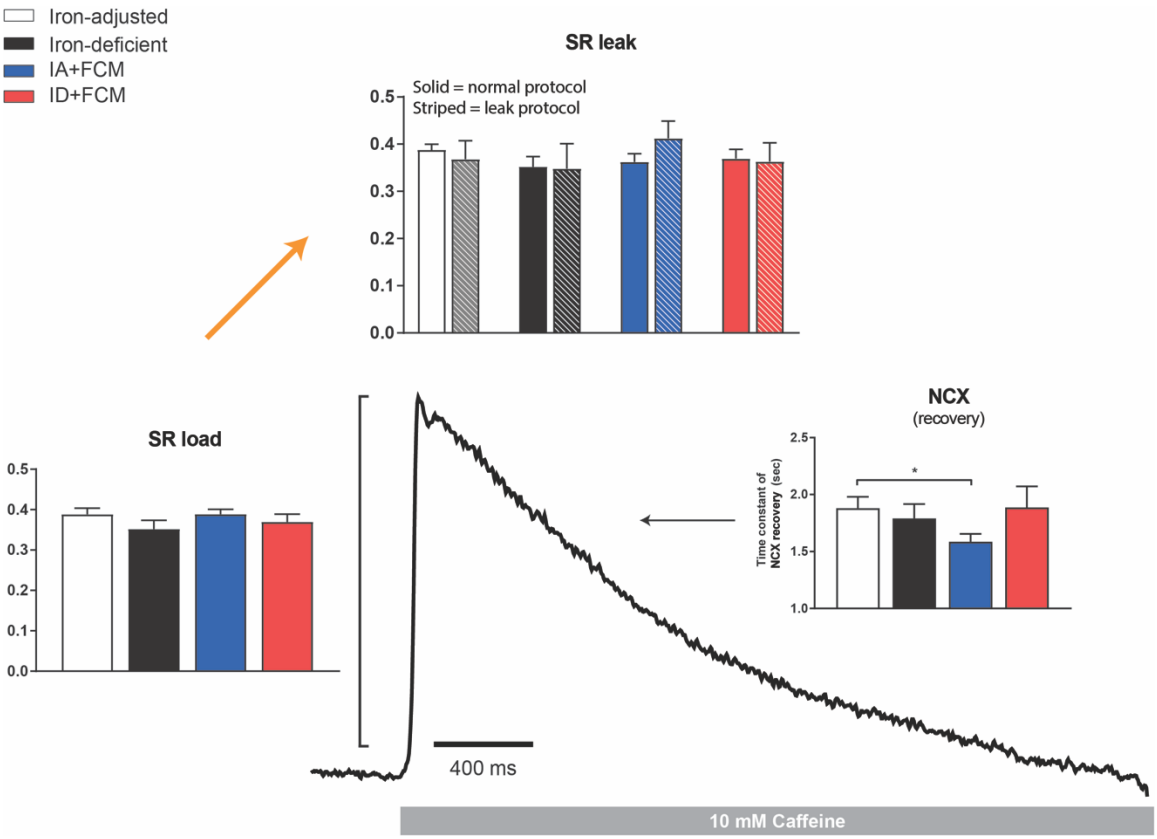


Figure 6.10 Summary of results involving caffeine-evoked response. SR Ca^{2+} load was investigated by measuring the caffeine-evoked Ca^{2+} response and was estimated as the difference between peak Ca^{2+} response and resting Ca^{2+} level. This assumes that Ca^{2+} buffering capacity is not affected by an iron-deficient diet. The time constant of recovery by NCX was also determined. No significant differences were observed in these parameters between the iron-adjusted and iron-deficient groups.

6.5.2 FCM supplementation restores Ca^{2+} handling in the heart

The correction of iron deficiency by FCM supplementation was able to reverse the adverse changes in Ca^{2+} handling to control levels. This effect on Ca^{2+} signaling in the myocytes was observed together with the improvement in ejection fraction (Chapter 3, Figure 3.15), suggesting a causative relationship between Ca^{2+} handling and iron deficiency. However, further experiments would be required to determine 1) whether restoration of Ca^{2+} signaling precedes, and therefore contributes, to improvements in ejection fraction and 2) the mechanistic link between improvements in Ca^{2+} signaling and cardiac function.

Another interesting finding presented in this chapter was that iron supplementation in iron-replete animals did not adversely affect cardiac Ca^{2+} handling. A major concern when administering iron supplementation in patients is the danger of iron-overload and adverse downstream effects (i.e. ROS damage). However, in this study, two doses of FCM, the equivalent amount required to correct iron deficiency, was well tolerated in the iron-replete animals.

6.5.3 Iron deficiency and supplementation does not affect response to β-adrenergic stimulation

The addition of the β-adrenergic agonist isoprenaline resulted in significant increases in CaT amplitudes in all treatment groups. Importantly, in the iron-deficient group, the additive inotropic response was comparable to that of the controls. This suggests that the mechanisms of response to sympathetic stimulation and downstream cAMP signaling pathway was not affected as a result of iron deficiency.

Furthermore, western blot analysis suggested a significant decrease in PLN phosphorylation of Thr17 (Figure 6.5) in iron deficiency, which raised the possibility that differences in baseline PLN phosphorylation state is one mechanism by which SERCA activity may be affected. This hypothesis gains strength as acute treatment of isoprenaline at a concentration (100 nM) sufficient to produce near-saturating phosphorylation of PLN Ser16 and Thr17 indeed raised amplitude of CaT in the cardiomyocytes derived from iron-deficient animals to levels comparable to the CaT amplitude of iso-stimulated control cardiomyocytes.

Finally, like the controls, the addition of isoprenaline also resulted in enhanced CaT amplitudes in the cardiomyocytes of FCM-supplemented animals, demonstrating that FCM does not adversely interfere with the β-adrenergic response.

6.5.4 Impaired cardiac energetics are not limiting for SERCA activity and SR Ca^{2+} loading

The study in Chapter 5 revealed a switch in substrate utilization towards anaerobic respiration at the 6 week time point. It was discussed that this would predict a decrease in the local energy supply in the heart, which was consistent with the cardiac dysfunction observed by cine-MRI.

As an ATPase, the activity of SERCA requires a supply of ATP and thus, would be functionally impaired in energy starved conditions. Indeed, reduction in the availability of ATP, by a reduction in ATP production and/or a decrease in PCr, diminishes SR Ca^{2+} loading capacity (Joubert *et al*., 2008). However, as seen above, SR [Ca^{2+}] remained

undisturbed in the iron-deficient mice, putting into question the degree to which diminished energetics affect SERCA.

Previously, Joubert *et al.* (2008) have shown that a maximal activation of glycolysis is sufficient to restore normal SR loading capacity in rat HF models, indicating that glycolysis plays an important role in supporting SERCA function in the context of HF. Furthermore, the addition of sugar phosphates to isolated SR microsomes produced sufficient amounts of ATP to support normal SERCA activity, suggesting that the ATP demands for SERCA can be met by glycolysis alone (Xu *et al*., 1995; Zima *et al.*, 2006). Thus, whilst the cardiomyocytes of iron-deficient animals may have diminished energy supply which ultimately puts a strain on normal cardiac performance, this impairment is not due to energetic limitations on SERCA, since the output of glycolysis and subsequent anaerobic metabolism appears to be sufficient to support SERCA's normal SR loading capacity.

6.5.5 Perturbations in Ca^{2+} handling can relate to cardiac dysfunction in iron-deficient animals

Diastolic dysfunction, a prominent feature in HF, is characterised by slow or incomplete relaxation of the ventricles during diastole and is recognised as a major contributor to the pathophysiology of HF (Asp *et al.*, 2013). Within this pathological setting, changes in diastolic [Ca^{2+}] have been reported. Both Beuckelmann *et al.* (1992) and Gwathmey *et al.* (1991) showed that the myocytes from end-stage HF patients tended to have higher diastolic [Ca^{2+}] levels compared to healthy hearts. Furthermore, a reduction in CaTs is recognised as a hallmark of the failing heart (Periasamy and Janssen, 2008).

Both of these features were observed in cardiomyocytes of iron-deficient animals are likely to contribute to the reduced ejection fraction observed by cine-MRI (*see* Chapter 3, Figure 3.15 and Table 3.6). The question remains as to the causal relationship of Ca^{2+} and cardiac performance. Since contraction of the cardiac muscle requires proper Ca^{2+} signaling, one would predict that alterations in Ca^{2+} handling precedes the functional phenotype at the organ level. There is a possibility that reduced ejection fraction is actually a consequence of increased arterial pressure (i.e. hypertension), which has previously been associated with iron deficiency (Cotroneo *et al*., 2015; Rhodes e*t al*., 2011), but this effect would not be evident in isolated myocyte preparations. Additional experiments would have to be carried out in order to test this hypothesis.

6.5.6 Role of iron in altering Ca^{2+} handling

It is interesting that cardiomyocytes from iron-deficient animals behave differently than the controls, given that the myocytes themselves are not iron-deficient, at least in terms of total iron (Chapter 3, Figure 3.7). However, a redistribution of iron between different intracellular pools in cardiomyocytes or different parts of the heart cannot be excluded.

Nevertheless, chronic hypoxia of the cardiac tissue is an attractive explanation to the observed phenomena given that the iron-deficient animals were anaemic. The induction of HIF in the iron-deficient animals, observed in Chapter 5 (Figure 5.4 and Figure 5.5), adds weight to this notion.

Indeed, chronic hypoxia is known to alter Ca^{2+} signaling in the heart (Chen and Li, 2012; Imahashi *et al.*, 2005; Kanatous *et al.*, 2009; Pei *et al*., 2003). Kanatous *et al*. (2009) showed that hypoxia reduces LTCC-mediated Ca^{2+} influx. A decrease in SR Ca^{2+} content

has also been reported in rat ventricular myocytes exposed to chronic hypoxia (Pei *et al.*, 2003). Although neither of these results are consistent with those presented in this study, this does not eliminate the role of hypoxia in effecting the results observed in this study. It is possible that the added effect of systemic iron deficiency in addition to anaemia may evoke a different response in the cardiomyocytes compared to hypoxia alone.

6.5.7 Novelty of the current study

Alterations in CaTs are known to contribute to the pathophysiology of HF. In current literature, this change typically involves dysregulated Ca^{2+} channel expression or activity, or a loss of t-tubule and/or dyad structural/coupling integrity. In this study, these parameters were explored and no significant perturbations were observed. This raises the possibility of a new paradigm in which iron deficiency influences cardiac Ca^{2+} handling through a non-canonical pathway which may be driven by chronic hypoxia, as a result of anaemia.

Although the importance of diastolic [Ca^{2+}] is recognised in the pathology of HF, it is an experimental parameter which is often missed because most Ca^{2+} imaging experiments are conducted using single wavelength Ca^{2+} dyes such as Fluo-3 or Fluo-4. These dyes are chosen for their unique properties that confer a high signal-to-noise ratio, fast Ca^{2+} "on" and "off" kinetics and high sensitivity in response to Ca^{2+} gradients (Guatimosim *et al.*, 2011). However, when bound to Ca^{2+}, there is very little shift in its excitation or emission spectrum, which makes it impossible to perform ratiometric measurements of Ca^{2+}. Instead, the raw data must be normalised to starting fluorescence to account for loading

efficiency of the dye, cell size, and fluorescent bleaching. The reported relative Ca^{2+} levels. Thus, in these measurements, diastolic Ca^{2+} is always 1.0 by definition.

In contrast, ratiometric dyes such as FuraRed, have two optimum excitation/emission wavelength corresponding to a Ca^{2+}-bound and Ca^{2+}-unbound state. An elevation of Ca^{2+} concentration induces an increase in FuraRed emission fluorescence when excited at 435 nm and a corresponding decrease in fluorescence when excited at 490 nm (Parys, 2013). The ratio between the two fluorescence can give absolute Ca^{2+}concentration (when calibrated). An additional advantage of FuraRed over other ratiometric dyes such as Indo-1 or Fura-2 is that the excitation wavelength is outside the UV region, thus autoflourescence is avoided as an artefact of measurement. However, because the dual wavelength properties of ratiometric dyes imposes limitations in temporal resolution and requires specialized equipment, single wavelength dyes are typically preferred over ratiometric dyes. As a result, diastolic [Ca^{2+}] is often not measured and therefore, little is known about diastolic Ca^{2+} levels in different models of HF.

Experimentally, it is known that altering diastolic [Ca^{2+}] can have a physiological impact on diastolic function. Elevated diastolic Ca^{2+} levels leads to incomplete relaxation during diastole, subsequently reducing ventricular filling and ejection fraction (Lei *et al*., 2016). Given these findings, it is possible to postulate that a chronic elevation in diastolic [Ca^{2+}] could initiate a vicious cycle wherein reduced ejection fraction could lead to compensatory reflex tachycardia in a continuous positive feedback loop, reducing the time allowed for CaT recovery and raising diastolic [Ca^{2}] further, thereby exacerbating diastolic

dysfunction and leading to HF (Figure 6.11C). In addition, these effects could be further amplified in stressed or injured hearts.

Furthermore, high diastolic Ca^{2+} concentrations will also raise nuclear [Ca^{2+}], which is a strong trigger of pro-hypertrophic cascades. This occurs via the nuclear Ca^{2+}/calmodulin–dependent protein kinase II (CaMKII), an enzyme which regulates histone modifiers, such as histone deacethylases, and transcription factors, such as MEF, and whose activity is regulated by Ca^{2+} (Figure 6.11D) (Li *et al.*, 2006; Ljubojevic and Bers, 2015). By driving diastolic [Ca^{2+}] upwards, iron deficiency can lead to maladaptive hypertrophy and ultimately HF.

When considering iron deficiency in the context of HF, these could be one of the reasons for why iron deficiency is detrimental to the injured heart and is associated with a worse prognosis in HF patients compared to those patients who are iron-replete.

6.5.8 Limitations of the current study

One important aspect of Ca^{2+} handling that was not surveyed in this study was cytoplasmic Ca^{2+} buffering. No changes in buffering capacity have been reported in ventricular myocytes in HF models thus far (Piacentino *et al*., 2003). However, an increase in Ca^{2+} buffering capacity would dampen the CaT amplitude and raise diastolic [Ca^{2+}] (Eisner *et al*., 2017). Thus, the observations presented in this chapter could be explained by increased Ca^{2+} buffering. However, higher buffering would also slow the upstroke of the CaT, which was not observed (Figure 6.8C).

Another possibility is that the mitochondria are less polarized in iron deficiency due to the hypoxia, which would result in reduced sequestration during Ca^{2+} signaling (Figure

6.11B). Normally, the highly negative mitochondrial membrane potential can drive the uptake of Ca^{2+} into the matrix, but if this is less effective, diastolic [Ca^{2+}] in cytoplasm would rise. Additional experiments would be required to demonstrate the effect of an iron-deficient diet on cardiac Ca^{2+} buffering as well as mitochondrial polarity.

It would be of particular interest to investigate the effect of iron deficiency on histidyl dipeptides which buffer a wide range of divalents, including Ca^{2+} and, putatively, Fe^{2+} (Boldyrev, 2007). In the heart, histidyl dipeptides are present in very high concentrations (up to 20 mM). Under iron-deficient conditions, it is plausible that these dipeptides are degraded in order to increase the labile iron pool; this would have a knock-on effect on Ca^{2+} dynamics. Histidyl dipeptides are particularly important as mobile Ca^{2+} carriers which diffusively couple different parts of the cell, such as the junctional and network SR, which correspond to the sites of Ca^{2+} release (RyR) and uptake (SERCA), respectively. Any reduction in this coupling would lengthen the time constant of Ca^{2+} cycling, hence raising diastolic [Ca^{2+}].

6.6 CONCLUSIONS

Alterations in CaTs are known to underlie the pathophysiology of at least some forms of HF. In current literature, this change has typically implicated dysregulation of the expression of Ca^{2+}-handling proteins or their biophysical properties, or ultra-structural changes such as detubulation and disintegration of the dyadic structure. However, changes in diastolic Ca^{2+} have rarely been measured and tested. Here, we present a new paradigm of failing hearts that involves a rise in diastolic [Ca^{2+}] and a fall in CaT amplitude, with

consequent changes in ejection fraction. The putative mechanisms for the change in Ca^{2+} handling does not involve hitherto reported mechanisms.

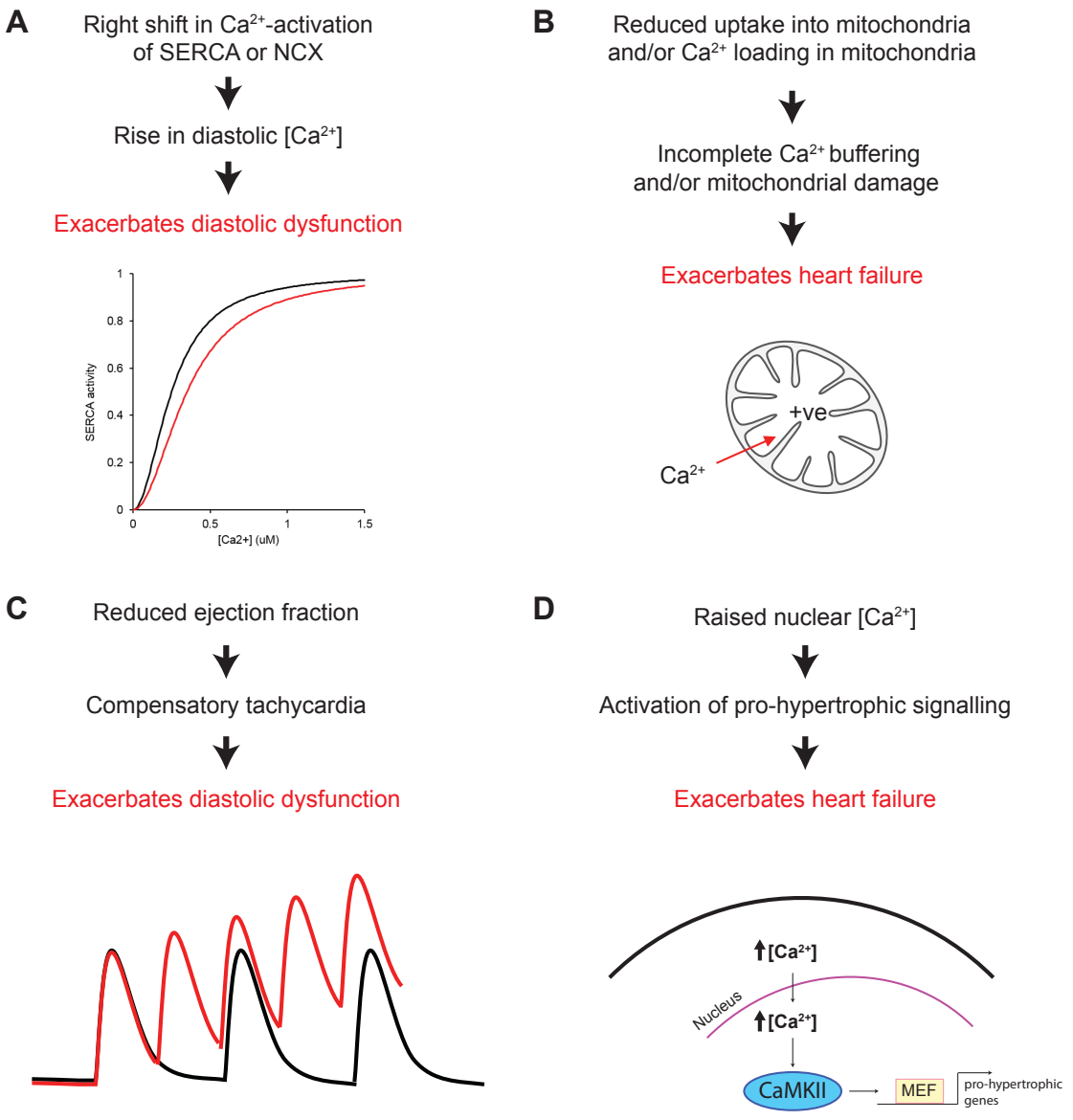


Figure 6.11 Consequences of perturbations in diastolic Ca^{2+} level. A) Elevation of diastolic [Ca^{2+}] in iron-deficient mice may be due to a shift in Ca^{2+}-activation of SERCA or NCX; B) Excess diastolic [Ca^{2+}] may reduce mitochondrial polarity, possibly resulting in either incomplete Ca^{2+} buffering or mitochondrial Ca^{2+} loading; C) Reduced ejection fraction could lead to exacerbating in diastolic dysfunction; D) Raised cytoplasmic [Ca^{2+}] in diastole may activate pro-hypertrophic signaling by raising nuclear [Ca^{2+}].

CHAPTER 7:

CONCLUSIONS

7.1 FINAL SUMMARY OF THESIS

This thesis set out to study the effects of iron deficiency on the heart in a mouse model of short-term iron deficiency. First, the effect of an iron-deficient diet was studied by serial measurement of blood haemoglobin and serum iron parameters, which allowed determination of the animals' iron status. One striking observation was the recovery of blood haemoglobin concentration over time in the absence of intervention, which is evidence of adaptive mechanisms in response to iron starvation. For this reason, the mouse model used in this thesis was that of short term iron-deficiency, rather than a chronic model.

In vivo studies have shown clear changes in cardiac function in response to dietary iron deficiency. These alterations appeared to be related to the animal's overall iron status, which, in turn, depended on the length of dietary treatment. Briefly, a cardiac phenotype was most apparent when the iron deficiency was severe, manifesting itself only when the animals were anaemic. Furthermore, the appearance of this phenotype was short-term, disappearing when the anaemia was corrected with time. Finally, intravenous iron supplementation in previously iron-deficient animals had a rescue effect on *in vivo* heart function. However, the rescue was only in ejection fraction, suggesting a compensation, either by sympathetic stimulation or mechanisms consistent with Frank-Starling Law, rather than a reversal of the phenotype developed due to iron deficiency.

Mechanistic insight into these whole-organ observations was gained using a range of experimental techniques. Alterations at the gene expression level was demonstrated using a bioinformatics approach. The gene expression profile of iron-deficient animals was

substantially different when compared to the controls, arguing that iron deficiency affects cardiac function at the most fundamental level. Because of the nature of iron deficiency, such genome-wide alterations are likely driven by epigenetic mechanisms, which is supported by the data showing changes in the histone methylation status.

Bioinformatic analysis highlighted changes in two pathways which were relevant to the cardiomyocyte biology, and these were explored further in functional studies. In the first study, metabolism of the heart was investigated to better understand the impact of iron deficiency on cardiac energetics. Using a combination of *in vivo* and *in vitro* methods, this study demonstrated clear alterations in substrate utilisation in iron deficiency and found that these perturbations were mostly likely driven by HIF stabilization in response to chronic hypoxia. Importantly, altered metabolism was consistent with the cardiac phenotype observed at the organ level.

In the second study, the functional impact of iron deficiency on the Ca^{2+} signaling pathway was investigated at the level of the cardiomyocyte. Notable findings included elevated diastolic Ca^{2+} levels and reduced Ca^{2+} transient amplitude, with other parameters mostly unaltered. Various aspects of this pathway, such as protein levels, L-type Ca^{2+} current, SR Ca^{2+} load and time constants of Ca^{2+} recovery, were studied in order to elucidate a mechanism by which Ca^{2+} signaling was perturbed by iron deficiency. Within the scope of this study, a molecular mechanism remained elusive. Nevertheless, these findings are in keeping with the observed iron-status-dependent alterations in ejection fraction in mice at this time point.

Based on the evidence gathered in thesis and published literature, it should be emphasised that *mild* iron deficiency alone does not appear to pose a health risk or lay additional burden on the heart in otherwise healthy individuals (both mouse and humans), and a modest cardiac dysfunction is observed only when anaemia is present. Rather, the detrimental effects of mild iron deficiency becomes more relevant in the diseased state. Whereas many clinical studies have shown this to be true in heart failure patients, it is of immense personal interest to investigate the physiological and molecular basis of this phenomenon.

7.2 FUTURE WORK

Possible future studies have already been discussed in the relevant chapters. Some of these are already in progress and will be re-iterated below.

7.2.1 Systemic vs cardiac-specific model of iron deficiency

In this thesis, a mouse model of systemic iron deficiency was used to address the aims of the study. This model of iron deficiency was chosen because systemic iron deficiency, rather than a cardiac-specific iron deficiency, more closely resembles the human state. However, given the biological importance of iron, deficiency of this micronutrient at the systemic level is expected to elicit numerous interconnected responses throughout the body. This poses a challenge when attempting to identify mechanisms of disease progression specifically in the heart because it is difficult to separate those reactions which occur secondary to systemic shock from those effects which directly impinge on the cardiomyocytes themselves. This difficulty was observed primarily in Chapter 4.

To minimize this confounding effect, the effect of iron deficiency on cardiac gene expression will be interrogated in a transgenic mouse model harbouring a cardiac-specific C326Y FPN mutant which is hepcidin resistant. These animals, previously characterised by Lakhal-Littleton *et al.* (2016), are iron deficient only in the cardiomyocytes against a background of normal systemic iron status and these animals develop fatal left ventricular dysfunction between the ages of 3 and 6 months.

Our laboratory is currently generating a taxomifen inducible Myh6.Cre C326Y FPN mouse line. Compared to the mouse model used by Lakhal-Littleton *et al.* (2016),

inducibility of the genetic mutation in this new model will give the added advantage of eliminating any effects of the mutation on the development of the mouse *in utero*. Therefore, in addition to comparing this animal model to the diet model, it would also be possible to identify any differences between the constitutive and the inducible model.

7.2.2 Effect of iron deficiency on cardiac buffering capacity

As mentioned in Chapter 6, one important aspect of Ca^{2+} signaling that was not investigated was the effect of iron deficiency on cytoplasmic Ca^{2+} buffering capacity. An increase in buffering capacity would result in an increase in diastolic Ca^{2+} levels. This is currently being pursued by imaging the caffeine-evoked Ca^{2+} response under voltage clamp conditions, which would give both the peak Ca^{2+} release in response to caffeine and the NCX current, from which the Ca^{2+} buffering capacity can be extracted. Further to this protocol, Ca^{2+} mobility will also be measured in order to determine any changes in dipeptide concentrations that may arise from iron deficiency.

7.2.3 Determination of RyR2 density in iron deficiency

As discussed in Chapter 6, a decrease in CaTs could be a consequence of a reduction in RyR2 density. This is currently being investigated by measuring the velocity of Ca^{2+} waves when cardiomyocytes are Ca^{2+} loaded by raising extracellular [Ca^{2+}].

7.2.4 Investigating the effects of iron deficiency in a model of heart failure

Typically, mild iron deficiency alone is not a major health risk in an otherwise healthy individual. In the heart, the burden imposed by iron deficiency becomes more relevant

after an episode of acute heart failure. To understand why iron deficiency is so detrimental in heart failure patients, it would be necessary to investigate the effects of iron deficiency in a model of heart failure.

Our laboratory is currently working on a model of heart failure in rats based on an infarct by cryo-injury. In this model, the following work is currently under way:

a) Establishing the time course of cardiac function in the cryo-infarct heart failure model by MRI;

b) Investigating whether cardiac function is worsened in infarcted animals on an iron deficient diet compared to those on a control diet;

c) Determining how cardiac metabolism is altered due to cryo-injury and whether iron deficiency results in a different or more exaggerated metabolic perturbation using both *in vivo* and *in vitro* methods;

d) Assessing whether changes in diastolic [Ca^{2+}] and CaT amplitude are replicated in a rat model of iron deficiency, and whether these changes become more pronounced in the iron-deficient animals following infarct.

7.3 CONCLUDING REMARKS

While iron deficiency is known to contribute to the development of cardiomyopathy and its progression into heart failure, the pathological mechanisms have not yet been fully determined. Given the detrimental effects of iron deficiency in the context of heart failure patients, there is a need to better understand the role of iron in cardiomyocyte physiology. The studies presented in this thesis contribute to the growing body of work showing the importance of iron homeostasis in the heart, demonstrating that iron deficiency in mice is capable of influencing diverse biological processes which impinge on cardiac performance.

CHAPTER 8:

REFERENCES

Anderson, G.J., and Frazer, D.M. (2017). Current understanding of iron homeostasis. Am. J. Clin. Nutr.Agarwal, M., Phan, A., Willix, R., Barber, M., and Schwarz, E.R. (2011). Is Vitamin D Deficiency Associated With Heart Failure? A Review of Current Evidence. J. Cardiovasc. Pharmacol. Ther. *16*, 354–363.

Anderson, G.J., and Frazer, D.M. (2017). Current understanding of iron homeostasis. Am. J. Clin. Nutr.

Anker, S.D., Comin Colet, J., Filippatos, G., Willenheimer, R., Dickstein, K., Drexler, H., Lüscher, T.F., Bart, B., Banasiak, W., Niegowska, J., et al. (2009). Ferric carboxymaltose in patients with heart failure and iron deficiency. N. Engl. J. Med. *361*, 2436–2448.

Arsenault, P.R., Song, D., Chung, Y.J., Khurana, T.S., and Lee, F.S. (2016). The Zinc Finger of Prolyl Hydroxylase Domain Protein 2 Is Essential for Efficient Hydroxylation of Hypoxia-Inducible Factor α. Mol. Cell. Biol. *36*, 2328–2343.

Asahi, M., Nakayama, H., Tada, M., and Otsu, K. (2003). Regulation of Sarco(endo)plasmic Reticulum Ca2+ Adenosine Triphosphatase by Phospholamban and Sarcolipin: Implication for Cardiac Hypertrophy and Failure. Trends Cardiovasc. Med. *13*, 152–157.

Asp, M.L., Martindale, J.J., Heinis, F.I., Wang, W., and Metzger, J.M. (2013). Calcium mishandling in diastolic dysfunction: mechanisms and potential therapies. Biochim. Biophys. Acta *1833*, 895–900.

Ather, S., Respress, J.L., Li, N., and Wehrens, X.H.T. (2013). Alterations in ryanodine receptors and related proteins in heart failure. Biochim. Biophys. Acta *1832*, 2425–2431.

Behjati, S., and Tarpey, P.S. (2013). What is next generation sequencing? Arch. Dis. Child. Educ. Pract. Ed. *98*, 236–238.

Berezin, A. (2016). Epigenetics in heart failure phenotypes. BBA Clin. *6*, 31–37.

Berg, J.M., Tymoczko, J.L., and Stryer, L. (2002). The Glycolytic Pathway Is Tightly Controlled.

Bermejo, F., and García-López, S. (2009). A guide to diagnosis of iron deficiency and iron deficiency anemia in digestive diseases. World J. Gastroenterol. WJG *15*, 4638–4643.

Betsuyaku, T., Kovacs, A., Saffitz, J.E., and Yamada, K.A. (2002). Cardiac structure and function in young and senescent mice heterozygous for a connexin43 null mutation. J. Mol. Cell. Cardiol. *34*, 175–184.

Beuckelmann, D.J., Näbauer, M., and Erdmann, E. (1992). Intracellular calcium handling in isolated ventricular myocytes from patients with terminal heart failure. Circulation *85*, 1046–1055.

Bianchi, L., Tacchini, L., and Cairo, G. (1999). HIF-1-mediated activation of transferrin receptor gene transcription by iron chelation. Nucleic Acids Res. *27*, 4223–4227.

van Bilsen, M., Smeets, P.J.H., Gilde, A.J., and van der Vusse, G.J. (2004). Metabolic remodelling of the failing heart: the cardiac burn-out syndrome? Cardiovasc. Res. *61*, 218–226.

Blaxall, B.C., Tschannen-Moran, B.M., Milano, C.A., and Koch, W.J. (2003). Differential gene expression and genomic patient stratification following left ventricular assist device support. J. Am. Coll. Cardiol. *41*, 1096–1106.

Bodi, I., Mikala, G., Koch, S.E., Akhter, S.A., and Schwartz, A. (2005). The L-type calcium channel in the heart: the beat goes on. J. Clin. Invest. *115*, 3306–3317.

Boldyrev, A.A. (2007). Carnosine and Oxidative Stress in Cells and Tissues (Nova Publishers).

Bolger, A.P., Bartlett, F.R., Penston, H.S., O'Leary, J., Pollock, N., Kaprielian, R., and Chapman, C.M. (2006). Intravenous Iron Alone for the Treatment of Anemia in Patients With Chronic Heart Failure. J. Am. Coll. Cardiol. *48*, 1225–1227.

Borlak, J., and Thum, T. (2003). Hallmarks of ion channel gene expression in end-stage heart failure. FASEB J. *17*, 1592–1608.

Brooks, K.J., Hargreaves, I.P., and Bates, T.E. (2000). Nitric-Oxide-Induced Inhibition of Mitochondrial Complexes following Aglycaemic Hypoxia in Neonatal Cortical Rat Brain Slices. Dev. Neurosci. *22*, 359–365.

Bugger, H., Schwarzer, M., Chen, D., Schrepper, A., Amorim, P.A., Schoepe, M., Nguyen, T.D., Mohr, F.W., Khalimonchuk, O., Weimer, B.C., et al. (2010). Proteomic remodelling of mitochondrial oxidative pathways in pressure overload-induced heart failure. Cardiovasc. Res. *85*, 376–384.

Buonocore, D., and Wallace, E. (2014). Comprehensive guideline for care of patients with heart failure. AACN Adv. Crit. Care *25*, 151–162.

Camaschella, C. (2015). Iron-Deficiency Anemia. N. Engl. J. Med. *372*, 1832–1843.

Camaschella, C. (2017). New insights into iron deficiency and iron deficiency anemia. Blood Rev.

Camelliti, P., Borg, T.K., and Kohl, P. (2005). Structural and functional characterisation of cardiac fibroblasts. Cardiovasc. Res. *65*, 40–51.

Catterall, W.A. (2015). Regulation of Cardiac Calcium Channels in the Fight-or-Flight Response. Curr. Mol. Pharmacol. *8*, 12–21.

Chattipakorn, N., Kumfu, S., Fucharoen, S., and Chattipakorn, S. (2011). Calcium channels and iron uptake into the heart. World J. Cardiol. *3*, 215–218.

Chen, S., and Li, S. (2012). The Na+/Ca2+ exchanger in cardiac ischemia/reperfusion injury. Med. Sci. Monit. Int. Med. J. Exp. Clin. Res. *18*, RA161-RA165.

Cioffi, G., Gatti, D., and Adami, S. (2010). [Vitamin D deficiency, left ventricular dysfunction and heart failure]. G. Ital. Cardiol. 2006 *11*, 645–653.

Cohen-Solal, A., Leclercq, C., Deray, G., Lasocki, S., Zambrowski, J.-J., Mebazaa, A., Groote, P. de, Damy, T., and Galinier, M. (2014). Iron deficiency: an emerging therapeutic target in heart failure. Heart *100*, 1414–1420.

Cotroneo, E., Ashek, A., Wang, L., Wharton, J., Dubois, O.D., Bozorgi, S.S., Busbridge, M., Alavian, K.N., Wilkins, M.R., and Zhao, L. (2015). Iron Homeostasis and Pulmonary Hypertension: Iron Deficiency Leads to Pulmonary Vascular Remodeling in the Rat. Circ. Res. CIRCRESAHA.114.305265.

Crocini, C., Coppini, R., Ferrantini, C., Yan, P., Loew, L.M., Tesi, C., Cerbai, E., Poggesi, C., Pavone, F.S., and Sacconi, L. (2014). Defects in T-tubular electrical activity underlie local alterations of calcium release in heart failure. Proc. Natl. Acad. Sci. U. S. A. *111*, 15196–15201.

Crossman, D.J., Jayasinghe, I.D., and Soeller, C. (2017). Transverse tubule remodelling: a cellular pathology driven by both sides of the plasmalemma? Biophys. Rev.

De Domenico, I., Ward, D.M., and Kaplan, J. (2007). Hepcidin regulation: ironing out the details. J. Clin. Invest. *117*, 1755–1758.

Depre, C., Shipley, G.L., Chen, W., Han, Q., Doenst, T., Moore, M.L., Stepkowski, S., Davies, P.J., and Taegtmeyer, H. (1998). Unloaded heart in vivo replicates fetal gene expression of cardiac hypertrophy. Nat. Med. *4*, 1269–1275.

Dewenter, M., Lieth, A. von der, Katus, H.A., and Backs, J. (2017). Calcium Signaling and Transcriptional Regulation in Cardiomyocytes. Circ. Res. *121*, 1000–1020.

Di Salvo, T.G., and Haldar, S.M. (2014). Epigenetic Mechanisms in Heart Failure Pathogenesis. Circ. Heart Fail. *7*, 850–863.

Dirkx, E., da Costa Martins, P.A., and De Windt, L.J. (2013). Regulation of fetal gene expression in heart failure. Biochim. Biophys. Acta BBA - Mol. Basis Dis. *1832*, 2414–2424.

Dobin, A., Davis, C.A., Schlesinger, F., Drenkow, J., Zaleski, C., Jha, S., Batut, P., Chaisson, M., and Gingeras, T.R. (2013). STAR: ultrafast universal RNA-seq aligner. Bioinformatics *29*, 15–21.

Dobrev, D., and Wehrens, X.H.T. (2014). Role of RyR2 Phosphorylation in Heart Failure and ArrhythmiasResponse to Dobrev and Wehrens: Controversies Around Ryanodine Receptor Phosphorylation in Cardiac Disease. Circ. Res. *114*, 1311–1319.

Dodd, M.S., Ball, V., Bray, R., Ashrafian, H., Watkins, H., Clarke, K., and Tyler, D.J. (2013). In vivo mouse cardiac hyperpolarized magnetic resonance spectroscopy. J. Cardiovasc. Magn. Reson. *15*, 19.

Doenst, T., Nguyen, T.D., and Abel, E.D. (2013). Cardiac Metabolism in Heart Failure: Implications Beyond ATP Production. Circ. Res. *113*, 709–724.

Drago, I., Stefani, D.D., Rizzuto, R., and Pozzan, T. (2012). Mitochondrial Ca2+ uptake contributes to buffering cytoplasmic Ca2+ peaks in cardiomyocytes. Proc. Natl. Acad. Sci. *109*, 12986–12991.

Dyck, J.R.B., and Lopaschuk, G.D. (2002). Malonyl CoA control of fatty acid oxidation in the ischemic heart. J. Mol. Cell. Cardiol. *34*, 1099–1109.

Ebner, N., and von Haehling, S. (2013). Iron deficiency in heart failure: a practical guide. Nutrients *5*, 3730–3739.

Eisner, D.A., Caldwell, J.L., Kistamás, K., and Trafford, A.W. (2017). Calcium and Excitation-Contraction Coupling in the Heart. Circ. Res. *121*, 181–195.

Ezekiel, E., and Morgan, E.H. (1963). Milk iron and its metabolism in the lactating rat. J. Physiol. *165*, 336–347.

Fernie, A.R., Carrari, F., and Sweetlove, L.J. (2004). Respiratory metabolism: glycolysis, the TCA cycle and mitochondrial electron transport. Curr. Opin. Plant Biol. *7*, 254–261.

Finch, C.A., Stray, S., Huebers, H.A., Bellotti, V., Lipschitz, D.A., Cook, J.D., and Pippard, M.J. (1986). Plasma Ferritin Determination as a Diagnostic Tool. West. J. Med. *145*, 657–663.

Frazer, D.M., Wilkins, S.J., Darshan, D., Mirciov, C.S.G., Dunn, L.A., and Anderson, G.J. (2016). Ferroportin Is Essential for Iron Absorption During Suckling, But Is

Hyporesponsive to the Regulatory Hormone Hepcidin. Cell. Mol. Gastroenterol. Hepatol. *3*, 410–421.

Frise, M.C., Cheng, H.-Y., Nickol, A.H., Curtis, M.K., Pollard, K.A., Roberts, D.J., Ratcliffe, P.J., Dorrington, K.L., and Robbins, P.A. (2016). Clinical iron deficiency disturbs normal human responses to hypoxia. J. Clin. Invest. *126*, 2139–2150.

Fujishiro, H., Yano, Y., Takada, Y., Tanihara, M., and Himeno, S. (2012). Roles of ZIP8, ZIP14, and DMT1 in transport of cadmium and manganese in mouse kidney proximal tubule cells. Met. Integr. Biometal Sci. *4*, 700–708.

Fukuda, R., Zhang, H., Kim, J., Shimoda, L., Dang, C.V., and Semenza, G.L. (2007). HIF-1 Regulates Cytochrome Oxidase Subunits to Optimize Efficiency of Respiration in Hypoxic Cells. Cell *129*, 111–122.

Gammella, E., Diaz, V., Recalcati, S., Buratti, P., Samaja, M., Dey, S., Noguchi, C.T., Gassmann, M., and Cairo, G. (2015a). Erythropoietin's inhibiting impact on hepcidin expression occurs indirectly. Am. J. Physiol. Regul. Integr. Comp. Physiol. *308*, R330-335.

Gammella, E., Recalcati, S., Rybinska, I., Buratti, P., and Cairo, G. (2015b). Iron-Induced Damage in Cardiomyopathy: Oxidative-Dependent and Independent Mechanisms. Oxid. Med. Cell. Longev. *2015*.

Ghigo, A., Laffargue, M., Li, M., and Hirsch, E. (2017). PI3K and Calcium Signaling in Cardiovascular Disease. Circ. Res. *121*, 282–292.

Ginsburg, K.S., and Bers, D.M. (2004). Modulation of excitation-contraction coupling by isoproterenol in cardiomyocytes with controlled SR Ca2+ load and Ca2+ current trigger. J. Physiol. *556*, 463–480.

Ginzburg, Y., and Rivella, S. (2011). β-thalassemia: a model for elucidating the dynamic regulation of ineffective erythropoiesis and iron metabolism. Blood *118*, 4321–4330.

Goldstein, D., Felzen, B., Youdim, M., Lotan, R., and Binah, O. (1996). Experimental Iron Deficiency in Rats: Mechanical and Electrophysiological Alterations in the Cardiac Muscle. Clin. Sci. *91*, 233–239.

Golman, K., in 't Zandt, R., and Thaning, M. (2006). Real-time metabolic imaging. Proc. Natl. Acad. Sci. U. S. A. *103*, 11270–11275.

Gomez-Ospina, N., Tsuruta, F., Barreto-Chang, O., Hu, L., and Dolmetsch, R. (2006). The C Terminus of the L-Type Voltage-Gated Calcium Channel CaV1.2 Encodes a Transcription Factor. Cell *127*, 591–606.

Goonasekera, S.A., Hammer, K., Auger-Messier, M., Bodi, I., Chen, X., Zhang, H., Reiken, S., Elrod, J.W., Correll, R.N., York, A.J., et al. (2012). Decreased cardiac L-type Ca^{2+} channel activity induces hypertrophy and heart failure in mice. J. Clin. Invest. *122*, 280–290.

Gray, L.R., Tompkins, S.C., and Taylor, E.B. (2014). Regulation of pyruvate metabolism and human disease. Cell. Mol. Life Sci. CMLS *71*, 2577–2604.

Grunstein, M. (1990). Histone Function in Transcription. Annu. Rev. Cell Biol. *6*, 643–676.

Guatimosim, S., Guatimosim, C., and Song, L.-S. (2011). Imaging Calcium Sparks in Cardiac Myocytes. Methods Mol. Biol. Clifton NJ *689*, 205–214.

Gujja, P., Rosing, D.R., Tripodi, D.J., and Shizukuda, Y. (2010). Iron Overload Cardiomyopathy, Better Understanding of An Increasing Disorder. J. Am. Coll. Cardiol. *56*, 1001–1012.

Gwathmey, J.K., Warren, S.E., Briggs, G.M., Copelas, L., Feldman, M.D., Phillips, P.J., Callahan, M., Schoen, F.J., Grossman, W., and Morgan, J.P. (1991). Diastolic dysfunction in hypertrophic cardiomyopathy. Effect on active force generation during systole. J. Clin. Invest. *87*, 1023–1031.

von Haehling, S., Jankowska, E.A., van Veldhuisen, D.J., Ponikowski, P., and Anker, S.D. (2015). Iron deficiency and cardiovascular disease. Nat. Rev. Cardiol. *12*, 659–669.

Heigenhauser, G.J., and Parolin, M.L. (1999). Role of pyruvate dehydrogenase in lactate production in exercising human skeletal muscle. Adv. Exp. Med. Biol. *474*, 205–218.

Hentze, M.W., Muckenthaler, M.U., and Andrews, N.C. (2004). Balancing Acts: Molecular Control of Mammalian Iron Metabolism. Cell *117*, 285–297.

Hentze, M.W., Muckenthaler, M.U., Galy, B., and Camaschella, C. (2010). Two to Tango: Regulation of Mammalian Iron Metabolism. Cell *142*, 24–38.

Herrmann, G., and Decherd, G. (1939). The Chemical Nature of Heart Failure. Ann. Intern. Med. *12*, 1233.

Hohl, M., Wagner, M., Reil, J.-C., Müller, S.-A., Tauchnitz, M., Zimmer, A.M., Lehmann, L.H., Thiel, G., Böhm, M., Backs, J., et al. (2013). HDAC4 controls histone methylation in response to elevated cardiac load. J. Clin. Invest. *123*, 1359–1370.

Hong, T., and Shaw, R.M. (2017). Cardiac T-Tubule Microanatomy and Function. Physiol. Rev. *97*, 227–252.

Huang, M.L.-H., Lane, D.J.R., and Richardson, D.R. (2011). Mitochondrial Mayhem: The Mitochondrion as a Modulator of Iron Metabolism and Its Role in Disease. Antioxid. Redox Signal. *15*, 3003–3019.

Imahashi, K., Pott, C., Goldhaber, J.I., Steenbergen, C., Philipson, K.D., and Murphy, E. (2005). Cardiac-specific ablation of the Na+-Ca2+ exchanger confers protection against ischemia/reperfusion injury. Circ. Res. *97*, 916–921.

Ingwall, J.S. (2009a). Energy metabolism in heart failure and remodelling. Cardiovasc. Res. *81*, 412–419.

Ingwall, J.S. (2009b). Energy metabolism in heart failure and remodelling. Cardiovasc. Res. *81*, 412–419.

Jankowska, E.A., Ponikowski, P., Piepoli, M.F., Banasiak, W., Anker, S.D., and Poole-Wilson, P.A. (2006). Autonomic imbalance and immune activation in chronic heart failure - pathophysiological links. Cardiovasc. Res. *70*, 434–445.

Jankowska, E.A., Haehling, S. von, Anker, S.D., Macdougall, I.C., and Ponikowski, P. (2012). Iron deficiency and heart failure: diagnostic dilemmas and therapeutic perspectives. Eur. Heart J. ehs224.

Jankowska, E.A., von Haehling, S., Anker, S.D., Macdougall, I.C., and Ponikowski, P. (2013). Iron deficiency and heart failure: diagnostic dilemmas and therapeutic perspectives. Eur. Heart J. *34*, 816–829.

Jaswal, J.S., Keung, W., Wang, W., Ussher, J.R., and Lopaschuk, G.D. (2011). Targeting fatty acid and carbohydrate oxidation--a novel therapeutic intervention in the ischemic and failing heart. Biochim. Biophys. Acta *1813*, 1333–1350.

Jeanteur, P. (2012). Cytoplasmic fate of messenger RNA (Springer Science & Business Media).

Jorgensen, P., and Is, S.R. (2014). Extracellular Matrix Modulates Morphology, Growth, Oxidative Stress Response and Functionality of Human Skin Fibroblasts during Aging In Vitro. J. Aging Sci. *2*.

Jorgensen, A.O., Shen, A.C., Arnold, W., McPherson, P.S., and Campbell, K.P. (1993). The Ca2+-release channel/ryanodine receptor is localized in junctional and corbular sarcoplasmic reticulum in cardiac muscle. J. Cell Biol. *120*, 969–980.

Joubert, F., Wilding, J.R., Fortin, D., Domergue-Dupont, V., Novotova, M., Ventura-Clapier, R., and Veksler, V. (2008). Local energetic regulation of sarcoplasmic and myosin ATPase is differently impaired in rats with heart failure. J. Physiol. *586*, 5181–5192.

Jurica, M.S., Mesecar, A., Heath, P.J., Shi, W., Nowak, T., and Stoddard, B.L. (1998). The allosteric regulation of pyruvate kinase by fructose-1,6-bisphosphate. Structure *6*, 195–210.

Kaldor, I., and Ezekiel, E. (1962). Iron Content of Mammalian Breast Milk: Measurements in the Rat and in a Marsupial. Nature *196*, 175–175.

Kamikawa, Y.F., and Donohoe, M.E. (2014). The localization of histone H3K27me3 demethylase Jmjd3 is dynamically regulated. Epigenetics *9*, 834–841.

Kanatous, S.B., Mammen, P.P.A., Rosenberg, P.B., Martin, C.M., White, M.D., DiMaio, J.M., Huang, G., Muallem, S., and Garry, D.J. (2009). Hypoxia reprograms calcium signaling and regulates myoglobin expression. Am. J. Physiol. - Cell Physiol. *296*, C393–C402.

Kaneda, R., Takada, S., Yamashita, Y., Choi, Y.L., Nonaka-Sarukawa, M., Soda, M., Misawa, Y., Isomura, T., Shimada, K., and Mano, H. (2009). Genome-wide histone methylation profile for heart failure. Genes Cells Devoted Mol. Cell. Mech. *14*, 69–77.

Kautz, L., Jung, G., Du, X., Gabayan, V., Chapman, J., Nasoff, M., Nemeth, E., and Ganz, T. (2015). Erythroferrone contributes to hepcidin suppression and iron overload in a mouse model of β-thalassemia. Blood *126*, 2031–2037.

Kawabata, H. (2017). The mechanisms of systemic iron homeostasis and etiology, diagnosis, and treatment of hereditary hemochromatosis. Int. J. Hematol. 1–13.

Kohlhaas, M., and Maack, C. (2013). Calcium release microdomains and mitochondria. Cardiovasc. Res. *98*, 259–268.

Kolwicz, S.C., and Tian, R. (2011). Glucose metabolism and cardiac hypertrophy. Cardiovasc. Res. *90*, 194–201.

Kolwicz, S.C., Purohit, S., and Tian, R. (2013). Cardiac Metabolism and its Interactions With Contraction, Growth, and Survival of Cardiomyocytes. Circ. Res. *113*, 603–616.

Laftah, A.H., Latunde-Dada, G.O., Fakih, S., Hider, R.C., Simpson, R.J., and McKie, A.T. (2009). Haem and folate transport by proton-coupled folate transporter/haem carrier protein 1 (SLC46A1). Br. J. Nutr. *101*, 1150–1156.

Lakhal-Littleton, S., Wolna, M., Carr, C.A., Miller, J.J.J., Christian, H.C., Ball, V., Santos, A., Diaz, R., Biggs, D., Stillion, R., et al. (2015). Cardiac ferroportin regulates cellular iron homeostasis and is important for cardiac function. Proc. Natl. Acad. Sci. U. S. A. *112*, 3164–3169.

Lakhal-Littleton, S., Wolna, M., Chung, Y.J., Christian, H.C., Heather, L.C., Brescia, M., Ball, V., Diaz, R., Santos, A., Biggs, D., et al. (2016). An essential cell-autonomous role for hepcidin in cardiac iron homeostasis. ELife *5*, e19804.

Landstrom, A.P., Dobrev, D., and Wehrens, X.H.T. (2017). Calcium Signaling and Cardiac Arrhythmias. Circ. Res. *120*, 1969–1993.

Le Blanc, S., Garrick, M.D., and Arredondo, M. (2012). Heme carrier protein 1 transports heme and is involved in heme-Fe metabolism. Am. J. Physiol. Cell Physiol. *302*, C1780-1785.

Le Page, L.M., Ball, D.R., Ball, V., Dodd, M.S., Miller, J.J., Heather, L.C., and Tyler, D.J. (2016). Simultaneous in vivo assessment of cardiac and hepatic metabolism in the diabetic rat using hyperpolarized MRS. NMR Biomed. *29*, 1759–1767.

Lee, F.S. (2008). Genetic causes of erythrocytosis and the oxygen-sensing pathway. Blood Rev. *22*, 321–332.

Lee, F.S., Percy, M.J., and McMullin, M.F. (2006). Oxygen sensing: recent insights from idiopathic erythrocytosis. Cell Cycle Georget. Tex *5*, 941–945.

Leecharoenkiat, K., Lithanatudom, P., Sornjai, W., and Smith, D.R. (2016). Iron dysregulation in beta-thalassemia. Asian Pac. J. Trop. Med. *9*, 1035–1043.

Lei, M., Huang, C.L.-H., Solaro, R.J., and Ke, Y. (2016). Ca2+ Signaling and Heart Rhythm (Frontiers Media SA).

Li, B., Dedman, J.R., and Kaetzel, M.A. (2006). Nuclear Ca2+/calmodulin-dependent protein kinase II in the murine heart. Biochim. Biophys. Acta *1763*, 1275–1281.

Li, H., Handsaker, B., Wysoker, A., Fennell, T., Ruan, J., Homer, N., Marth, G., Abecasis, G., Durbin, R., and 1000 Genome Project Data Processing Subgroup (2009). The Sequence Alignment/Map format and SAMtools. Bioinforma. Oxf. Engl. *25*, 2078–2079.

Liao, Y., Smyth, G.K., and Shi, W. (2014). featureCounts: an efficient general purpose program for assigning sequence reads to genomic features. Bioinforma. Oxf. Engl. *30*, 923–930.

Liu, Q., Davidoff, O., Niss, K., and Haase, V.H. (2012). Hypoxia-inducible factor regulates hepcidin via erythropoietin-induced erythropoiesis. J. Clin. Invest. *122*, 4635–4644.

Liu, Y., Morley, M., Brandimarto, J., Hannenhalli, S., Hu, Y., Ashley, E.A., Tang, W.H.W., Moravec, C.S., Margulies, K.B., Cappola, T.P., et al. (2015). RNA-Seq identifies novel myocardial gene expression signatures of heart failure. Genomics *105*, 83–89.

Ljubojevic, S., and Bers, D.M. (2015). Nuclear Calcium in Cardiac Myocytes. J. Cardiovasc. Pharmacol. *65*, 211–217.

Lodish, H., Berk, A., Zipursky, S.L., Matsudaira, P., Baltimore, D., and Darnell, J. (2000). Electron Transport and Oxidative Phosphorylation.

Lopez, A., Cacoub, P., Macdougall, I.C., and Peyrin-Biroulet, L. (2016). Iron deficiency anaemia. The Lancet *387*, 907–916.

Love, M.I., Huber, W., and Anders, S. (2014). Moderated estimation of fold change and dispersion for RNA-seq data with DESeq2. Genome Biol. *15*, 550.

Lowes, B.D., Gilbert, E.M., Abraham, W.T., Minobe, W.A., Larrabee, P., Ferguson, D., Wolfel, E.E., Lindenfeld, J., Tsvetkova, T., Robertson, A.D., et al. (2002). Myocardial Gene Expression in Dilated Cardiomyopathy Treated with Beta-Blocking Agents. N. Engl. J. Med. *346*, 1357–1365.

Lozoff, B. (2007). Iron deficiency and child development. Food Nutr. Bull. *28*, S560–S571.

Luo, W., and Brouwer, C. (2013). Pathview: an R/Bioconductor package for pathway-based data integration and visualization. Bioinformatics *29*, 1830–1831.

Luo, W., Friedman, M.S., Shedden, K., Hankenson, K.D., and Woolf, P.J. (2009). GAGE: generally applicable gene set enrichment for pathway analysis. BMC Bioinformatics *10*, 161.

Lyseng-Williamson, K.A., and Keating, G.M. (2009). Ferric carboxymaltose: a review of its use in iron-deficiency anaemia. Drugs *69*, 739–756.

Maack, C., Cortassa, S., Aon, M.A., Ganesan, A.N., Liu, T., and O'Rourke, B. (2006). Elevated Cytosolic Na+ Decreases Mitochondrial Ca2+ Uptake During Excitation-Contraction Coupling and Impairs Energetic Adaptation in Cardiac Myocytes. Circ. Res. *99*, 172–182.

MacLennan, D.H., and Kranias, E.G. (2003). Calcium: Phospholamban: a crucial regulator of cardiac contractility. Nat. Rev. Mol. Cell Biol. *4*, 566.

Marín-García, J., and Akhmedov, A.T. (2015). Epigenetics of the failing heart. Heart Fail. Rev. *20*, 435–459.

Mastrogiannaki, M., Matak, P., and Peyssonnaux, C. (2013). The gut in iron homeostasis: role of HIF-2 under normal and pathological conditions. Blood *122*, 885–892.

Mathiyalagan, P., Keating, S.T., Du, X.-J., and El-Osta, A. (2014). Chromatin modifications remodel cardiac gene expression. Cardiovasc. Res. *103*, 7–16.

McCarthy, D.J., Chen, Y., and Smyth, G.K. (2012). Differential expression analysis of multifactor RNA-Seq experiments with respect to biological variation. Nucleic Acids Res. *40*, 4288–4297.

McDonagh, T., and Macdougall, I.C. (2015). Iron therapy for the treatment of iron deficiency in chronic heart failure: intravenous or oral? Eur. J. Heart Fail. *17*, 248–262.

McKie, A.T., Barrow, D., Latunde-Dada, G.O., Rolfs, A., Sager, G., Mudaly, E., Mudaly, M., Richardson, C., Barlow, D., Bomford, A., et al. (2001). An iron-regulated ferric reductase associated with the absorption of dietary iron. Science *291*, 1755–1759.

Medeiros, D.M., and Beard, J.L. (1998). Dietary iron deficiency results in cardiac eccentric hypertrophy in rats. Proc. Soc. Exp. Biol. Med. Soc. Exp. Biol. Med. N. Y. N *218*, 370–375.

Mercurio, S., Petrillo, S., Chiabrando, D., Bassi, Z.I., Gays, D., Camporeale, A., Vacaru, A., Miniscalco, B., Valperga, G., Silengo, L., et al. (2015). The heme exporter Flvcr1 regulates expansion and differentiation of committed erythroid progenitors by controlling intracellular heme accumulation. Haematologica *100*, 720–729.

Meynard, D., Vaja, V., Sun, C.C., Corradini, E., Chen, S., López-Otín, C., Grgurevic, L., Hong, C.C., Stirnberg, M., Gütschow, M., et al. (2011). Regulation of TMPRSS6 by BMP6 and iron in human cells and mice. Blood *118*, 747–756.

Miller, J.J., Lau, A.Z., Teh, I., Schneider, J.E., Kinchesh, P., Smart, S., Ball, V., Sibson, N.R., and Tyler, D.J. (2016). Robust and high resolution hyperpolarized metabolic imaging of the rat heart at 7 T with 3D spectral-spatial EPI. Magn. Reson. Med. *75*, 1515–1524.

Mørk, H.K., Sjaastad, I., Sande, J.B., Periasamy, M., Sejersted, O.M., and Louch, W.E. (2007). Increased cardiomyocyte function and Ca2+ transients in mice during early congestive heart failure. J. Mol. Cell. Cardiol. *43*, 177–186.

Morris, M.R., Hughes, D.J., Tian, Y.-M., Ricketts, C.J., Lau, K.W., Gentle, D., Shuib, S., Serrano-Fernandez, P., Lubinski, J., Wiesener, M.S., et al. (2009). Mutation analysis of hypoxia-inducible factors HIF1A and HIF2A in renal cell carcinoma. Anticancer Res. *29*, 4337–4343.

de Nadal, E., Ammerer, G., and Posas, F. (2011). Controlling gene expression in response to stress. Nat. Rev. Genet. *12*, 833–845.

Nakayama, H., Chen, X., Baines, C.P., Klevitsky, R., Zhang, X., Zhang, H., Jaleel, N., Chua, B.H.L., Hewett, T.E., Robbins, J., et al. (2007). Ca2+- and mitochondrial-dependent cardiomyocyte necrosis as a primary mediator of heart failure. J. Clin. Invest. *117*, 2431–2444.

Nam, H., and Knutson, M.D. (2012). Effect of dietary iron deficiency and overload on the expression of ZIP metal-ion transporters in rat liver. Biometals Int. J. Role Met. Ions Biol. Biochem. Med. *25*, 115–124.

Naranjo, J.R., and Mellström, B. (2012). Ca2+-dependent Transcriptional Control of Ca2+ Homeostasis. J. Biol. Chem. *287*, 31674–31680.

Neglia, D., De Caterina, A., Marraccini, P., Natali, A., Ciardetti, M., Vecoli, C., Gastaldelli, A., Ciociaro, D., Pellegrini, P., Testa, R., et al. (2007). Impaired myocardial metabolic reserve and substrate selection flexibility during stress in patients with idiopathic dilated cardiomyopathy. Am. J. Physiol. Heart Circ. Physiol. *293*, H3270-3278.

Neu, J. (2008). Neonatology: Questions and Controversies Series: Gastroenterology and Nutrition (Elsevier Health Sciences).

Neubauer, S. (2007). The failing heart--an engine out of fuel. N. Engl. J. Med. *356*, 1140–1151.

Noordali, H., Loudon, B.L., Frenneaux, M.P., and Madhani, M. (2017). Cardiac metabolism — A promising therapeutic target for heart failure. Pharmacol. Ther.

Oexle, H., Gnaiger, E., and Weiss, G. (1999). Iron-dependent changes in cellular energy metabolism: influence on citric acid cycle and oxidative phosphorylation. Biochim. Biophys. Acta BBA - Bioenerg. *1413*, 99–107.

Okonko, D.O., Grzeslo, A., Witkowski, T., Mandal, A.K.J., Slater, R.M., Roughton, M., Foldes, G., Thum, T., Majda, J., Banasiak, W., et al. (2008). Effect of intravenous iron sucrose on exercise tolerance in anemic and nonanemic patients with symptomatic chronic heart failure and iron deficiency FERRIC-HF: a randomized, controlled, observer-blinded trial. J. Am. Coll. Cardiol. *51*, 103–112.

Opie, L.H. (2004). Heart Physiology: From Cell to Circulation (Lippincott Williams & Wilkins).

Otto-Duessel, M., Brewer, C., and Wood, J.C. (2011). Interdependence of Cardiac Iron and Calcium in a Murine Model of Iron Overload. Transl. Res. J. Lab. Clin. Med. *157*, 92–99.

Oxenham, H., and Sharpe, N. (2003). Cardiovascular aging and heart failure. Eur. J. Heart Fail. *5*, 427–434.

Özcelik, C., Erdmann, B., Pilz, B., Wettschureck, N., Britsch, S., Hübner, N., Chien, K.R., Birchmeier, C., and Garratt, A.N. (2002). Conditional mutation of the ErbB2 (HER2) receptor in cardiomyocytes leads to dilated cardiomyopathy. Proc. Natl. Acad. Sci. *99*, 8880–8885.

Pantopoulos, K. (2008). Function of the hemochromatosis protein HFE: Lessons from animal models. World J. Gastroenterol. *14*, 6893–6901.

Papait, R., Greco, C., Kunderfranco, P., Latronico, M.V.G., and Condorelli, G. (2013a). Epigenetics: a new mechanism of regulation of heart failure? Basic Res. Cardiol. *108*, 361.

Papait, R., Cattaneo, P., Kunderfranco, P., Greco, C., Carullo, P., Guffanti, A., Viganò, V., Stirparo, G.G., Latronico, M.V.G., Hasenfuss, G., et al. (2013b). Genome-wide analysis of histone marks identifying an epigenetic signature of promoters and enhancers underlying cardiac hypertrophy. Proc. Natl. Acad. Sci. *110*, 20164–20169.

Papait, R., Corrado, N., Rusconi, F., Serio, S., and V.G. Latronico, M. (2015). It's Time for An Epigenomics Roadmap of Heart Failure. Curr. Genomics *16*, 237–244.

Papanikolaou, G., and Pantopoulos, K. (2005). Iron metabolism and toxicity. Toxicol. Appl. Pharmacol. *202*, 199–211.

Parys, J.B. (2013). Calcium Techniques: A Laboratory Manual (Cold Spring Harbor, New York: Cold Spring Harbor Press).

Pedro-Segura, E., Vergara, S.V., Rodríguez-Navarro, S., Parker, R., Thiele, D.J., and Puig, S. (2008). The Cth2 ARE-binding Protein Recruits the Dhh1 Helicase to Promote the Decay of Succinate Dehydrogenase SDH4 mRNA in Response to Iron Deficiency. J. Biol. Chem. *283*, 28527–28535.

Pei, J.-M., Kravtsov, G.M., Wu, S., Das, R., Fung, M.L., and Wong, T.M. (2003). Calcium homeostasis in rat cardiomyocytes during chronic hypoxia: a time course study. Am. J. Physiol. Cell Physiol. *285*, C1420-1428.

Periasamy, M., and Janssen, P.M.L. (2008). Molecular basis of diastolic dysfunction. Heart Fail. Clin. *4*, 13–21.

Periasamy, M., Bhupathy, P., and Babu, G.J. (2008). Regulation of sarcoplasmic reticulum Ca2+ ATPase pump expression and its relevance to cardiac muscle physiology and pathology. Cardiovasc. Res. *77*, 265–273.

Petering, D.H., Stemmer, K.L., Lyman, S., Krezoski, S., and Petering, H.G. (1990). Iron deficiency in growing male rats: a cause of development of cardiomyopathy. Ann. Nutr. Metab. *34*, 232–243.

Peyssonnaux, C., Zinkernagel, A.S., Schuepbach, R.A., Rankin, E., Vaulont, S., Haase, V.H., Nizet, V., and Johnson, R.S. (2007). Regulation of iron homeostasis by the hypoxia-inducible transcription factors (HIFs). J. Clin. Invest. *117*, 1926–1932.

Peyssonnaux, C., Nizet, V., and Johnson, R.S. (2008). Role of the hypoxia inducible factors HIF in iron metabolism. Cell Cycle Georget. Tex *7*, 28–32.

Piacentino, V., Weber, C.R., Chen, X., Weisser-Thomas, J., Margulies, K.B., Bers, D.M., and Houser, S.R. (2003). Cellular Basis of Abnormal Calcium Transients of Failing Human Ventricular Myocytes. Circ. Res. *92*, 651–658.

Polin, R.A., Fox, W.W., and Abman, S.H. (2011). Fetal and Neonatal Physiology: Expert Consult - Online and Print (Elsevier Health Sciences).

Ponikowski, P., van Veldhuisen, D.J., Comin-Colet, J., Ertl, G., Komajda, M., Mareev, V., McDonagh, T., Parkhomenko, A., Tavazzi, L., Levesque, V., et al. (2015). Beneficial effects of long-term intravenous iron therapy with ferric carboxymaltose in patients with symptomatic heart failure and iron deficiency. Eur. Heart J. *36*, 657–668.

Ponka, P. (1999). Cellular iron metabolism. Kidney Int. *55*, S2–S11.

Porto, C.M., Silva, V.D.L., da Luz, J.S.B., Filho, B.M., and da Silveira, V.M. (2018). Association between vitamin D deficiency and heart failure risk in the elderly. ESC Heart Fail. *5*, 63–74.

Ren, X., Dorrington, K.L., Maxwell, P.H., and Robbins, P.A. (2000). Effects of desferrioxamine on serum erythropoietin and ventilatory sensitivity to hypoxia in humans. J. Appl. Physiol. Bethesda Md 1985 *89*, 680–686.

Respress, J.L., van Oort, R.J., Li, N., Rolim, N., Dixit, S., deAlmeida, A., Voigt, N., Lawrence, W.S., Skapura, D.G., Skårdal, K., et al. (2012). Role of RyR2 Phosphorylation at S2814 during Heart Failure Progression. Circ. Res. *110*, 1474–1483.

Rhodes, C.J., Wharton, J., Howard, L., Gibbs, J.S.R., Vonk-Noordegraaf, A., and Wilkins, M.R. (2011). Iron deficiency in pulmonary arterial hypertension: a potential therapeutic target. Eur. Respir. J. *38*, 1453–1460.

Ringnér, M. (2008). What is principal component analysis? Nat. Biotechnol. *26*, 303–304.

Rishi, G., and Subramaniam, V.N. (2017). The liver in regulation of iron homeostasis. Am. J. Physiol. - Gastrointest. Liver Physiol. ajpgi.00004.2017.

Rishi, G., Wallace, D.F., and Subramaniam, V.N. (2015). Hepcidin: regulation of the master iron regulator. Biosci. Rep. *35*.

Robinson, M.D., McCarthy, D.J., and Smyth, G.K. (2010). edgeR: a Bioconductor package for differential expression analysis of digital gene expression data. Bioinforma. Oxf. Engl. *26*, 139–140.

Rosca, M.G., Tandler, B., and Hoppel, C.L. (2013). Mitochondria in cardiac hypertrophy and heart failure. J. Mol. Cell. Cardiol. *55*, 31–41.

Rosenbaum, D. (2002). Quantitative Cardiac Electrophysiology (CRC Press).

Sato, D., and Bers, D.M. (2011). How Does Stochastic Ryanodine Receptor-Mediated Ca Leak Fail to Initiate a Ca Spark? Biophys. J. *101*, 2370–2379.

Sato, T., Chang, H.-C., Martínez-Pastor, M.T., Puig, S., Bayeva, M., Blackshear, P., Wilsbacher, L.D., and Ardehali, H. (2016). Abstract 12530: Tristetraprolin-mediated mRNA Degradation of Mitochondrial Electron Transport Chain Proteins Protects the Heart Against Iron Deficiency. Circulation *134*, A12530–A12530.

Satoh, M., Minami, Y., Takahashi, Y., and Nakamura, M. (2008). Immune modulation: role of the inflammatory cytokine cascade in the failing human heart. Curr. Heart Fail. Rep. *5*, 69–74.

Schipper, H.M. (2012). Neurodegeneration with brain iron accumulation — Clinical syndromes and neuroimaging. Biochim. Biophys. Acta BBA - Mol. Basis Dis. *1822*, 350–360.

Schofield, C., and Hausinger, R. (2015). 2-Oxoglutarate-Dependent Oxygenases (Royal Society of Chemistry).

Schröder, F., Handrock, R., Beuckelmann, D.J., Hirt, S., Hullin, R., Priebe, L., Schwinger, R.H.G., Weil, J., and Herzig, S. (1998). Increased Availability and Open Probability of Single L-Type Calcium Channels From Failing Compared With Nonfailing Human Ventricle. Circulation *98*, 969–976.

Schroeder, M.A., Clarke, K., Neubauer, S., and Tyler, D.J. (2011). Hyperpolarized Magnetic Resonance: A Novel Technique for the In Vivo Assessment of Cardiovascular Disease. Circulation *124*, 1580–1594.

Schwaller, B. (2010). Cytosolic Ca2+ Buffers. Cold Spring Harb. Perspect. Biol. *2*, a004051.

Semenza, G.L. (2000). HIF-1 and human disease: one highly involved factor. Genes Dev. *14*, 1983–1991.

Shanmugam, M., Gao, S., Hong, C., Fefelova, N., Nowycky, M.C., Xie, L.-H., Periasamy, M., and Babu, G.J. (2011). Ablation of phospholamban and sarcolipin results in cardiac hypertrophy and decreased cardiac contractility. Cardiovasc. Res. *89*, 353–361.

Shao, D., and Tian, R. (2015). Glucose Transporters in Cardiac Metabolism and Hypertrophy. Compr. Physiol. *6*, 331–351.

Simon, A. (2010). Babraham Bioinformatics - FastQC: A Quality Control tool for High Throughput Sequence Data.

Soltysinska, E., Olesen, S.-P., Christ, T., Wettwer, E., Varró, A., Grunnet, M., and Jespersen, T. (2009). Transmural expression of ion channels and transporters in human nondiseased and end-stage failing hearts. Pflüg. Arch. - Eur. J. Physiol. *459*, 11.

Song, D., Li, L.-S., Heaton-Johnson, K.J., Arsenault, P.R., Master, S.R., and Lee, F.S. (2013). Prolyl hydroxylase domain protein 2 (PHD2) binds a Pro-Xaa-Leu-Glu motif, linking it to the heat shock protein 90 pathway. J. Biol. Chem. *288*, 9662–9674.

Stein, A.B., Jones, T.A., Herron, T.J., Patel, S.R., Day, S.M., Noujaim, S.F., Milstein, M.L., Klos, M., Furspan, P.B., Jalife, J., et al. (2011). Loss of H3K4 methylation destabilizes gene expression patterns and physiological functions in adult murine cardiomyocytes. J. Clin. Invest. *121*, 2641–2650.

Stoltzfus, R.J. (2003). Iron Deficiency: Global Prevalence and Consequences. Food Nutr. Bull. *24*, S99–S103.

Stoltzfus, R.J., and Dreyfuss, M.L. (1998). Guidelines for the Use of Iron Supplements to Prevent and Treat Iron Deficiency Anemia (ILSI Press).

Strait, J.B., and Lakatta, E.G. (2012). Aging-associated cardiovascular changes and their relationship to heart failure. Heart Fail. Clin. *8*, 143–164.

Stuckey, D.J., Carr, C.A., Tyler, D.J., and Clarke, K. (2008). Cine-MRI versus two-dimensional echocardiography to measure in vivo left ventricular function in rat heart. NMR Biomed. *21*, 765–772.

Supek, F., Bošnjak, M., Škunca, N., and Šmuc, T. (2011). REVIGO Summarizes and Visualizes Long Lists of Gene Ontology Terms. PLOS ONE *6*, e21800.

Taegtmeyer, H., and Overturf, M.L. (1988). Effects of moderate hypertension on cardiac function and metabolism in the rabbit. Hypertens. Dallas Tex 1979 *11*, 416–426.

Taegtmeyer, H., Peterson, M.B., Ragavan, V.V., Ferguson, A.G., and Lesch, M. (1977). De novo alanine synthesis in isolated oxygen-deprived rabbit myocardium. J. Biol. Chem.

252, 5010–5018.

Taur, Y., and Frishman, W.H. (2005). The cardiac ryanodine receptor (RyR2) and its role in heart disease. Cardiol. Rev. *13*, 142–146.

Templeton, D. (2002). Molecular and Cellular Iron Transport (CRC Press).

Tyler, D.J., Lygate, C.A., Schneider, J.E., Cassidy, P.J., Neubauer, S., and Clarke, K. (2006). CINE-MR imaging of the normal and infarcted rat heart using an 11.7 T vertical bore MR system. J. Cardiovasc. Magn. Reson. Off. J. Soc. Cardiovasc. Magn. Reson. *8*, 327–333.

Valore, E.V., and Ganz, T. (2008). Posttranslational processing of hepcidin in human hepatocytes is mediated by the prohormone convertase furin. Blood Cells. Mol. Dis. *40*, 132–138.

Wal, H.H. van der, Comin-Colet, J., Klip, I.T., Enjuanes, C., Beverborg, N.G., Voors, A.A., Banasiak, W., Veldhuisen, D.J. van, Bruguera, J., Ponikowski, P., et al. (2015). Vitamin B12 and folate deficiency in chronic heart failure. Heart *101*, 302–310.

Wallace, D.F. (2016). The Regulation of Iron Absorption and Homeostasis. Clin. Biochem. Rev. *37*, 51–62.

Wang, G.L., and Semenza, G.L. (1993). Desferrioxamine induces erythropoietin gene expression and hypoxia-inducible factor 1 DNA-binding activity: implications for models of hypoxia signal transduction. Blood *82*, 3610–3615.

Wang, Z., Gerstein, M., and Snyder, M. (2009). RNA-Seq: a revolutionary tool for transcriptomics. Nat. Rev. Genet. *10*, 57–63.

Whetstine, J.R., Nottke, A., Lan, F., Huarte, M., Smolikov, S., Chen, Z., Spooner, E., Li, E., Zhang, G., Colaiacovo, M., et al. (2006). Reversal of histone lysine trimethylation by the JMJD2 family of histone demethylases. Cell *125*, 467–481.

van Wijk, R., Sutherland, S., Van Wesel, A.C.W., Huizinga, E.G., Percy, M.J., Bierings, M., and Lee, F.S. (2010). Erythrocytosis associated with a novel missense mutation in the HIF2A gene. Haematologica *95*, 829–832.

Wofford, J.D., Chakrabarti, M., and Lindahl, P.A. (2017). Mössbauer Spectra of Mouse Hearts Reveal Age-dependent Changes in Mitochondrial and Ferritin Iron Levels. J. Biol. Chem. *292*, 5546–5554.

Wongjaikam, S., Kumfu, S., Khamseekaew, J., Chattipakorn, S.C., and Chattipakorn, N. (2017). Restoring the impaired cardiac calcium homeostasis and cardiac function in iron

overload rats by the combined deferiprone and N-acetyl cysteine. Sci. Rep. *7*, srep44460.

Xie, W., Brochet, D.X.P., Wei, S., Wang, X., and Cheng, H. (2010). Deciphering ryanodine receptor array operation in cardiac myocytes. J. Gen. Physiol. *136*, 129–133.

Xu, K.Y., Zweier, J.L., and Becker, L.C. (1995). Functional coupling between glycolysis and sarcoplasmic reticulum Ca2+ transport. Circ. Res. *77*, 88–97.

Xu, W., Barrientos, T., Mao, L., Rockman, H.A., Sauve, A.A., and Andrews, N.C. (2015). Lethal cardiomyopathy in mice lacking transferrin receptor in the heart. Cell Rep. *13*, 533–545.

Zamora, T.G., Guiang 3rd, S.F., Widness, J.A., and Georgieff, M.K. (2016). Iron is prioritized to red blood cells over the brain in phlebotomized anemic newborn lambs. Pediatr. Res. *79*, 922–928.

Zhabyeyev, P., and Oudit, G.Y. (2017). Unravelling the molecular basis for cardiac iron metabolism and deficiency in heart failure. Eur. Heart J. *38*, 373–375.

Zhang, Y., and Reinberg, D. (2001). Transcription regulation by histone methylation: interplay between different covalent modifications of the core histone tails. Genes Dev. *15*, 2343–2360.

Zhang, Q.-J., Chen, H.-Z., Wang, L., Liu, D.-P., Hill, J.A., and Liu, Z.-P. (2011). The histone trimethyllysine demethylase JMJD2A promotes cardiac hypertrophy in response to hypertrophic stimuli in mice. J. Clin. Invest. *121*, 2447–2456.

Zhao, S., Fung-Leung, W.-P., Bittner, A., Ngo, K., and Liu, X. (2014). Comparison of RNA-Seq and Microarray in Transcriptome Profiling of Activated T Cells. PLOS ONE *9*, e78644.

Zima, A.V., Kockskämper, J., and Blatter, L.A. (2006). Cytosolic energy reserves determine the effect of glycolytic sugar phosphates on sarcoplasmic reticulum Ca2+ release in cat ventricular myocytes. J. Physiol. *577*, 281–293.

Zou, Y., Liang, Y., Gong, H., Zhou, N., Ma, H., Guan, A., Sun, A., Wang, P., Niu, Y., Jiang, H., et al. (2011). Ryanodine receptor type 2 is required for the development of pressure overload-induced cardiac hypertrophy. Hypertens. Dallas Tex 1979 *58*, 1099–1110.